

1989

A measurement of the decay rate for the process kaon(L) going to positive muon negative muon

Christopher John Kenney
College of William & Mary - Arts & Sciences

Follow this and additional works at: <https://scholarworks.wm.edu/etd>



Part of the [Physics Commons](#)

Recommended Citation

Kenney, Christopher John, "A measurement of the decay rate for the process kaon(L) going to positive muon negative muon" (1989). *Dissertations, Theses, and Masters Projects*. Paper 1539623786.
<https://dx.doi.org/doi:10.21220/s2-dv7n-cj19>

This Dissertation is brought to you for free and open access by the Theses, Dissertations, & Master Projects at W&M ScholarWorks. It has been accepted for inclusion in Dissertations, Theses, and Masters Projects by an authorized administrator of W&M ScholarWorks. For more information, please contact scholarworks@wm.edu.

INFORMATION TO USERS

The most advanced technology has been used to photograph and reproduce this manuscript from the microfilm master. UMI films the text directly from the original or copy submitted. Thus, some thesis and dissertation copies are in typewriter face, while others may be from any type of computer printer.

The quality of this reproduction is dependent upon the quality of the copy submitted. Broken or indistinct print, colored or poor quality illustrations and photographs, print bleedthrough, substandard margins, and improper alignment can adversely affect reproduction.

In the unlikely event that the author did not send UMI a complete manuscript and there are missing pages, these will be noted. Also, if unauthorized copyright material had to be removed, a note will indicate the deletion.

Oversize materials (e.g., maps, drawings, charts) are reproduced by sectioning the original, beginning at the upper left-hand corner and continuing from left to right in equal sections with small overlaps. Each original is also photographed in one exposure and is included in reduced form at the back of the book.

Photographs included in the original manuscript have been reproduced xerographically in this copy. Higher quality 6" x 9" black and white photographic prints are available for any photographs or illustrations appearing in this copy for an additional charge. Contact UMI directly to order.

U·M·I

University Microfilms International
A Bell & Howell Information Company
300 North Zeeb Road, Ann Arbor, MI 48106-1346 USA
313/761-4700 800/521-0600



Order Number 9022043

A measurement of the decay rate for the process $K_L \rightarrow \mu^+ \mu^-$

Kenney, Christopher John, Ph.D.

The College of William and Mary, 1989

U·M·I
300 N. Zeeb Rd.
Ann Arbor, MI 48106



A MEASUREMENT OF THE DECAY RATE
FOR THE PROCESS $K_L \rightarrow \mu^+ \mu^-$

A Dissertation

Presented to

The Faculty of the Department of Physics
The College of William and Mary in Virginia

In Partial Fulfillment

Of the Requirements for the Degree of
Doctor of Philosophy

by

Christopher John Kenney

1989

A MEASUREMENT OF THE DECAY RATE
FOR THE PROCESS $K_L \rightarrow \mu^+ \mu^-$

Christopher John Kenney

September 1989


WMHEG-89-5

Supported in part by the
National Science Foundation
Grant PHY-8517485

APPROVAL SHEET

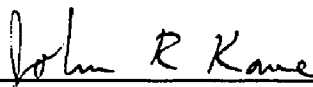
This dissertation is submitted in partial fulfillment of
the requirements for the degree of

Doctor of Philosophy



Christopher J. Kenney

Approved, September 1989



John R. Kane



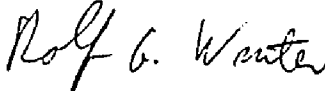
Carl E. Carlson



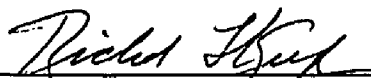
Morton Eckhause



Robert E. Welsh



Rolf G. Winter



Richard L. Kiefer
Department of Chemistry

DEDICATION

To my parents, John and Anne,
and to my wife Marie
for their patience and craftsmanship

TABLE OF CONTENTS

ACKNOWLEDGMENTS	vi
LIST OF TABLES.	viii
FIGURE CAPTIONS.	ix
ABSTRACT	xvi

<u>Chapter</u>	<u>Page</u>
I. INTRODUCTION	2
II. THEORETICAL CONSIDERATIONS	7
GIM Mechanism	7
Unitarity Limit	10
What Can We Learn	14
Muon Polarization	19
III. BEAMLINER AND DETECTORS	22
Drift Chambers	27
Trigger Scintillation Hodoscope	30
Cerenkov Counters	33
Electromagnetic Calorimeter	36
Muon Hodoscope	39
Muon Rangfinder	42
IV. DATA ACQUISITION	55
Level 1 Trigger	57
Level 2 Trigger	61
Level 3 Trigger	63
Readout of the Data	66

V.	ANALYSIS OF THE DATA	69
	Pattern Recognition	75
	Final Event Fitting	78
	Aperture Restrictions	82
	Calculation of Acceptances	84
	Pion Hadronic Interactions	87
	Hadron Decay Backgrounds	89
	Normalization of Sample	93
	Level 1 Trigger Bit Correction	95
	Level 3 Correction	96
	Muon Identification	99
	Number of $K_L \rightarrow \mu^+ \mu^-$ Candidates	108
	Determination of $B(K_{\pi\pi})/B(K_{\mu 3})$	112
VI.	CONCLUSION	115
	Future of Rare Kaon Experiments	118
	APPENDIX A	120
	BIBLIOGRAPHY	121
	VITA	125
	FIGURES	126

ACKNOWLEDGMENTS

I would like to thank the following individuals for their contributions to this work and to my education:

Dr. John Kane, my advisor throughout graduate school, for his patience, for his thoroughness, and for his dedication to teaching. John is one of the few people I have spent any time with, whom I have never been even slightly annoyed.

Dr. Morton Eckhause, for his insight and understanding as well as always having an open door.

Dr. Robert Welsh, for his savoir-faire and enthusiasm.

Dr. Rolf Winter, for clearing muddy waters and for writing a textbook on quantum mechanics.

Mr. William Vulcan, for sharing his knowledge regarding both technology and life.

James Mills, for never letting us down.

The AGS riggers, for always delivering the package.

The AGS operators, for many hours of good beam.

The staff of the Brookhaven computer facilities, for quick service.

Micheal Chapman, John Ginkel, and Jim Kraiman, for whatever was needed at the time.

Dr. Henry Weller, for starting me on the path of experimental physics.

All my teachers over the years, for imparting some of their knowledge to me.

Drs. Paul Guss, Dayle Hancock, Donald Joyce, Yunan Kuang, and Robert Whyley, for all their help and for their example.

Diane Fannin, Paula Spratley, and Sylvia Stout, for their invaluable assistance.

All of my fellow 791ers: K. Arisaka, L. Auerbach, S. Axelrod, K. Biery, G. Bonneaud, P. Buchholtz, M. Chapman, R. Cousins, G. Daniel, J. Frank, G. Hart, V. Highland, M. Ierano, G. Irwin, W. W. Kinnison, P. Knibbe, J. Konigsberg, J. Kubic, K. Lang, D. Lee, J. Margulies, C. Mathiazhagan, W. McFarlane, P. Melese, E. Milner, W. Molzon, D. Ouimette, J. Ritchie, P. Rubin, G. Sanders, M. Sivertz, W. Slater, Q. Trang, J. Urheim, D. Wagner, W. Wales, S. Wojcicki, and H. Ziock.

LIST OF TABLES

<u>Table</u>		<u>Page</u>
I	List of previous measurements of $B(K_L \rightarrow \mu^+ \mu^-)$	5
II	KM-matrix mixing elements versus the top mass.	15
III	Momenta associated with each rangefinder gap.	46
IV	Detector rates.	58
V	Level 1 logic for each trigger type.	59
VI	Distribution of Level 1 trigger bits.	70
VII	Stage 2 summary tapes.	72
VIII	Reasons for failing pattern recognition.	77
IX	Selection requirements for $K_L \rightarrow \mu^+ \mu^-$ events.	85
X	Geometric acceptances for various decay modes.	86
XI	Pion interaction probabilities.	88
XII	Muon selection efficiency versus momentum.	102
XIII	Rejection of pion interaction secondaries.	106
XIV	Values of factors used in the final calculation.	116
XV	Branching fractions for K_L decays	120

FIGURE CAPTIONS

- Figure 1. Examples of the GIM mechanism: (a) Z^0 exchange involving the first quark doublet, (b) Z^0 exchange involving the second quark doublet, (c) diagram for $K^+ \rightarrow \mu^+ \nu$.
- Figure 2. (a) The two-photon intermediate state contribution to $K_{\mu\mu}$ decay, (b) the single-particle intermediate state contributions to $K_{\gamma\gamma}$.
- Figure 3. Second order weak contributions to $K_{\mu\mu}$ decays: (a) the two W-boson exchange box diagram, (b) triangle graph involving the exchange of a Z^0 and 2 W-bosons, (c) triangle graph involving exchange of a Z^0 and a W.
- Figure 4. Dependence of $|s_2|$ on $|s_3|$, as found by Inami and Lim, assuming a top mass of 60 GeV/c².
- Figure 5. Relationship between branching fractions of $K_L \rightarrow \mu^+ \mu^-$ and $K^+ \rightarrow \pi^+ \nu \nu$.
- Figure 6. Possible diagrams contributing to muon polarization in the decay $K_L \rightarrow \mu^+ \mu^-$: (a) Higgs boson exchange, (b) Higgs boson exchange involving supersymmetric particles, (c) left-right box diagram, (d) leptoquark exchange.
- Figure 7. Layout of AGS experiment 791.
- Figure 8. Side view of the target, collimators, vacuum region, and shielding.
- Figure 9. Definition of the event collinearity.
- Figure 10. Geometry of a wire cell in the drift chambers.

- Figure 11. Beamright trigger scintillation hodoscope bank.
- Figure 12. Side view of the Cerenkov counter.
- Figure 13. Exploded view of the leadglass and finger hodoscope electromagnetic calorimetry system.
- Figure 14. Exploded view of the iron and muon hodoscope on the left side of the beam.
- Figure 15. Plan view of the entire muon rangefinder.
- Figure 16. Exploded diagram of the end of an proportional tube extrusion.
- Figure 17. Drawing of an x-measuring proportional tube plane.
- Figure 18. Drawing of a y-measuring proportional tube plane.
- Figure 19. Diagram of the gas distribution system for the rangefinder.
- Figure 20. Diagram of the gas control setup for the rangefinder.
- Figure 21. Level 0 trigger logic involving the trigger scintillator hodoscope. LTFX1T refers to the left-side, forward or upstream, x-measuring, phototube on attached to the top of the first counter.
- Figure 22. Level 1 logic for the drift chambers.
- Figure 23. Lepton identification logic used in the Level 1.
- Figure 24. Photon identification logic used in the Level 1.
- Figure 25. Overall logic for the Level 1.
- Figure 26. Schematic of the data acquisition architecture.
- Figure 27. Flowchart of the offline analysis.

- Figure 28. Fraction of events on a tape which are identified as being $K_L \rightarrow \pi^+\pi^-$ candidates for all tapes analyzed.
- Figure 29. Pattern recognition reconstruction efficiency per tape for prescaled dipion events.
- Figure 30. Pattern recognition reconstruction efficiency per tape for dilepton events.
- Figure 31. Comparison of x- and y-view track χ^2 s calculated by pattern recognition for pion and muon samples.
- Figure 32. Iterative fit vertex χ^2 distributions for Monte Carlo and data. The dashed and solid lines represent Monte Carlo and data events, respectively.
- Figure 33. Iterative fit x-track χ^2 distributions for Monte Carlo and data, normalized to the same number of events.
- Figure 34. Iterative fit y-track χ^2 distributions for Monte Carlo and data.
- Figure 35. Z-location of vertex for $K_L \rightarrow \pi^+\pi^-$ events.
- Figure 36. Vertex x/z positions for $K_L \rightarrow \pi^+\pi^-$ events.
- Figure 37. Vertex y/z positions for $K_L \rightarrow \pi^+\pi^-$ events.
- Figure 38. The uncut kaon momentum spectrum as generated by the offline Monte Carlo.
- Figure 39. Comparison of data and Monte Carlo accepted kaon momentum spectrum for $K_L \rightarrow \pi^+\pi^-$ events.
- Figure 40. Comparison of data and Monte Carlo track momentum spectrum for $K_L \rightarrow \pi^+\pi^-$ events.
- Figure 41. Comparison of data and Monte Carlo collinearity distributions for $K_L \rightarrow \pi^+\pi^-$ events.

- Figure 42. Comparison of data and Monte Carlo invariant mass for $K_L \rightarrow \pi^+ \pi^-$ events.
- Figure 43. Restricting the dipion invariant mass to lie between 493 and 503 MeV/c^2 , the invariant mass assuming the proton's and pion's masses for the tracks, is plotted for events with collinearity below 0.001 radians.
- Figure 44. Momentum asymmetry for events in minimum bias sample with collinearity less than 0.001 radians and masses between 493 and 503 MeV/c^2 .
- Figure 45. Momentum asymmetry for minimum bias events falling within $\pm 25 \text{ MeV}/c^2$ of the Λ^0 's mass using the proton/pion mass hypothesis.
- Figure 46. Invariant mass of Λ^0 s using the dipion mass hypothesis.
- Figure 47. Collinearity squared versus invariant mass for minimum bias events.
- Figure 48. Invariant mass of minimum bias events with collinearity below 0.001 radians. Monte Carlo simulated background is superimposed as a dashed line.
- Figure 49. Level 3 mass versus mass determined by the iterative fit.
- Figure 50. Vertex z-position distribution for minimum bias $K_{\pi\pi}$ events with the distribution for events satisfying the Level 3 cuts superimposed as a dashed line.
- Figure 51. X-view opening angle distribution for minimum bias $K_{\pi\pi}$ events with the distribution for events satisfying the Level 3 cuts superimposed as a dashed line.
- Figure 52. Y-view opening angle distribution for minimum bias $K_{\pi\pi}$ events with the distribution for events

satisfying the Level 3 cuts superimposed as a dashed line.

- Figure 53. X-position at first drift chamber distribution for minimum bias $K_{\pi\pi}$ events with the distribution for events satisfying the Level 3 cuts superimposed as a dashed line.
- Figure 54. Kaon momentum distribution for minimum bias $K_{\pi\pi}$ events with the distribution for events satisfying the Level 3 cuts superimposed as a dashed line.
- Figure 55. Invariant mass for simulated $K_{\pi\pi}$ events as calculated by pattern recognition.
- Figure 56. Invariant mass for simulated $K_{\pi 3}$ events as calculated by pattern recognition.
- Figure 57. Invariant mass for simulated $K_{\mu 3}$ events as calculated by pattern recognition.
- Figure 58. Invariant mass for simulated $K_{e 3}$ events as calculated by pattern recognition.
- Figure 59. Distributions of energy measured by the leadglass over the momentum determined by the drift chambers for both electrons and muons.
- Figure 60. Actual gap minus the expected gap in the rangefinder as simulated by GEANT for $K_{\mu\mu}$ decays.
- Figure 61. Actual gap minus the expected gap in the rangefinder for muons from $K_{\mu 3}$ decay.
- Figure 62. Actual gap minus the expected gap in the rangefinder for pions from $K_{\mu 3}$ decay.
- Figure 63. Collinearity squared versus invariant mass for the final sample of $K_{\mu\mu}$ events.
- Figure 64. Invariant mass of final $K_{\mu\mu}$ event sample.

- Figure 65. Collinearity squared of final $K_{\mu\mu}$ event sample.
- Figure 66. Distribution of energy measured by the leadglass over the momentum determined by the drift chambers for the dimuon sample with no offline muon identification cuts.
- Figure 67. Vertex z-location for the final $K_L \rightarrow \mu^+\mu^-$ event sample.
- Figure 68. Kaon momentum for the final $K_L \rightarrow \mu^+\mu^-$ event sample.
- Figure 69. Track momentum for the final $K_L \rightarrow \mu^+\mu^-$ event sample.
- Figure 70. Vertex χ^2 s for the final $K_L \rightarrow \mu^+\mu^-$ event sample.
- Figure 71. X-view track χ^2 s for the final $K_L \rightarrow \mu^+\mu^-$ event sample.
- Figure 72. Y-view track χ^2 s for the final $K_L \rightarrow \mu^+\mu^-$ event sample.
- Figure 73. Vertex x/z for the final $K_L \rightarrow \mu^+\mu^-$ event sample.
- Figure 74. Vertex y/z for the final $K_L \rightarrow \mu^+\mu^-$ event sample.
- Figure 75. Actual minus expected gap in the rangefinder for the final $K_L \rightarrow \mu^+\mu^-$ event sample.
- Figure 76. Muon hodoscope confidence level distribution for the final $K_L \rightarrow \mu^+\mu^-$ event sample.
- Figure 77. Distribution of energy measured by the leadglass over the momentum determined by the drift chambers for the final $K_L \rightarrow \mu^+\mu^-$ sample.
- Figure 78. Invariant mass distribution for the dimuon sample with all cuts imposed except for muon selection.

- Figure 79. Collinearity squared distribution for the dimuon sample with all cuts imposed except for muon selection.
- Figure 80. X view of one of the 87 $K_L \rightarrow \mu^+ \mu^-$ events with an invariant mass of $0.502 \text{ GeV}/c^2$ and collinearity of 0.0006.
- Figure 81. Y view of the event in Figure 80.
- Figure 82. X view of one of the 87 $K_L \rightarrow \mu^+ \mu^-$ events with an invariant mass of $0.502 \text{ GeV}/c^2$ and collinearity of 0.0003.
- Figure 83. Y view of the event in Figure 82.

ABSTRACT

A sample of 87 events of the GIM suppressed decay $K_L \rightarrow \mu^+ \mu^-$ were observed in an experiment performed in 1988 at the Brookhaven National Laboratory. Concurrently, 8,887 examples of the CP-violating decay $K_L \rightarrow \pi^+ \pi^-$ were also seen. The apparatus consisted of a double-magnet spectrometer as well as electromagnetic and muon detector systems. From the previously measured branching ratio for $K_L \rightarrow \pi^+ \pi^-$ and the different instrumental acceptances of the detector for the two decays, the data sample was normalized to the effective number of K_L decays observed. A value for the ratio $(K_L \rightarrow \mu^+ \mu^-) / (K_L \rightarrow \text{anything})$ of $(5.7 \pm 0.6(\text{stat.}) \pm 0.3(\text{syst.})) \times 10^{-9}$ was obtained.

A MEASUREMENT OF THE DECAY RATE
FOR THE PROCESS $K_L \rightarrow \mu^+ \mu^-$

CHAPTER I

INTRODUCTION

During the 1960's and 1970's, three landmark discoveries were made at the Alternating Gradient Synchrotron of the Brookhaven National Laboratory. In the first experiment the existence of distinct neutrino species was demonstrated.¹ This helped establish the concept of multiple generations of fermions. The second of these experiments² involved the observation of the rare decay $K_L \rightarrow \pi^+ \pi^-$. This provided the first evidence that nature did not respect the combined symmetries of charge-conjugation and space-inversion (i.e. CP). The last of the three experiments³ found the charmed quark in 1974. This discovery validated the explanation of Glashow, Iliopoulos, and Maiani (GIM)⁴ for the absence of strangeness-changing neutral currents and completed the second generation of fermion doublets.

Based on the empirical knowledge gained in these and other experiments, the $SU(3)_C \times SU(2)_L \times U(1)_Y$ gauge theory of nature was formed.⁵ This model has been sufficiently successful in its representation of experimental data, that it is now generally known as the Standard Model. Although able to accommodate all the currently available experimental information, the Standard Model does not furnish adequate explanations of several features, the most glaring of which is the clear structure in the fermion sector. Three generations of fermions are known to exist with the last two being

similar to the first.⁶ These three generations differ only in the masses of the fermions. No predictive account of the origin of mass exists within the Standard Model. While CP-violation can occur in the six-quark theory, it seems to "just happen." We don't know why the probability of a long-lived neutral kaon decaying into a pair of pions, and thus violating CP-invariance, is 0.002 instead of the infinity of other possible values.

In addition to the above short-comings, there are many parameters of the model which have not been measured very precisely, if at all. There is strong evidence for the existence of three complete generations, but the top quark, which is the heaviest member of the third generation, has not yet been seen. The mass and couplings of the top quark are therefore unknown. Evidence⁷, arising from preliminary width measurements of the Z^0 , suggests that there are only three fermion generations, but a fourth generation could still exist. In the Standard Model, particle masses result through interactions with the Higgs field. This necessitates the existence of at least one physical Higgs boson. Whether there are more than one Higgs particle and what their masses and couplings are remain unknown. Gravity has not been incorporated into the Standard Model and quantum chromodynamics has not been unified with the electroweak interactions. Many new theories have been proposed in order to resolve these problems.

To discern which of these new models most correctly describes the universe, requires more empirical information. The seven-hundred-and-ninety-first experiment accepted to be performed at the Alternating Gradient Synchrotron (i.e. E791) addresses several of

these questions and helps to differentiate among the various theoretical answers.⁸ The primary goal of the experiment is to search for the decay $K_L \rightarrow \mu e$ at a sensitivity as great as possible; the original goal was a sensitivity of 10^{-12} . This decay violates the conservation of separate lepton generation number and is forbidden in the Standard Model. Since transformations between the distinct generations of leptons occur in such a reaction, the experiment is a sensitive probe of new interactions and can help to elucidate the reason for multiple fermion generations and their mass structure.⁹

There are three secondary objectives of E791: to measure the branching fraction of $K_L \rightarrow \mu^+ \mu^-$, to search for $K_L \rightarrow e^+ e^-$, and to search for $K_L \rightarrow \pi^0 e^+ e^-$. A measurement of the longitudinal polarization of the positive muons in $K_L \rightarrow \mu^+ \mu^-$ decay at a sensitivity of 15% was also an original goal; if seen, this would indicate a new source of CP-violation. The observation of $K_L \rightarrow \pi^0 e^+ e^-$ at a rate above that expected in the Standard Model would be evidence of direct CP-violation through a mechanism other than K_L - K_S mixing.¹⁰

Measuring the branching fraction for $K_L \rightarrow \mu^+ \mu^-$ is the topic of this dissertation. During the 1960's the low upper limits on the branching fraction of this decay provided part of the evidence motivating development of the GIM mechanism for the suppression of strangeness-changing neutral current processes. Since the decay is only mediated by higher-order electroweak mechanisms, this allows a sensitive test of the predictive accuracy of the Standard Model. One can use the value of this decay rate to place limits on the masses and mixing angles associated with undiscovered heavy quarks. Bounds can also be derived on the masses and couplings of particles which

mediate new interactions. The decay $K_L \rightarrow e^+e^-$ involves the same processes as $K_L \rightarrow \mu^+\mu^-$. In addition to the GIM mechanism the decay into a pair of electrons is also further suppressed by helicity constraints. This leads to an expected branching fraction of 2.3×10^{-12} in the Standard Model. New physics might manifest itself through a greater branching fraction for this process.

Five experiments¹¹, in addition to E791, have previously observed the decay $K_L \rightarrow \mu^+\mu^-$. These results are listed in Table I.

Table I

Past results for $B(K_L \rightarrow \mu^+\mu^-)$

Year	Authors	Machine	#Events	$B(K_L \rightarrow \mu^+\mu^-)$
1973	Carithers et al.	AGS	6	12×10^{-9}
1976	Fukushima et al.	AGS	3	8.8×10^{-9}
1979	Shochet et al.	ZGS	16	8.1×10^{-9}
1988	Greenlee et al.	AGS	2	9.2×10^{-9}
1988	Inagaki et al.	KEK	7	14×10^{-9}
1988	Cousins et al.(791)	AGS	2	10×10^{-9}

In 1971 Clark et al.¹² set an upper limit on this reaction of 1.8×10^{-9} . Much theoretical interest was generated by this since it appeared to violate the lower bound determined from the Standard Model. Carithers et al. later observed the decay at the 10^{-8} level, thus resolving the contradiction. At the start of the present experiment only 25 examples of $K_L \rightarrow \mu^+\mu^-$ had been observed and the branching fraction was known only to within 21%. Preliminary results, listed as 1988 in Table I, from this and two other experiments provided little improvement in this situation.

To achieve the above objectives, a neutral beamline and a detector system were constructed at the Brookhaven AGS. A high intensity beam of 24.1 GeV/c protons from the AGS were directed onto a copper target. Decay products, from kaons which decayed in an evacuated volume downstream of the target, were examined. The momentum of charged daughter particles was measured with a pair of magnets and a set of precision drift chambers. Muons and electrons were separately identified by two distinct sets of detectors for each species. Determining a track's momentum and particle type by two independent methods was used to isolate rare kaon decay channels from the background resulting from the high intensity beam.

The body of this paper is organized into six chapters. Why the particular decay $K_L \rightarrow \mu^+ \mu^-$ is of scientific interest is examined in the next chapter. The third chapter details the beamline and detectors. The trigger and data acquisition systems are described in Chapter IV. The data analysis technique is covered in Chapter V. In the last chapter the results of the experiment are discussed. A compendium of the decay modes of the long-lived neutral kaon is provided in Appendix A.¹³

CHAPTER II

THEORETICAL CONSIDERATIONS

II.1 GIM Mechanism

As noted in the introduction, one of the puzzles confronting physicists during the 1960's was the absence of strangeness-changing neutral currents. If a neutral gauge boson, with fermion-couplings similar to those of the charged gauge bosons, exists, the decay $K_L \rightarrow \mu^+ \mu^-$ should occur as a first order weak process, as shown in Fig.1a. One would expect $K_L \rightarrow \mu^+ \mu^-$ to proceed at a rate similar to that of $K^+ \rightarrow \mu^+ \nu_\mu$. The latter involves the exchange of a W-boson, depicted in Fig.1c, in place of a Z^0 . At the time, experiments had placed an upper limit on the ratio of $\Gamma(K_L \rightarrow \mu^+ \mu^-) / \Gamma(K^+ \rightarrow \mu \nu) < 10^{-5}$. No other neutral current reactions had then been observed. However, the Weinberg-Salam electroweak model, along with other models of the weak interactions, required the existence of neutral gauge bosons. For these models to remain viable, some mechanism for suppressing strangeness-changing neutral current processes had to be found.

In 1970 Glashow, Iliopoulos, and Maiani (GIM) proposed such a mechanism⁴. In the 1960's, a single quark doublet and a pair of lepton doublets were known:

$$\begin{pmatrix} u \\ d \cos \theta_c + s \sin \theta_c \end{pmatrix}, \begin{pmatrix} \nu_e \\ e \end{pmatrix}, \begin{pmatrix} \nu_\mu \\ \mu \end{pmatrix} \quad (2.1)$$

The GIM paper suggested incorporating a second doublet of quarks

$$\begin{pmatrix} c \\ s \cos \theta_c - d \sin \theta_c \end{pmatrix} \quad (2.2)$$

This second quark doublet contained a new flavor of quark, the charmed quark. A second diagram, Fig.1b, involving exchange of a Z^0 , must now be included in the calculation of the $K_{\mu\mu}$ rate. The contribution, to the Z^0 exchange decay amplitude, of this second doublet exactly cancels the contribution of the original doublet.¹⁴ However, other processes can mediate the decay $K_L \rightarrow \mu^+ \mu^-$.

The box diagram in Fig. 2a involves the exchange of a pair of W-bosons. This is a second order weak process. All of the quarks, with a charge of $(2/3)e$, can be involved in the intermediate states contributing to this process. If they exist, this includes the top quark as well as a possible fourth generation quark with a weak isospin projection of $+1/2$. For now we will only consider diagrams containing the up and charm quarks.¹⁵ Since this is a low energy reaction, the transferred momentum is small compared to the W-mass; and so the boson propagator can be approximated by $1/M_W^2$. In the limit $M_W \rightarrow \infty$, the amplitude, to order (m_f^2/M_W^4) , for the diagram in Fig. 2a is

$$A = g_W^4 * \int d^D k \left\{ \left[\frac{\cos \theta_c \sin \theta_c}{(k - p_1' + p_1)^2 - m_u^2} \right] - \left[\frac{\cos \theta_c \sin \theta_c}{(k - p_1' + p_1)^2 - m_c^2} \right] \right\} * \left\{ \frac{F}{k^2 M_W^4} \right\} \quad (2.3)$$

where g_w is the weak coupling constant, θ_c is the Cabibbo angle, m_f is the mass of the exchanged quark, and F is a function, depending on k , p_1' , and p_2 , which represents the weak current-current operator. The $\sin\theta_c \cos\theta_c$ factor accounts for the weak mass mixing and leads to the up and charm quarks coupling to the strange quark with opposite strength. If the up and charm quarks possessed the same mass, their propagators would be equal and the amplitude would vanish. Taking $m_u \rightarrow 0$, Eq. (2.3) can be rewritten as

$$A = g_w^4 * \cos\theta_c \sin\theta_c \int d^D k \left\{ \frac{m_c^2}{[(k - p_1' + p_2)^2] * [(k - p_1' + p_2)^2 - m_c^2]} \right\} * \left\{ \frac{F}{k^2 M_w^4} \right\} \quad (2.4)$$

The integral in Eq. (2.4) contains a logarithmic singularity which is cancelled by contributions from other diagrams. With these approximations the rates for the diagrams in Fig. 3 are proportional to m_c^4 . Therefore, to the extent m_c differs from m_u , the GIM cancellation is inexact for second order weak processes. Using the limit on the branching fraction of $K_L \rightarrow \mu^+ \mu^-$, together with constraints from $K_L \rightarrow \gamma\gamma$ and the $K_S - K_L$ mass difference, Gaillard and Lee¹⁵ predicted the mass of the charm quark to be 1.5 GeV/c². This prediction was made before the experimental observation of the Ψ meson and compares well with the measured mass.

II.2 Unitarity Limit

As we have shown, the GIM mechanism suppresses or eliminates the contribution of diagrams involving only first or second order weak interactions to the $K_L \rightarrow \mu^+ \mu^-$ rate. This allows processes containing both first order weak and second order electromagnetic couplings to be the prevalent terms in the $K_{\mu\mu}$ decay amplitude. Figure 3a pictures such a process: the two-photon intermediate state. One can estimate the contribution of this diagram to the $K_L \rightarrow \mu^+ \mu^-$ rate by considering the decay $K_L \rightarrow \gamma\gamma$. This reaction has been observed in many experiments¹³ and found to have a branching fraction of $5.70 \pm 0.23 \times 10^{-4}$. Taking the two additional electromagnetic vertices into account, leads one to expect $K_{\mu\mu}$ to proceed at a rate about a factor of α^2 slower than $K_L \rightarrow \gamma\gamma$.

With certain assumptions¹⁶ it is possible to set a lower limit on $B(K_L \rightarrow \mu^+ \mu^-)/B(K_L \rightarrow \gamma\gamma)$. Two of these postulates, CPT-invariance and unitarity of the scattering matrix, are quite well established and unlikely to be false. Use is also made of CP invariance, even though this symmetry is known to be violated at a low level. The absorptive part of the $K_L \rightarrow \mu^+ \mu^-$ amplitude is assumed to be mostly due to the two-photon intermediate process. The $K_L \rightarrow \gamma\gamma$ amplitude is taken to be real. These last two statements are thought to be good approximations.

Employing these five assumptions, Martin, Rafael, and Smith¹⁷ arrived at the following inequality for the $K_{\mu\mu}$ decay rate

$$\begin{aligned}
\Gamma(K_L \rightarrow \mu^+ \mu^-) &\geq \frac{M_K}{4\pi} \beta_\mu \left[\frac{\alpha}{\sqrt{2}} \left(\frac{m_\mu}{M_K} \right) \frac{1}{\beta_\mu} \ln \left(\frac{1 + \beta_\mu}{1 - \beta_\mu} \right) \right. \\
&\left. \left(4\pi \frac{1}{M_K} \Gamma(K_L \rightarrow \gamma\gamma) - \frac{\Gamma(K_2 \rightarrow \text{all})}{8M_K} M_K^2 \sigma_{\gamma\gamma} \right)^{1/2} \right. \\
&\left. - \frac{1}{2\beta_\mu} \left[\beta_\mu M_K \sigma_2 \right]^{1/2} \left(\frac{\Gamma_2}{M_K} \right) \right]^2
\end{aligned} \tag{2.5}$$

where $\beta_\mu = (1 - 4m_\mu^2/M_K^2)^{1/2}$, Γ_2 is the rate for $K_2 \rightarrow$ all states except $\gamma\gamma$, σ_2 is the total cross section for $(\mu^+\mu^-)$ in the $1S_0$ state annihilating into all states except $\gamma\gamma$ at a center of mass energy of 497.7 MeV/c², and $\sigma_{\gamma\gamma}$ is the cross section for $\gamma\gamma \rightarrow$ all states with $J=0$ and odd parity. The unitarity bound is usually obtained by neglecting the pair of terms containing $\sigma_{\gamma\gamma}$ and σ_2 and dividing by $\Gamma(K_L \rightarrow \gamma\gamma)$, yielding

$$R = \frac{\Gamma(K_L \rightarrow \mu^+ \mu^-)}{\Gamma(K_L \rightarrow \gamma\gamma)} \geq \alpha^2 \left(\frac{m_\mu}{M_K} \right)^2 \frac{1}{2\beta_\mu} \ln^2 \left(\frac{1 + \beta_\mu}{1 - \beta_\mu} \right) \tag{2.6}$$

Evaluating this expression for R , one finds that the $K_{\mu\mu}$ decay rate should be at least 1.2×10^{-5} times the $K_{\gamma\gamma}$ decay rate.

Several studies have been done on ways in which this limit could be modified. Martin et al.¹⁷ estimate that the term containing $\sigma_{\gamma\gamma}$ in Eq. (2.5) could lower the bound by 20%, to 0.96×10^{-5} relative to $K_{\gamma\gamma}$. Radiative corrections¹⁸ may increase R by as much as 17%. It is calculated that other intermediate states, such as $3\pi^0$, $\pi^+\pi^-\pi^0$, $2\pi\gamma$, and

$3\pi\gamma$, contribute between 10^{-4} and 10^{-5} less than the $\gamma\gamma$ intermediate state.¹⁹ CP violation can lead to interference effects in the absorptive portions of the $K_{\mu\mu}$ and $K_{\gamma\gamma}$ amplitudes. However, models incorporating CP violation are limited by experimental restrictions on the decays $K_S \rightarrow \gamma\gamma$ and $K_S \rightarrow \mu^+\mu^-$, as well as by other observations.¹⁶

Multiplying the branching fraction for $K_L \rightarrow \gamma\gamma$ by R , suggests that the process $K_L \rightarrow \mu^+\mu^-$ should have a branching fraction greater than $6.84 \pm 0.28 \times 10^{-9}$. It should be kept in mind that the measured value of the $K_{\gamma\gamma}$ branching fraction has increased by 16% during the last four years.

One would naively expect $K_L \rightarrow \gamma\gamma$ also to be GIM suppressed in the same manner as the box diagram. However, the structure of the two diagrams is different. This difference allows low momentum one-particle intermediate resonances to dominate the $K_{\gamma\gamma}$ amplitude. Ma and Pramudita²⁰ have calculated $\Gamma(K_L \rightarrow \gamma\gamma)$ using a phenomenological model. They included the contributions from the π^0 , η , and η' intermediate states, as in Fig. 3b. Their result is 20% lower than the observed rate.

The process $K_L \rightarrow e^+e^-$ can proceed via the same electroweak interactions as $K_L \rightarrow \mu^+\mu^-$. The unitarity limit can then be used to set a lower bound for the branching fraction of K_{ee} decays. Since the V-A theory only couples to left-handed leptons and right-handed anti-leptons, both the $K_{\mu\mu}$ and K_{ee} decays are helicity suppressed.²¹ This follows because, to respect CP, the lepton pair must be in a 1S_0 final state but, due to the V-A nature of the interaction, the leptons will tend to have their spins aligned. Both reactions are therefore helicity-suppressed by a factor of $(1-v/c)$. Combining the relative

helicity-suppression factor and the unitarity limit for $K_{\mu\mu}$ decays leads to a lower bound of about 2.3×10^{-12} for the branching fraction for $K_L \rightarrow e^+e^-$. Observation of K_{ee} decays, at a rate significantly higher than helicity-suppression of the measured $K_L \rightarrow \mu^+\mu^-$ rate predicts, would indicate the presence of interactions outside of the Standard Model.

II.3 What Can We Learn?

By comparing the experimentally observed decay rate for $K_L \rightarrow \mu^+ \mu^-$ with the rate predicted by the unitarity limit, bounds can be placed on the partial decay rates due to other processes. In this way knowledge regarding higher order electroweak modes as well as more exotic mechanisms can be gained from examining the decay $K_L \rightarrow \mu^+ \mu^-$. From unitarity we know that

$$\Gamma_{Disp.}(K_{\mu 2}) = \Gamma_{Total}(K_{\mu 2}) - \Gamma_{Abs.}(K_{\mu 2}) \quad (2.7)$$

If the contribution from $K_L \rightarrow \gamma \gamma$ dominates the absorptive decay rate, then the decay rate due to any other process must be of the order of $\Gamma_{Disp}(K_{\mu\mu})$. This assumes there are no fortuitous cancellations among terms in the dispersive portion of the scattering matrix.

Processes proportional to G_F^2 are probably dominated by contributions involving the top quark. Three diagrams containing second-order weak interactions are given in Fig. 2. One can derive bounds on V_{dt} , V_{st} , and m_t from the dispersive part of the $K_{\mu\mu}$ decay rate. The amplitudes for all three processes are similar to Eq. (2.4). Calculations show that the short-distance QCD corrections to the free quark amplitudes are negligible.²² Nasrallah and Schilcher²³ find that the long-distance QCD effects generate corrections of the same size as the terms proportional to the square of the mass of the exchanged quarks. Table II shows the dependence of $V_{dt}V_{st}$ on the mass of the top quark. This includes the contributions from all the diagrams in Fig. 2.

Table II

KM-matrix mixing elements as a function of the top quark mass

Mass of top (GeV/c ²)	Real(V _{ts} *V _{td})
25.6	0.014
36.2	0.021
44.4	0.034
51.2	0.052
57.3	0.10
62.7	0.89
67.8	0.11

Assuming a top quark mass of 60 GeV/c² and comparing the decay $K_L \rightarrow \mu^+ \mu^-$ to $K^+ \rightarrow \mu^+ \nu_\mu$, Inami and Lim²⁴ find the magnitudes of s_2 and s_3 to vary as in Fig. 4. They used the following definitions: $\xi = \text{sign}(t_2 t_3 c_\delta c_1^{-1})$, $t_i = \tan \theta_i$, $s_i = \sin \theta_i$, $c_i = \cos \theta_i$, where θ_i are the three Kobayashi-Maskawa mixing angles and δ is the phase. The same authors also use the bound on the dispersive part of the $K_L \rightarrow \mu^+ \mu^-$ rate to estimate the branching fraction for the decay $K^+ \rightarrow \pi^+ \nu \nu$. The ratio of the branching fractions for the two decays is shown in Fig. 5 as a function of the top quark mass. Shrock and Voloshin²⁵ arrive at the inequality

$$\left| c_2 (c_1 c_2 - s_2 t_3 c_\delta) m_c^2 + s_2 (c_1 c_2 - s_2 t_3 c_\delta) m_t^2 \right| < 57 \text{ GeV}/c^2 \quad (2.8)$$

This inequality leads to an upper limit on $|s_2|$ as a function of $|s_3|$ very similar to that obtained by Inami and Lim.

Alternatively, bounds can be placed on the masses of charge $(+2/3)e$ heavy quarks using the available limits on the mixing angles.

Buras²⁶ considers the K_L - K_S mass difference and the branching fraction of $K_L \rightarrow \mu^+ \mu^-$ to estimate an upper bound on the top quark mass. He calculates the value of the matrix element $\langle K^0 | [\gamma_\mu (1 - \gamma_5)]^2 | K^0 \rangle$ in various models: MIT bag model, QCD, and the free quark approximation. The top quark mass is thus estimated to lie within the range of 30 to 50 GeV/c². This would seem to contradict recent preliminary results of the CDF experiment²⁷, which indicate a lower bound of 75 GeV/c². Presently, there is evidence for three generations of fermion doublets. If a fourth generation exists, its quarks would likely be quite massive. The decay rate of $K_L \rightarrow \mu^+ \mu^-$ is sensitive to the mixing angles and masses of a fourth generation²⁴ in an analogous manner to those of the third generation. Involving a charm quark instead of a strange quark, the decay rate of $D^0 \rightarrow \mu^+ \mu^-$ is highly sensitive to the presence of a fourth quark doublet. Babu et al.²⁸ estimate the branching fraction of $D^0 \rightarrow \mu^+ \mu^-$ to be 10^{-16} and 10^{-9} with three and four generations, respectively. Although it provides an opportunity to make a definitive test for a fourth generation, the observation of $D_{\mu\mu}$ decays is considerably more challenging than observation of $K_{\mu\mu}$ decays. A precision measurement of the branching fraction for $K_L \rightarrow \mu^+ \mu^-$ provides a test of higher-order electroweak processes and helps to constrain some parameters of the Standard Model.

In attempts to explain some of the arbitrary features of the Standard Model, new interactions, involving the exchange of exotic particles, have been proposed. The masses of some of these new particles can be limited by the branching fraction of the decay $K_L \rightarrow \mu^+ \mu^-$. Several of these new models are reviewed in an article by

Shanker.²⁹ The simplest model reviewed is the Standard Model with two Higgs doublets, instead of one.³⁰ This results in five physical Higgs states. The fermions acquire mass from the vacuum expectation values of the Higgs fields. In this model the Higgs particles are allowed to change quark flavor. Assuming the Higgs-fermion coupling is proportional to the average of the fermion masses of a given type of fermion (i.e. m_b and m_τ), Shanker derives the following relationship

$$\frac{\Gamma(K_L \rightarrow \mu^+ \mu^-)}{\Gamma(K_L \rightarrow \text{all})} = 4.6 * 10^4 \left(\frac{m_b m_\tau}{m_H^2} \right) \quad (2.9)$$

If the Higgs contribution to the decay rate does not exceed the dispersive part, the mass of the Higgs particles must exceed 6.1 TeV/c². Shanker next considers an extended technicolor theory. In the model considered,³¹ pseudoscalar leptoquarks can mediate flavor-changing processes. These leptoquarks are composite particles consisting of a technifermion-antitechnifermion pair. Since these interactions must occur between quarks and leptons, the rates of reactions involving only quarks or leptons are not affected by this theory. Limiting the rate of the pseudoscalar leptoquark process via the dispersive part of the $K_L \rightarrow \mu^+ \mu^-$ rate leads to a lower bound of 4.5 TeV/c² on the masses of the leptoquarks. In a similar type of theory,³² one involving vector bosons which mediate flavor changing reactions such as proton decay, Shanker uses the $K_{\mu\mu}$ branching ratio to limit the masses of such vector leptoquarks to greater than 62 TeV/c². Thus, in conjunction with other observations, $K_L \rightarrow \mu^+ \mu^-$ can

restrict parameters in a variety of theoretical models.³³ Other measurements, for instance $K_L \rightarrow \mu e$ and nucleon decay, often place more stringent limits on these and other exotic new theories. Nevertheless, the precise measurement of this branching fraction furnishes extremely useful information.

II.4 Muon Polarization in $K_L \rightarrow \mu^+ \mu^-$

In addition to the branching fraction of the decay $K_L \rightarrow \mu^+ \mu^-$, one can also measure the longitudinal polarization of the resulting positive muon, which offers a probe of new physics.³⁴ This involves determining the component of the muon's spin in the direction of the muon's momentum. Due to the V-A nature of the weak interaction, the positron, produced in the reaction $\mu^+ \rightarrow e^+ \nu_e \nu_\mu$, is predominantly emitted parallel to the muon's spin vector.³⁵ By recording the directions of emission of the decay positrons, one can determine the polarization of the parent muon sample. The longitudinal polarization is defined as:

$$P_L = \frac{N_L - N_R}{N_L + N_R} \quad (2.10)$$

where N_L and N_R are the observed number of left-handed and right-handed muons, respectively. The muon pair resulting from the decay can be produced in two possible states: the CP-conserving 1S_0 state and the P- and CP-violating 3P_0 state. Parity is violated, if both the muons from kaon decay preferentially have their spins aligned with their momentum. An observation of parity violation in this decay would imply that the muon pair was created in the CP-violating 3P_0 state.

Since the K_L state contains a small component of the CP-even K_1 state, one would expect some polarization of muons in $K_L \rightarrow \mu^+ \mu^-$ decay. Herczeg³⁶ obtains a value for the polarization due to this mechanism of about 0.001. Therefore, the Standard Model of electroweak

interactions predicts a small, but nonzero polarization. Clearly, the detection of polarization significantly greater than 0.001 would evince the existence of a new interaction. Following Herczeg, the effective Hamiltonian for the K_2 component of K_L decaying into a pair of muons can be written as:

$$M(K_2 \rightarrow \mu^+ \mu^-) = a_2 \bar{u}(p_-) \gamma_5 v(p_+) + i b_2 \bar{u}(p_-) v(p_+) \quad (2.11)$$

where a_2 corresponds to the CP-conserving mode and b_2 represents the CP-violating mode. From this one can derive the following relation between the decay amplitudes and the longitudinal polarization:

$$P_L = \frac{2r \operatorname{Im}(b_2 a_2^*)}{[|a_2|^2 + r^2 |b_2|^2]} \quad (2.12)$$

where $r = (1 - 4m_\mu^2/m_K^2)^{1/2}$. When CP-conserving processes dominate, this equation can be approximated by $P_L \sim b_2/a_2$. A measurement of polarization at the 1% level would indicate the presence of a mechanism outside of the Standard Model contributing a partial decay rate about 10^4 times smaller than that due to electroweak processes. Given the theoretical uncertainty in the calculation of the $K_L \rightarrow \mu^+ \mu^-$ branching fraction, a polarization measurement is a more sensitive probe of new phenomena than a determination of the branching fraction.

The value of b_2 has been calculated in several models containing CP-violating mechanisms. Within an extension of the Standard Model, with four fermion generations, the exchange of neutral scalar Higgs bosons, as depicted in Fig. 6a, can induce a nonzero polarization. For a

Higg's mass below 11 GeV, Botella and Lim³⁷ have calculated a muon polarization as high as 0.96. In left-right-symmetric models incorporating processes such as the one shown in Fig. 6c, a muon polarization a factor of ten above that expected from the K_L - K_S mass mixing^{38,39} could result. In a supersymmetric extension of the Standard Model, Kurimoto⁴⁰ estimates that gauge interactions involving gauge fermions, Higgs bosons, squarks, and sleptons, such as the process represented in Fig. 6b, result in muon polarizations no greater than 10^{-3} . $E_8 \times E_8$ superstring models are expected to generate negligible muon polarization.⁴¹ If CP is violated by leptoquark-fermion interactions as diagrammed in Fig. 6d, a muon polarization as great as unity might occur.⁴² A measurement of the longitudinal polarization in the decay $K_L \rightarrow \mu^+ \mu^-$ would help to restrict the present range of theories which incorporate CP-violation.

CHAPTER III

BEAMLINE AND DETECTORS

Common to all the physically interesting decay modes searched for in this experiment (i.e. $K_L \rightarrow \mu e$, $K_L \rightarrow \mu^+ \mu^-$, $K_L \rightarrow e^+ e^-$, $K_L \rightarrow \pi^0 e^+ e^-$) is the presence of two charged daughter particles. Additionally, we need to observe the decay $K_L \rightarrow \pi^+ \pi^-$ in order to ascertain the sensitivity of our search. With the exception of $K_L \rightarrow \pi^0 e^+ e^-$, we are interested in two-body decays. One hundred million times more frequent than the only observed rare two-body mode (i.e. $K_L \rightarrow \mu^+ \mu^-$) are the three-body decays (see Appendix A), which also generally contain two charged tracks. The goal of this experiment is to conduct as sensitive a search as possible for the rare or forbidden decay modes. This goal dictates recording as many kaon decays as possible, which leads to the use of a high intensity proton beam. With this high intensity beam, backgrounds from other reactions and the primary beam dump are a potential limiting factor. Accurate determination of the momentum vectors of the observed charged tracks is one method of separating the two-body decays from the three-body decays and other backgrounds. A second method is based upon establishing the types of the particles observed. To prevent the data acquisition system from being overwhelmed by the number of tracks traversing the detectors, a multi-level trigger is implemented.

This experiment is performed in the B5 line of the Brookhaven National Laboratory's Alternating Gradient Synchrotron (AGS). A plan

view of the experiment is depicted in Figure 7. The design and construction of the proton and neutral beamlines are crucial to the success of the experiment. Protons with a momentum of 24 GeV/c are continuously extracted from the AGS main ring over a period of 1.4 seconds. It takes an additional 1.8 seconds to refill the AGS main ring with protons, making the complete cycle time 3.2 seconds. This is known as the slow-extraction mode of AGS operation. The slow-extraction mode provides a high duty cycle and minimizes the instantaneous intensity.

Protons from the AGS impinge on the B5 production target at an angle of 2.75° from the horizontal as shown in Fig. 8. The copper target, similarly tilted, has dimensions of 0.318 cm x 0.318 cm x 20.3 cm. An assortment of baryons, mesons, and photons is created as protons in the beam interact with the target nuclei. Immediately downstream of the target is a sweeping dipole magnet, which deflects positively charged particles downward. Located underneath the beam is a recessed beam dump into which most of the remaining beam protons and like charged secondaries are bent. A set of lead foils is positioned within the first sweeping magnet. The purpose of these foils is to convert high energy photons in the neutral beam. The resulting electrons and positrons can then be removed by the sweeping dipoles.

Rectangular collimators, located upstream of the second sweeping magnet, restrict the paths of particles in the neutral beam. Relative to the target, the collimated neutral beam illuminates, at full-width-at-half maximum, an x by y solid angle of 4 milliradians by 15 milliradians. After passing through the second sweeping magnet,

which sweeps away any charged particles produced in the collimators and lead foils, the neutral beam enters a 8.0 meter long vacuum region. Only events with a reconstructed vertex located within this vacuum region are accepted as possible kaon decays. The downstream end of the vacuum region is sealed with a thin endcap containing a Mylar window for the neutral beam and separate rectangular windows for the kaon decay products on either side of the neutral beam. These thin windows minimize multiple scattering and hadronic interactions of particles crossing through them.

Completely encapsulating the proton beam dump, sweeping magnets, and decay region, is material selected to absorb extraneous particles. These unwanted particles originate in the proton beam dump and B5 target. Abutting the neutral beam are plates of iron, lead, and assorted heavy metals to attenuate charged particles, photons, and relativistic hadrons. About the metal shielding are arranged blocks of hydrogen-rich concrete and cans of Borax. These compounds are effective at moderating and capturing nonrelativistic neutrons. Without this extensive and carefully selected shielding, our detectors might be unable to distinguish kaon decay products against an overwhelming background.

In order to measure a track's momentum, the deflection of the track in a magnetic field is measured. To reduce the uncertainty associated with the momentum measurement, the trajectory of a track is observed in two independent magnets. The upstream magnet has a gap with x, y, and z dimensions of 122 cm x 94 cm x 122 cm. The gap of the second magnet measures 244 cm x 112 cm x 102 cm. As an aid to the pattern recognition and triggering, the magnets are

designed to impart transverse momentum kicks of equal magnitude, but opposite in direction. The second kick, therefore, restores the track to its original direction. Each magnet bestows a momentum kick equal to approximately 300 MeV/c to particles traversing its volume. The field was measured with Hall probes in and about the two magnets in a three-dimensional 5 cm grid. Both magnets generate peak fields of about 0.7 Tesla. Permanent Hall probes, positioned within each magnet, continuously monitor the fields throughout the data-taking period.

Precision drift chambers (e.g. DC1 through DC5) record the position of tracks upstream, between, and downstream of the two spectrometer magnets. The kinematics of an event are reconstructed based on information from the drift chambers. Uncertainty in the momentum measurement arises from four main sources: the intrinsic resolution of the drift chambers, knowledge of the positions of the chambers, multiple scattering, and the magnetic field map. Multiple scattering, as well as hadronic interactions, are reduced by filling the volume about all the detectors with helium. The initial trigger uses information from a set of scintillation hodoscopes (e.g. TSC1 and TSC2) downstream of the drift chambers. Together with the upstream pair of drift-chamber modules, the scintillation hodoscopes indicate the presence of a charged track on each side of the beam.

Multicell Cerenkov counters furnish the electron trigger. The Cerenkov distinguishes electrons from other species of particles, but provides no knowledge regarding a track's momentum. A leadglass array, following the Cerenkov counters, serves as an electromagnetic calorimeter. This leadglass system further distinguishes between

electrons and other particles, and additionally measures an electron's or photon's energy. A set of scintillators, located within the leadglass array, is used to trigger on converted photons.

Identification of muons is performed by two systems: the muon scintillation hodoscope and the rangefinder. Behind the leadglass is situated a block wall of iron 91 cm in depth along the beam axis. Muons are the only type of particle likely to penetrate this amount of material. The muon trigger uses the muon hodoscope to select muons. With its good time resolution, the muon hodoscope is quite effective at eliminating accidental tracks downstream of the iron. The rangefinder consists of plates of absorber material interspersed with planes of proportional tubes. The energy of a muon is determined by the depth to which a track penetrated into the rangefinder.

In order to handle the high flux of particles through the detector systems, a three-level triggering scheme is used. An event is initiated by the presence of charged tracks in the trigger scintillation hodoscope and the drift chambers. Based on data from the particle identification detectors, the trigger system labels events as being candidates for the various decay modes of the long-lived kaon. Interesting events are read out and written to tape for further analysis offline. Details regarding the detectors are given in the remainder of this chapter and the data acquisition system is described in the following chapter.

III.1 Drift Chambers

Central to the success of this experiment is the ability to measure accurately the trajectory of charged particles passing through the pair of spectrometer magnets. This is a necessary prerequisite to determination of the momenta of the tracks. Given the momenta and trajectories of the kaon daughter products, the decay vertex and the initial invariant mass can be calculated. A difference between the mass of the kaon and the reconstructed mass indicates the presence of neutral daughter particles, unobserved decay products, or an incorrect mass assignment to a track based on faulty particle identification. A quantity known as the collinearity is defined as the angle between the unit vector from the target to the reconstructed vertex and the unit vector of the total reconstructed momentum. This is presented visually in Figure 9. A large collinearity indicates missing transverse momentum. Both the mass and collinearity are crucial in differentiating two-body decays from the more abundant three-body decays. A set of five drift chambers together with the two spectrometer magnets allow a particle's momentum to be independently measured twice.

There are five drift-chamber modules located symmetrically on each side of the beam. Each module contains two planes of horizontal sense wires and two planes of vertical sense wires. Two planes in each dimension permit the left-right ambiguity to be resolved for every module. In addition to the sense wires, there are also field and guard wires, which help shape the electric field surrounding the sense wires. A drawing of a unit cell is shown in Figure 10. Field

wires are nominally held at -2,500 volts relative to the grounded sense wires. Wires are soldered under tension in precisely positioned holes in a printed circuit board. The printed circuit board is secured in a prestressed aluminum frame. Aluminized Mylar skins are stretched across the frame forming sealed walls. The skins are grounded and help to electromagnetically shield the wires.

Shielded cables carry the signals from the sense wires to nearby amplifier boards. The amplifiers use LeCroy Hil440 chips as their active elements. Following amplification, the signals are discriminated with a minimum threshold of about $0.3 \mu\text{A}$. The discriminators produce differential ECL logic signals, which are transmitted over 131-meter long custom flat Ansley cables, each containing 97 copper traces imbedded in polyethylene.

A 6-bit linear⁴³ TDC accepts the 32 channels associated with each cable. These TDC's have a fullscale count of 160 nanoseconds with a channel representing 2.5 ns. The root-mean-square time resolution of the TDC system is 0.8 ns. Both the leading and trailing edges of a 100 MHz clock are employed. To decrease further the effective cycle time, the clock is phase delayed one quarter cycle and both phase signals are employed. A Gray code scheme is used instead of simple binary to count the cycles. Only the first hit on each channel is recorded. As with the other digitizing modules in this experiment, the digitized information is double buffered and flip-flops are employed to indicate which channels are hit. The pipelining reduces the deadtime to an acceptable level and the flip-flops implement a sparse data scan.

A gas mixture consisting of 49% argon, 49% ethane, and 2% ethanol fills the volume formed by the skins and frame. A mass flow controller determines the mixing ratio of the argon and ethane. The gas is then bubbled through refrigerated ethanol. Charged particles traversing the gas ionize some of its constituent molecules, mostly the argon. As the resulting electrons and cations move in the electric field, they further ionize the gas. Free electrons move at a known velocity in a specified electric field. An electron drift-time can thus be translated into a position. A typical drift speed is 50 $\mu\text{m/ns}$. The spatial r.m.s. resolution of the drift-chamber system is 120 microns. This resolution, combined with uncertainties in the values of the spectrometer magnets' fields and multiple scattering, results in reconstructed mass and collinearity distributions with standard deviations of 1.5 MeV/c^2 and 0.3 milliradians, respectively, for $K_L \rightarrow \pi^+ \pi^-$ decays.

III.2 Trigger Scintillation Hodoscope

The trigger scintillators are primarily used in the experimental trigger during data taking. There are two complete banks on each side of the beam: one upstream and one downstream of the Cerenkov counters. Since one bank of the scintillators is located upstream of the Cerenkov counters, it is important to keep its thickness to a minimum in order to reduce the number of knock-on electrons produced by particles traversing it. An expanded drawing of the upstream beam right hodoscope is shown in Fig. 11. The mechanical properties and the performance of the trigger scintillators are described in the rest of this section.

Each of the four two-dimensional banks contains 64 x-measuring and 64 y-measuring strips of scintillant. Kyowa glass, a brand of doped polystyrene, is used as the scintillating material. X-measuring counters and y-measuring counters are 1.80 meters and 1.28 meters in length, respectively. The width of the x-measuring counters is 0.02014 meters, while the y-measuring counters are slightly wider at 0.02814 meters. Since the downstream hodoscope banks are located after the Cerenkov counters and close to the leadglass array, constraints on the amount of material in the counters are less stringent, allowing the back counters to be 1.0-cm thick, whereas the upstream counters are half as thick. To reflect scintillation photons which exit the sides of the counters back into a counter, the scintillators are wrapped in aluminized Mylar. In order to keep external light from striking the system, each two-dimensional bank is enclosed in a light-tight box.

One-inch diameter Hamamatsu R1398 photomultiplier tubes are used to sense the scintillation light from the counters. Tubes are bonded to the scintillators using an organic adhesive with the same refractive index as the counters. Each y-measuring counter is attached to a single phototube at the end farthest from the neutral beam. A phototube is attached to both ends of each x-measuring slat. Each x-phototube is bonded to two neighboring x-slats due to space limitations and to reduce the number of channels. The upper and lower tubes are offset by one slat allowing unambiguous determination of which slat is struck. This topology allows n tubes to provide double-ended sensing of n counters. Since no lightguides are used, each x-slat has to be twisted so that two contiguous slats can abut a single phototube face.

Analog signals from the base of each photomultiplier tube are carried over RG8 cables to the counting house, where the signals are discriminated. Outputs from all discriminators are fed into the same type of TDC's used for the drift chambers. Discriminated signals from x-slats are sent to meantimers as well as to the TDC's. The results from the meantimers are used in the Level 0 trigger. An OR of all the y-slat discriminator outputs from a given bank is generated for the Level 0 trigger.

During the offline analysis, the efficiency of the trigger scintillators for registering the passage of a charged track was determined to be 0.998. The efficiency of each tube is included in the offline software and thus taken into account when using the Monte Carlo code to calculate the relative acceptances for the different decay modes. After correcting offline for event time-zeroes,

individual time-offsets, and the propagation time of light along a slat, the r.m.s time resolution of the system is 1.7 ns. The effective full-width time resolution of the system, as used in the Level 0 trigger, is 14 ns due to varying cable lengths and other channel-to-channel differences. The doped polystyrene scintillating material has an attenuation length of 1.3 meters and light propagates at a speed of 0.138 meters per ns in the counters.

III.3 Cerenkov Counter

The Cerenkov counter is employed to distinguish electrons from slower particles.⁴⁴ The principle of operation of the detector is the observation of Cerenkov radiation emitted by charged particles travelling faster than the group velocity of light in a medium. Given the momentum distribution of electrons from kaon decays in the E791 beamline, all of the relevant electrons are moving fast enough to generate Cerenkov photons. Due to their larger masses, muons, pions, and protons must have considerably more momentum than electrons to fire the Cerenkov detector. Information from the Cerenkov detectors is used in both the trigger and the offline data analysis.

Several objectives determine the design of the detector: high efficiency for electrons, low efficiency for other particle types, and a minimum amount of material through which tracks must pass. A drawing of the Cerenkov detector is shown in Figure 12. To minimize the number of radiation lengths through which particles pass, the detector is constructed as a rectangular aluminum box, three meters in length, with the front and back sides being 0.076 cm thick. This configuration reduces the probabilities for high-energy photon conversion and of knock-on electrons from charged tracks. A mixture of N₂ and He in the ratio of 6 to 4 fills the interior of the aluminum boxes. This mixture has an index of refraction of 1.000140, which is selected in order to optimize the separation of electrons from pions in the momentum range of 1 to 10 GeV/c, appropriate to this experiment. Through the use of an interferometry technique, the

refractive index is regulated to a precision of 4 ppm. An overpressure of approximately one inch of water is maintained within the Cerenkov volume.

Photons radiated within the gaseous volume are reflected by eight spherical mirrors located at the downstream end of each of the two aluminum boxes. These mirrors focus the Cerenkov photons onto eight RCA 8854 Quantacon 5" phototubes. Each phototube's glass window is covered by a film of p-terphenyl as a waveshifter. A continuous flow of dry N₂ gas is maintained around the phototubes to prevent damage from helium diffusion into the tubes. Signals from each of the 16 phototubes are transmitted over RG8 coaxial cables to the counting house. Upon arrival at the counting house a signal is split in two. Fractions of the pulse are sent to flash analog-to-digital converters (ADC) and discriminators in the ratio of eight to two, respectively.

Level 1 uses the output of the discriminators to determine if the Level 0 trigger contains any electrons. Any track generating a pulse above the discriminator's threshold is treated as an electron in the trigger. After a 300 ns delay, the other portion of the split signal is fed into a charge-integrating bilinear flash ADC.⁴⁵ The ADC is built around the 8-bit Sony CX20052A 20 MHz chip and requires 200 ns to digitize a signal. Full scale corresponds to a charge of 100 pC. The first 64 channel linear region has a conversion factor of 150 fC/channel and the remaining 192 channel linear region has a conversion factor of 470 fC/channel. A signal from Level 1 starts the gate during which charge is integrated. If the integrated charge is greater than a set value, a flip-flop is set indicating the presence of a

hit channel. There are two pipelined sets of buffers and associated flip-flops which can each hold the information for a hit until the Readout Supervisor is ready to transfer the data to 3081/E processors. Readout requires 100 ns.

Using the formula $\beta_{\text{Threshold}}=1/n$, where n is the index of refraction, the Cerenkov momentum thresholds for pions and muons are found to be 8.34 GeV/c and 6.31 GeV/c, respectively. Based on the performance of the Cerenkov for actual particles, the momentum at which the efficiency starts to increase quickly is 8.62 ± 0.12 for pions and 6.37 ± 0.12 for muons. For momenta below these thresholds, 1.5% of the pions and muons fire the Cerenkov. At the beam intensities at which data were taken, about half of these low-momentum signals are from accidentals and the remainder are due to knock-on electrons from the upstream trigger scintillators. The cell hit rate averaged over the eight phototubes on one side of the beam is 1.6 MHz. The efficiency for electrons from $K_L \rightarrow \pi e \nu$ was 0.935 ± 0.004 for the first part of the data taking. This efficiency improved to 0.953 ± 0.006 after an adjustment of the mirrors performed midway through the run. For the dimuon analysis the Cerenkov data are primarily used offline to isolate pure samples of a specific particle type.

III.4 Electromagnetic Calorimeter

For the observation of the $K_L \rightarrow \pi^0 e^+ e^-$, $K_L \rightarrow e^+ e^-$, and $K_L \rightarrow \mu e$ decay modes it is necessary to identify electrons and photons and record their energies. A system containing two layers of leadglass separated by a scintillation hodoscope, and known as the finger counters, serves as the electromagnetic calorimetry system for this experiment.⁴⁶ The upstream layer of leadglass, representing 3.3 radiation lengths, converts the majority of photons and electrons into electromagnetic showers; hence its designation as the converter blocks. The presence of multiple hits in the finger counters indicates that a particle has initiated an electromagnetic shower in the converter blocks. Level 3 uses information from the finger counters to identify possible $K_L \rightarrow \pi^0 l^+ l^-$ decays. In the downstream leadglass array, known as the back blocks, the particles created in an electromagnetic shower are ranged out. With an index of refraction of 1.62, almost all charged tracks produce Cerenkov radiation in the leadglass. This radiation is sensed with photomultiplier tubes attached to the blocks. An exploded view of the calorimetry system is depicted in Fig. 13.

There are a total of 52 converter blocks arranged in arrays of two by 13 blocks on each side of the beam. All the converter blocks have x and y dimensions of 0.109 and 0.90 meters, respectively, and are 0.10 meters in depth. Since the flux of incident particles decreases with distance from the center of the beamline, phototubes with different time responses are matched to blocks, based on their hit

rates. Fast Amperex 3462 phototubes are glued to the blocks nearest the beam, while slower EMI 9531r phototubes are used for the blocks farther away from the beam.

The finger scintillation hodoscope consists of a set of x and y-measuring counters located between the converter and back blocks on both sides of the beam. There are 36 y-measuring slats and 27 x-measuring slats on either side. All the slats are 1.5 cm deep and 5.1 cm wide. The x- and y-measuring counters are 1.861 and 1.394 meters in length, respectively. As for the trigger scintillation hodoscope, Kyowa Glass is used as the scintillation material for the finger counters. The effective speed of light in the scintillator is 0.122 m/ns and the attenuation length of scintillation photons is 1.3 meters. Y-measuring slats have a single XP2230 phototube attached to the end away from the beam. X-measuring counters have an Amperex 56AVP phototube appended to the top end and an EMI9902 phototube affixed to the bottom. On either side of the beam, behind the finger hodoscope, are located the back blocks, a 9 by 12 array of leadglass blocks. Each block has a square cross section 15.3 cm on a side and is 32.2 cm in depth. For the back blocks EMI 9618r phototubes are used on blocks away from the beam and a mixture of Amperex 58AVP and 58DVP tubes are attached to blocks with a high singles rate. The leadglass has a nuclear interaction length of 35 cm and a radiation length of 3.06 cm.

A wooden hut is constructed around the electromagnetic calorimetry system to keep out light. RG58 coaxial cables carry the analog signals from the phototube bases to patch panels in the hut walls. RG8 cables transmit the signals from the patch panels to the

counting house where the signals are split. The finger hodoscope signals are first discriminated and then used either in the trigger or sent to TDC's. A gate 35 ns wide is used for the finger counters in the trigger logic. A typical singles rate for a slat is 0.5 MHz. The finger counters' efficiency for detecting muons is 95%. Signals from the leadglass are discriminated and sent to TDC's or are input to ADC's. Two ratios, derived from the leadglass, are used to select electrons and photons: 1) the total energy deposited in the leadglass over the momentum determined by the spectrometer, and 2) the energy deposited in the converter blocks over the total energy deposited in the leadglass. The energy resolution of the leadglass system varies, due to the use of different phototubes, from $\sigma/E = 2\% + 15\%/ \sqrt{E}$ near the beam to $\sigma/E = 2\% + 7\%/ \sqrt{E}$ at the outside edge, where E is the energy in GeV/c². The reconstructed mass resolution is 5 MeV/c² and 11 MeV/c² for the decays $K_L \rightarrow \pi^0 \pi^+ \pi^-$ and $\pi^0 \rightarrow \gamma \gamma$, respectively.

III.5 Muon Hodoscope

Located on either side of the beam immediately downstream of the hut which houses the leadglass array are two walls of block iron. Each wall is 0.91 meters in depth along the z-axis. This amount of iron represents 52 radiation lengths and 8.7 nuclear interaction lengths. It is referred to as the muon filter, since few hadrons, electrons, or photons can pass through the iron. Just behind the downstream face of the iron is the muon hodoscope.⁴⁷ This scintillator-based system indicates the presence of a charged particle downstream of the iron. The fast time response of the hodoscope allows it to be used as a muon trigger in Level 1 and to be used to reject out-of-time accidentals in the offline analysis.

The muon hodoscope is composed of two sets of vertical and horizontal slats of Bicron BC408 plastic scintillator. Figure 14 shows an exploded view of the beamleft part of the hodoscope and iron system. All the slats are 2.54 cm thick and 18.8 cm wide. On each side of the beam there are eleven 2.69 meter-long x-measuring counters and fourteen 2.29-meter long y-measuring counters. In order to prevent external light from entering the scintillator, each slat is individually wrapped with an opaque sheet. This sheet contains three laminar layers, which from the scintillator side outward are: eight μm of aluminum, 13 μm of Mylar, and 150 μm of polyethylene. Scintillation photons from a slat are sensed by 5-cm diameter Amperex XP2230 photomultiplier tubes attached to the tapered counter ends. Every x-measuring slat has a phototube

attached at both the top and bottom, whereas a y-measuring slat has a phototube only on the end away from the beam. The phototubes are bonded directly to the scintillant with Double Bubble Hardman's Epoxy. Analog signals from the phototube bases are transmitted to the counting house over RG8 cables.

In the counting house, signals from the phototubes are discriminated with a threshold of approximately one fifth of the level caused by a minimum ionizing particle. For use in the Level 1 trigger, discriminator outputs for the y-measuring counters from each side of the beam are separately OR'd together. The discriminated x-counter signals from each end of a slat are meantimed and then OR'd for the Level 1. TDC's, receiving the discriminated output from each phototube, determine the time of all hits in the muon hodoscope.

A few variables serve to parameterize the performance of the muon hodoscope system. After various offline corrections the time distribution of hits for the system has a full width of 4 ns. Averaging over all the phototubes in the hodoscope, a typical phototube has a singles rate of about 0.45 KHz at a beam intensity of 3×10^{12} protons per AGS pulse on the B5 target. Although less than one pion in 10^3 is expected to pass through the iron without suffering any hadronic collisions, a few percent of the pions entering the iron produce secondary charged tracks in the muon hodoscope. A further 3% of the pions decay into a muon and a muon-type neutrino between the fifth drift-chamber module and the leadglass. Based on the fraction of early hits and a calculation using the singles rates, several electrons in a thousand are expected to mimic a muon in the hodoscope due to an accidental hit from a neutron interaction or a coincidental muon

track. The efficiency of the muon hodoscope for registering the passage of a muon from $K_L \rightarrow \mu^+ \mu^-$ is 0.973 ± 0.003 . Muons of momentum less than 1.4 GeV/c are generally stopped before exiting the downstream face of the iron due to electromagnetic scattering in the leadglass and iron.

III.6 Muon Rangefinder

Since differentiation between the various types of particles is crucial to rejecting backgrounds due to semileptonic decays and other processes, two independent detector systems are used to identify both muons and electrons. In addition to the muon hodoscope the muon rangefinder was constructed, jointly by the College of William and Mary and the Los Alamos National Laboratory, to further distinguish muons from other particles.⁴⁸ The rangefinder is based on the same principle as the muon hodoscope: muons are the only charged particles which can penetrate substantial amounts of matter. Most particles in the detector volume are mesons or baryons, which interact strongly with atomic nuclei and therefore quickly lose energy both through elastic processes and by the creation of secondary particles. Only the three species of charged leptons are not subject to the hadronic force and lose energy predominantly through electromagnetic interactions. Their greater acceleration causes electrons to radiate energy more rapidly than muons. Tau leptons are too short-lived to produce tracks in the detectors. Thus muons are the only charged particles capable of leaving long tracks in the rangefinder with appreciable probability.

Muons lose energy in an effectively continuous manner as they move through the rangefinder. With a Monte Carlo simulation one can calculate the distribution of the depths to which muons with a given momentum will penetrate. For an actual track the penetration depth is the quantity measured by the detector. Employing a

correlation matrix this depth is converted into a momentum for the track. This momentum is then compared to the momentum measured by the drift-chamber spectrometer system. If the rangefinder and drift-chamber momenta agree within a set limit, the track is considered a muon. The pattern-recognition algorithm, used to find tracks in the rangefinder, considers only that area of the rangefinder which is spatially compatible with the particle's projected trajectory as determined by the drift chambers.

There are four possible sources of false muon tracks downstream of the iron: muons from the decay $\pi \rightarrow \mu \nu$, leak through of charged secondaries from pion interactions in the iron, accidental muons from coincidental kaon or pion decays not associated with the primary kaon decay, and interactions of particles in the neutral beam with the iron or rangefinder. Considering the tight time and spatial restrictions imposed by the muon hodoscope as well as the range requirement, accidental muons and neutral beam interactions should be correlated with less than 0.5% of the non-muon tracks. Although up to a few percent of pions will generate secondaries from hadronic interactions in the iron, very few of these secondaries can penetrate far into the rangefinder. Since the probability of pion leak through increases sharply with momentum and the rangefinder is quite effective for high momentum tracks, pion leak through should result in a pion mimicking a muon about one percent of the time. Muons from pions decaying downstream of the fifth drift chamber have momentum vectors which are essentially indistinguishable from those of primary muons. About 3% of the pions from kaon decay

themselves decay into muons in the back of the detector system and therefore represent the most serious background.

Besides its use in the offline identification of muons, the rangefinder was originally intended to provide a part of the Level 2 trigger and a measurement of the polarization of positive muons from the decay $K_L \rightarrow \mu^+ \mu^-$. Electronics to implement a crude track-finding algorithm, which would provide a range measurement for muons to the Level 2 trigger in less than a μs , were designed. Due to other factors which limited the maximum beam intensity which the detector system could accept, the Level 2 rangefinder electronics were unnecessary and never manufactured. Although not implemented, the intended use of the rangefinder in the Level 2 trigger necessitated a quick response from the proportional tubes. To minimize the electron drift-times in the proportional tubes, two wires were strung in each tube and the use of gas mixtures with fast drift-times was explored. In case the rangefinder is later expanded into a full-scale polarimeter, the system is built with the ability to read out every tube. This can be done to localize the muon's stopping position and the decay positron's trajectory as finely as possible.⁴⁹ The feasibility of using proportional tubes to measure a muon's polarization was tested at the Los Alamos Meson Physics Facility, with promising results.⁵⁰ A polarimeter must be built with absorber plates which do not depolarize stopping muons.

The requirement that the absorber plates retain a muon's polarization led to the selection of Carrara marble and 6063-T6 aluminum alloy for the bulk of the rangefinder. The thickness and transverse dimensions of the absorber slabs are determined with a

Monte Carlo simulation. Optimizing the number of muons stopped as well as the fraction and energy distribution of the positrons from the decay $\mu^+ \rightarrow e^+ \nu \bar{\nu}$ escaping from the absorber, results in a design with 7.62-cm thick absorber plates with x and y dimensions of 2.25 and 3.05 meters, respectively. Each slab is constructed from four separate plates of marble bonded together with 3M 2216 B/A adhesive. A steel band is also affixed to the outside edge of every slab to improve its structural integrity and provide a means of lifting it. An aluminum stand is used to position the slabs relative to each other and the beam. With one slab having a mass of 1455 Kg, the complete set of 200 represents a total mass of 2.91×10^5 Kg. Aluminum is three times as expensive as marble and possesses a cross section of 0.23 barns for thermal neutron capture. During neutron capture, a 7 MeV γ ray is radiated; the resulting nucleus then decays with a lifetime of 144 seconds by emitting a β particle and a 1.7 MeV gamma ray. Brookhaven provided 50 slabs of Aluminum; the remaining 150 absorber slabs are made of marble. To reduce the singles rates in the proportional tubes the slabs located immediately on either side of a detector plane are always of marble. The 100 slabs on each side of the beam results in 99 5.08-cm deep gaps into which detector planes can be placed.

There are 13 pairs of x- and y-measuring planes of proportional tubes on each side of the beam. The spacing of the 13 instrumented gaps is selected to yield momentum measurements with a relative precision of 10% (see Fig. 15). Table III gives the range of momenta for muons which stop in a particular gap.

Table III

Range of momenta associated with each rangefinder gap

Gap Number	Lower momentum	Upper momentum
1	1.93	2.06
2	2.06	2.29
3	2.29	2.54
4	2.54	2.79
5	2.79	3.05
6	3.05	3.35
7	3.35	3.70
8	3.70	4.05
9	4.05	4.48
10	4.48	4.98
11	4.98	5.45
12	5.45	6.14
13	6.14	-

A plane is comprised of individual extruded aluminum sections. An extrusion⁵¹ cross section is shown in Fig. 16. Two gold-plated tungsten wires with diameters of $75 \pm 3 \mu\text{m}$ are strung in every tube. Two wires, separated by 1.06 cm, are used in a tube in order to reduce the electron collection time, allowing narrower time gates. All wires are cleaned with propanol and visually inspected before being drawn into an extrusion. Each wire is inserted into a stainless steel minitube with an inner diameter of $125 \mu\text{m}$. The minitubes are held in plastic Noryl holders, which in turn are positioned in the Lexan endcaps.⁵² Bondmaster 666 epoxy is used to hold the endcaps in the ends of the extrusions and to provide a gas seal. There are four distinct types of molded endcaps characterized by their control of gas flow: electronics end on beam right, non-instrumented end-on beam right, electronics end-on beam left, and non-instrumented end-on

beam left. A Starrett Cut Nipper tool is used to crimp the wire within the minitube at the non-instrumented end of the extrusion.

After tensioning the wire by suspending a 500 gram weight from it over a pulley, the minitube at the electronics end is crimped. Two potential problems, slippage of the wire and breaking of the wire, can be caused by too loose or tight a crimp as well as too high a tension. Tests were performed by crimping wires under various tensions and crimping methods to determine conditions which optimized the reliability of the system and kept the wires sufficiently straight in the presence of electrostatic and gravitational forces. These studies revealed a plateau structure as a function of the amount of crimping. The wires have a nominal elastic limit of 925 grams, but given the 3% variation in diameters, a conservative limit would be around 850 grams. Given this information it was decided to crush the minitubes to an outer thickness of 500 μm from their original diameter of 1000 μm . This value is in the middle of the plateau. The gain and high voltage at which a trip occurred depended sensitively on the wire-to-wall separation. A typical distance from the wire to the wall of the extrusions is 5 mm with the wire held at positive high voltage and the wall at ground. To improve the gas seal of the extrusions, the last mm of all the minitubes is crimped closed and dabbed with epoxy.

For quality control, the extrusions were tested at William and Mary, generally on the day they were manufactured. This allowed us to discover problems in the assembly process and correct them quickly. The resistance between the two wires within a single tube is checked to determine if the wires are crossed. The tension of every

wire is measured by a magnetic induction technique.⁵³ A magnetic field of about 7,000 Gauss is imposed on the central portion of a wire and an oscillating electric current is passed through the wire and the extrusion. This current drives the wire into oscillation. Motion of the wire in the magnetic field induces a voltage on the wire. This induced voltage is small except when the wire is driven at a multiple of its fundamental frequency. At resonance an out-of-phase voltage of several millivolts is observed with the visual aid of a Lissajous figure on an oscilloscope. The tension is related to the measured frequency by the formula: $Tension = 4\mu L^2 f^2$, where μ is the linear mass density, L is the effective free length of the wire, and f is the observed fundamental frequency. If the tension is less than a set limit the wire is restrung.

Extensive evaluation of the performance of the detectors was performed in a Faraday cage using the preamplifier and discriminator employed in the experiment. A 50/50 mixture of argon/ethane gas was flowed through the extrusion and a crude leak test performed with rotameters. After several volume exchanges the singles rate and current drawn were recorded as a function of high voltage. Employing scintillators positioned above and below the detector, a high voltage versus efficiency plateau curve was taken on cosmic-ray muons. The voltage at which an extrusion trips the voltage supply was also noted. Individual tubes were then irradiated with a Strontium-90 beta source and the rate recorded. This test procedure revealed defects in individual tubes and problems involving the entire extrusion. All detectors were color coded, indicating their beamside and orientation, and numbered.

The finished detectors were packaged in styrofoam and transported to Brookhaven. The wires were tension-tested again at Brookhaven. None of the wires lost a significant amount of tension during this journey. Since the rangefinder is filled with ethane, a flammable gas, extensive leak chasing was done on extrusions prior to their assembly into complete detector planes. A combustible-gas leak detector, which is also sensitive to hydrocarbons to a level of 50 ppm, was employed to test every joint in the system (of which there are about 70,000).

After leak testing, the extrusions were edge bonded into planes with Loctite Depend, an anaerobic adhesive. The x- and y-measuring planes contain 12 and 16 extrusions, respectively (see Figs. 17 and 18). To avoid introducing any curvature in the finished plane, which could reduce the maximum high voltage attainable, the table on which the bonding was done was carefully constructed from marble blocks so as to be flat to 250 μm . Polyethylene tubing manufactured by PolyFlo with an outer diameter of 0.64 cm carries the gas mixture between the extrusions within a plane. Since polyethylene is notoriously difficult to bond, the tubing's outer diameter was first roughened with a die to prepare the surface and then bonded into the endcap input/output ports with Bondmaster 666 epoxy.

Aluminum sheets, 0.16 cm in thickness, were bonded across the edge-bonded extrusions with Loctite adhesive and a silver-based conductive epoxy. Copper tape was also laid down so as to overlap all extrusions in a plane and the aluminum sheets. These sheets provide structural strength and connect the separate extrusions electrically. The steel minitubes at the non-instrumented end of the plane are

cleaned and covered with insulating electrical tape to prevent arcing to the aluminum. Near the top of each plane aluminum pieces, termed "ears", were bonded to the outer edges. These ears support the weight of a plane as it hangs from the aluminum stand in the experimental cave. The completed planes are lifted using eye-bolts threaded into brass nuts imbedded in the aluminum ears. Hall cranes lift the planes into and out of a Unistrut transfer fixture, which can hold as many as ten finished planes. A large fork-lift carries a full transfer fixture from the building in which the detectors are assembled to the AGS experimental area. Once the detectors are installed in the B5 beamline, the electronics and gas distribution system are connections are made.

The interior of a proportional tube contains an electric field with intensities as high as several KV/cm. As a charged particle traverses the gas surrounding a wire, molecules in the gas are ionized. Electrons drift toward the wire anode and cations toward the aluminum walls. Drifting electrons suffer repeated collisions with molecules of the gas resulting in further ionization. This process causes the initial number of electron-ion pairs to be multiplied by a factor of 10^5 . The time response of the detector is determined by how long electrons take to drift to the wire. A highly active chemical environment exists about a wire in which large molecules could form deposits on the wire surface. Such local deposits increase the diameter of a wire and therefore decrease the local electric field. Fibers can also grow outward from a wire and can result in arcing to the tube walls. These processes are referred to as aging of proportional wire detectors. Due to these processes it is imperative

that the gas mixture be free of contaminants. Some researchers report that wire aging decreases with an increased flow of gas through the system. Minimization of this wire aging dictates many parameters of the system.

The gas mixture used in the rangefinder consists of 49.2% ethane, 49.2% argon, and 1.6% ethyl alcohol. This is an established mixture which is known to result in a long wire life. Contamination due to simple hydrocarbons represents about 0.5%. Drawings of the gas distribution system are shown in Figures 19 and 20. Equal flows of argon and ethane into a mixing volume are obtained using two channels of a mass flow controller. The resulting gas mixture is then bubbled through a gas washer bottle containing ethanol at a constant temperature of 1° C. Evaporation of the ethanol into the argon/ethane gas flow determines the relative concentrations. Following the addition of the ethanol, the gas enters two 13 meter long, 10-cm diameter polyethylene pipes located on each side of the beam. From the pipes, PolyFlo tubing distributes the gas to sets of extrusions. Extrusions subject to the highest particle flux are grouped in sets of four, whereas other extrusions are arranged in groups of 8. Gas flow within an extrusion proceeds serially from tube to tube. It requires between 7 and 20 hours to exchange the gas volume in an extrusion. Gas flows into the rangefinder at a rate of eight liters per minute. Exhaust gas from the proportional tubes is collected in another pair of polyethylene pipes and is then expelled into the atmosphere. A third channel of the mass flow controller measures the exhaust flow rate to provide evidence of leaks.

A small (30 cm long) proportional chamber extrusion located outside of the experimental cave is used to monitor the quality of the inflowing and exhaust gases. The aluminum wall above a single tube was replaced with a thin beryllium window. An ^{55}Fe x-ray source irradiates the gas beneath the window. The gas gain of the proportional tube is monitored by observing the position and width of the x-ray peak on a multichannel analyzer.

To establish the electric field within a proportional tube, the wires are kept at a potential of +2,650 volts, while holding the aluminum extrusion at ground. High voltage is supplied by a multichannel Bertan unit. The Bertan unit is remotely controlled using a DEC GIGI computer. A program resident on the GIGI continuously monitors the current and voltage on each channel and trips a visual and audible alarm if certain limits are violated. SHV cables carry the high voltage from the supply to amplifier boards attached to the planes. The HV is fanned out from the amplifier boards⁵⁴ to every wire. The amplifying circuitry is isolated from the high voltage by 2200 pF capacitors and input protection is provided by a pair of diodes.

Proportional tube pulses are AC coupled to a three-stage ECL 10116 line-receiver. The two wires in a tube are connected together and treated as a single channel. Only a single differential input is used in the first and last amplification stages, while the middle stage employs both differential inputs. The total gain is 128. To suppress high-frequency noise the amplifier boards are grounded to the aluminum planes along their entire length. Each amplifier board receives signals from the 16 tubes in two contiguous extrusions.

A 46-cm long, 17-pair twist-n-flat ribbon cable carries the enhanced signals from the amplifier board to the discriminator board. Sixteen of the pairs transmit analog signals, while the seventeenth pair furnishes DC power to the amplifier board. A set of 78 linear power supplies provides DC power to the amplifier and discriminator boards. The amplified pulses are input to a TL810 voltage comparator. If the pulses exceed a specified threshold, the comparator fires a 74LS123 monostable multivibrator. Threshold levels for each plane are set with a dedicated unit located outside of the cave. The width of output pulses from the multivibrator is set to 160 ns. Although not used, discriminated ECL outputs are available for each tube separately, as would be necessary for a polarimeter. Discriminated signals from all eight tubes in an extrusion are logically OR'd together to form the basic hit channel.

This OR signal is transmitted over twisted pair cables to a simple printed-circuit adapter card, from which the signals are further propagated over 91 meters of Ansley cables to Fasterbus latches. Whether a latch channel fires is determined by the overlap of the leading edge of a strobe signal with the discriminated ECL signal from the detectors. Each Ansley cable carries the 28 signals from the x-y pair of planes in a single gap. A latch board accepts up to three Ansley cables. A distinct strobe signal is used for each x-y pair of planes. Unlike the other digitizing modules, no sparse data scan is implemented by the latches; instead a switch on the board selects the number of words to be read out.

A set of ECL Output Register CAMAC modules is used to test the complete rangefinder electronics system. A pulse can be sent to the

portion of a discriminator board associated with a particular extrusion. An ECL-to-TTL converter on the discriminator board sends a signal to the amplifier board. The pulse is capacitively coupled to the amplifier inputs through a trace located on the boards. This system facilitates finding dead channels.

No deterioration in the performance of the rangefinder has been observed during the first two years of data taking. The integrated charge collected by a typical wire is estimated to range from 10^{-3} to 10^{-5} Coulombs/cm. Following the initial turn-on period, very few channels are found to have failed. The efficiency of a typical rangefinder plane for registering the passage of a muon was established to be about 93%. This efficiency was determined to be independent of beam intensity up to a flux of 8×10^{12} protons per pulse on the target. Apparently, this low efficiency was partially due to improper timing of the latch strobes relative to the detector signals in the 1988 running period.⁵⁵ In the second year of operation, better timing improved the single-plane efficiency to 96%.

CHAPTER IV

DATA ACQUISITION

During every AGS pulse the detector systems in this experiment register the passage of tens of millions of particles. If all the information generated by these particles in the detectors is digitized, the system would generate more than a Gigabyte of data per second. Since the tape drives are only capable of recording approximately 250 Kilobytes per second, the majority of this information has to be selectively rejected. This is accomplished by implementing a three level triggering system. Each successive level of the triggering system is more restrictive than the preceding level, thus reducing the number of events the next level has to examine. This progressive reduction in the number of events allows succeeding trigger levels an increasing amount of time to process each event. Due to this triggering scheme the experiment is not limited by tape writing speed.

Another problem associated with the high intensity of the beamline is the possibility of deadtime in the data acquisition system. Deadtime in the readout process is minimized through the use of a three-stage pipeline for each channel as well as the implementation of a highly parallel data-transfer mechanism. Information can be transmitted from the front end crates to the third level trigger processors at rates of up to 0.4 Gigabytes per second.

The overall readout system as well as the several levels of triggering are explained in detail in the following sections.

IV.1 Level 1 Trigger

Implemented with fast electronics, the Level 0 and Level 1 triggers perform several functions.⁵⁶ Their primary purpose is to indicate the presence of the products of a kaon decay in the detector system. The occurrence of a Level 1 trigger prompts the TDC's, ADC's, and latches to sense the state of every channel in the detector. Based on the status of the particle identification systems, events are determined to be possible examples of distinct kaon decay modes.

Signals from the trigger scintillation hodoscope are used to form the Level 0 trigger. All the scintillators are examined, with the exception of the upstream y-measuring banks. Pulses from the two phototubes attached to a given x-measuring scintillator are input into meantimers. All the upstream x-meantimer signals are OR'd together to form a single logical signal for each side of the beamline. The downstream x-meantimer outputs from each side of the beam are subdivided into four groups, where each group consists of 16 contiguous counters, and are used as inputs into four logical OR gates. These four OR gate outputs are individually timed in with the OR of all the downstream y-measuring signals from the same side of the beam. The signals from the left upstream, left downstream, right upstream and right downstream trigger scintillator banks are input to a LeCroy 4508 programmable logic unit (PLU). If all four banks register an in-time hit, the PLU enables the Level 0 strobe, indicating the presence of one or more charged particles on each side of the beamline. A schematic of the Level 0 logic is shown in Fig. 21.

Table IV

Typical rates for some of the detectors and triggers

Type of Detector	Typical Rate(MHz)
1st Drift Chamber(Total)	2.9
Trigger Counter	4.2
Cerenkov	5.0
Muon Hodoscope	5.3
Muon Rangefinder	4.0
Level 0	0.6
Level 1	0.006
Level 3	0.0002

When the Level 0 strobe is enabled a second PLU examines signals from the drift chambers, Cerenkov counters, the finger hodoscope, and the muon hodoscope. Average rates in several detector systems are listed in Table IV. To satisfy the requirements of the Level 1 trigger, information from the upstream drift chambers has to indicate the passage of a charged particle on both sides of the spectrometer. Logic diagrams for the drift chambers, particle identification, and photon systems are depicted in Figures 22, 23, and 24, respectively. Events follow three possible paths out of the PLU. As diagrammed in Fig. 25, all events satisfying the Level 0 and drift-chamber logic, regardless of the particle identification, are labelled as "minimum bias" events and follow path SC1. The minimum bias events are then prescaled by an initial factor of 1,000, which was later increased to 2,000. If, in addition to the minimum bias criteria, there are no hits in the Cerenkov and muon hodoscope counters, an event is considered a "prescaled $\pi^+\pi^-$ " trigger. Prescaled $\pi^+\pi^-$ triggers

follow the SC2 path and are prescaled by a factor of 500. The third class of triggers is comprised of events satisfying one of four dilepton topologies (i.e. μe , $e\mu$, $\mu\mu$, and ee) in the particle identification systems. The dilepton triggers are not prescaled. Logic for each of the possible triggers is shown in Table V. All of the logically compatible triggers are non-exclusive. As an example, an event could be written to tape by following both the minimum bias and dilepton trigger paths. A separate PLU, using logic identical to the primary Level 1 PLU, also determines which of the possible Level 1 trigger requirements an event passed. The output of this secondary PLU sets bits in a trigger latch module (TLM). These bits are known as the trigger bits and are written to tape along with the rest of the event information, if the remaining trigger selection mechanisms are satisfied.

Table V

Defining logic for Level 1 trigger bits

Level 1 Event Type	Logic Definition
μe Triggers	$L0*DC12*\mu_L*e_R$
$e\mu$ Triggers	$L0*DC12*\mu_R*e_L$
$\mu\mu$ Triggers	$L0*DC12*\mu_L*\mu_R$
ee Triggers	$L0*DC12*e_L*e_R$
Minimum Bias	$L0*DC12*Prescale1$
Prescaled $\pi\pi$	$L0*DC12*\bar{e}_L*\bar{e}_R*\bar{\mu}_L*\bar{\mu}_R*Prescale2$
$ee\gamma\gamma$ Triggers	$L0*DC12*e_L*e_R*2$ Clusters
$\mu\mu\gamma\gamma$ Triggers	$L0*DC12*\mu_L*\mu_R*2$ Clusters

A Temple University 8702 logic box receives the outputs of the primary Level 1 PLU along with signals from the Readout Supervisor,

the AGS beam gate, and the calibration logic. Physics events are vetoed if the Readout Supervisor indicates the system is busy processing a previous trigger or if a calibration trigger is occurring. If the readout system is not engaged in processing another trigger, the final Level 1 logic signal is sent to the front-end crates in order to commence the reading out of the event. This Level 1 pulse provides the start for the TDC's, gates for the ADC's, and strobes for the latches. The Level 1 output is also sent to the Readout Supervisor.

IV.2 Level 2 Trigger

If Level 1 indicates the presence of a charged particle on each side of the beam, information from the trigger scintillation hodoscope is used by the Level 2 trigger to filter out events not associated with a K_L decay.⁵⁷ Signals from the trigger scintillators are sent into LANL latch modules after passing through repeater boxes. The output of the latches is read into a set of custom priority encoders. The priority encoders are capable of encoding up to two hits in each scintillator bank. If there are more than a pair of hits in a given bank, only hits in the counters located closest to and farthest from the beam are encoded. The pattern of extreme hits is then sent to a set of 43 configurable memory lookup units (CMLU).

A decision to reject or keep an event is made by the CMLU's in less than 1 μ s following a Level 1 trigger and a strobe signal sent to the Readout Supervisor. For a hit in a particular upstream scintillator, only hits in a small set of downstream counters are compatible with a track resulting from a K_L decay within the acceptance volume of the spectrometer. Tests are done independently for x- and y-views and separately for each track to determine whether the upstream and downstream hits are consistent with a K_L decay. From the location of the hits in the x-view, the momentum of a track could be determined to 20%. An invariant mass can be calculated using the track momentum as determined by Level 2. To summarize, Level 2 can cut an event based on the following: upstream and downstream hit correlations, divergence of the tracks, and the reconstructed invariant mass. At a beam intensity of 4×10^{12} protons per pulse,

the Level 2 correlation cut alone rejects one third of the raw events, while losing 15% of the good two-body decays. Due to the limited beam intensity available during the 1988 data taking, the Level 2 filter was not used to actively select events.

IV.3 Level 3 Trigger

A fast track finding algorithm is applied to all events read into the 3081/E processors⁵⁸ and loose cuts are made on the calculated kinematics of the event. A typical event requires 2 ms of 3081/E CPU time for the Level 3 calculation. About 50% of the 3.2 second beam spill is available for the calculation with the remainder of the spill taken up with the readout of the data into the turbo-memory and the uploading of the data to the μ VAX. With eight processors running, a rough upper limit on the average number of events which could be examined per beam spill is about 6,400. About 95% of the Level 1 triggers fail the Level 3 cut. No cut is made on the minimum bias events.

The Level 3 software code⁵⁹ uses information from the three upstream x-measuring drift-chamber modules and the two most upstream y-measuring drift-chamber modules. The initial stage of the algorithm searches for pairs of adjacent hit wires within a module which form a good time-sum. Up to four good time-sum hit pairs per plane are allowed. If no good time-sums are located in a plane, a single bad timesum hit pair is used if present. At a preliminary stage, events are rejected in which one of the 10 relevant planes possesses less than two struck wires.

The set of selected hit pairs is then examined for possible tracks on each side of the spectrometer in the two upstream pairs of x- and y-planes. Initially the two sides of the beam and the x- and y-views are considered separately. Hit pairs in the first and second set of chambers are checked for consistency with a kaon decay track by

looking up the hit pattern in a correlation matrix. The elements of the correlation matrix are determined from actual data.

X-view tracks on one side of the beam are then combined with x-view tracks on the opposite side of the beam and the divergence of the resulting pair of tracks is checked for compatibility with the divergence expected from a kaon decay. Y-view tracks on opposite sides of the beam are similarly combined and are required to project through the most downstream drift chamber. The z-position of the vertex formed by the x-view tracks is then compared to the z-position of the vertex formed by the y-view tracks. The z-positions of the x- and y-vertices are required to be within 5 cm of each other. If the set of wire hits does not satisfy the vertex cut, other hits are tried. The third x-measuring drift-chamber plane is examined for hits in a limited region compatible with the bending of the previously selected x tracks in the first two planes.

The last step is to calculate the momentum of each track based on its deflection in the field of the 48D48 magnet. To minimize the time necessary for the momentum calculation, a table consisting only of the y component of the magnetic field in a 5.08-cm grid is used instead of the full field map. The field is integrated along a simplified trajectory which consists of a straight-line projection from hits in the first two planes to the center of the magnet and the line connecting this center position to the hit in the third plane. This field integral determines the transverse momentum kick imparted to the particle. This momentum kick is then divided by the angular deflection undergone by the particle to determine the track's momentum. A small angle approximation is employed to calculate

the track's deflection by taking the difference between the tangent of the track upstream of the magnet's center and downstream of the magnet's center.

From the calculated track momenta, the collinearity angle of the kaon decay is calculated. In order to reject decays with missing momentum, primarily three-body decays containing an unobserved neutral daughter, a cut is then imposed which only accepts events with a Level 3 collinearity below 20 milliradians. If an event is found to satisfy the Level 3 collinearity cut, invariant masses are then calculated using all the particle type hypotheses indicated by the set Level 1 trigger bits. All the reconstructed masses for an event are checked to see if they are within a predetermined mass range. The accepted mass range is from $0.460 \text{ GeV}/c^2$ to $0.550 \text{ GeV}/c^2$. No cuts are made on minimum bias events by the third Level 3 algorithm.

IV.4 Readout of the Data

Information from the detectors follows a path from the front end electronics to the output tape drive under the control of the Readout Supervisor. The Readout Supervisor (RS) is a set of twelve custom-built CAMAC modules which reside in a single crate. Communication between the RS and the online μ VAX II is carried out via the CAMAC dataway. All other signals to or from the RS are transmitted over dedicated cables. The readout architecture⁶⁰ is shown schematically in Fig. 26 and is elaborated on in the rest of this section.

Signals from some of the detectors are amplified and/or discriminated by fast electronics located within the experimental cave, while the pulses from other detectors are sent directly to the digitizing modules. As discussed in the previous chapter, there are three distinct types of digitizing units: analog-to-digital converters, time-to-digital converters, and leading-edge strobe latches. All three types of units digitize signals only upon receipt of a Level 1 signal. Digitization requires less than 200 ns. The results of the digitization are then stored in the Stage 1 latch. If there is no event in the Stage 2 Latch, the RS instructs the modules, via the Crate Scanners, to transfer the event information into the Stage 2 Latch. The RS disables the Level 1 trigger while an event is present in the Stage 1 latches. Since all events are treated as having passed the Level 2 trigger, events contained in the Stage 2 latches are immediately transferred to the 3081/E turbo-memories. This transfer is initiated by the RS by sending signals to the Crate Scanners. A Crate Scanner reads the data from each module installed within its crate, one module at a time.

Only channels which contain hit information for the current event are read out using a sparse data scan technique. Pairs of crates are connected as master and slave with the readout of the slave crate's modules proceeding via its Crate Scanner and the master crate's Crate Scanner. Every master Crate Scanner is separately connected to all eight 3081/E turbo-memories using eight 17 twisted-pair cables.

The RS keeps a record of which 3081/E processors are currently available to accept raw data. When the memory of a 3081/E is full, the RS initiates the Level 3 algorithm and marks the processor as busy, redirecting new events to another third level trigger processor, if one is available. A processor indicates to the μ VAX II when it has examined all the events in its memory. The μ VAX II then uploads the events, which have passed the Level 3 trigger, from the finished processor. Uploading of the data from the 3081/E's is done with a DR11W parallel interface. Upon completing the uploading of all the events from a third level trigger processor, the μ VAX II informs the RS that the processor is available to accept more events.

Resident on the μ VAX II is the online data acquisition program. The online program consists of several interacting processes. As events are uploaded from the 3081/E's, the information is temporarily stored in a buffer. When this buffer is full, the contents of the buffer are written to one of the two 6250 BPI tape drives. Upon reaching the end of an output tape, the μ VAX II automatically switches to the other tape drive and starts the next data run. Runs can also be started and stopped manually by an operator. With few exceptions an individual run corresponds to an entire tape. As events are uploaded to the μ VAX II, one of the online processes samples a

fraction of them. Information from sample events can be displayed graphically. This visual display provides information on the status of the various detector systems as well as on the data acquisition system. Any anomalies in the performance of the experimental apparatus can thus be recognized. A precompiled Level 3 code is downloaded to the 3081/E's from the μ VAX II during the initialization of the system. An operator can also run diagnostic tests on the 3081/E's from the μ VAX II. In general the online μ VAX II provides the human interface to the experiment.

CHAPTER V

ANALYSIS OF THE DATA

In order to measure the $K_L \rightarrow \mu^+ \mu^-$ branching fraction, the number of $K_L \rightarrow \mu^+ \mu^-$ events in the dimuon sample and the number of $K_L \rightarrow \pi^+ \pi^-$ events in the minimum bias sample must be established. The branching fraction of the decay $K_L \rightarrow \pi^+ \pi^-$, which is well determined by other experiments,¹³ is then used to normalize the event sample to the absolute number of kaon decays observed. The relative number of $K_L \rightarrow \mu^+ \mu^-$ and $K_L \rightarrow \pi^+ \pi^-$ events must be corrected for any differences in geometric acceptance as well as possible unequal effects of the analysis cuts for the two decay modes. In order to minimize these corrections, the analyses for the two decay modes are identical except for the requirement of muon identification for the $\mu^+ \mu^-$ events. No particle identification is employed in the selection of the dipion normalization sample.

Rejection of background events is a central goal of the analysis. For the decay $K_L \rightarrow \mu^+ \mu^-$, the major sources of background are expected to be the two semileptonic decay modes, in which the daughter pion decays in flight to a muon and a neutrino. Restrictions on the collinearity eliminate these two decays unless the neutrino is emitted with low energy. The requirement of a good vertex and continuous tracks through the spectrometer can reject the majority of pion decays in flight. However, if a pion decays in flight after the most downstream drift chamber there is no effective means of

distinguishing it from a primary decay muon. For the decay $K_L \rightarrow \pi \mu \nu$, where $\pi \rightarrow \mu \nu \mu$, these events have an invariant mass less than 489 MeV/c², assuming zero mass resolution. If the electron from the decay $K_L \rightarrow \pi e \nu$ is misidentified as a muon, due to an accidental muon or to a neutron interaction downstream of the iron filter, there is no mechanism to distinguish this class of event from an actual $K_L \rightarrow \mu^+ \mu^-$ decay.

The data analyzed in this work were recorded during the winter and spring of 1988. During 815 hours of active data taking, 180 million events were written onto 2,134 magnetic tapes at a density of 6250 BPI. This represents approximately 340 Gigabytes of information. The distribution of these events by Level 1 trigger bit is shown in Table VI. From the table it is evident that events containing a γ comprise a considerable fraction of all events.

Table VI

Distribution of raw non-exclusive Level 1 trigger bits

Level 1 Event Type	Fraction of Uncut Data With Bit Set
μe Triggers	0.1262
$e \mu$ Triggers	0.1270
$\mu \mu$ Triggers	0.2163
ee Triggers	0.4576
Minimum Bias	0.1427
Prescaled $\pi \pi$	0.1143
$\pi \pi$ Triggers	0.0556
$ee \gamma \gamma$ Triggers	0.4416
$\mu \mu \gamma \gamma$ Triggers	0.1095
Calibration Triggers	0.0552
Pedestal Triggers	0.0150

Since events associated with a neutral particle are not relevant to this analysis, these events must be removed from the data sample. In the first stage of the analysis, loose cuts are made on the Level 3 invariant mass and collinearity in order to reject decays containing neutral particles. The mass is required to be between $460 \text{ MeV}/c^2$ and $550 \text{ MeV}/c^2$ and the collinearity has to be less than 10 milliradians. These cuts eliminate 89% of the dilepton and $\pi\pi$ triggers. A flowchart of the offline data analysis is depicted in Figure 27. To keep the minimum bias events from numerically overwhelming the physics events, minimum bias events are further prescaled by a factor of either 3 or 6, in addition to the online prescale of 2,000 or 1,000, in order to maintain a constant total prescale factor of 6,000.

A pattern recognition algorithm is then applied to the events surviving the Level 3 cuts. This algorithm searches the set of hits in the drift chambers for a good pair of tracks. These tracks are required to reconstruct to a vertex and to satisfy loose chi-square requirements on the particle orbits through the magnetic fields. Applying the offline Level 3 cuts and the pattern recognition algorithm to 2,134 raw tapes used approximately 100 hours of CPU time on Brookhaven National Laboratory's IBM 3090 computer. This pass of the data analysis reduced the raw data tapes to 229 Pass 1 output tapes which contained all the original information about the accepted events as well as the pattern recognition results.

The consistency of the data and the analysis over time is important. In Fig. 28 the fraction of events on a tape which are identified as minimum bias $K_L \rightarrow \pi^+\pi^-$ candidates is shown. The reconstruction efficiencies for prescaled dipion events and for

dilepton events is histogrammed in Figures 29 and 30 for all the data tapes used as input for pass 1 of the analysis. All three of these plots are quite flat throughout the run.

Table VII

Tapes resulting from stage 2 of the analysis

Tape	Number of Events	Level 1 Trigger Bit
1	48371	$K_L \rightarrow \mu^+ \mu^-$
2	38303	$K_L \rightarrow \mu^+ \mu^-$
3	54081	$K_L \rightarrow \mu^+ \mu^-$
4	44357	$K_L \rightarrow \mu^+ \mu^-$
5	51111	$K_L \rightarrow \mu^+ \mu^-$
6	42648	$K_L \rightarrow \mu^+ \mu^-$
7	31424	$K_L \rightarrow \mu^+ \mu^-$
8	55672	$K_L \rightarrow \mu e$
9	55799	$K_L \rightarrow \mu e$
10	55365	$K_L \rightarrow \mu e$
11	47667	$K_L \rightarrow \mu e$
12	41659	$K_L \rightarrow \mu e$
13	43313	$K_L \rightarrow e^+ e^-$
14	28511	$K_L \rightarrow e^+ e^-$
15	45851	Prescaled $K_L \rightarrow \pi^+ \pi^-$
16	47446	Prescaled $K_L \rightarrow \pi^+ \pi^-$
17	59182	Prescaled $K_L \rightarrow \pi^+ \pi^-$
18	53564	Prescaled $K_L \rightarrow \pi^+ \pi^-$
19	42334	Prescaled $K_L \rightarrow \pi^+ \pi^-$
20	14793	Prescaled $K_L \rightarrow \pi^+ \pi^-$
21	48246	Minimum Bias
22	37294	Minimum Bias

In the second pass of the analysis, events are selected on the basis of the pattern recognition results. The collinearity, as calculated

by the pattern recognition algorithm, is required to be less than 0.003 radians. Minimum bias and dimuon event types are rejected if their reconstructed invariant mass is less than 450 MeV/c² and 475 MeV/c², respectively. Similar invariant mass restrictions are applied to the other event types. The tracks identified by the pattern recognition algorithm have their orbits through the magnetic fields calculated using a table of the integrated magnetic field. The final orbit calculation employs the full set of magnetic field measurements and steps the particles through the field using the Runge-Kutta technique, which provides more accurate trajectories. This second analysis pass takes about the same amount of computer time as the initial pass and reduces the data to 22 data summary tapes. These summary tapes are sorted according to Level 1 trigger bit. The number of tapes and events for each event class is given in Table VII.

A set of constraints is then imposed on the kinematic parameters, as determined by the iterative calculation, of each recorded event. Identical kinematic constraints are applied to both the dimuon and minimum bias samples. This set of cuts selects events on the basis of the quality of the vertex, the location of the vertex, the continuity of the particle orbits, and the volume through which the particles passed. These cuts help to further eliminate three-body decays and events in which a pion decays. A specific cut is imposed to reject lambda decays. The muon hodoscope and the muon rangefinder signals are examined to insure that both particles in each dimuon event are indeed muons. The number of background events in the mass-collinearity region for both decay modes is then estimated

from the Monte Carlo, and the number of events corrected accordingly. In the following sections, a description of the analysis cuts, the relative correction factors, and the background estimation for the two decay modes is given.

The equation determining the branching fraction of $K_L \rightarrow \mu^+ \mu^-$ is :

$$B(K_L \rightarrow \mu^+ \mu^-) = \frac{N_{\mu\mu} * A_{\pi\pi} * B_{\pi\pi} * \epsilon_{\pi\pi}}{N_{\pi\pi} * PS_{MB} * A_{\mu\mu} * \epsilon_{\mu\mu}} \quad (5.1)$$

In Eq. (5.1) $N_{\mu\mu}$ is the number of dimuon events remaining after background is subtracted and $N_{\pi\pi}$ is the number of dipion events in the minimum bias sample remaining following subtraction of the background. $A_{\mu\mu}$ and $A_{\pi\pi}$ are the geometric acceptances of $K_{\mu\mu}$ and $K_{\pi\pi}$ events, respectively. $\epsilon_{\mu\mu}$ is the correction factor for $K_{\mu\mu}$ events lost due to mechanisms which do not affect $K_{\pi\pi}$ decays, and $\epsilon_{\pi\pi}$ is the correction factor for $K_{\pi\pi}$ events which are lost due to mechanisms which do not affect $K_{\mu\mu}$ decays. PS_{MB} is the product of the online and offline prescale factors for minimum bias events. $B_{\pi\pi}$ is the established branching fraction of $K_{\pi\pi}$ decays. The final branching fraction calculation is presented in the last chapter.

V.1 Pattern Recognition

In the first pass of the offline analysis, following the cuts on the Level 3 mass and collinearity, a pattern recognition algorithm is applied to the surviving events. This set of routines takes all the wire hits in the drift chambers and searches for combinations of these hits which form tracks. All combinations of the found tracks are then examined to determine which pair form the best vertex. The momentum of each track is then calculated along with the invariant mass formed by the two tracks. Cuts are made on the mass and collinearity as determined by the pattern recognition routines in the second analysis pass prior to the final event fitting. The results of the pattern recognition are used as initial guesses in the event fitting.

Initially, the pattern recognition algorithm searches for sets of good wire hits. Most charged tracks will fire a pair of neighboring wires in every chamber. Occasionally, only a single wire will fire or three wires will fire due to a delta ray or the track passing near a cell edge. The drift times, as registered by the TDC's, for pairs and trios of wires are examined. Only those sets of wires whose combinations of drift times are compatible with a physical hit are kept. Single hit wires are matched with neighboring unhit wires to form pseudo pairs. Only one wire, out of ten possible wires, in each view on a side is allowed to be missing a hit. If more than seven wire planes contain greater than 10 hits the event is rejected as too noisy.

In the x-view, a search is then made for pairs of hits in the first and second chambers and the fourth and fifth chambers which form one-dimensional lines, which are compatible with a track from a

kaon decay. Possible tracks from the upstream and downstream portions of the spectrometer are then combined. If the angles between the front and back portions of a possible track agree within 0.07 radians, they are treated as being a single track. The momentum of these tracks is then crudely calculated. In this method a track is assumed to undergo a 300 MeV/c kick in the center of each magnet. Hits in the middle drift chamber are in this way correlated with hits in the other planes. A hit in the third chamber is required to lie within 4 cm of the projections from the upstream and downstream chambers. If there are only nine hits in a view this maximum distance is relaxed to 8 cm. Y-view hits in the front and back pair of chambers are subjected to a least-squares fit to select complete tracks. The allowable difference in position of a hit in the third chamber and the front and back projections must be less than 2 cm or 4 cm, for 10 and 9 wire hits in a track, respectively. If there are too many tracks at this point in the algorithm, the event is dropped.

At this time the left-right ambiguity, for chambers with one or three wires hit, is resolved by checking which side yields the best track. The wire hits are then transformed into a single hit location. Next, the tracks are combined to form 3-dimensional events. A second least-squares fit is performed on the front and back portions of the tracks. The front and back tracks are then stepped through the magnets to the third chamber. The magnetic field is taken from a table of B-dl values. A χ^2 is formed independently for each view by summing the χ^2 's for the front, back, and middle portions of a track. The x- and y- χ^2 's are required to be less than 25. The x- and y- χ^2 's are compared for muons and pions in Fig. 31. An event vertex is now

found by considering all the tracks and taking the pair of tracks, on opposite sides of the beam, which have the smallest distance of closest approach. All other tracks are then deleted. The reasons that events fail are shown in Table VIII.

Table VIII

Pattern recognition outcome for minimum bias events

Pattern Recognition Outcome	Fraction of events
Pattern recognition finds a good event	0.442
No hit in at least 1 plane on left	0.038
No hit in at least 1 plane on right	0.054
No hit in planes on both left and right	0.005
7 planes have more than 10 hits	0.031
Less than 4 left-x planes have good time pairs	0.017
Less than 4 right-x planes have good time pairs	0.022
Less than 4 left-y planes have good time pairs	0.028
Less than 4 right-y planes have good time pairs	0.050
Too many x-view tracks	0.044
No x-view track on left	0.054
No x-view track on right	0.054
No x-view track on either left or right	0.017
Too many y-view tracks	0.001
No y-view track on left	0.041
No y-view track on right	0.041
No y-view track on either left or right	0.009
Too many 3 dimensional tracks	0.059
All of left x-tracks have too large χ^2	0.004
All of right x-tracks have too large χ^2	0.004
All of left y-tracks have too large χ^2	0.001
All of right y-tracks have too large χ^2	0.001

The largest losses are due to noisy events. Most of the remaining failures are due to missing hits or tracks. There is no evidence for a dependence of the pattern recognition efficiency on particle type.

V.2 Final Event Fitting

In the second pass of the offline analysis, following reduction of the data sample by cuts on the pattern recognition mass and collinearity quantities, all the remaining events are fit using an iterative approximation technique.⁶¹ This fitting produces the final track trajectories and vertex information for an event. Fitting is performed after the size of the data sample is reduced by the Level 3 and pattern recognition cuts. Most of the selection criteria, such as the final mass and collinearity, are based on the results of this fitting. A set of five χ^2 's is used to judge the quality of the fit determination.

The final fitting steps a particle through the magnetic field volume between two successive drift chambers. Differences between the projected and actual positions in the downstream chambers are then used as feedback for the next iteration through the magnetic field. This process is repeated until the fit trajectory agrees with the hit wire positions within a predetermined set of limits. The magnitude of the momentum and the positions of the hit wires associated with the two tracks, as calculated by the pattern recognition, are used for the initial iteration. In the y-view the particle begins at the hit positions in the first and fourth drift-chamber planes, at the angle formed by the hit positions in the successive planes, and is stepped through to the second and fifth planes. The differences in the projected positions and the actual hit locations, in the second and fifth planes, are used to correct the angle of the particle's trajectory at the first and fourth planes. This

procedure is repeated until the projected and actual hit locations in the second and fourth planes differ by less than a set value.

A similar routine is employed for the x-view trajectories. For the x-view, particles are started at the first and fifth drift-chamber modules and stepped toward the third plane. The differences between the projected and actual hit locations in the third and second or fourth planes is used to correct both the magnitude of the momentum and the initial angle at the first and fifth planes.

A χ^2 is calculated for the x- and y-view of each track based on how well the front and back fit trajectories match. The χ^2 for x depends on the calculated momenta and the angles at the third plane as determined by the upstream and downstream fits:

$$\chi^2_x = \frac{[\theta_{XF} - \theta_{XB}]^2}{\sigma_{\theta x}^2} + \frac{[P_F - P_B]^2}{\sigma_P^2} \quad (5.2)$$

where P_F and P_B are the momenta as measured in the front and back portions of the spectrometer and θ_{XF} and θ_{XB} are the track angles at the third plane. A Monte Carlo simulation, incorporating multiple scattering and the intrinsic position resolution of the drift chambers, is employed to find the expected root-mean square deviations, $\sigma_{\theta x}$ and σ_P . The χ^2 for the y-view is determined by the following formula and depends on the projected position in the third plane as well as the angle:

$$\chi^2_y = \frac{[\theta_{XF} - \theta_{XB}]^2}{\sigma_{\theta y}^2} + \frac{[Y_{3F} - Y_{3B}]^2}{\sigma_{3Y}^2} \quad (5.3)$$

where Y_{3F} and Y_{3B} are the projected hit location in the third plane as determined by fits to the upstream and downstream sections of the spectrometer, respectively.

Lastly, the portion of the trajectories relating to the vertex is examined. A common vertex, from which both tracks are presumed to have originated, is determined by finding the points on each trajectory where the tracks achieve their distance of closest approach. The vertex is taken to lie on the line segment joining the closest points on each trajectory. Since the uncertainty associated with each track in the vacuum region is dominated by multiple scattering, the distance along the line segment from the vertex to each track is inversely proportional to its momentum. The vertex χ^2 is equal to the distance of closest approach of the two tracks normalized by dividing it by the root-mean-square deviation as determined with the Monte Carlo.

These χ^2 serve an important purpose in the analysis. A critical test as to whether a pair of tracks originate from the same kaon decay is the goodness of the vertex χ^2 . In Fig. 32 the vertex χ^2 distribution is shown for $K_L \rightarrow \pi^+\pi^-$ events, with data represented by the solid line and Monte Carlo the dashed line. The Monte Carlo and data distributions for the track χ^2 are depicted in Figures 33 and 34 for $K_L \rightarrow \pi^+\pi^-$ decays. The Monte Carlo distribution is represented by a dashed line and the data by a solid line. This convention will be followed throughout the rest of this work. There is some disagreement between data and Monte Carlo in the track χ^2 distributions. There is a similar amount of disagreement for muon tracks. Basically, the distributions are more smeared for data events,

possibly from uncertainties in the magnetic field map or contamination in the data samples. Events are required to have all four of their track χ^2 be less than 20.0. The systematic uncertainty in the dimuon branching fraction associated with the track χ^2 anomaly is at most 1.6% and probably less.⁶²

V.3 Aperture Restrictions

A set of cuts is made to restrict particle trajectories to regions in which a track's path can be reliably predicted. This is done to exclude particles which pass through solid objects or regions in which the magnetic field is unknown. Particles traversing a solid are subject to large multiple scattering, hadronic interactions, and other forms of energy loss. Trajectories passing within an unknown magnetic field maybe bent in an unknown and therefore uncorrectable manner. Either of the previously mentioned mechanisms can result in a false calculation of the trajectories and thus cause the reconstructed mass and other kinematic variables to be incorrect. Since it is not possible to include such effects in the Monte Carlo, the calculated relative geometric acceptances will also be wrong.

Events with reconstructed vertexes with a z-position of less than 9.5 meters are cut to eliminate decays occurring within the fringe field of the last sweeping magnet. To insure that the kaon path was compatible with the divergence of the beam as defined by the collimators, the solid angles, from the target to the primary reconstructed vertex, are required to satisfy $|x/z| < 0.0027$ and $|y/z| < 0.010$, where x, y, and z are the coordinates of the reconstructed vertex. Tracks are cut which pass through the flange of the vacuum window located near the most upstream drift chambers. Distributions for the vertex z-position, vertex x/z, and vertex y/z are shown in Figures 35, 36, and 37, respectively.

A few percent of the $K_{\pi\pi}$ decays produce a daughter particle which passes through part of the 48D48 spectrometer magnet. In order to determine if a particle's trajectory intersects part of the magnet, the track has to be reswum through the magnetic field using the Runge-Kutta algorithm. If a track is swum back through one of the magnet's mirror plates or the 48D48 coils, the event is dropped from the analysis. All-of these aperture restrictions are also imposed on events in the Monte Carlo simulation of the geometric acceptances of the different decay modes.

V.4 Calculation of Acceptances

Determining the branching fraction of $K_L \rightarrow \mu^+ \mu^-$ entails knowing the fraction of kaon decays for which all of the decay products are recorded by our apparatus. This fraction is known as the geometric acceptance of our detector system. Since the geometric acceptance depends on the kinematics of a decay, it is different for the various decay modes. In order to properly normalize our event samples, we must know the geometric acceptance for $K_{\pi\pi}$ decays. Similarly, the number of $K_{\mu\mu}$ events has to be corrected for the acceptance of the detectors for this particular decay mode. $K_{\mu\mu}$ decays have a lower acceptance than $K_{\pi\pi}$ decays, primarily because of the muon's smaller mass. The geometric acceptance of each decay mode is calculated using the offline Monte Carlo.

Implemented in the Monte Carlo is a model of the detector systems, the target, and the collimators. The spectrum of kaons produced at the target is generated from an experimentally-derived parameterized distribution.⁶³ The physics of the decays which occur in the vacuum decay region is also simulated. This includes the major decay modes of lambdas, pions, kaon, neutrons, and muons. The kinematics of each of these reactions is determined from conservation of energy, momentum, angular momentum, etc. and from Dalitz distributions for the more complicated cases. The decays of unstable particles which are generated at the target or result from the decay of another particle are fully modelled. All the resulting particles are then stepped through the detector systems. The

multiple scattering and continuous energy loss for charged particles, in the detectors and other material along their path, is calculated. Bremsstrahlung is also calculated for electrons. If a track passes through a detector, the effect on the detector is simulated. This hit simulation includes time and pulse height information in the appropriate counters. The efficiency of the individual detector elements is incorporated into the software as well. Accidental backgrounds are produced through the decay of two or more kaons in the same event.

Table IX

Selection requirements for $K_L \rightarrow \mu^+ \mu^-$ sample

Description of Cut	Cut Value
Level 3: collinearity(radians)	<0.010
Level 3: invariant mass(GeV/c^2)	>0.460
Pattern recognition: collinearity(radians)	<0.003
Pattern recognition: invariant mass(GeV/c^2)	>0.475
Iterative fit: collinearity(radians)	<0.001
Iterative fit: invariant mass(GeV/c^2)	>0.4927
Iterative fit: invariant mass(GeV/c^2)	<0.5027
Iterative fit: vertex χ^2	<10.0
Iterative fit: x-track χ^2	<20.0
Iterative fit: y-track χ^2	<20.0
Iterative fit: vertex $ x/z $ position	<0.0027
Iterative fit: vertex $ y/z $ position	<0.010
Iterative fit: vertex z-position(meters)	>9.5
Iterative fit: Λ^0 mass, outbend, and $ \Delta P/\Sigma P $	<0.62
Iterative fit: track momentum(GeV/c)	>1.5
Muon hodoscope total confidence level	>0.01
Muon rangefinder (actual gap - expected gap)	>-4

For the acceptance calculation the same cuts are placed on the simulated events as are imposed on the data. As for the actual analysis, pattern recognition and the iterative fitting are performed on the Monte Carlo events. The full set of analysis cuts, as listed in Table IX, are used. The exceptions being that the Level 1, the Level 3, and muon identification are not simulated. Separate corrections must be used for the previous three classes of cuts, as well as for the nuclear interactions of the tracks with the material of the apparatus, since they are not included in the software. Trajectories of particles are required to intercept the trigger hodoscope and the muon hodoscope. Acceptances of the different decay modes is given in Table X. The acceptance of $K_{\mu\mu}$ relative to $K_{\pi\pi}$ is 0.8235 ± 0.0077 . The degree of agreement between Monte Carlo and $K_{\pi\pi}$ data is displayed in Figures 38, 39, 40, 41, and 42.

Table X

Geometric acceptances of the various decay modes

Decay Mode	Acceptance
$K_L \rightarrow \pi^+\pi^-$	0.0272
$K_L \rightarrow \mu^+\mu^-$	0.0224
$K_L \rightarrow \mu^+\mu^-\gamma$	0.0164
$K_L \rightarrow \pi\mu\nu$	0.0131
$K_L \rightarrow \pi e\nu$	0.0114
$K_L \rightarrow \pi^+\pi^-\pi^0$	0.0166

V.5 Pion Hadronic Interactions

One of the major distinctions between muons and pions is that pions are hadrons and are therefore subject to strong interactions. As pions from $K_{\pi\pi}$ decays pass through the spectrometer and other detector systems, some of them are hadronically scattered by nucleons in the apparatus and the surrounding atmosphere. The placement of helium bags throughout the detector system significantly reduces the probability of these interactions, since helium nuclei have a small hadronic cross section. Pions, which scatter within the spectrometer, are likely to be rejected by collinearity or χ^2 cuts. A necessary condition for a $K_L \rightarrow \pi^+\pi^-$ event to be included in the normalization sample is that it must have generated a level zero trigger by firing the first three drift-chamber modules and all the trigger scintillation hodoscope modules. If a pion suffers a deflection or undergoes a nuclear interaction in which only neutral daughter particles are produced, a Level 0 trigger may not result and the event will be lost. A correction to account for this missing fraction of $K_{\pi\pi}$ events must be factored into the $K_{\mu\mu}$ branching ratio calculation.

The portion of $K_{\pi\pi}$ events which are lost because of nuclear scattering between the vacuum window and the fifth drift chamber is calculated from the total or geometric cross section. It is assumed that any hadronic scattering within the spectrometer volume will cause a pion track to be discarded. The fraction of dipion decays which scatter in the spectrometer is calculated⁶⁴ to be 0.59%.

In estimating the percentage of pions which fail to fire the trigger hodoscope, the measured nuclear absorption cross sections are used. Calculations show that 2.87% of the $K_L \rightarrow \pi^+\pi^-$ events have at least one track suffer an inelastic scatter in the upstream trigger hodoscope or Cerenkov. The GEANT Monte Carlo code is employed to find the fraction of these inelastic scatters which fails to produce a charged track in the downstream trigger hodoscope. Simulations show that 71% of the inelastically scattered particles generate hits in the downstream trigger hodoscope. Combining these factors gives a correction for $K_{\pi\pi}$ events which are lost due to nuclear interactions of 1.5%. The probability of a $K_L \rightarrow \pi^+\pi^-$ event undergoing a hadronic interaction in the various elements of the apparatus is given in Table XI.

Table XI

Probabilities for a pion to hadronically interact with the apparatus

Apparatus	Total cross section	Inelastic Scattering
Vacuum window	0.00097	0.00045
Drift chambers	0.00160	0.00130
Helium bags	0.00337	0.00246
Trigger counters	0.02103	0.01560
Cerenkov	0.01950	0.01224
Air	0.00052	0.00421
Window-DC5	0.00594	0.00421
Trigger & Cerenkov	0.04105	0.02829

V.6 Hadron Decay Backgrounds

An assortment of particle species is generated by the proton beam interacting with the copper target. Most varieties are charged and are therefore deflected out of the beam by the sweeping magnets. Some of the neutrals; e.g., neutrons, neutrinos, and photons, only register in the spectrometer if they interact with the vacuum window or the drift chambers. Other neutrals such as π^0 and Σ^0 are too short-lived by many orders of magnitude to reach the decay region. Three neutral particles are relevant to this analysis: Ξ^0 , Λ^0 , and K_S in that they can kinematically mimic the decay $K_L \rightarrow \pi^+\pi^-$.

Potentially the most difficult background to reject is that which results from the decay of $K_S \rightarrow \pi^+\pi^-$, which is the K_S major decay mode. This decay is kinematically identical to the decay $K_L \rightarrow \pi^+\pi^-$, which is used to normalize this experiment. Due to decays, the intensity of K_S is reduced relative to that of K_L by the beginning of the vacuum volume. The smaller number of K_S relative to K_L is partially compensated by the greater probability of a K_S decaying if it reaches the vacuum region. Requiring the z-position of the reconstructed vertex to be greater than 9.5 meters reduces the number of accepted K_S to a low level. Demanding that the reconstructed vertex satisfy the conditions $|x/z| < 0.0027$ and $|y/z| < 0.010$, as well as having a collinearity less than 1 milliradian, rejects decaying primary particles which were not produced at the target, such as a regenerated K_S . However, some high momentum K_S do enter the vacuum region before decaying.

The number of $K_{\pi\pi}$ events in our minimum bias normalization sample must be corrected for the contamination of K_S decays. There are two distinct contributions to this contamination: 1) K_S produced at the target and decaying into a pair of charged pions and 2) interference between the $K_S \rightarrow \pi^+\pi^-$ and $K_L \rightarrow \pi^+\pi^-$ amplitudes. The probability for a K^0 to decay into a pair of charged pions is found by squaring the sum of the $K_S \rightarrow \pi^+\pi^-$ and $K_L \rightarrow \pi^+\pi^-$ amplitudes:

$$\left| \langle \pi^+\pi^- | H | K^0(t) \rangle \right|^2 = e^{-t/\tau_S} + |\eta_{+-}|^2 e^{-t/\tau_L} + 2|\eta_{+-}| e^{-(t/2\tau_S + t/2\tau_L)} \cos(\Delta m_K t/\hbar - \phi_{+-}) \quad (5.4)$$

where Δm_K is the $K_S - K_L$ mass difference and τ_L and τ_S are the lifetimes of the K_L and K_S , respectively. From the Monte Carlo, kaons decaying into a pair of charged pions are simulated. Each simulated event is weighted by the relative probabilities of the decay having resulted from a K_L , K_S , or from the interference term. Summing these three probabilities over many events and taking the effects of the kaon's momentum and decay position into account, yields the percentage of dipion events not resulting from K_L decays. Calculations⁶⁵ show that the fractions of the normalization sample coming from K_S and K^0 interference are 0.0089 and 0.0128, respectively.

The Λ^0 and the Ξ^0 have proper lifetimes of 2.6×10^{-10} and 2.9×10^{-10} , respectively. Thus the number of Λ^0 and Ξ^0 is significantly reduced in traversing the distance from the target to the upstream edge of the decay region. Still, potentially millions of these hyperons decay within the vacuum region during data taking. The primary

decay mode of the neutral cascade hyperon is $\Xi^0 \rightarrow \Lambda^0 \pi^0$, producing a Λ^0 in almost every decay. In turn the Λ^0 decays into a proton and a negative pion 64% of the time. A fraction of the phase space of this decay can imitate the decay $K_L \rightarrow \pi^+ \pi^-$, thus causing the dilepton branching ratio to be normalized improperly. The invariant reconstructed masses of the events in the normalization sample are shown in Fig. 43, where the positive track has been assigned the proton's rest mass and the negative track the pion's rest mass. The invariant mass of these events, using the dipion mass hypothesis, is restricted to the range 492.7 to 502.7 MeV/c². There is clear evidence of Λ^0 s at 1.115 GeV/c² in this plot.

There are several properties of the decay $\Lambda^0 \rightarrow p^+ \pi^-$ which distinguish it from $K_L \rightarrow \pi^+ \pi^-$. One finds that the ranges of momentum asymmetries for $K_L \rightarrow \pi^+ \pi^-$ and $\Lambda^0 \rightarrow p^+ \pi^-$ are 0.00 to 0.83 and 0.51 to 0.87, respectively. The momentum asymmetry distribution for the $K_L \rightarrow \pi^+ \pi^-$ minimum bias data set is shown in Fig. 44. There is a distinct peak in the data plot, which is not present in the Monte Carlo plot. The events in the high momentum asymmetry peak are the same events with reconstructed masses in the Λ^0 mass peak in Fig. 43. The momentum asymmetry of events selected with the proton and pion mass hypothesis, which have invariant masses within 25 MeV/c² of the Λ^0 mass, is displayed in Fig. 45. This plot shows that the majority of Λ^0 's in our minimum bias sample possess a momentum asymmetry greater than 0.6. The invariant mass of Λ^0 events is plotted in Fig. 46, after selecting Λ^0 's with momentum asymmetry above 0.6. If not removed, Λ^0 's will introduce an error into the estimation of the number of $K_L \rightarrow \pi^+ \pi^-$ events in the minimum

bias sample. Due to the geometric acceptance of the spectrometer only Λ^0 decays with the proton on beam left are capable of causing a Level 1 trigger. Events with a positive track on beam left are outbend events.

A set of requirements is used to determine if an event is a Λ^0 decay and to exclude them from the normalization sample. If an event satisfies all three of the following criteria then it is rejected: outbend topology, momentum asymmetry greater than 0.62, and a proton/pion reconstructed mass between 1.090 GeV/c and 1.140 GeV/c. This cut eliminates 90 events from the final normalization sample. All of these events are probably from the decay $\Lambda^0 \rightarrow p^+\pi^-$.

V.7 Normalization of Sample

To establish the number of kaon decays observed in our experiment, we record a sample of events with no cuts. The number of $K_L \rightarrow \pi^+ \pi^-$ decays in this minimum bias data set is used to normalize the dilepton physics samples. The accepted branching fraction for $K_L \rightarrow \pi^+ \pi^-$, as given in the Particle Data Booklet, in combination with the geometric acceptance for the various decays modes, allows us to determine the number of kaon decays occurring in our detector.

To the extent possible, identical selection criteria are imposed on the $K_{\mu\mu}$ and minimum bias $K_{\pi\pi}$ samples. This procedure minimizes the number of correction factors needed to account for differences in the two samples. Since the efficiency of vetoes is difficult to ascertain, no particle identification cuts are placed on the $K_{\pi\pi}$ events. So that we could study the Level 3 offline, the Level 3 mass and collinearity restrictions are not imposed on the minimum bias events. Effects, such as nuclear interactions, which are relevant only for pions, must also be taken into account. After applying all the cuts listed in Table IX, except muon identification and Level 3, a subset of the minimum bias sample of $K_{\pi\pi}$ events appears in Fig. 47. Clearly a significant amount of background is present.

The offline Monte Carlo is employed to estimate the shape of this background. We assume that this background is due to the known decays of the long-lived kaon. The mass spectrum of the minimum bias sample with a simulated background due to $K_{\mu 3}$ and $K_{e 3}$ superimposed is depicted in Fig. 48. The ratio of the number of

simulated background events under the $K_{\pi\pi}$ peak and in the regions to either side of the peak is used to estimate the contamination in the mass region of 492.7 to 502.7 MeV/c². The ratio of the absolute number of events to either side of the peak in the data and Monte Carlo samples is used to scale the simulated sample to data. After subtracting 1,021 background events under the $K_{\pi\pi}$ peak, this method yields 8887 \pm 126 $K_L \rightarrow \pi^+\pi^-$ events in the minimum bias sample.

V.8 Level 1 Trigger Bit Correction

All events satisfying the Level 1 trigger have their logic signals passed to a second PLU, which classifies each event according to the reason it passed the Level 1 (i.e. $\mu\mu$, μe , $\pi\pi$, minimum bias, etc.). The results from the PLU are then sent to a latch module. If there are associated hits in the muon hodoscope or Cerenkov detectors, events have a dilepton Level 1 trigger bit set in the trigger latch module (TLM). This additional set of logic may cause some dilepton physics events to be lost. This is possible because their particle identification signals may arrive out of time at the trigger bit PLU or because of some inefficiency within the PLU itself. This can result in the appropriate lepton trigger bit not being set. To establish the fraction of dimuon events which fail to satisfy the trigger bit logic, the minimum bias data set is examined for events in which both tracks are identified as muons. A track was considered a muon, if it met the same requirements as used for the final offline selection of $K_L \rightarrow \mu^+ \mu^-$: the muon hodoscope probability has to be greater than 1% and the track must penetrate the rangefinder to within three gaps of the gap expected from the momentum measured in the spectrometer. The event also has to satisfy all the aperture, track, and vertex analysis cuts as well. The subset of minimum bias events which have two muons is then examined to see how many have the $K_L \rightarrow \mu^+ \mu^-$ Level 1 trigger bit set. Using this technique the Level 1 trigger bit efficiency is found to be 0.981 ± 0.007 for dimuon events. Statistically equivalent efficiencies were found for the other three dilepton triggers.

V.9 Level 3 Correction

The preliminary stage of the analysis, both online and offline, involves the third level trigger calculation which is performed in the 3081/E emulators. As discussed in the chapter on data acquisition, a rough track-finding algorithm is performed online and cuts are made on mass and collinearity for all the event types except minimum bias. Although no cuts are made on the minimum bias sample, Level 3 calculations are performed on these events and the results are written to tape as they are for all events which pass the Level 3 cuts. Since some dimuon events are rejected by the Level 3 and no cut is made on $K_L \rightarrow \pi^+ \pi^-$ normalization events, a correction must be made to account for the inefficiency of the third level trigger algorithm for $K_L \rightarrow \mu^+ \mu^-$ decays.

There is no minimum bias $K_L \rightarrow \mu^+ \mu^-$ sample with which to measure directly the Level 3 efficiency. Nevertheless, an estimate for the Level 3 correction can be obtained by studying minimum bias $K_{\pi\pi}$ and $K_{\mu\mu}$ events. Using the same selection requirements as for the actual $K_L \rightarrow \mu^+ \mu^-$ analysis along with vetoes on the muon hodoscope and Cerenkov counters to reject semileptonic decays, a sample of good $K_L \rightarrow \pi^+ \pi^-$ decays are obtained from the minimum bias data set. This $K_{\pi\pi}$ sample is then subjected to the same Level 3 mass and collinearity cuts which are made on the $K_{\mu\mu}$ candidates. The ratio of the numbers of events before and after the Level 3 cuts gives the efficiency of the Level 3 algorithm for $K_L \rightarrow \pi^+ \pi^-$ decays as $0.785 \pm$.

0.007. A plot of the Level 3 mass versus the mass calculated by the iterative fit is shown in Fig. 49.

By examining minimum bias $K_{\mu 3}$ events with high mass and small collinearity a value of the systematic uncertainty associated with the Level 3 correction can be derived. The same aperture, track, vertex, and muon identification cuts as employed for the $K_{\mu\mu}$ analysis are used to select $K_{\mu 3}$ events with collinearity less than 0.001 radians. The Level 3 mass and collinearity cuts are then applied to this $K_{\mu 3}$ sample with the ratio of the number of events before and after the Level 3 cuts giving the efficiency for $K_{\mu 3}$ events. The efficiency of the third level trigger for $K_{\mu 3}$ decays is found to be 0.770 ± 0.013 . Taking the difference between the Level 3 efficiencies for $K_{\mu 3}$ and $K_{\pi\pi}$ to be a lower bound gives 0.015 as the systematic uncertainty to be associated with the Level 3 cuts for $K_L \rightarrow \mu^+\mu^-$.

This is probably an over-estimate of the Level 3 systematic error. Sixty-four percent of the events which fail Level 3 do so due to wire inefficiencies in the drift chambers. Studies of the data show the wire efficiency to be statistically indistinguishable for muons and pions. There is also a slight dependence of the Level 3 efficiency on the multiplicity of an event. Events which Level 3 fail to reconstruct have an average multiplicity of 35.2, summed over the 10 upstream planes, whereas events reconstructed by Level 3 have an average multiplicity of 32.6. Since both the $K_{\pi\pi}$ normalization and $K_{\mu\mu}$ samples are collected at the same beam intensities, the rate dependence of the Level 3 should be uncorrelated with decay mode. The Level 3 efficiency for good dipion decays varies during the period of data collection. Since the dimuon and minimum bias samples are collected

simultaneously, this time dependence of the Level 3 efficiency does not introduce a relative bias between the two samples.

Studies are also done of the dependence of the Level 3 efficiency on the z-vertex position of the decay, the x-view opening angle, the y-view opening angle, the x-position of a track at the first drift chamber, and the kaon momentum. Distributions for all events and also for those passing Level 3 are shown in Figures 50 and 54 for each of these kinematic parameters. The distribution of passing events is shown as a dashed line. No evidence for a systematic dependence of Level 3 on these kinematic parameters is found.

V.10 Muon Identification

Selecting candidates for the decay $K_L \rightarrow \mu^+ \mu^-$ requires differentiating among muons, pions, electrons, and other particle types present in the beam. The muon hodoscope and the muon rangefinder are used to identify muons, the basic idea is that muons are more likely to pass through the leadglass and iron filter without interacting significantly. To use the muon hodoscope and the muon rangefinder for particle identification, the behavior of the various particle types in these detectors must be understood. Two methods are employed to obtain this understanding: the response of the detector to actual particles is studied using data and the interactions of particles are simulated with the E791 offline and GEANT Monte Carlo codes.

To study the behavior of muons, a sample of $K_L \rightarrow \pi \mu \nu$ decays is culled from six minimum bias tapes with a set of cuts designed to eliminate the other major decay modes. A detailed explanation of these cuts follows.

Due to the presence of unobserved decay products and the ambiguity of assigning various masses to the secondary particles, the reconstructed invariant mass will generally differ from that of the neutral kaon's rest mass. The reconstructed invariant mass distributions with the pion mass assigned to both tracks, as generated with the E791 offline Monte Carlo, of $K_L \rightarrow \pi^+ \pi^-$, $K_L \rightarrow \pi^+ \pi^- \pi^0$, $K_L \rightarrow \pi \mu \nu$, $K_L \rightarrow \pi e \nu$ decays are shown in Figures 55, 56, 57, and 58. Assigning the pion rest mass to both charged tracks, the invariant kaon mass is required to be between 0.410 GeV/c and 0.460 GeV/c.

By restricting the invariant mass to the previously mentioned range, the $K_L \rightarrow \pi^+\pi^-$ and $K_L \rightarrow \pi^+\pi^-\pi^0$ events are effectively eliminated.

The decay $K_L \rightarrow \pi\mu\nu$ only populates a certain area of the mass-collinearity phase space. The mass-collinearity distributions for $K_{\mu 3}$ decays were studied for both data and Monte Carlo. The data sample of $K_{\mu 3}$ events is found to have an excess of high collinearity events relative to the Monte Carlo sample. A cut is therefore made at 16 milliradians to remove these high collinearity events.

The next step is to suppress the $K_L \rightarrow \pi e \nu$ decays. To accomplish this, one track is designated as the "pion track" and the other as the "muon track". If either track has a momentum of less than 6.0 GeV/c and there is a hit in one of the Cerenkov tubes associated with that track, the event is rejected. The Cerenkov thresholds for muons and pions are 6.3 GeV/c and 8.3 GeV/c, respectively. Distributions of the energy observed in the lead glass divided by the track momentum are shown in Fig. 59 for muons and electrons. To reject electrons, both tracks in an event are required to have the ratio of energy to momentum be less than 0.30. To establish that the "pion track" is not actually a muon, the track's momentum is required to be greater than 2.5 GeV/c and the muon hodoscope on the "pion track's" side had to be free of hits.

Since the probability of accidental background events depends on the beam intensity, the data set used for muon studies is selected so as to have the same average beam intensity as the dilepton data set. The average beam intensity is 3.1×10^{12} protons per AGS pulse.

The sample described above is used to study the muon hodoscope. Two parameters of a muon hodoscope hit are used for

particle identification: the phototube times and the separation between the hit scintillator's center position and the drift-chamber track projection. Raw times are adjusted for the propagation time of light along the scintillator to the phototube. An event-time zero, determined from the trigger scintillator counters and the drift chambers, is subtracted from the adjusted time. A time offset for each phototube is determined by fitting a distribution of corrected hit times with a Gaussian and a flat background. The centroid of the Gaussian is used as the time offset for each channel. Taking the propagation delay, event-time zero, and channel offset into account yields the corrected hit time.

All hits in the muon hodoscope have their positions compared with the intersection of the trigger tracks with the muon hodoscope. The two most downstream drift chambers are used to project the tracks back to the muon hodoscope. Residuals are calculated for both horizontal and vertical counters by taking the absolute value of the difference between a hit's position and the track's projection.

Distributions are made for both the space residuals and times of hits for muon tracks in the muon sample. Confidence level arrays are calculated from these distributions by integrating the fraction of hits which have a time or space residual greater than a particular set of values. These sets of values define the limits of the bins which correspond to the array entries. The space residuals are primarily due to multiple Coulomb scattering in the leadglass and iron hadron filter and are therefore momentum dependent. To take this into account, the space-match confidence levels are divided into five sets, where each set contains information for a distinct momentum range.

Associated with each track are confidence levels for: x-position, y-position, two x-phototube times, and a single y-phototube time. These individual confidence levels are then converted into a χ^2 value. It is assumed for this conversion that the confidence level distributions are Gaussian and independent of each other. The five χ^2 's are then summed to form a single overall χ^2 . This overall χ^2 is then converted back to an integrated confidence level for the track.

For the dimuon analysis a track is required to have a muon hodoscope integrated confidence level of greater than 0.01. Since the individual confidence levels are not independent and their distributions are not exactly Gaussian, the efficiency of the integrated confidence level cut has to be measured. Using muons from the $K_{\mu 3}$ sample, the efficiency of the muon hodoscope cut is determined to be 0.974 ± 0.003 . Since this efficiency is momentum dependent, the efficiency must be integrated over the momentum distribution of muons from $K_L \rightarrow \mu^+ \mu^-$. The muon hodoscope efficiency is shown in Table XII.

Table XII

Muon efficiency versus track momentum

Track Momentum	μ -Rangefinder eff.	μ -Hodoscope eff.
1.5 - 10 GeV/c	0.9936 \pm 0.0013	0.973 \pm 0.003
1.5 - 2.0 GeV/c	1.0000 \pm 0.0001	0.86 \pm 0.02
2.0 - 3.0 GeV/c	0.9963 \pm 0.0015	0.977 \pm 0.003
3.0 - 4.0 GeV/c	0.9928 \pm 0.0023	0.977 \pm 0.003
4.0 - 5.0 GeV/c	0.9917 \pm 0.0042	0.977 \pm 0.003
5.0 - 6.0 GeV/c	0.966 \pm 0.032	0.977 \pm 0.003
6.0 - 10 GeV/c	0.977 \pm 0.013	0.977 \pm 0.003

The inefficiency has three causes: cracks between the scintillators, out-of-time hits, and large multiple scattering. Since a one percent confidence level cut is made, the tails of the time and space residual distributions are lost. This loss represents about a 1.2% inefficiency. There are more early than late time hits, indicating accidentals occasionally fire a phototube before the trigger particle does. Early accidentals contribute an inefficiency of about 0.5%. The remaining 0.6% inefficiency is assumed to be due to cracks between the scintillator paddles. This corresponds to inactive gaps of approximately 0.05 cm between detectors, assuming the particles are normally incident.

A given muon, depending on its momentum, will have a certain probability of passing completely through the iron filter. In order to correct for the loss of low-momentum muons in the iron, one of these probability functions has to be integrated over the muon momentum spectrum for $K_L \rightarrow \mu^+ \mu^-$ decays. This method involves uncertainties associated with the momentum spectrum generated by the offline Monte Carlo and the muon loss probability function from GEANT or data. Another method employed is to make a low-momentum cut on each track. The momentum cut also involves uncertainties in the muon momentum spectrum. Since the muon loss probability function is not used, a source of uncertainty is eliminated. To minimize the uncertainty, the momentum of a track is required to be greater than 1.5 GeV/c. This also reduces the number of low-energy electrons, from K_{e3} decays.

Additional muon identification is provided by the muon rangefinder. Muons of a given momentum will on average penetrate

a certain distance into the rangefinder. By comparing the observed penetration in the rangefinder with the penetration expected from the momentum measured with the drift-chamber spectrometer, it is possible to reject events involving the leakage of pion interaction products through the iron filter and accidentals in the muon identification detectors.

A pattern recognition algorithm is used to find the terminal gap of a track in the rangefinder. The first step of the algorithm is to project the charged particle track from the downstream drift chambers to the first gap of proportional tube planes in the rangefinder. The extrusion intersected by the track projection is used as the initial guess as to the starting position of the track in the rangefinder. Due to multiple Coulomb scattering, some of the actual trajectories do not intersect the projected extrusion.

Taking this scattering into account, the single extrusions to either side of the projected one, as well as the central extrusion, are checked for hits. If one of these three extrusions in the current gap is found to have fired, the corresponding extrusion and the single extrusions to either side of it in the following downstream plane are examined for hits. Furthermore, if none of the three extrusions in the current gap are hit, the three corresponding extrusions in the following downstream plane are examined for hits. This procedure is repeated until two consecutive planes are found with no hits in the extrusions associated with the track or until the most downstream gap is reached.

The above procedure is carried out independently for the x- and y views. The observed terminal gap for a track is taken to be the

maximum of the x- and y-terminal gaps. Tracks which exit from a side of the rangefinder are treated as if the track had stopped at the point of exit. If a track penetrates to within at least three gaps upstream of the gap expected from the momentum measured in the spectrometer, it is considered a muon.

The rangefinder response is simulated by generating kaon decays with the E791 offline code and then passing the kinematics of the event to the GEANT code. There are no accidentals present in these simulated events. Using this software, it is found that multiple Coulomb scattering causes 3.3% of the muons to exit the side of the rangefinder before stopping. However, only 0.8% of the muons exit more than 3 gaps upstream of the expected gap and would thus fail the muon identification cut.⁶⁶ Again these numbers do not take accidentals into account. The stopping distribution of muons from $K_L \rightarrow \mu^+ \mu^-$, as calculated with GEANT, is shown in Fig. 60. The stopping distribution for the $K_{\mu 3}$ muon data sample is shown in Fig. 61. The distribution in Fig. 61 shows that a cut at -4 gaps yields an efficiency of 0.9944 ± 0.0014 for muons from $K_{\mu 3}$ decay.

The attenuation of pions passing through the lead glass array and the iron hadron filter is studied with the GEANT Monte Carlo. Simulations show that 0.7% of the pions from $K_{\pi\pi}$ decays hadronically interact in the iron or glass and generate secondary charged particles which then fire the muon hodoscope and satisfy the rangefinder requirement. Table XIII gives the probability of pion interaction products leaking through the iron and the rejection factor resulting from our muon selection criteria. About one tenth of the

Table XIII

Leakage of pions through the iron

π Momentum	Leakage Probability	Rejection Factor	Fake μ
1.5 - 15 GeV/c	0.117	0.942	0.007
1.5 - 2.0 GeV/c	0.005	0.023	0.000
2.0 - 3.0 GeV/c	0.024	0.023	0.023
3.0 - 4.0 GeV/c	0.048	0.973	0.001
4.0 - 5.0 GeV/c	0.097	1.000	0.000
5.0 - 6.0 GeV/c	0.142	1.000	0.000
6.0 - 15 GeV/c	0.224	1.000	0.000

pions generate photons which reach the muon hodoscope. The typical energy of these photons is less than 10 MeV/c². Two-thirds of the charged secondaries exiting the downstream face of the iron are pions which have an average energy of 0.53 GeV/c². Electrons and positrons make up most of the remaining charged tracks. The pions are the only one of these which can possibly fire more than a single proportional tube module in the rangefinder.

Pions which decay in flight between the last drift chamber and the lead glass array produce muons which pass through the iron and fire the muon hodoscope. About 3.2% of the pions from $K_L \rightarrow \pi\mu\nu$ decay in this region. The pion-decay muons possess less momentum than the parent pion and are emitted at a slight angle to the pion's original trajectory. However, studies indicate that our muon identification cuts reject less than one quarter of these muons. The differential gap distribution for pions is given in Fig. 62. Notice the peak centered about zero from pion decays in flight.

In order to properly incorporate the momentum dependence of the muon-selection cuts, $K_{\mu\mu}$ decays are simulated with the Monte

Carlo and events are weighted by their chance of satisfying the muon cuts. This probability is determined using a lookup table similar to Table XII. The fraction of $K_{\mu\mu}$ events passing the muon hodoscope and rangefinder requirements is 0.922 ± 0.005 .

V.11 Number of $K_L \rightarrow \mu^+ \mu^-$ Candidates

The last number required to calculate the branching fraction of $K_L \rightarrow \mu^+ \mu^-$ is the number of $K_L \rightarrow \mu^+ \mu^-$ events observed. Obtaining this entails estimating the number of background events within the acceptable mass and collinearity region. Since $K_L \rightarrow \mu^+ \mu^-$ is kinematically similar to $K_L \rightarrow \pi^+ \pi^-$, candidate events are accepted within the same mass and collinearity region. A scatter plot of the dimuon data sample, after application of all the cuts in Table IX, is shown in Fig. 63. Figures 64 and 65 show the mass and collinearity projections of this scatter plot. The mass histogram contains a distinct peak centered at $498.0 \text{ MeV}/c^2$ with a standard deviation of $1.6 \text{ MeV}/c^2$. There is little background immediately outside of the fiducial area. There are 87 events with collinearity less than 0.001 radians and an invariant mass between 0.4927 and 0.5027 GeV/c^2 .

Two possible major sources of background exist: 1) $K_L \rightarrow \pi \mu \nu$ where the pion decays as $\pi \rightarrow \mu \nu$, 2) $K_L \rightarrow \pi e \nu$ where the pion decays and the electron is misidentified as a muon. Most of the events with invariant mass below $0.489 \text{ GeV}/c^2$ are probably due to $K_L \rightarrow \pi \mu \nu$. The invariant mass spectrum for this reaction, assuming the pion is misidentified as a muon, has an endpoint of $0.489.3 \text{ GeV}/c^2$. Errors in the measurement of the tracks' momenta can result in invariant masses higher than the Dalitz endpoint. If the pion decays in flight, there will be two muons downstream of the iron. It is difficult to distinguish this pair of muons from a genuine $K_{\mu\mu}$ decay with only the muon hodoscope and rangefinder. Pions which decay upstream of the first

drift chamber are rejected by the collinearity and vertex χ^2 cuts. The track χ^2 s reject the majority of pion decays occurring between the first and fifth drift chambers.

K_{e3} decays can mimic $K_{\mu\mu}$ decays, if the pion decays into a muon and neutrino and the electron is misidentified as a muon. The muon's mass is used to calculate the invariant mass of the two tracks and shows that the mass and collinearity fall evenly about the region occupied by $K_{\mu\mu}$ decays. Collinearity and χ^2 cuts help to eliminate this source of background. However, the muon hodoscope and rangefinder requirements are crucial in rejecting K_{e3} decays. From energy measurements in the leadglass (see Fig. 66 showing the dimuon sample without muon identification), it is clear that K_{e3} events are a serious background. Since these events are expected to be evenly distributed in mass and collinearity, as opposed to $K_{\mu3}$ decays which should be predominantly at low mass, it is possible to distinguish them from $K_{\mu3}$ events.

Two methods are used to determine the background in the fiducial region. The collinearity projection for events with invariant masses between 0.4927 and 0.5027 GeV/c^2 is the distribution used to estimate the number of background events from K_{e3} decays. For small angles the solid angle is proportional to the square of the collinearity. So the number of events per unit of collinearity should be constant away from the $K_{\mu\mu}$ peak. Using the average number of events per 0.000001 (radians)² for events with masses within the accepted range and collinearities above 0.001 radians, leads to an estimate of 0.7 background events. There is a single track in the final

$K_{\mu\mu}$ sample with a leadglass energy indicative of an electron. This source of background is probably associated with K_{e3} decays.

The second way to estimate the background is to project a fit, to the low-mass events, under the peak. This is difficult to do since the form of the distribution is not known and there are a limited number of events to fit. This calculation involves events from $K_{\mu 3}$ decays. A logarithmic function seems to work the best. Use of this method yields 86.5 $K_L \rightarrow \mu^+ \mu^-$ events. Given the uncertainties associated with the second method, I chose to use the first method and thus find the number of $K_L \rightarrow \mu^+ \mu^-$ events to be 86.3.

Many of the distributions of the kinematic and particle identification of the 87 $K_L \rightarrow \mu^+ \mu^-$ candidates are compared with Monte Carlo simulations of the same quantities in Figures 67 through 77. The Monte Carlo predicts that 70% of the events should have tracks which bend inward in the upstream magnet. this compares well with the 68% found in the data. Given the low statistics the data agrees quite well with the Monte Carlo simulation.

As a check on the muon identification requirements, the number of $K_L \rightarrow \mu^+ \mu^-$ events is estimated without using any particle type determination. The invariant mass and collinearity squared for these events are displayed in Figures 78 and 79. Use of the form $N_{\text{events}} = 118.629 * (\text{mass} - 480 \text{ MeV}/c^2)^{-0.6763}$, leads to 173.9 background events and 83.1 good events. The collinearity method gives the number of background events with collinearity less than 0.001 radians, as 173.3 +/- 8. This leaves 83.7 $K_{\mu\mu}$ events. Many of these background events are clearly from K_{e3} as shown by the peak at 1.0 in the energy measured in the leadglass divided by the momentum

determined by the drift chamber (see Fig. 66). This peak at 1.0 indicates that one of the tracks is an electron.

In addition to all the correction factors previously discussed, the number of events where one of the muons decays in flight must be considered. Any decays within the decay volume, the drift-chamber system, or the rangefinder should be rejected by the selection cuts. This effect is accounted for by the Monte Carlo calculation of the geometric acceptances or by the efficiency for the rangefinder cut. However, if a muon decays after the fifth drift chamber and before the muon hodoscope it will not satisfy the muon identification requirements and possibly not cause a Level 1 trigger. The loss of these events must be taken into account. Averaging of the momentum spectrum for $K_{\mu\mu}$ decays yields a correction factor of 1.0007. In Figures 80 through 83 event displays for two of the final 87 $K_{\mu\mu}$ events are shown.

V.12 Measurement of the Ratio $\Gamma(K_L \rightarrow \pi^+\pi^-)/\Gamma(K_L \rightarrow \pi\mu\nu_\mu)$

Most of the methods used to measure the decay rate for $K_L \rightarrow \mu^+\mu^-$ can be verified by measuring the branching fraction of $K_L \rightarrow \pi^+\pi^-$. This calculation involves: kinematic cuts, muon selection, background subtraction, and the geometric acceptance, and so is sensitive to systematic errors in these quantities. Determining the branching fraction of $K_L \rightarrow \pi\mu\nu_\mu$ serves as an additional test of the data analysis. This second check provides a test of the Monte Carlo acceptance simulation for all the major decay modes of the K_L . Also, background from a source other K_L decays should result in a discrepancy in the branching fraction of $K_L \rightarrow \pi\mu\nu_\mu$. These studies do not test the Level 1 or the Level 3, since uncut minimum bias events are used in this study.

In general all the cuts placed on the dimuon sample and $\pi\pi$ normalization sample are to select events for this study. However, some of the specific cut values are different. All three data samples (i.e. $K_L \rightarrow \pi\mu\nu_\mu$, $K_L \rightarrow \pi^+\pi^-$, and $K_L \rightarrow$ all) are chosen using the following restrictions: track x $\chi^2 < 20.0$, track y $\chi^2 < 20.0$, vertex $\chi^2 < 10.0$, $|x/z| < 0.0027$, $|y/z| < 0.010$, $|(P_L - P_R)/(P_L + P_R)| < 0.62$, and $P_{\text{Track}} < 10.0$ GeV/c, where P_L and P_R refer to the left and right side track momenta, and x, y, and z are the coordinates of the vertex. All the above quantities are the result of the iterative event fitting. Only events with invariant mass between 0.493 and 0.503 GeV/c² and collinearity less than 1 mR are counted as $K_{\pi\pi}$ decays. The Monte Carlo is used to estimate the background in the $K_{\pi\pi}$ sample. The

standard muon selection criteria are employed to identify $K_{\mu 3}$ events. That is at least one of the tracks in an event had to possess a muon hodoscope confidence level greater than 0.01 and penetrate into the rangefinder to within three gaps or less of the gap expected based on the momentum measured by the spectrometer.

After the application of the above selection criteria, there remain 126 $K_{\pi\pi}$ events, 9,132 $K_{\mu 3}$ events, and 23,918 total kaon decay events. The relative decay rates are given by the following two formulae:

$$\frac{\Gamma_{K\pi 2}}{\Gamma_{K\mu 3}} = \frac{A_{K\mu 3} \epsilon_{\mu} N_{K\pi 2}}{N_{K\mu 3} A_{K\pi 2} - \alpha A_{K\pi 3} N_{K\pi 2} \left(\frac{\Gamma_{K\pi 3}}{\Gamma_{K\pi 2}} \right) - 2\alpha A_{K\pi 3} N_{K\pi 2} \left(\frac{\Gamma_{K\pi 3}}{\Gamma_{K\pi 2}} \right)} \quad (5.5)$$

$$\frac{\Gamma_{K\mu 3}}{\Gamma_{\text{all}}} = \frac{A_{\text{all}} N_{K\mu 3} - \alpha A_{K\pi 3} N_{\text{all}} \left(\frac{\Gamma_{K\pi 3}}{\Gamma_{\text{all}}} \right) - 2\alpha A_{K\pi 3} N_{\text{all}} \left(\frac{\Gamma_{K\pi 3}}{\Gamma_{\text{all}}} \right)}{N_{\text{all}} A_{K\mu 3} \epsilon_{\mu}} \quad (5.6)$$

where $A_{K\mu 3}$, $A_{K\pi 3}$, $A_{K\pi\pi}$, $A_{K\pi 2}$, and A_{all} are the geometric acceptances; $\Gamma_{K\mu 3}$, $\Gamma_{K\pi 3}$, $\Gamma_{K\pi\pi}$, $\Gamma_{K\pi 2}$, and Γ_{all} are the decay rates; ϵ_{μ} is the single muon efficiency; ϵ_{π} is a correction for a single pion loss due to nuclear interactions; $N_{K\mu 3}$, $N_{K\pi\pi}$, and N_{all} are the number of observed events; and α is the fraction of pions decaying after the last drift-chamber. The geometric acceptances are determined with the iterative fitting method employed in Pass2. The efficiency, 97.4%, for a single muon is the same as that derived in section V.7 except that the $K_{\mu 3}$ momentum spectrum is used. Values for the ratios $(\Gamma_{K\pi 3}/\Gamma_{K\pi\pi})$ and $(\Gamma_{K\pi 3}/\Gamma_{K\pi 2})$ are taken from the Particle Data Booklet. I am not including a correction for $K_S \rightarrow \pi^+\pi^-$, since the cut at 10.0 meters on the z-position of the vertex removes most of these decays.

Using the E791 offline Monte Carlo, I find the following geometric acceptances: $A_{\text{all}}=0.0144$, $A_{K\pi\pi}=0.0422$, $A_{K\mu 3}=0.0203$, $A_{Ke3}=0.0169$, $A_{K\pi 3}=0.0290$. A correction factor of 1.008 for the loss of $K_{\pi\pi}$ events from nuclear interactions is used. For Eq.(5.6) I find $\Gamma(K_L \rightarrow \pi^+\pi^-)/\Gamma(K_L \rightarrow \pi\mu\nu_\mu)=0.00690$, which, using 0.271 for the branching fraction of $K_{\mu 3}$, yields a branching fraction of $1.87 \pm 0.25 \times 10^{-3}$ for $K_{\pi\pi}$. This differs with the Particle Data Booklet value of 2.03×10^{-3} by 0.64 standard deviations. My value for the branching fraction of is somewhat low. However, this is not statistically significant. For the branching fraction of $K_L \rightarrow \pi\mu\nu_\mu$ I find $26.0 \pm 2.1\%$. The accepted number is $27.1 \pm 0.4\%$. My result is only off by half a standard deviation. This result, although not statistically significant, suggests I may be under-counting dimuon events by as much as 8% or that the minimum bias sample is contaminated at the 4% level. Again my results are in good agreement with accepted values.

CHAPTER VI
CONCLUSIONS

We now possess all the information necessary to compute the branching fraction of $K_L \rightarrow \mu^+ \mu^-$. Equation 6.1 gives the branching fraction.

$$B(K_L \rightarrow \mu^+ \mu^-) = \frac{N_{\mu\mu} * A_{\pi\pi} * B_{\pi\pi} * \epsilon_{K_s} * \epsilon_{Int.}}{N_{\pi\pi} * PS_{MB} * A_{\mu\mu} * \epsilon_{\mu\mu} * \epsilon_{\mu \rightarrow e\nu\nu} * \epsilon_{L3} * \epsilon_{L1}} \quad (6.1)$$

The factors in Eq.(6.1) are explained in Table XIV and their values given, assuming the standard set of cuts detailed in Table IX. Using the values in Table XIV, the final result is found to be:

$$B(K_L \rightarrow \mu^+ \mu^-) = (5.7 \pm 0.6 \pm 0.3) \times 10^{-9} \quad (6.2)$$

Where the first error is statistical only and the second error is the uncertainty due to systematic effects.

My result is 15% lower than the unitarity limit derived in Chapter II. It is also 39% lower than the current world average as listed in the 1988 Particle Properties Data Booklet. In addition to these numbers, experiment 137 at KEK has released a preliminary result⁶⁷ of 8.4×10^{-9} based on the observation of 54 events. These comparisons lead one to suspect my number of minimum bias $K_{\pi\pi}$ events and $K_{\mu\mu}$ candidates.

Table XIV

Values of factors used in the final branching fraction calculation

Factor	Description	Value
$N_{\mu\mu}$	Number of $K_{\mu\mu}$ candidates	86.3
$N_{\pi\pi}$	Number of $K_{\pi\pi}$ candidates	8887
$A_{\mu\mu}$	Geometric acceptance for $K_{\mu\mu}$	0.0224
$A_{\pi\pi}$	Geometric acceptance for $K_{\pi\pi}$	0.0272
$B_{\pi\pi}$	Established branching fraction of $K_{\pi\pi}$	0.00204
PS_{MB}	Prescale factor for minimum bias	6000
ϵ_{L1}	Correction for Level 1 trigger bit	0.981
ϵ_{L3}	Correction for Level 3 cuts	0.785
$\epsilon_{\mu\mu}$	Efficiency of $K_{\mu\mu}$ particle identification	0.922
$\epsilon_{\mu \rightarrow e\nu\nu}$	Lose due to $\mu \rightarrow e\nu\nu$ decays	0.999
ϵ_{Ks}	Correction for Ks contamination of $K_{\pi\pi}$	1.021
$\epsilon_{Int.}$	Correction for pion nuclear interactions	0.985

Several checks are performed to validate my result. Perhaps the best confirmation is the measurement of the branching ratios $B(K_L \rightarrow \pi^+\pi^-)/B(K_L \rightarrow \pi\mu\nu)$ and $B(K_L \rightarrow \pi\mu\nu)/B(K_L \rightarrow \text{all})$ explained in section V.12. Both of these results agree with the results of previous experiments within statistics. Regretfully, this does not check the Level 3 or Level 1. The second test of the consistency of my result involves calculating the branching fraction using a different set of cuts from the one listed in Table IX. To check the muon identification the analyzed is performed with no particle selection cuts. The level of background in the dimuon sample increases by two orders of magnitude, while the minimum bias $K_{\pi\pi}$ sample remains unchanged. Using the distribution of background as a function of collinearity squared to estimate the background under the $K_{\mu\mu}$ peak yields 83.7

$K_L \rightarrow \mu^+ \mu^-$ events with an additional uncertainty due to the more significant amount of background of ± 8 events. This lowers the branching fraction of $K_L \rightarrow \mu^+ \mu^-$ to $(5.1 \pm 0.8 \pm 0.2) \times 10^{-9}$.

VI.1 Prospects for Rare Kaon Experiments

AGS experiment 791 took data in the winter and spring of 1989. Improvements were made in the pattern recognition, Level 1, and Level 3 hardware and software for this run. It is hoped that the 1989 run has recorded 3 times as many $K_L \rightarrow \mu^+ \mu^-$ decays as reported in this thesis. A run in 1990 is also planned. Experiment 137 at KEK is also continuing to take data. The combination of these two experiments may observe up to a thousand $K_{\mu\mu}$ events.

Factors which limit the sensitivity of rare kaon decay searches are: beam intensity, triggering and data acquisition, and the ability of the detectors to resolve genuine events against backgrounds and to survive in a high flux environment. Advances in RISC computers and continuing improvements in electronics should enable physicists to implement acquisition and triggering systems capable of handling the necessary amount of data. At Brookhaven the construction of the stretcher and booster systems will allow beam intensities perhaps an order of magnitude greater than those available today. TRIUMF II will provide the most intense source of kaons ever. New detector designs are required to take advantage of these high flux neutral beams. One concept is the use of a solenoidal spectrometer, which would have a geometric acceptance perhaps ten times greater than present day designs. Use of scintillating fibers or other systems with spatial and time resolutions of about 10 microns and 1 ns, respectively, is also necessary. Hopefully, sufficient $K_L \rightarrow \mu^+ \mu^-$ events

will be seen by these future experiments to determine the longitudinal polarization of the muons to better than the 10% level.

Appendix A

Table XV

Branching fractions and upper limits of the various K_L decay modes

Decay Mode	Branching fraction
$\pi^0\pi^0\pi^0$	0.217 +/- 0.007
$\pi^+\pi^-\pi^0$	0.1237 +/- 0.0018
$\pi\mu\nu$	0.2701 +/- 0.0034
$\pi e\nu$	0.386 +/- 0.004
$\pi^+\pi^-$	(2.04 +/- 0.04) x 10 ⁻³
$\pi^0\pi^0$	(0.909 +/- 0.029) x 10 ⁻³
$\gamma\gamma$	(5.70 +/- 0.23) x 10 ⁻⁴
$\pi e\nu\gamma$	0.013 +/- 0.008
$\pi^0\pi e\nu$	(6.2 +/- 2.90) x 10 ⁻⁵
$\pi^+\pi^-\gamma$	(4.41 +/- 0.32) x 10 ⁻⁵
$e^+e^-\gamma$	(1.7 +/- 0.9) x 10 ⁻⁵
$\mu^+\mu^-\gamma$	(2.8 +/- 2.8) x 10 ⁻⁷
$(\pi\mu \text{ atom})\nu$	(1.05 +/- 0.11) x 10 ⁻⁷
$\mu^+\mu^-$	(9.5 +2.4 -1.5) x 10 ⁻⁹
$\pi^0\gamma\gamma$	<2.4 x 10 ⁻⁴
μe	<7 x 10 ⁻⁹
e^+e^-	<5 x 10 ⁻⁹
$\pi^0e^+e^-$	<2.3 x 10 ⁻⁶
$\pi^0\mu^+\mu^-$	<1.2 x 10 ⁻⁶

Bibliography

- 1) G. Danby et al., Phys. Rev. Lett. 9, 36 (1962).
- 2) J. Christenson, et al., Phys. Rev. Lett. 13, 138 (1964).
- 3) Aubert J., et al., Phys. Rev. Lett. 33, 1404 (1974). Augustin J., et al., Phys. Rev. Lett. 33, 1406 (1974).
- 4) S. L. Glashow, J. Iliopoulos, and L. Maiani, Phys. Rev. D2, 1 285(1970).
- 5) F. Halzen and A. Martin, Quarks and Leptons, (John Wiley and Sons, New York, N. Y.,1984).
- 6) S. Herb, et al., Phys. Rev. Lett. 39, 252 (1977). W. Innes, et al., Phys. Rev. Lett. 39,1240 (1977).
- 7) F. Abe et al., Phys. Rev. Lett. 63, 720 (1989), G. S. Abrams et al., Phys. Rev. Lett. 63, 724 (1989).
- 8) AGS Experiment 791 Proposal.
- 9) R. Cahn and H. Harari, Nucl. Phys. B299, 1 (1988).
- 10) F. Gilman and M. Wise, Phys. Rev. D21, 3150 (1980), J. Konigsberg, AGS E791 Memo-KL214.
- 11) W. Carithers et al., Phys. Rev. Lett. 30, 1336 (1973); W. Carithers et al., Phys. Rev. Lett. 31, 1025 (1973); Y. Fukushima et al., Phys. Rev. Lett. 36, 348 (1976); Shochet et al., Phys. Rev. D19, 1965 (1979); H. Greenlee et al., Phys. Rev. Lett. 60, 893 (1988); T. Inagaki et al., to be published (1988); R. Cousins et al. Phys. Rev. D38, 2914 (1988).
- 12) A. Clark et al., Phys. Rev. Lett. 26, 1667 (1971).
- 13) Review of Particle Properties, Phys, Lett. B204 (1988).

- 14) D. H. Perkins, Introduction to High Energy Physics, pp. 232-235 (Addison-Wesley, Reading, 1987).
- 15) M. K. Gaillard and B. W. Lee, Phys. Rev. D10, pp 897 (1974), F. J. Yndurain, Quantum Chromodynamics, 156-160 (1983).
- 16) H. Stern and M. K. Gaillard, Annals of Physics 76, pp. 580-606 (1973).
- 17) B. R. Martin, E. De Rafael, and J. Smith, Phys. Rev. D2, 179 (1970).
- 18) M. P. Gokhale and S. H. Patil, Phys. Rev. D10, 1619 (1974).
- 19) S. L. Adler, G. R. Farrar, and S. B. Treiman, Phys. Rev. D5, 770 (1972).
- 20) E. Ma and A. Pramudita, Phys. Rev. D24, 2476 (1981).
- 21) D. H. Perkins, op. cit., pp. 223-226.
- 22) V. A. Novikov, M. A. Shifman, A. I. Vainshtein, and V. I. Zakharov, Phys. Rev. D16, 223 (1977).
- 23) N. F. Nasrallah and K. Schilcher, Z. Phys. C - Particles and Fields 36, 467-471 (1987).
- 24) T. Inami and C. S. Lim, Prog. Theor. Phys. 65, 297 (1981).
- 25) R. E. Shrock and M. B. Voloshin, Phys. Lett. B87, 375 (1979).
- 26) A. J. Buras, Phys. Rev. Lett., Vol. 46, 1354 (1981).
- 27) Talk presented at Lawrence Berkeley Laboratory, June 22 (1989).
- 28) K. S. Babu, X-G. He, X-Q. Li, and S. Pakvasa, university of Rochester reprint, UR-1037.
- 29) O. Shanker, Nucl. Phys. B206, 253 (1982).
- 30) J. D. Bjorken and S. Weinberg, Phys. Rev. Lett. 38, 622 (1977).

- 31) J. Ellis et al., Nucl. Phys. B182, 529 (1981).
- 32) J. Pati and A. Salam, Phys. Rev. D10, 275 (1974).
- 33) R. Arnowitt and P. Nath, Phys. Rev. D36, 3423 (1987).
- 34) G. Sanders, AGS E791 Memo-KL211 (1989).
- 35) S. DeBenedetti, Nuclear Interactions, 573-579 (Robert E. Krieger, Huntington, N.Y.,1964).
- 36) P. Herczeg, Phys. Rev. D27, 1512 (1983).
- 37) F. J. Botella and C. S. Lim, Phys. Rev. Lett. 56, 1651 (1986).
- 38) D. Chang and R. N. Mohapatra, Phys. Rev. D30, 2005 (1984).
- 39) J. Liu, Phys. Rev. D36, 2178 (1987).
- 40) T. Kurimoto, Phys. Lett. B172, 357 (1986).
- 41) J. Liu, Z. Phys. C - Particles and Fields 37, 139-142 (1987).
- 42) P. Herczeg, op. cit..
- 43) R. Cousins et al., IEEE Trans. Nucl. Sci., 36, 646 (1989).
- 44) M. Sivertz, AGS E791 Memo-KL167.
- 45) K. Biery et al., IEEE Trans. Nucl. Sci., 36, 650 (1989).
- 46) J. Ritchie, AGS E791 Memo-KL151; J. Konisberg, AGS E791 Memo-KL147.
- 47) M. Sivertz, AGS E791 Memo-KL168 and Memo-KL171.
- 48) J. Frank et al., IEEE Trans. Nucl. Sci. 36, 79 (1989).
- 49) G. Sanders, AGS E791 Memo-KL071.
- 50) C. Kenney et al., IEEE Trans. Nucl. Sci. 36, 74 (1989).

- 51) W. Ford, The MAC Calorimeters and Applications, SLAC-PUB-2894, (1982).
- 52) M. Atac, Wire Chamber Aging, Proceedings of the Workshop on Radiation Damage to Wire Chambers, LBL-21170, 55 (1986).
- 53) Y. Hoshi et al., Nucl. Instr. Methods A236, 82 (1985).
- 54) G. Hart, AGS E791 Memo-KL141.
- 55) J. Ginkel, AGS E791 Memo-KL169.
- 56) P. Buchholz and K. McFarlane, AGS E791 Memo-KL135; P. Buchholz and K. McFarlane, AGS E791 Memo-KL140.
- 57) W. Slater, AGS E791 Memo-KL122; W. Slater, AGS E791 Memo-KL127; W. Slater, AGS E791 Memo-KL150.
- 58) P. Kunz, M. Gravina, G. Oxoby, and Q. Trang, CERN DD/83/3 SLAC-PUB-3069 (E/1) March, (1983).
- 59) W. Molzon, Private Communication (1989).
- 60) R. Cousins et al., Nucl. Instru. Meth. A277, 517 (1989).
- 61) W. Molzon and S. Imlay, AGS E791 Memo-KL237.
- 62) J. Ginkel, Private Communication (1989).
- 63) P. Skubic et al., Phys. Rev. D18, 3115 (1978).
- 64) M. Chapman, Private Communication (1989).
- 65) J. Urheim and R. Cousins, AGS E791 Memo-KL229.
- 66) M. Chapman, Private Communication (1989).
- 67) T. Inagaki et al., Phys. Rev. D40, 1712 (1989).

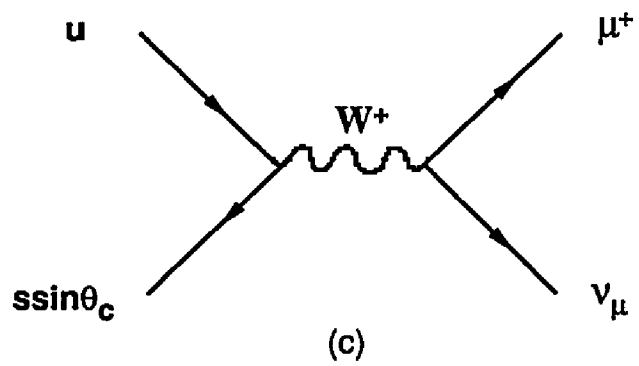
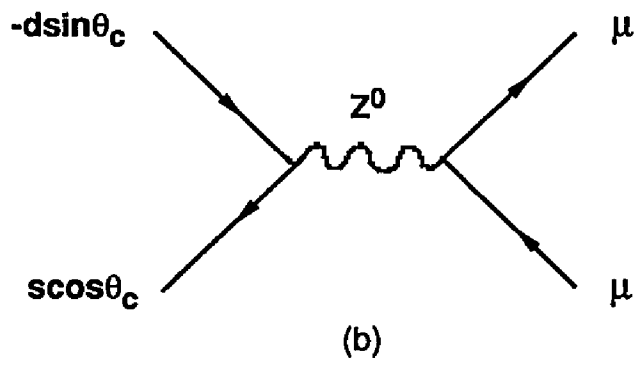
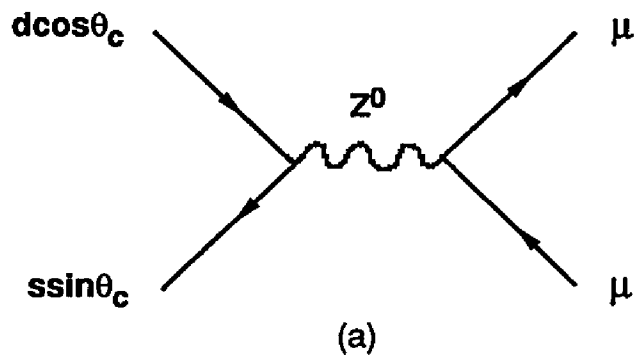


Figure 1

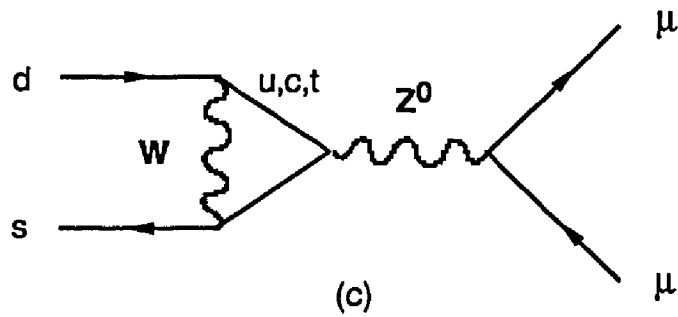
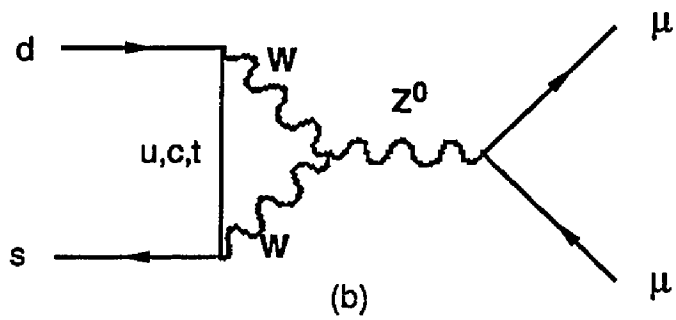
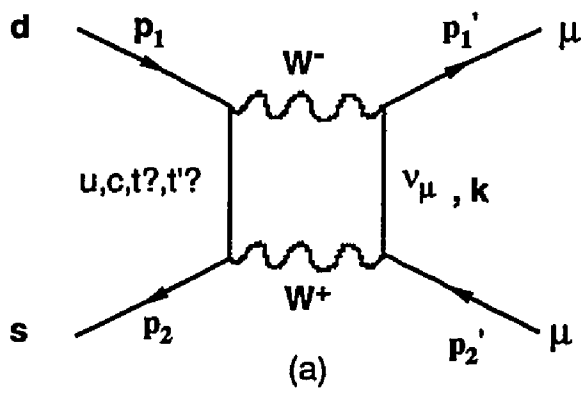


Figure 2

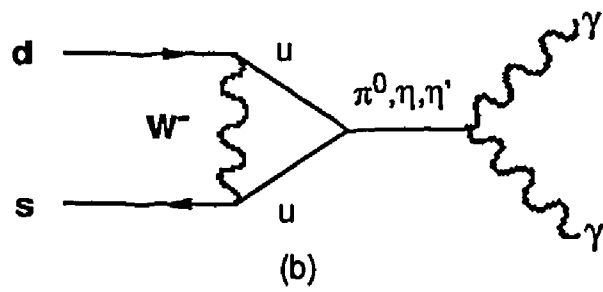
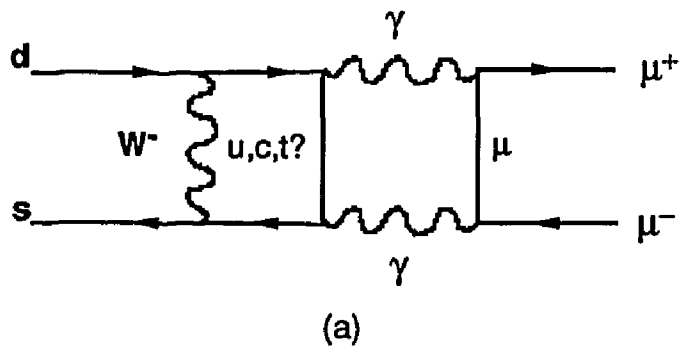


Figure 3

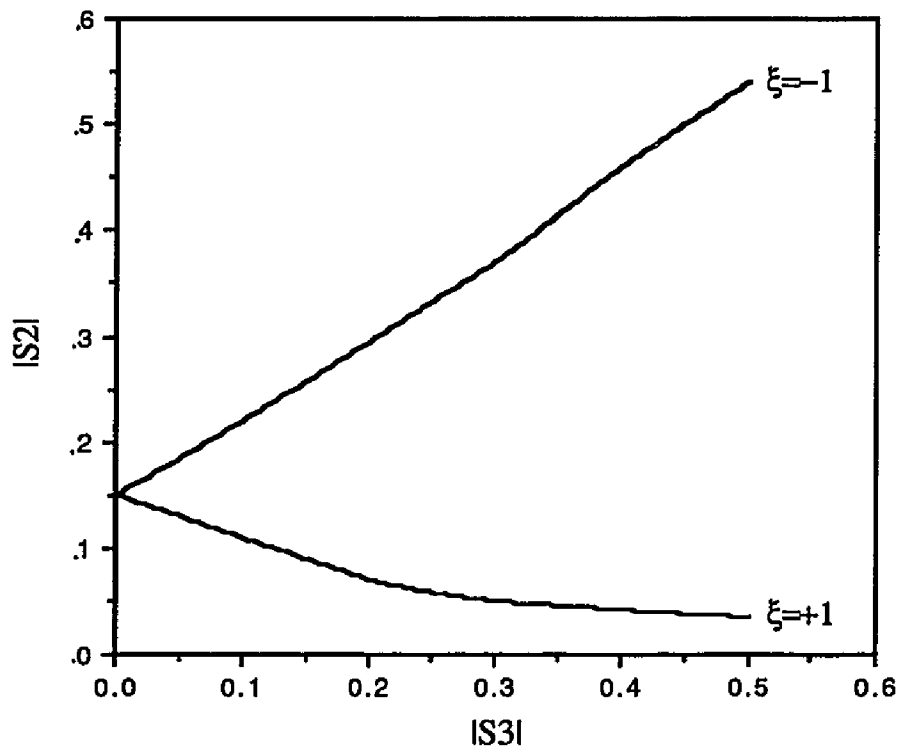


Figure 4

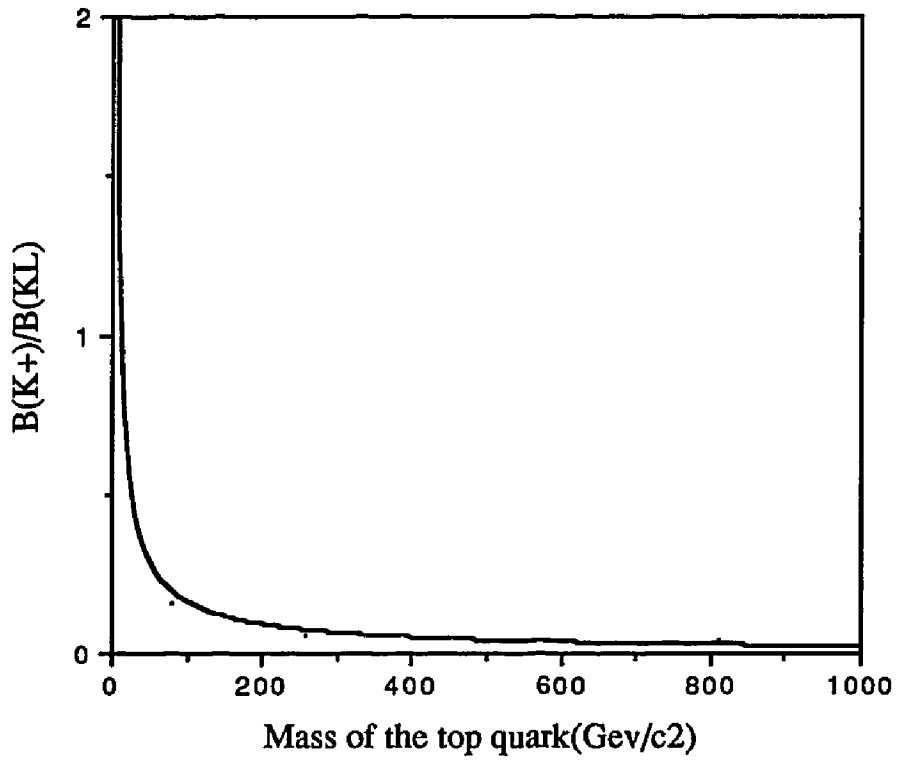


Figure 5

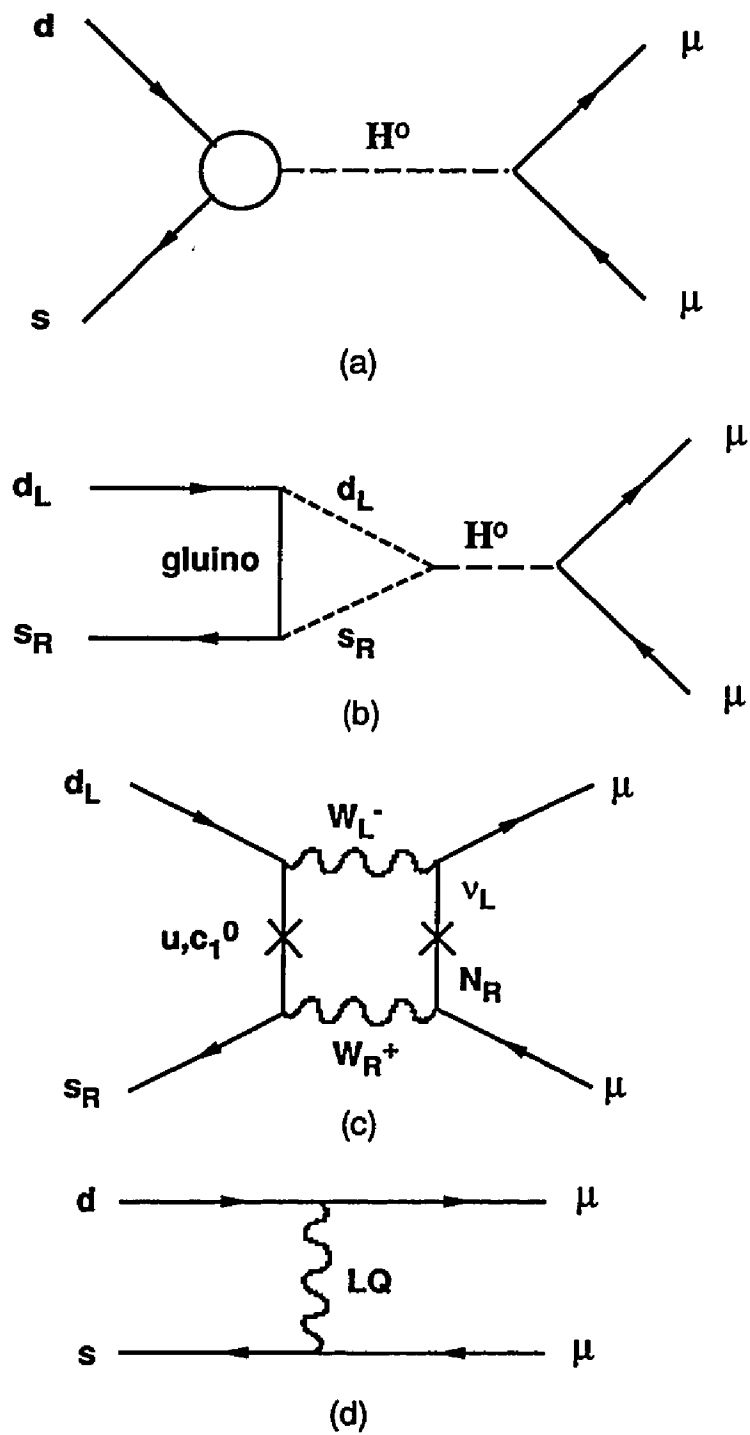
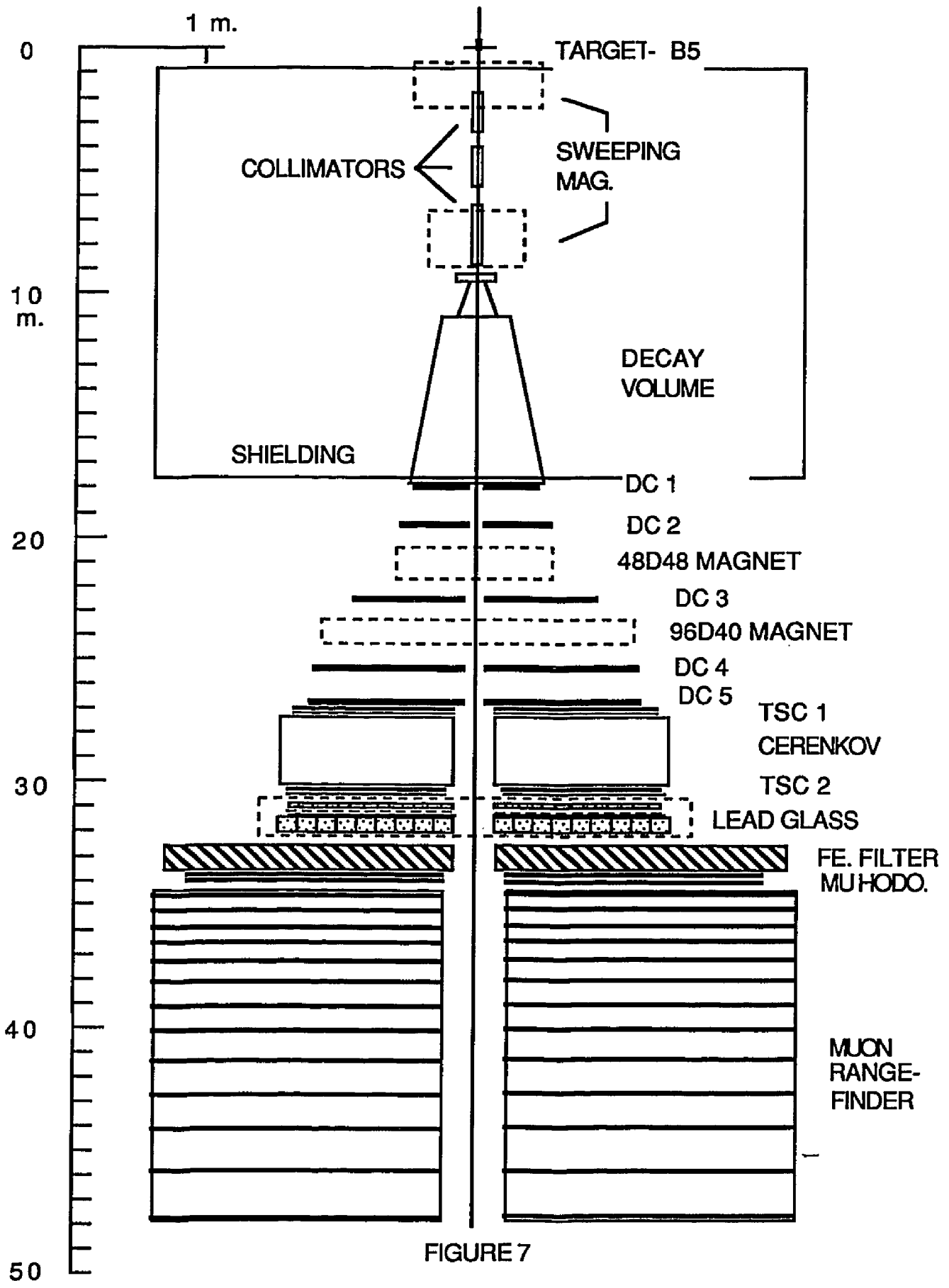
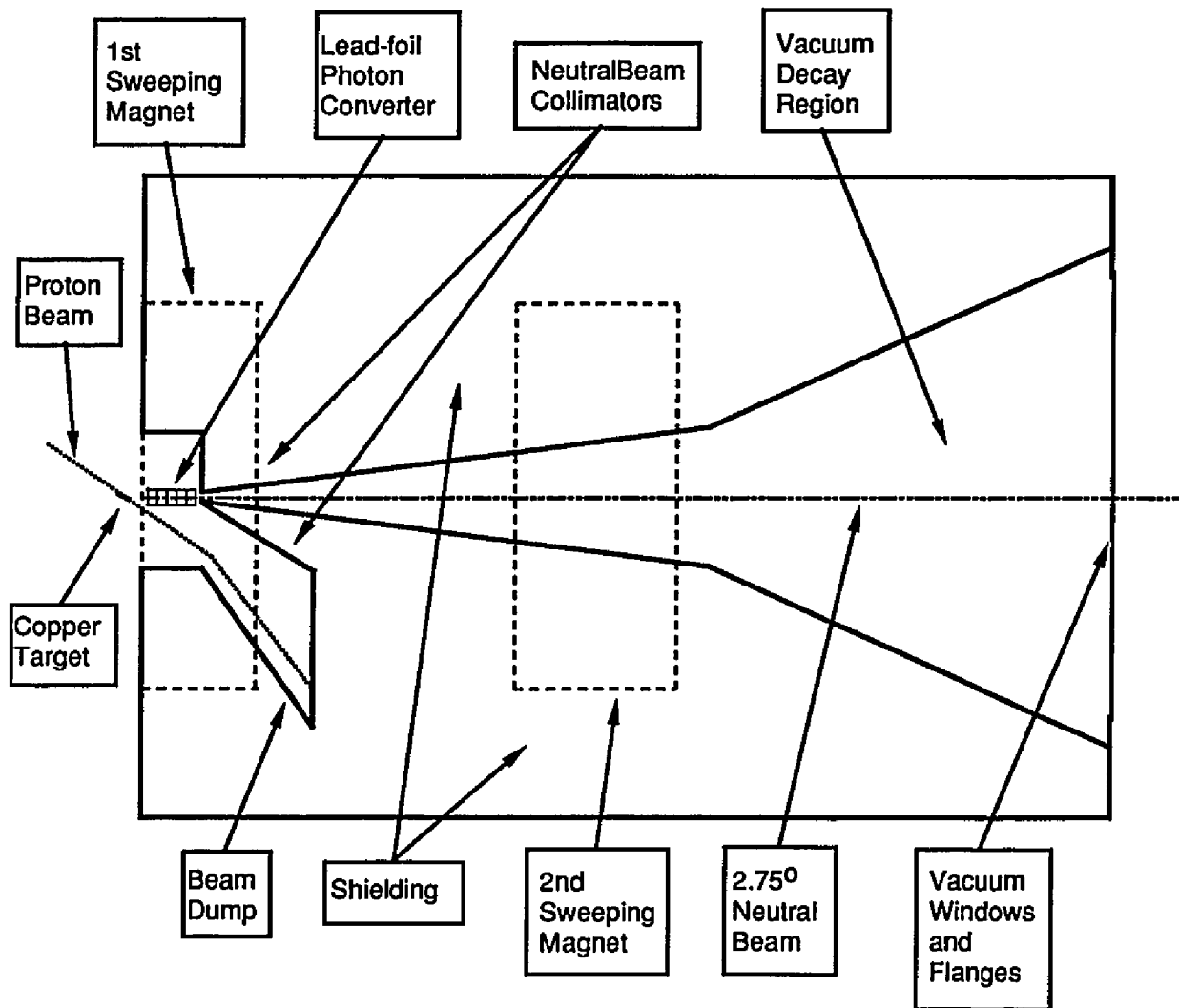


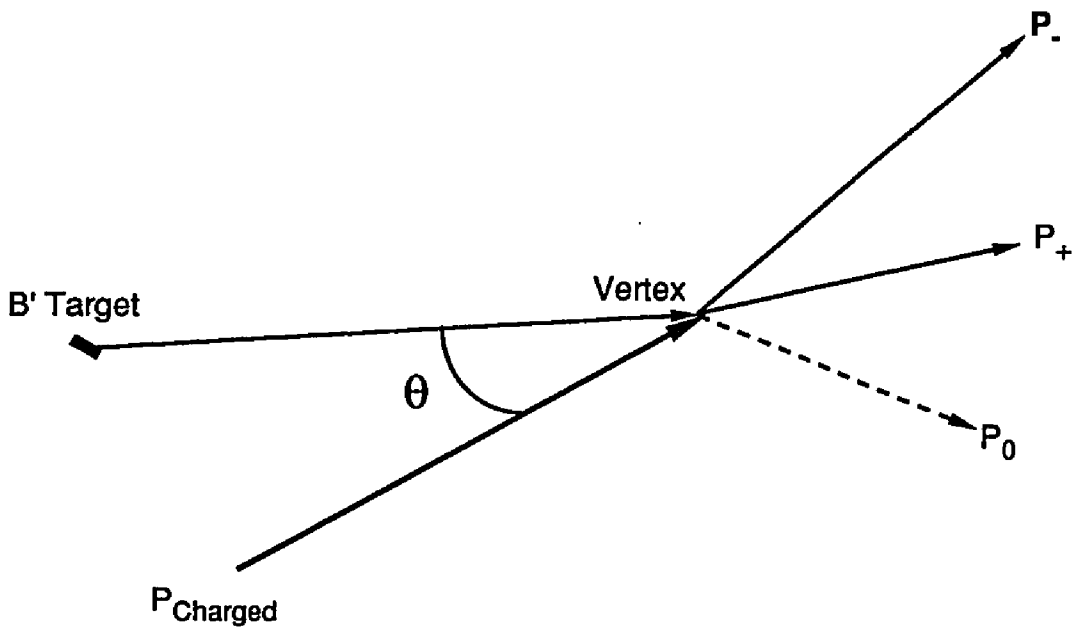
Figure 6





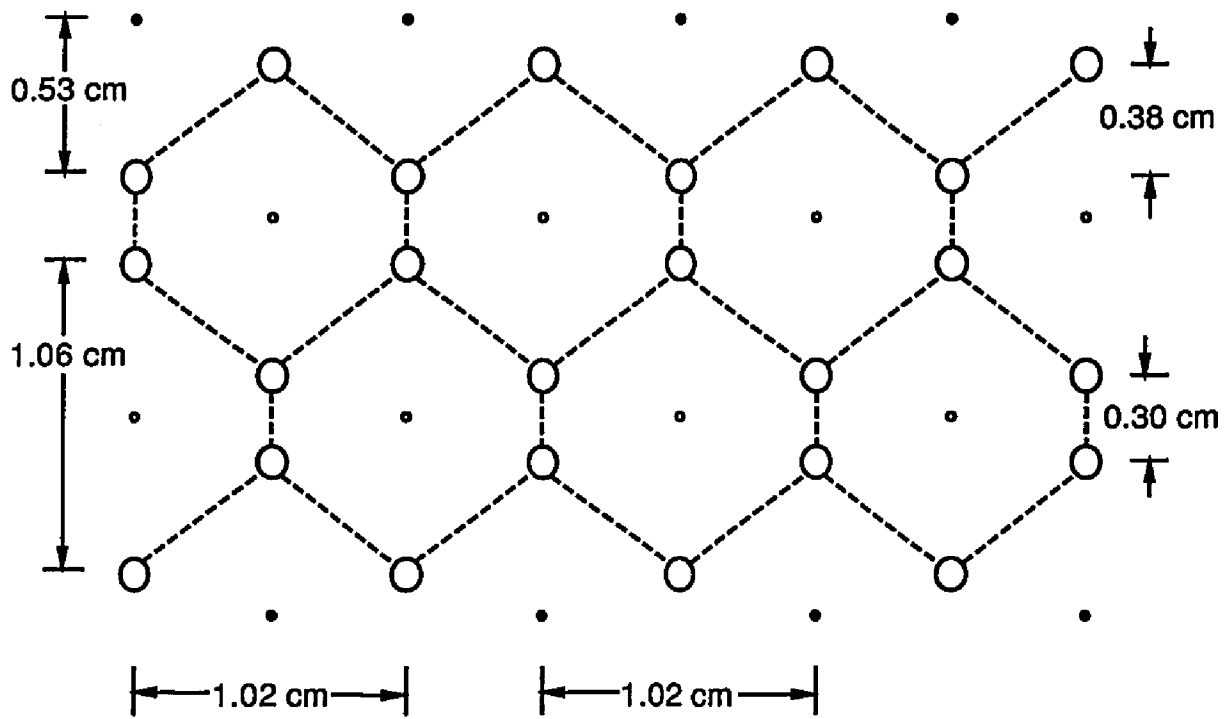
0.1 Meters
 1.0 Meters

Figure 8.



$$P_{\text{charged}} = P_+ + P_-$$

Figure 9.



- — Field Wire - diameter=109 μm , potential=-2.500 V
- — Guard Wire - diameter=25 μm , potential=ground
- — Sense Wire - diameter=25 μm , potential=ground

Figure 10.

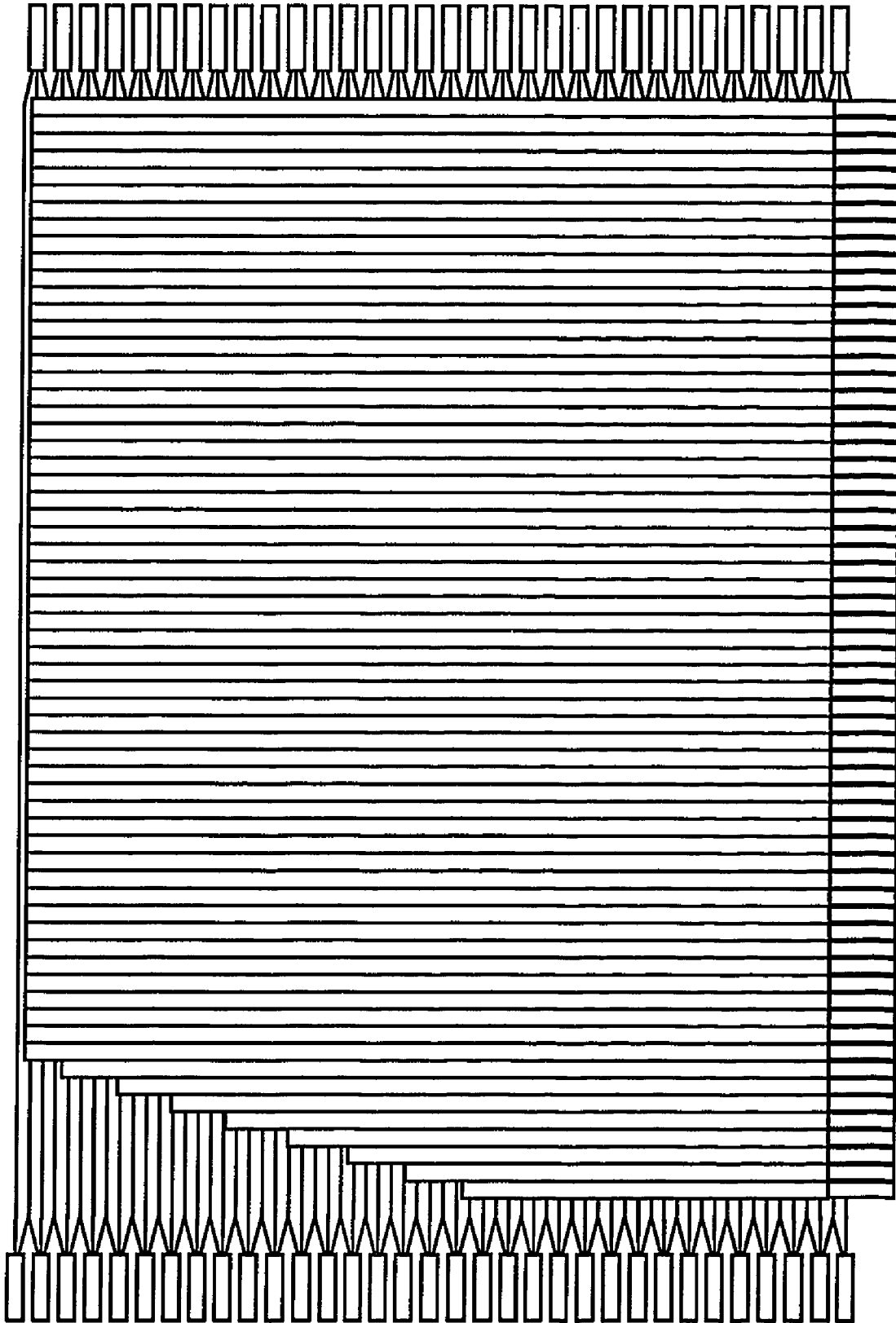


Figure 11.

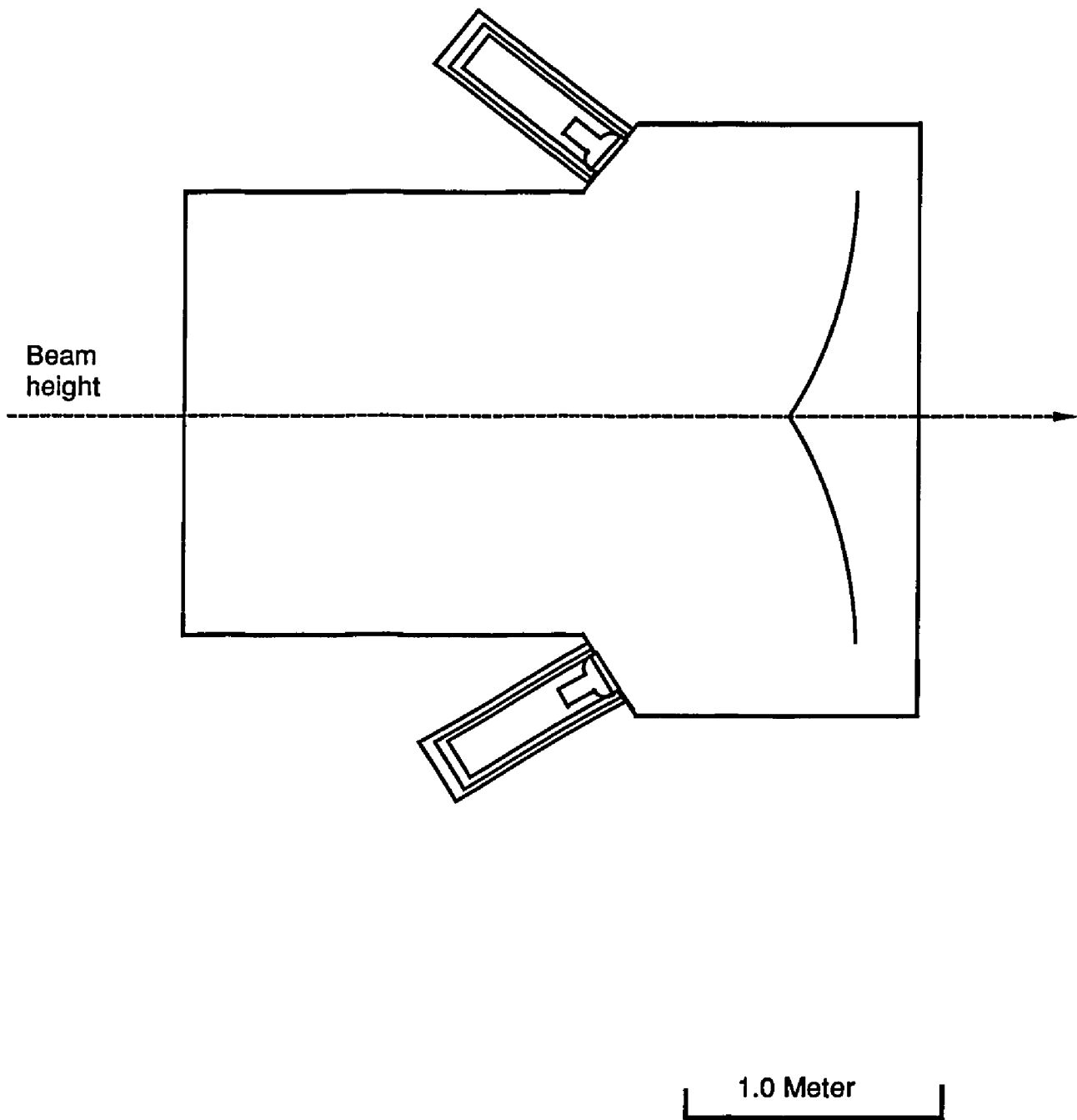


Figure 12.

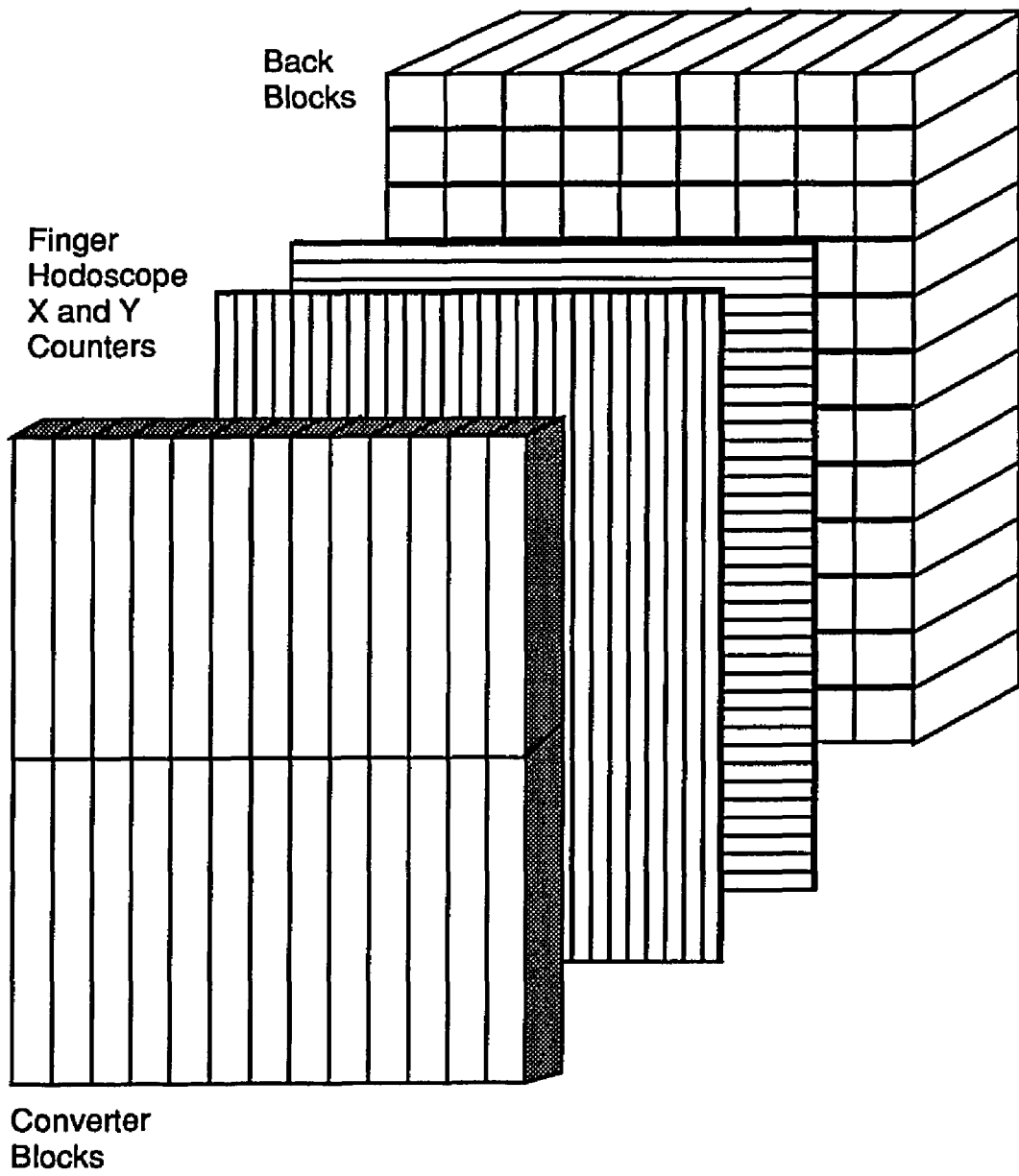


Figure 13.

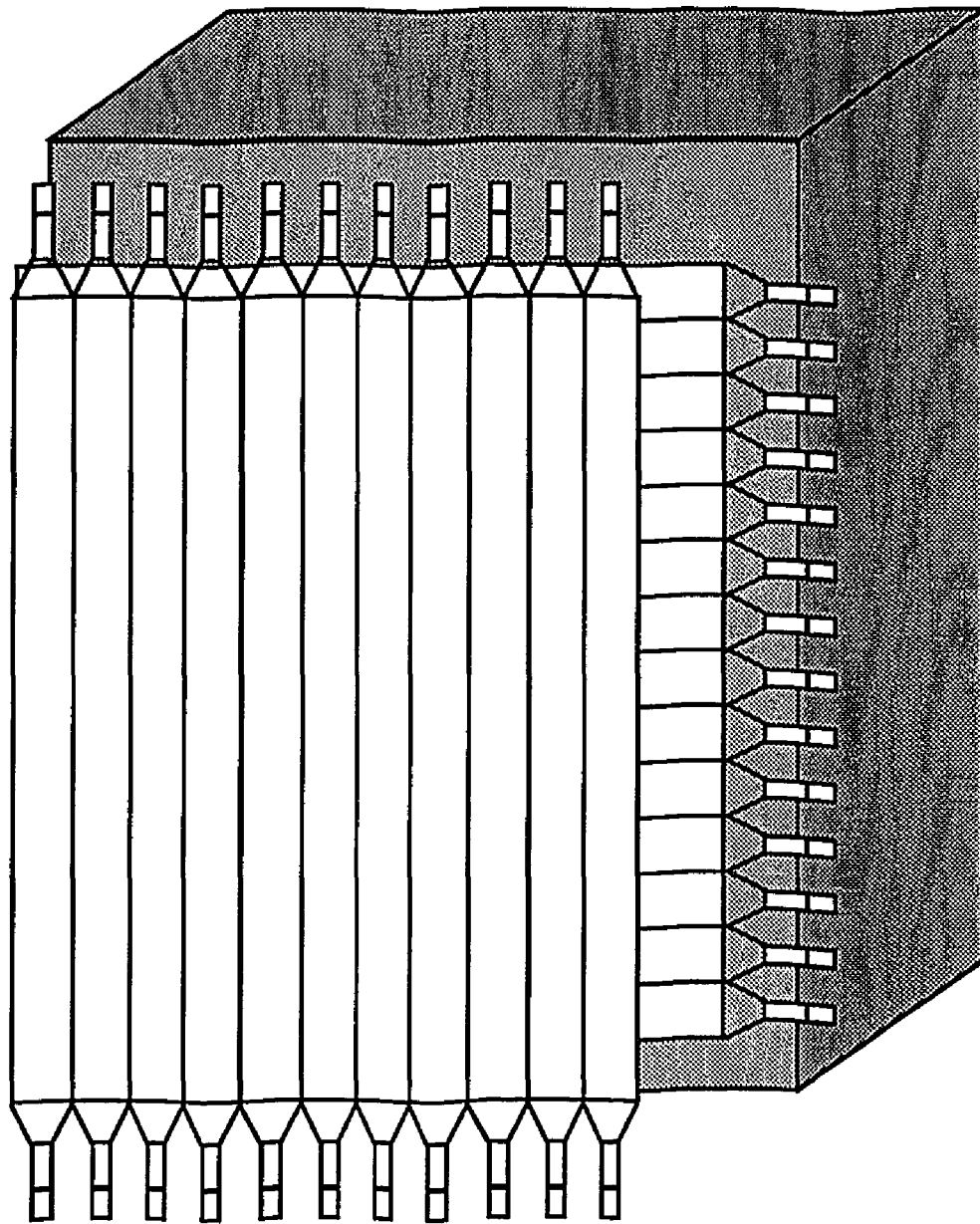


Figure 14.

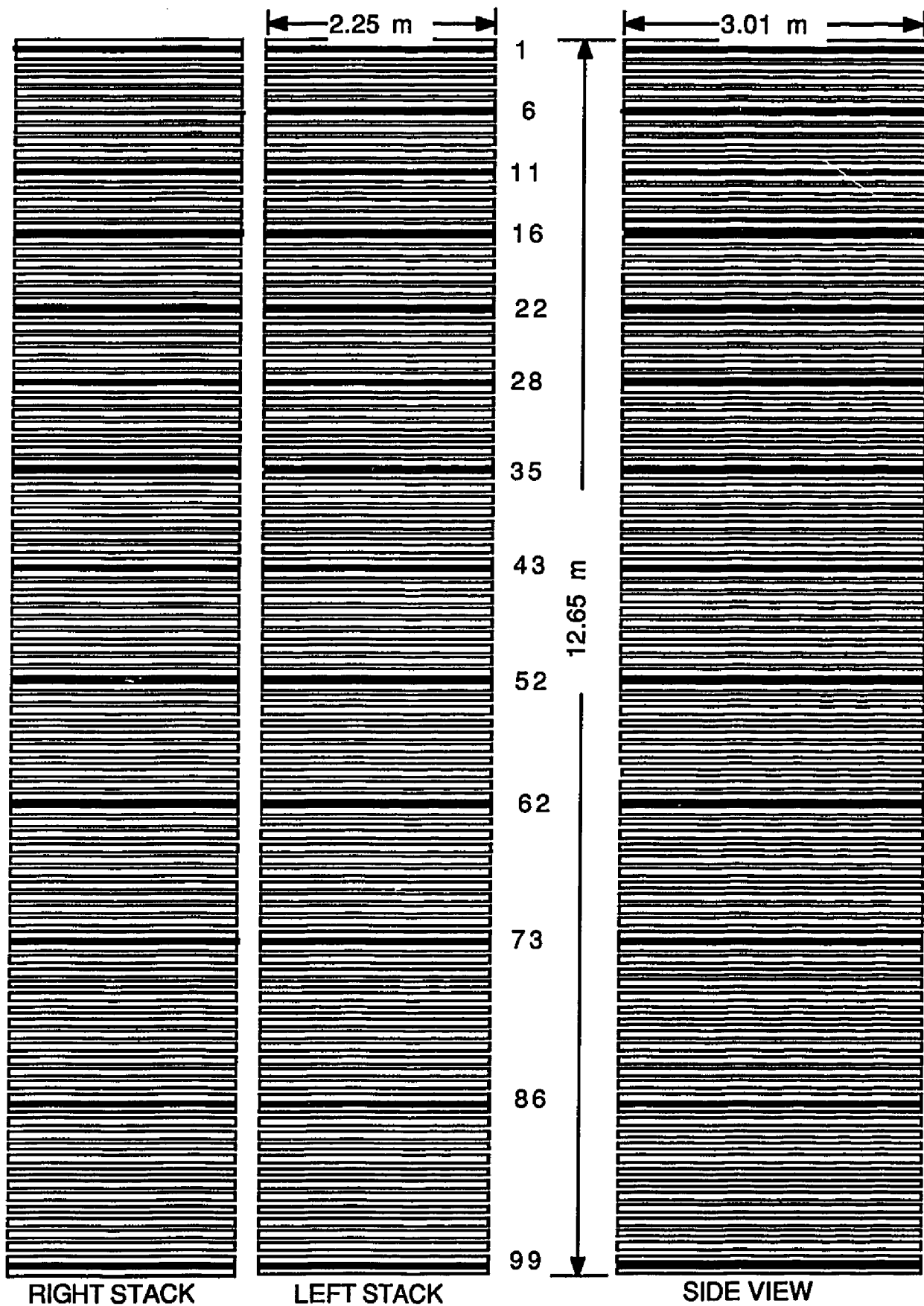


Figure 15.

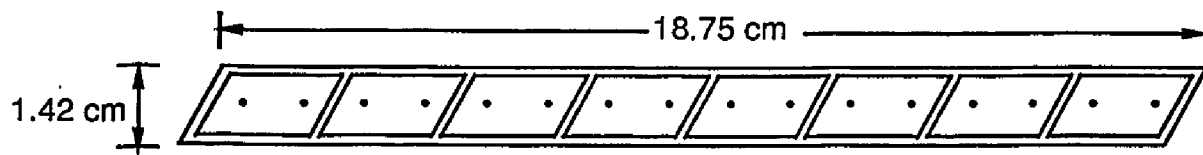
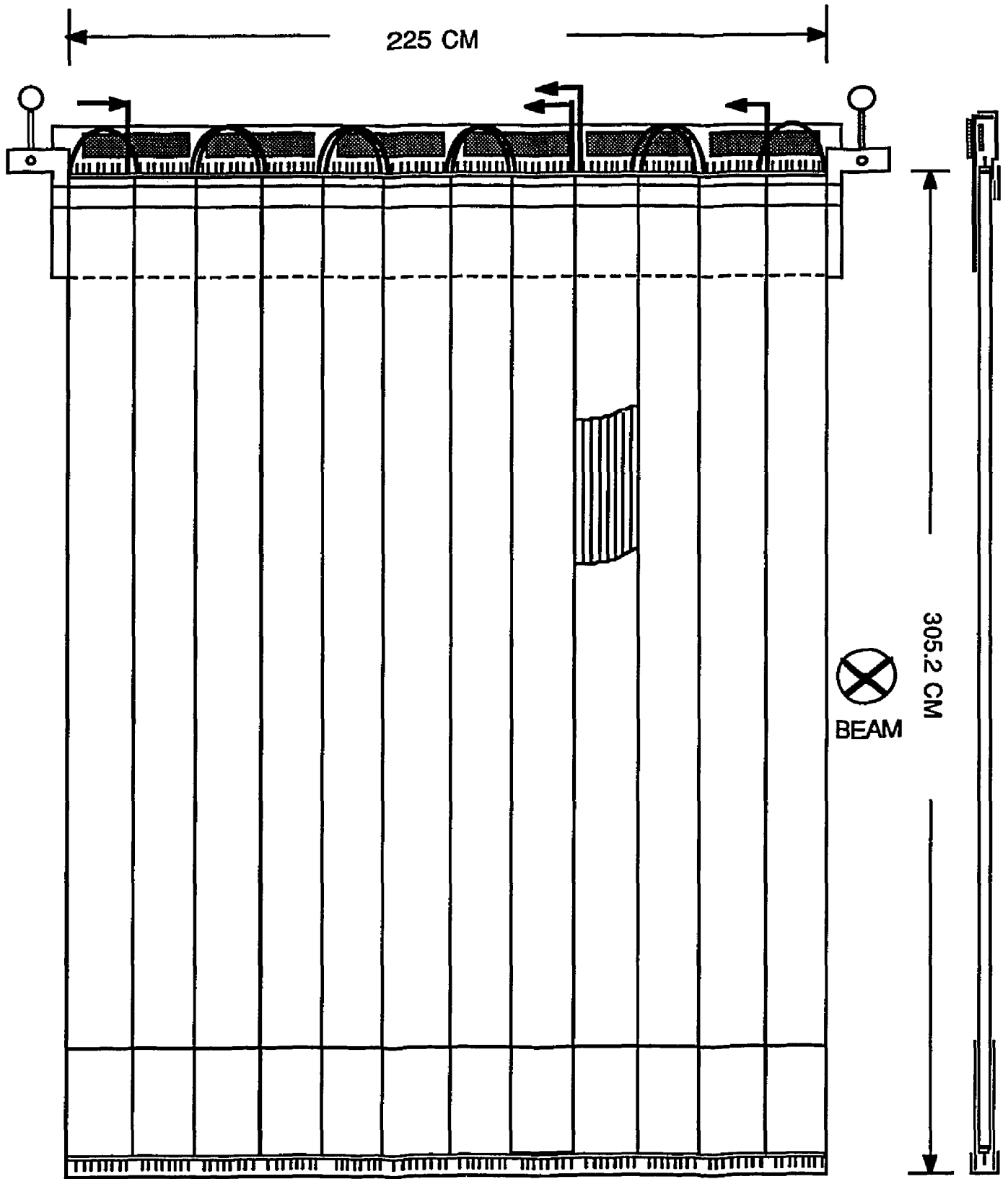
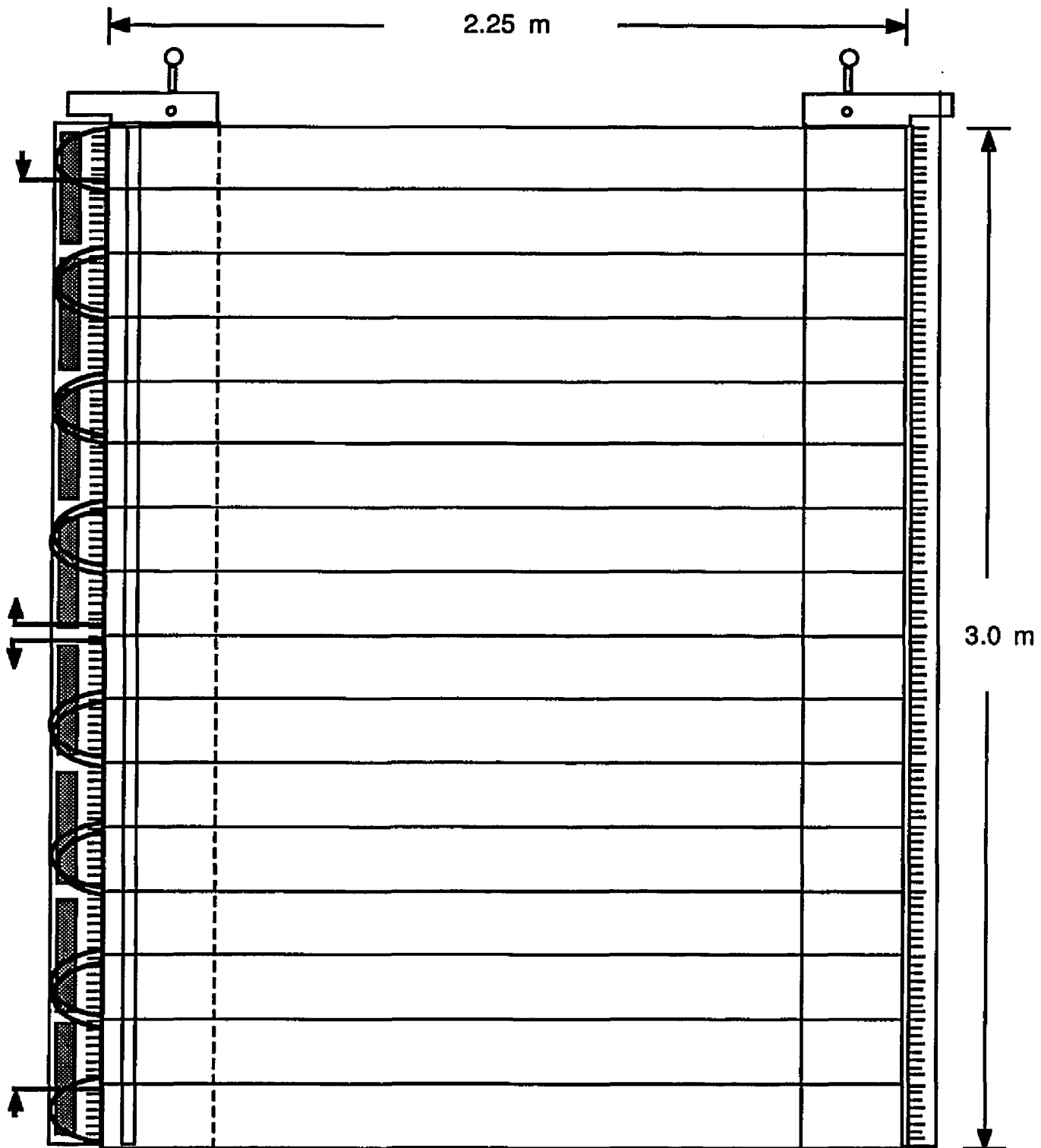


Figure 16.



X-PLANE BEAM LEFT

Figure 17.



Y-PLANE ASSEMBLY

Figure 18.

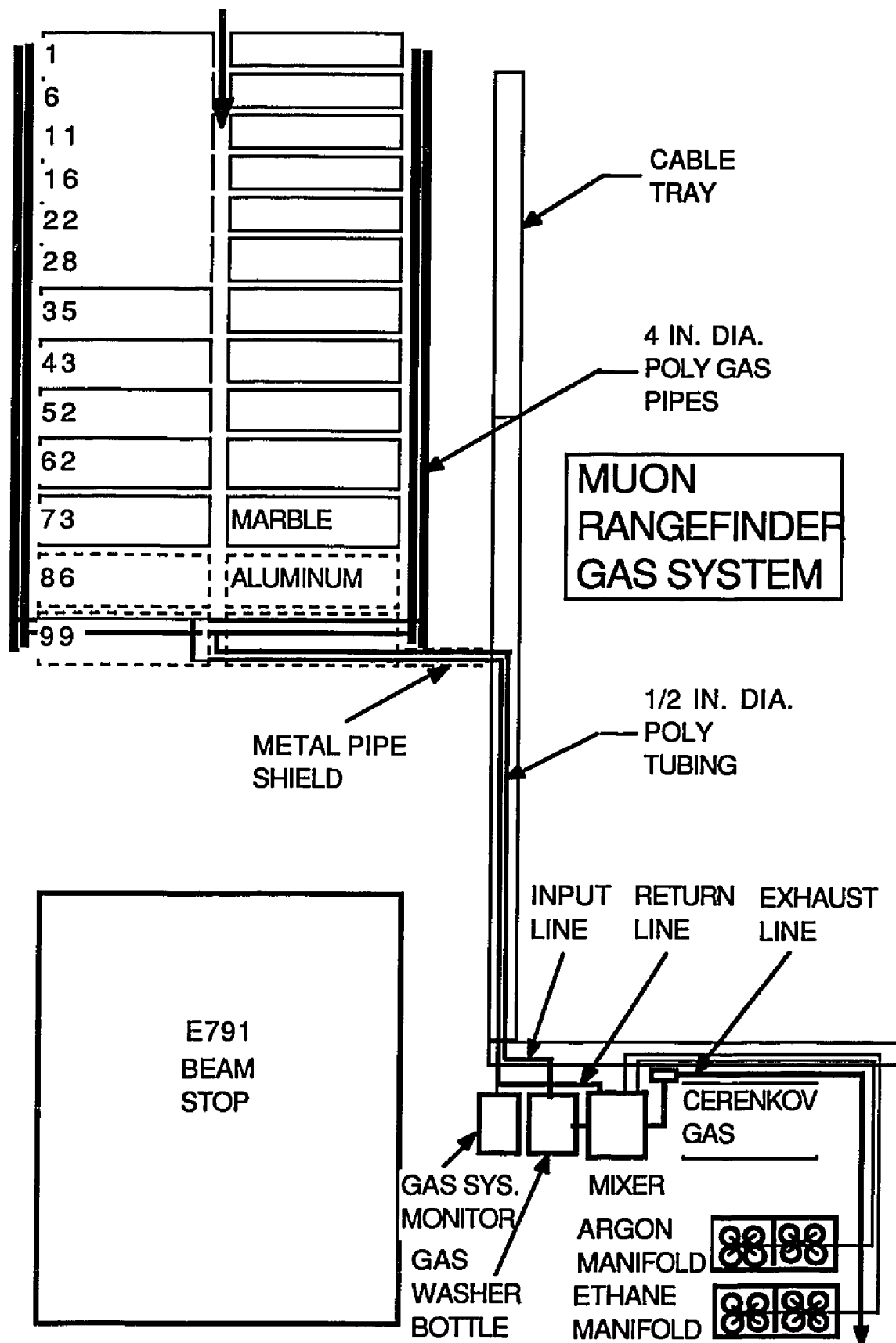
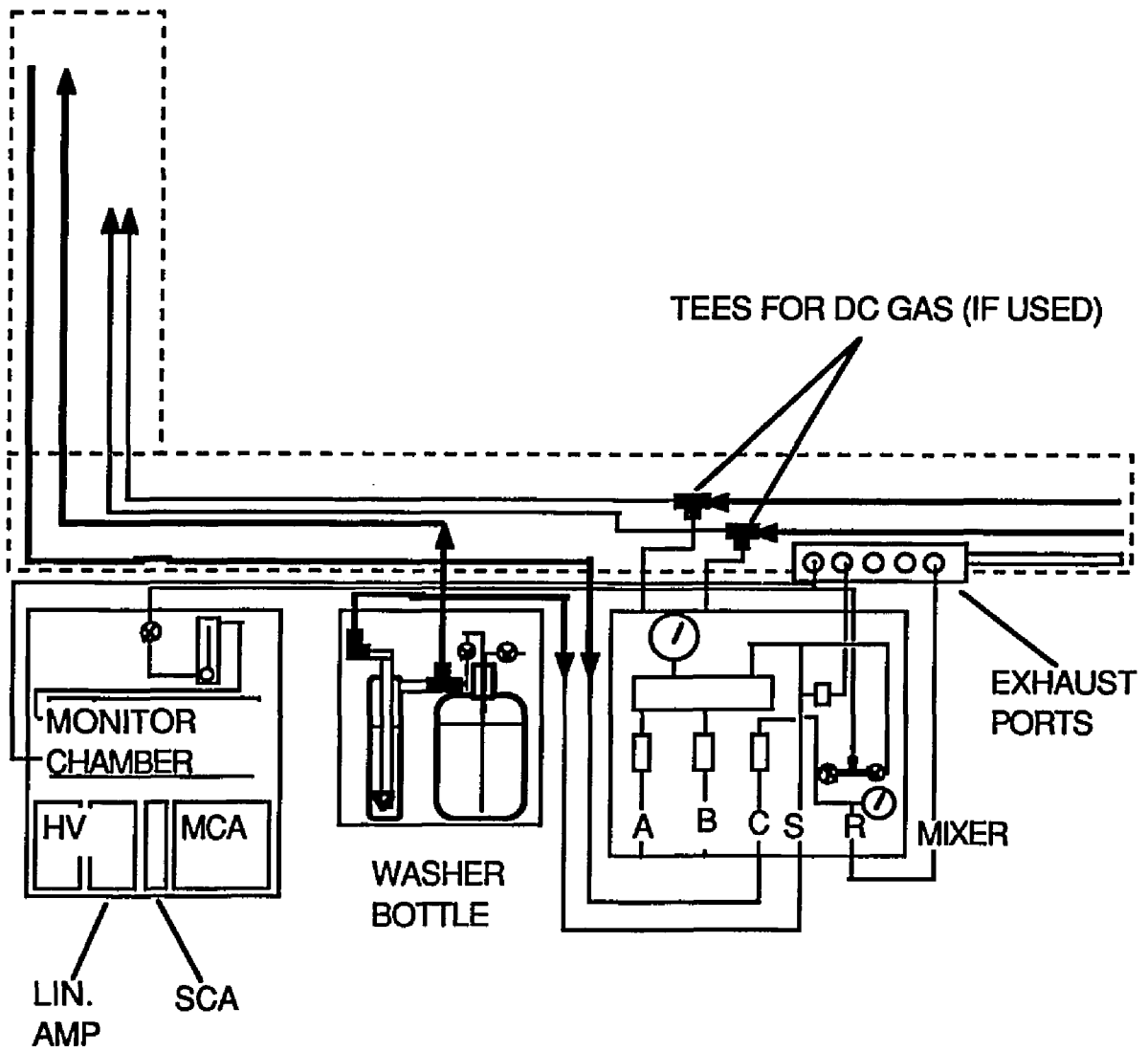


Figure 19.



GAS CONTROL AND MONITORING

Figure 20.

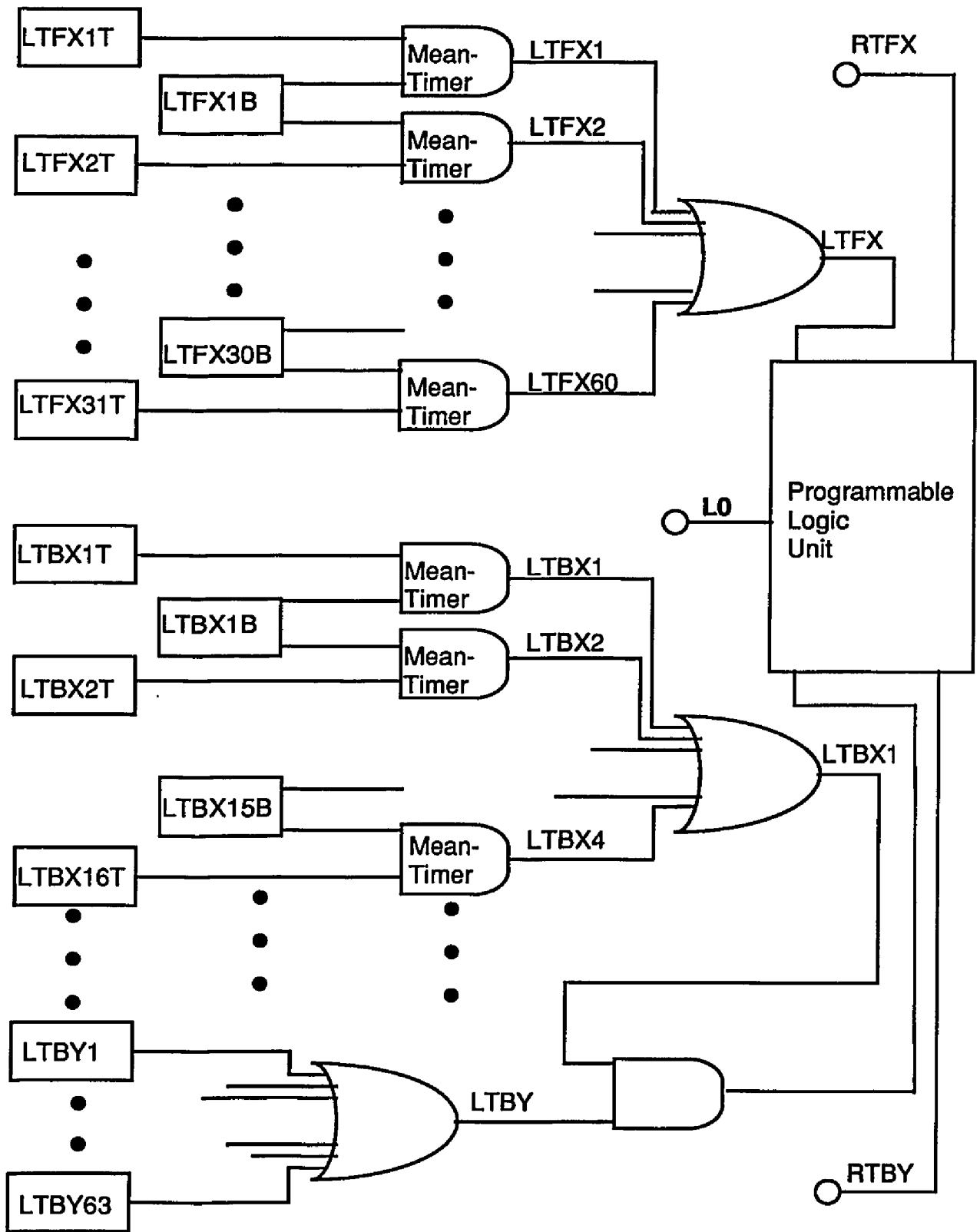


Figure 21.

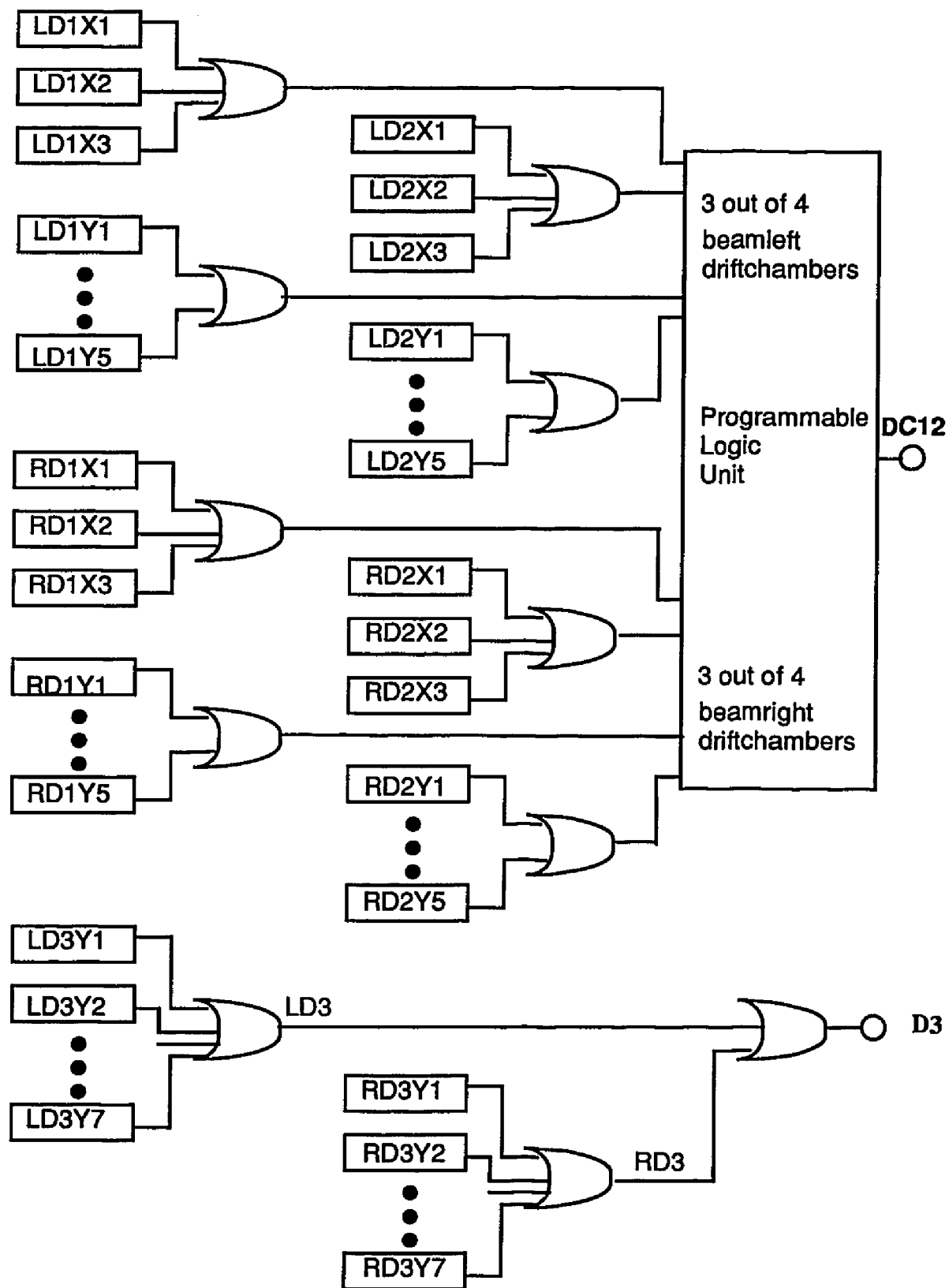


Figure 22.

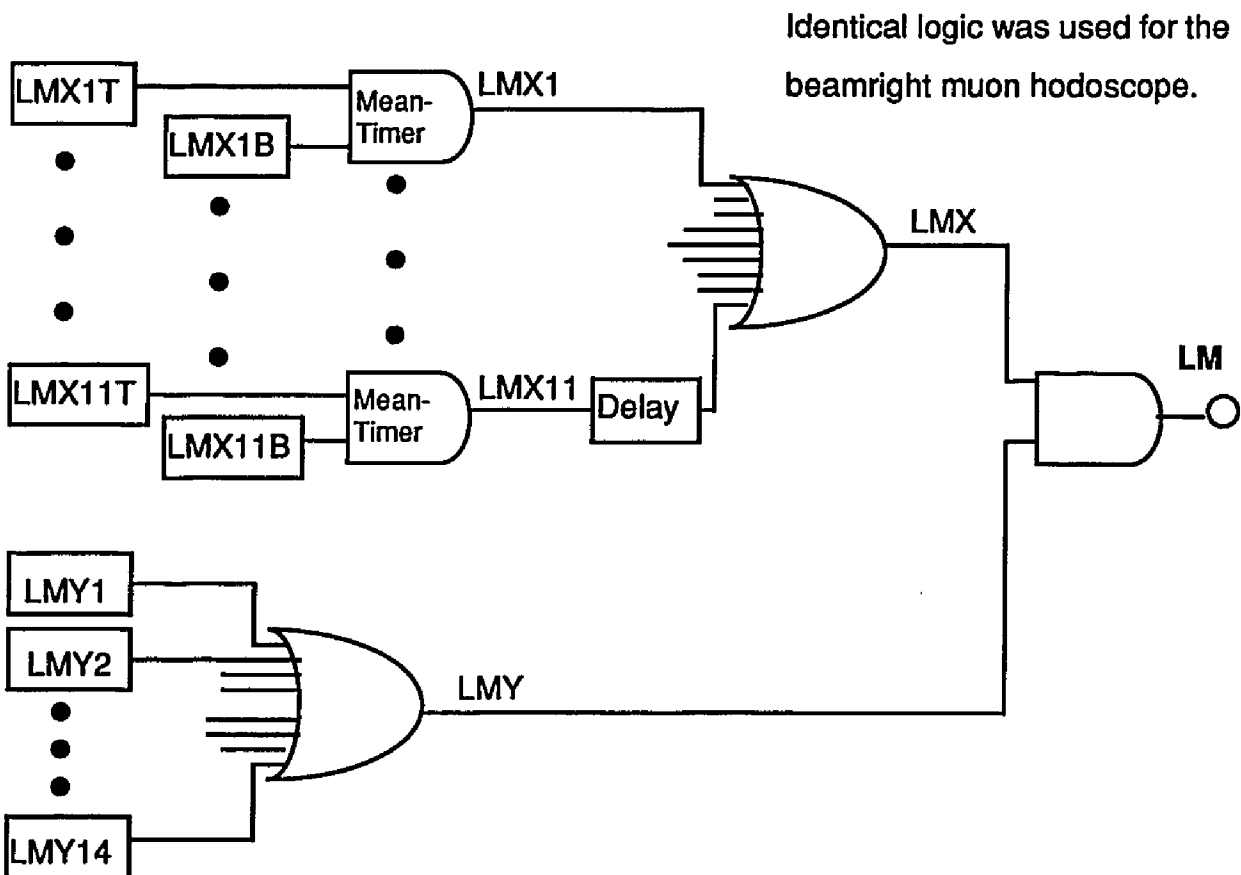
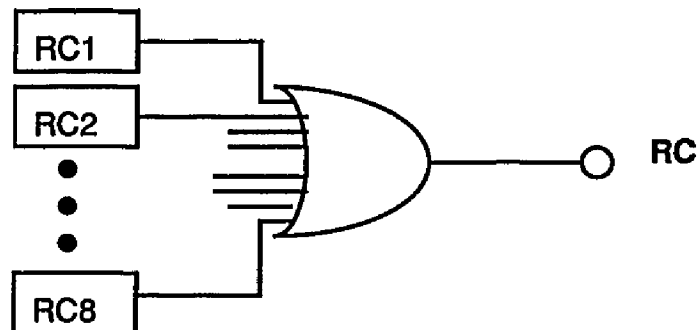
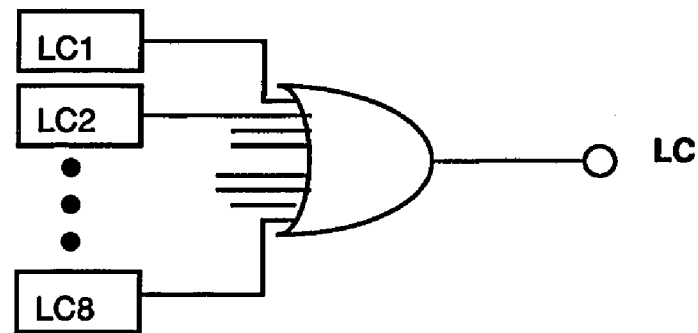


Figure 23

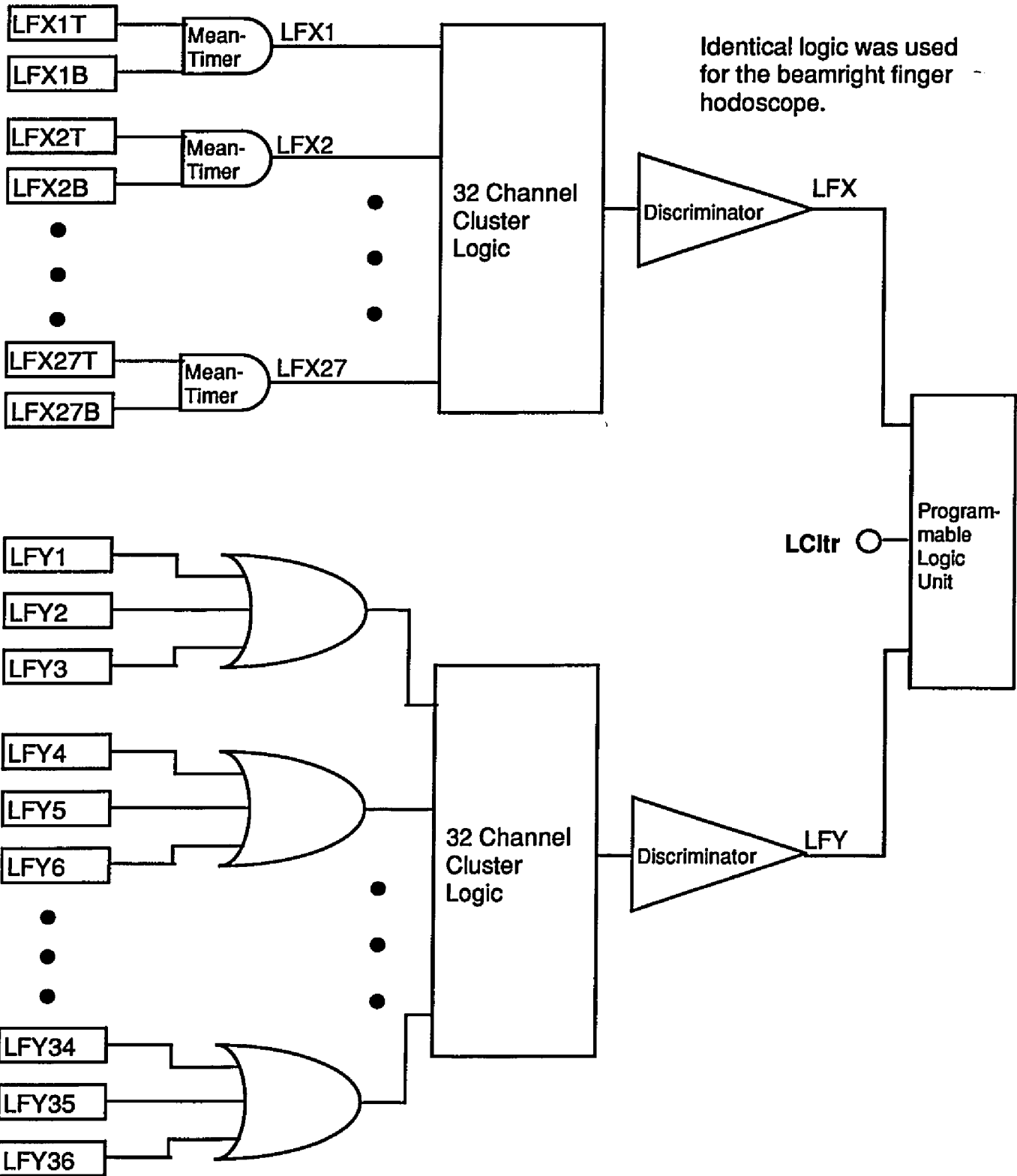


Figure 24.

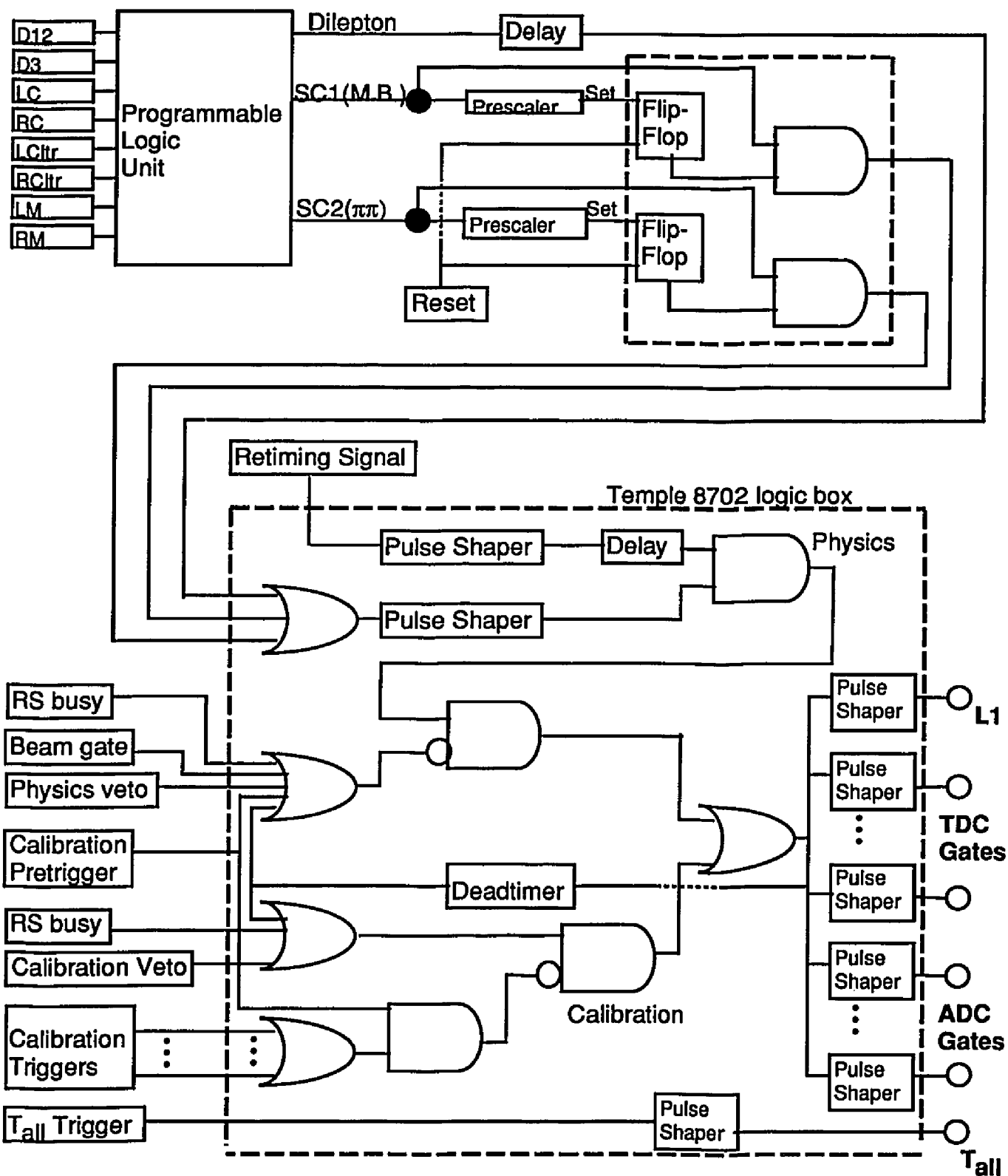


Figure 25.

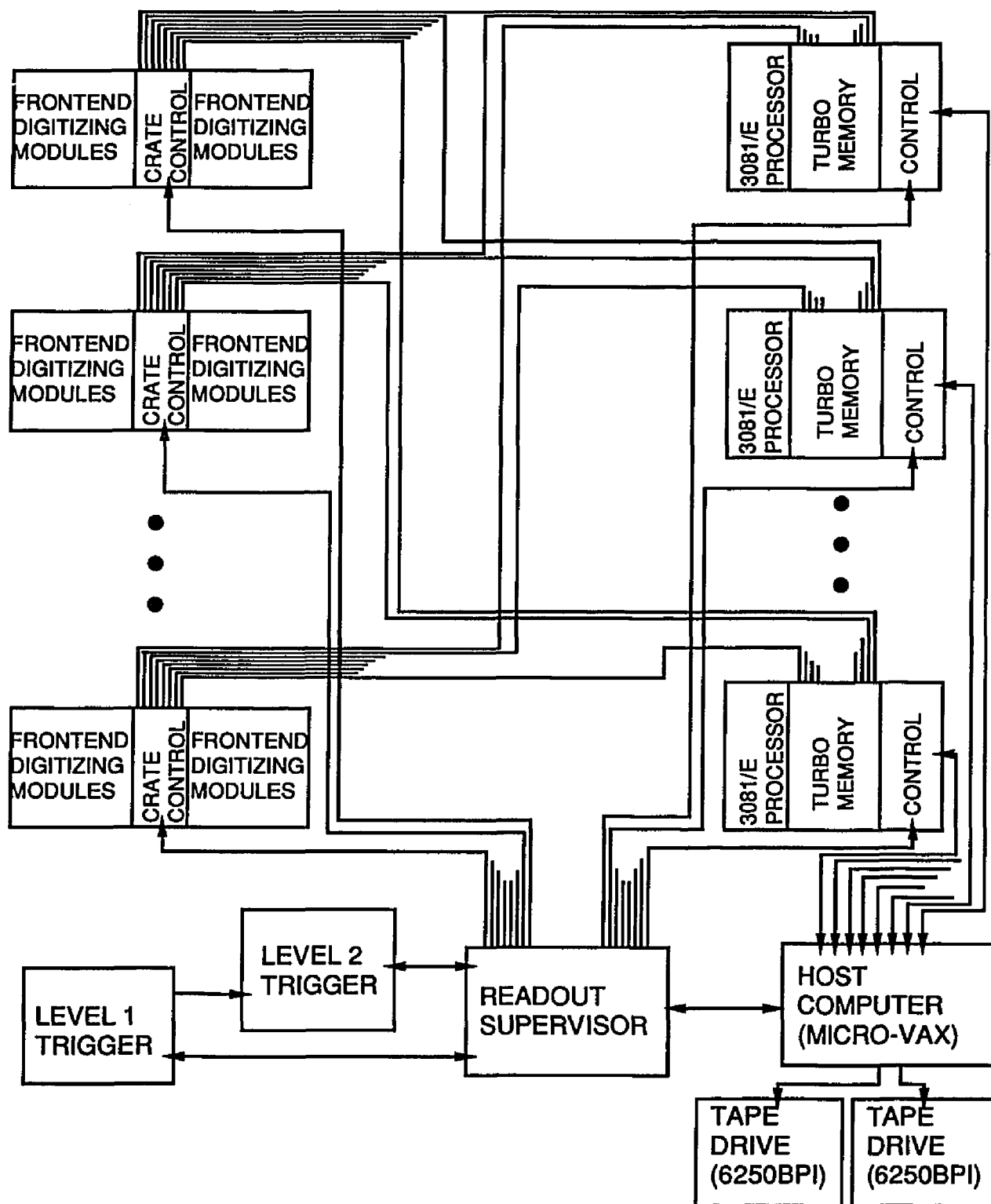


Figure 26.

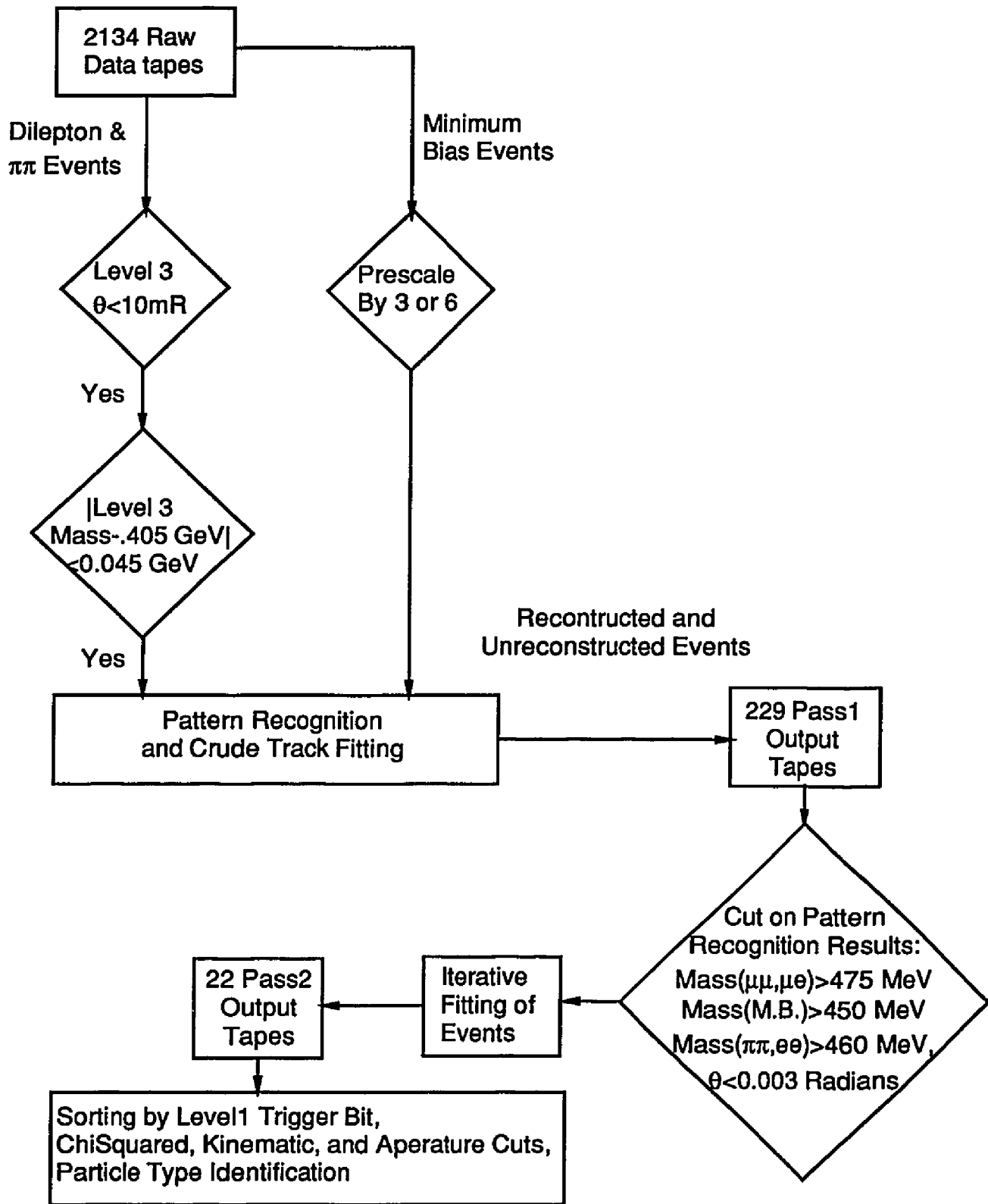


Figure 27.

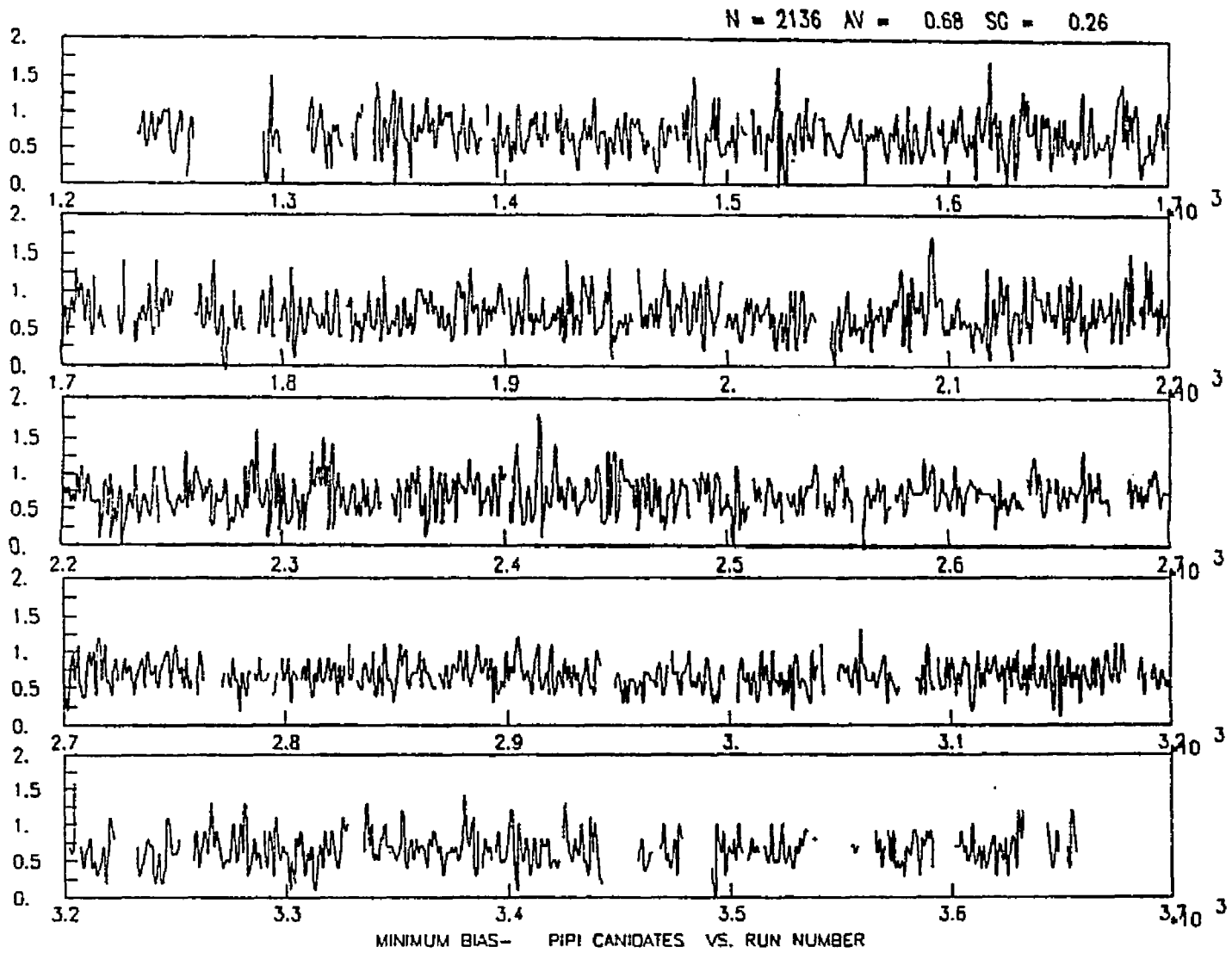


Figure 28

N = 2137 AV = 59.85 SC = 5.53

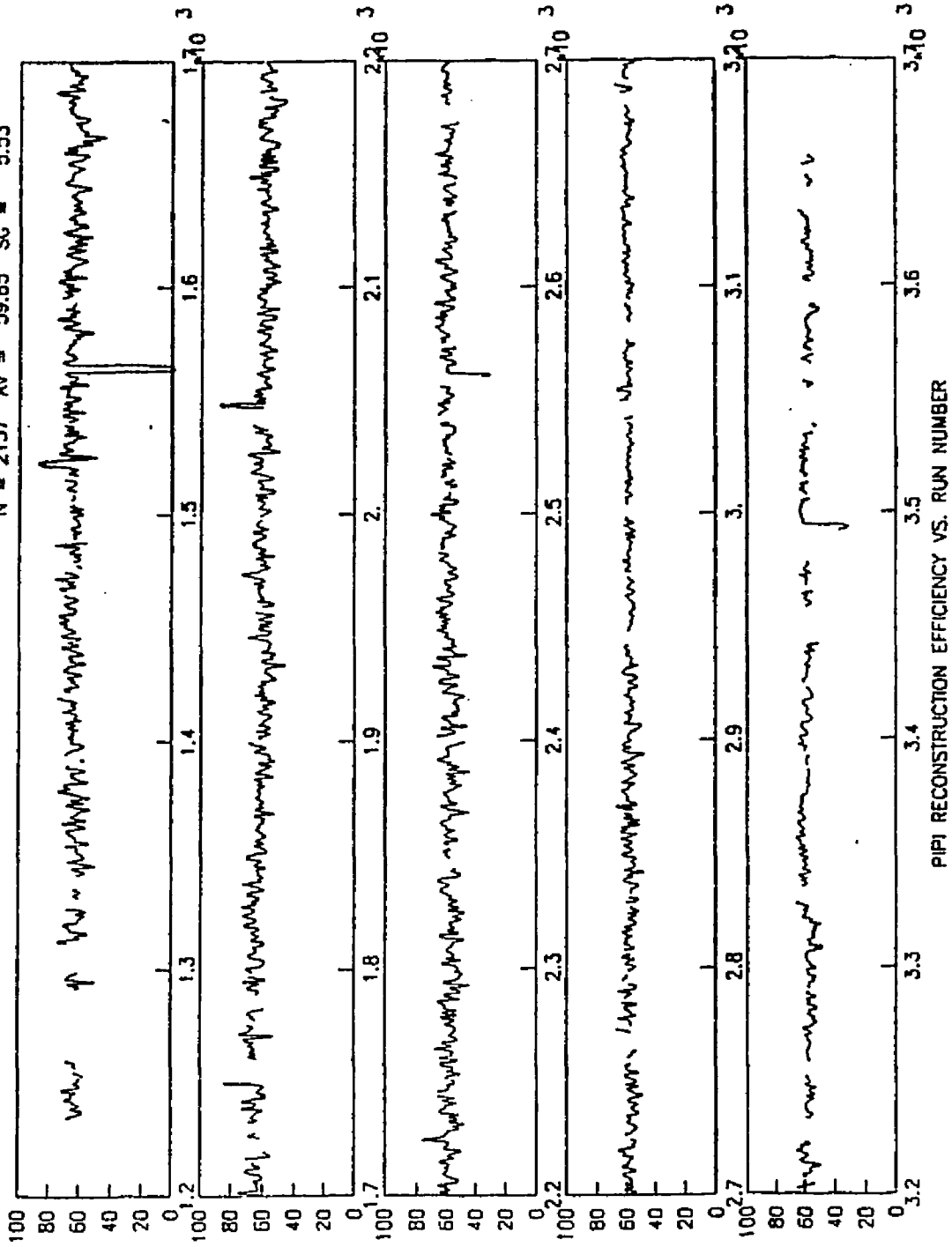


Figure 29

N = 2137. AV = 55.84 SG = 5.90

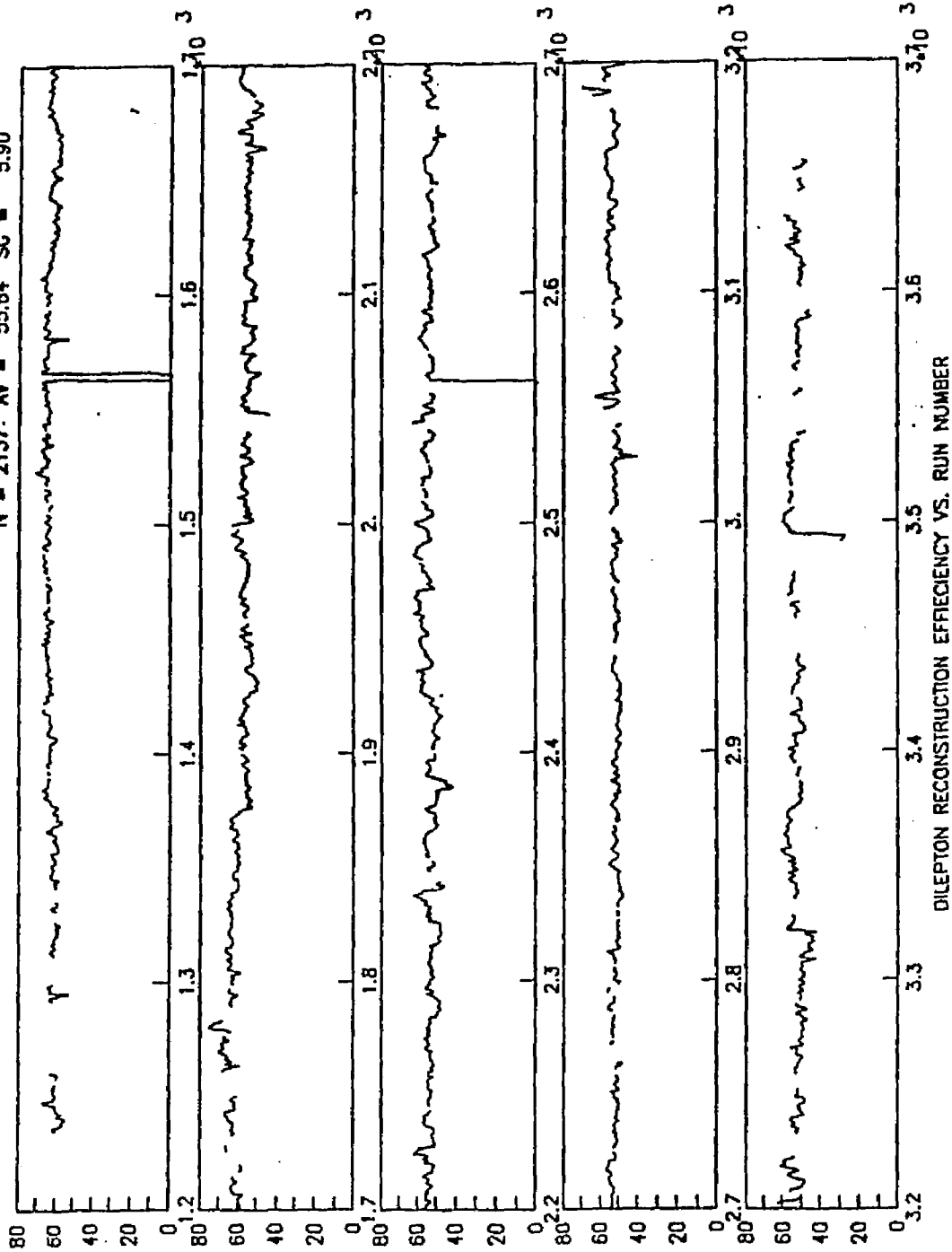


Figure 30

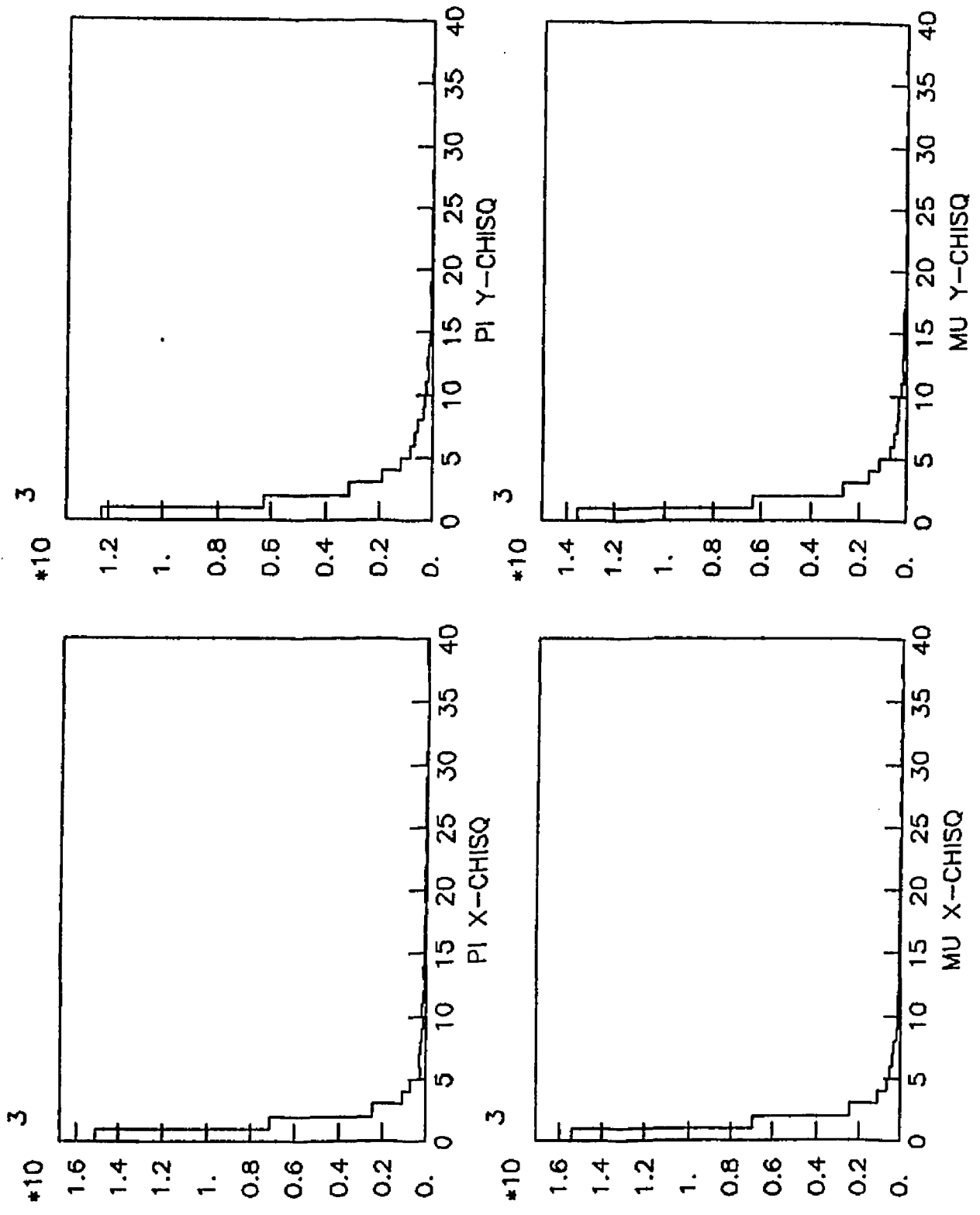


Figure 31

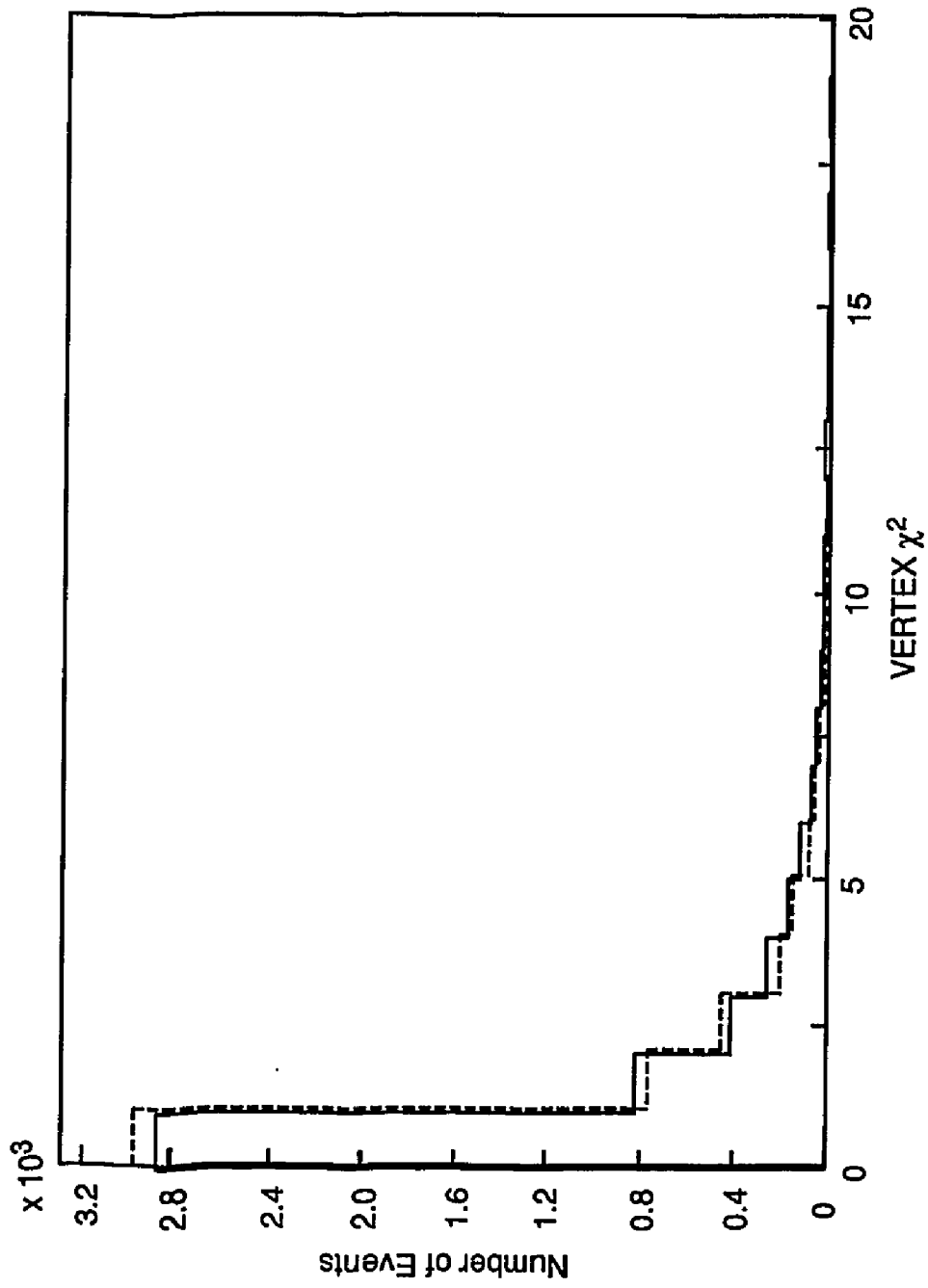


Figure 32.



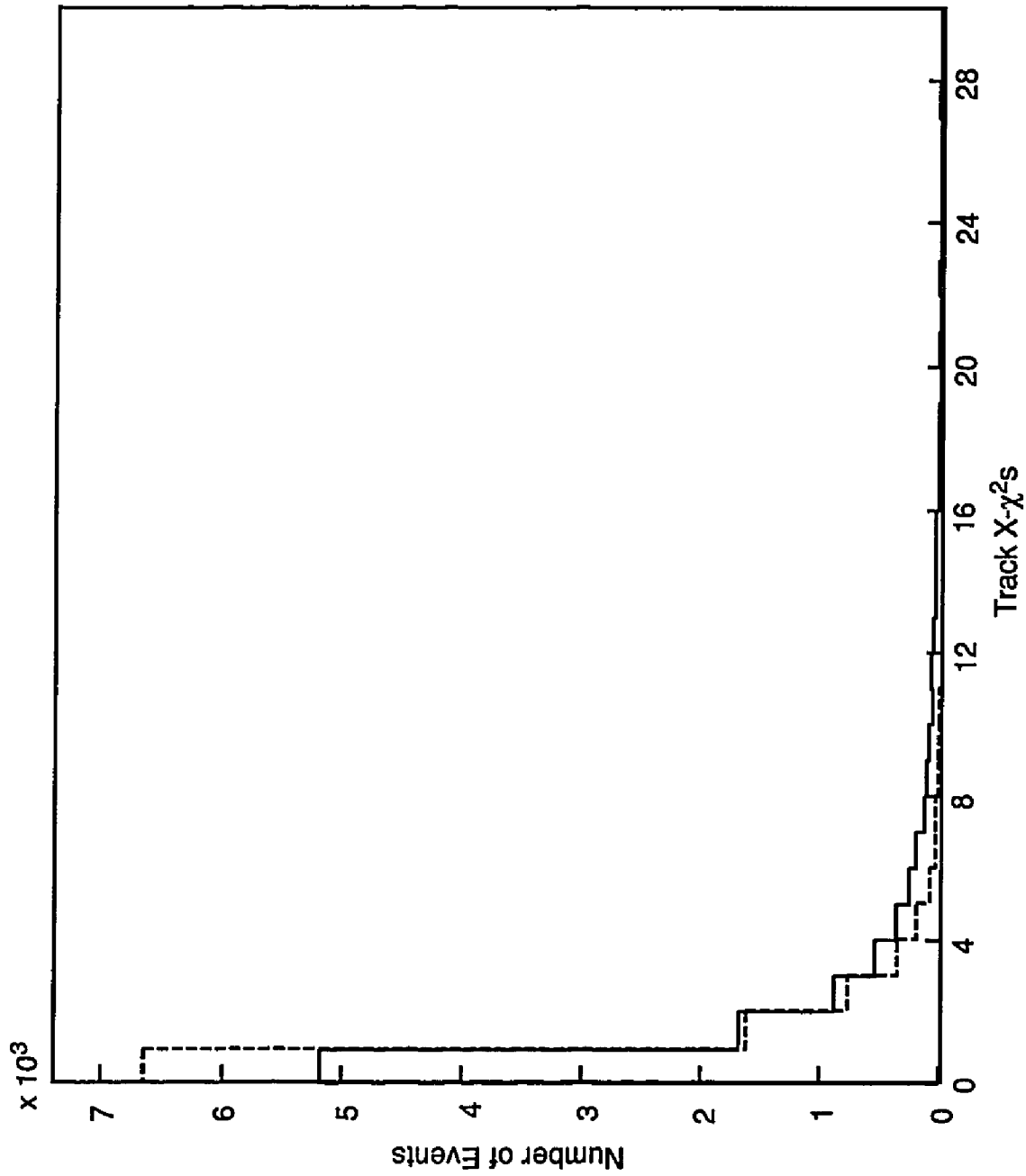


Figure 33

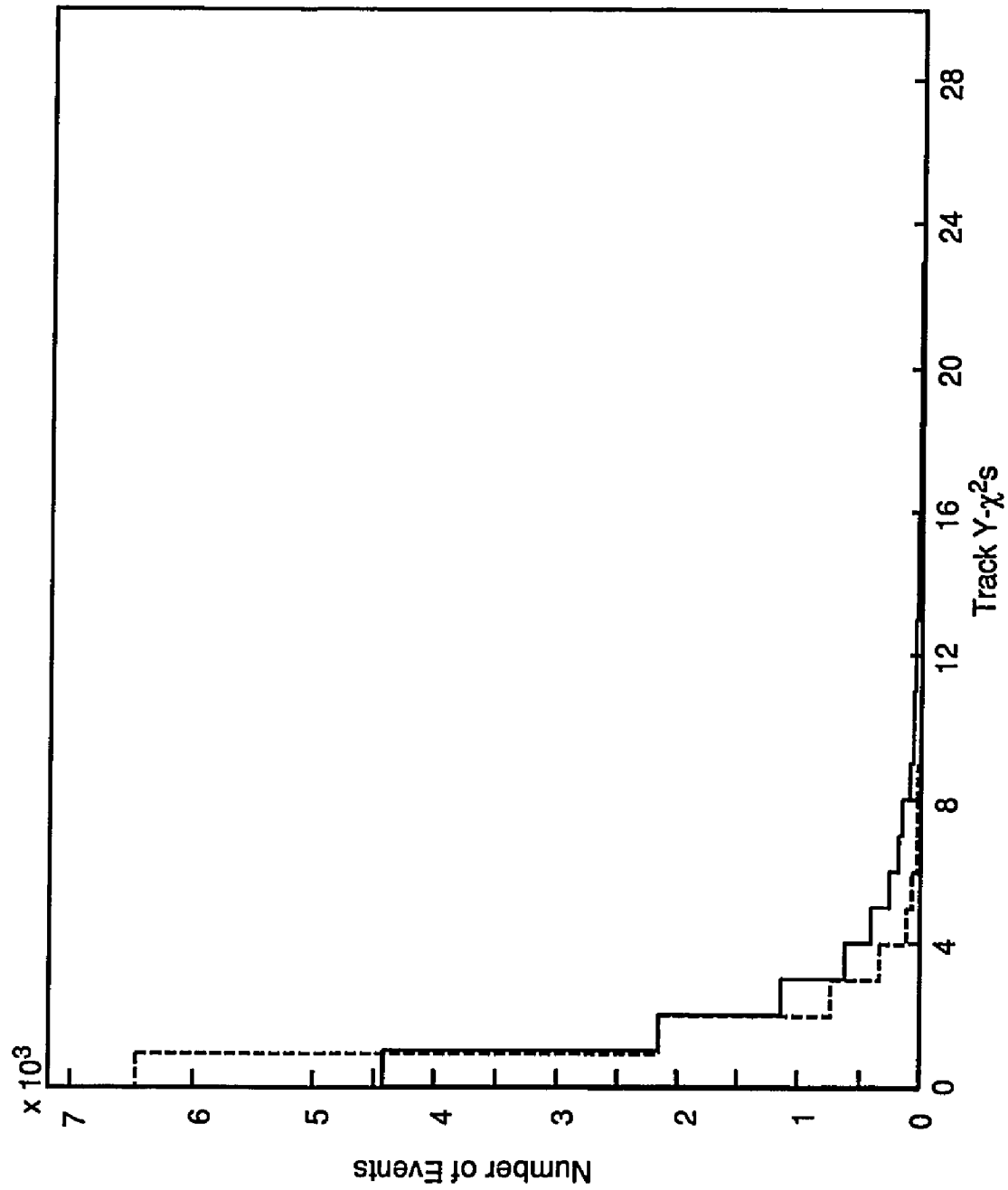


Figure 34.

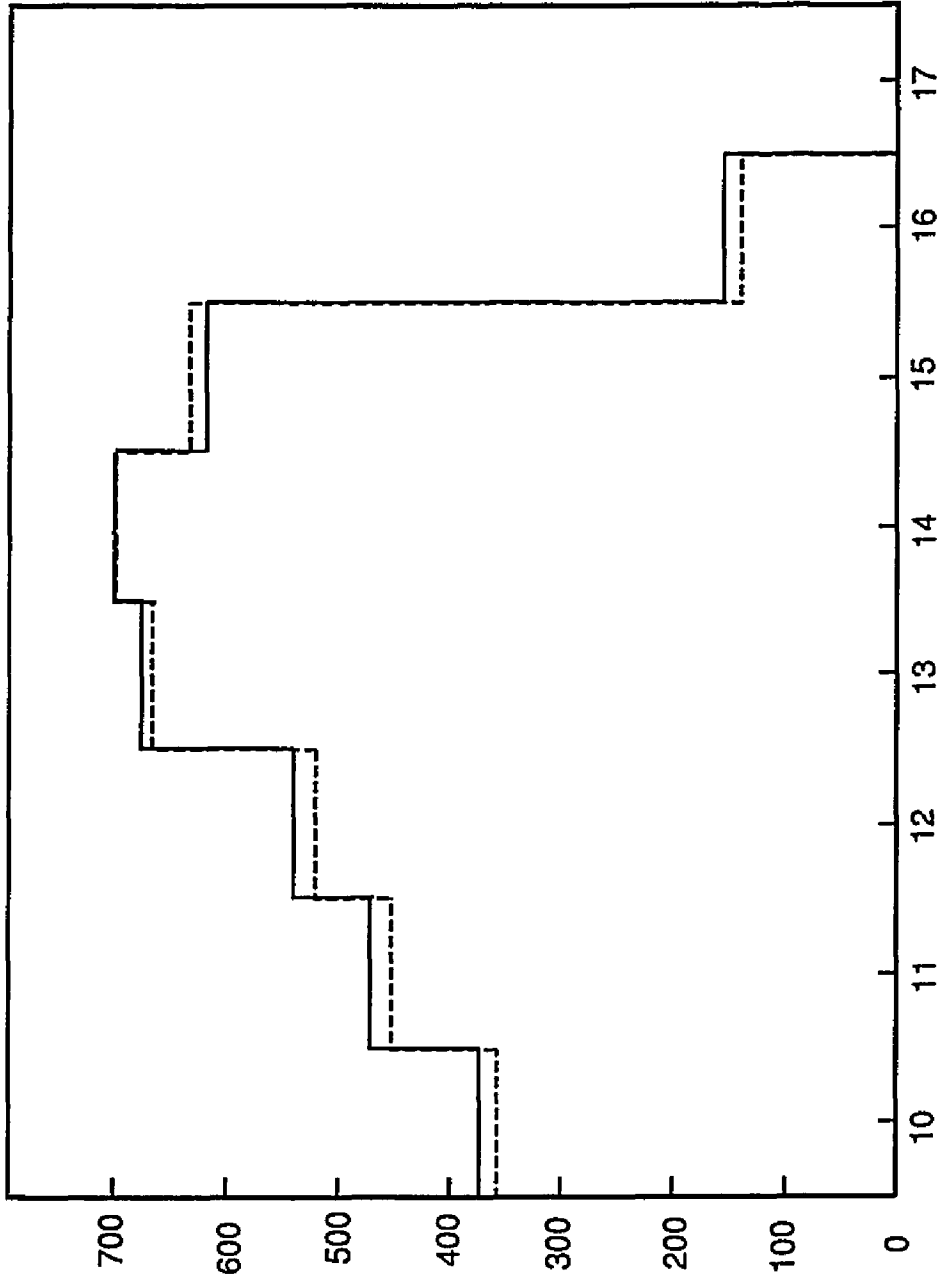


Figure 35.

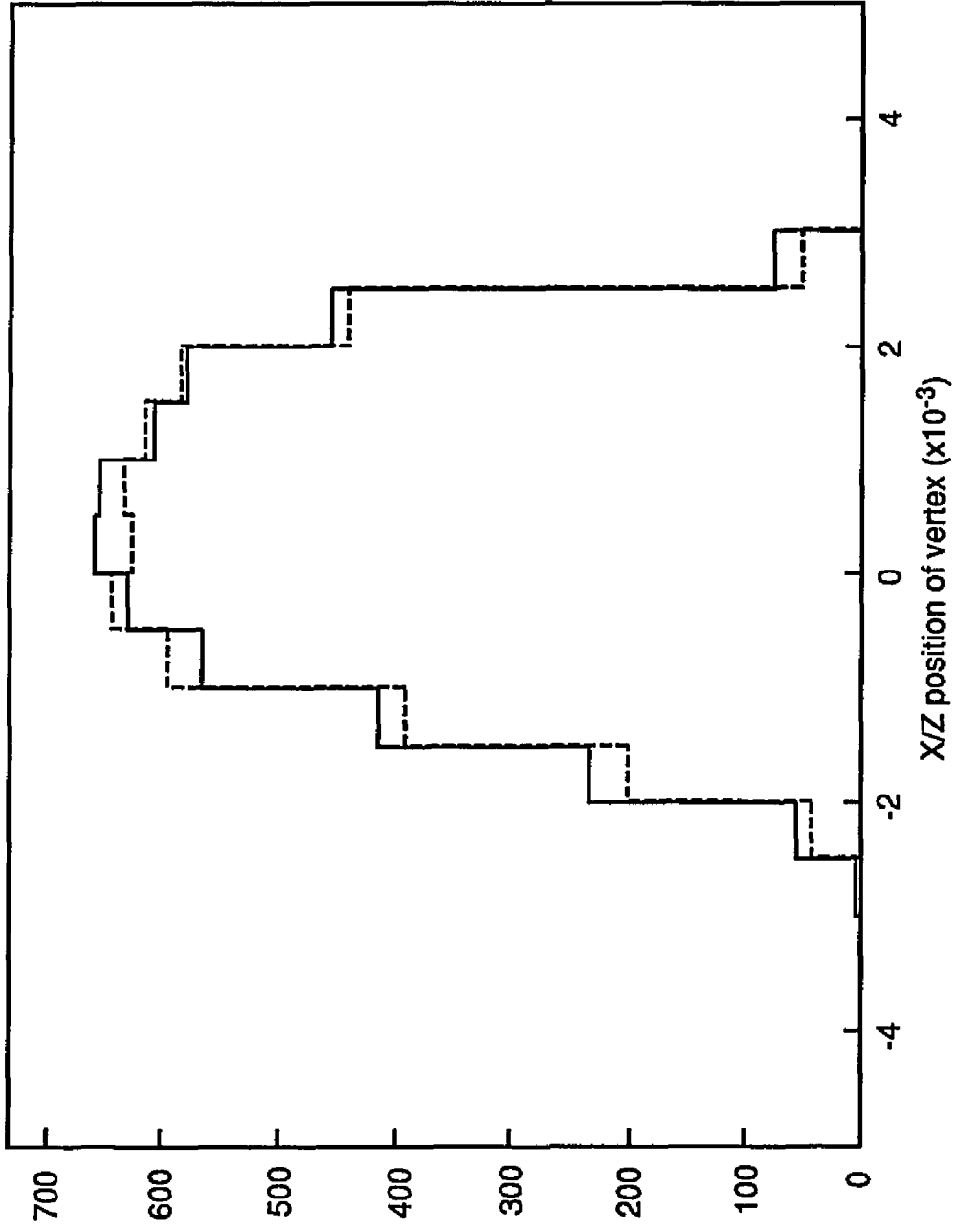


Figure 36.

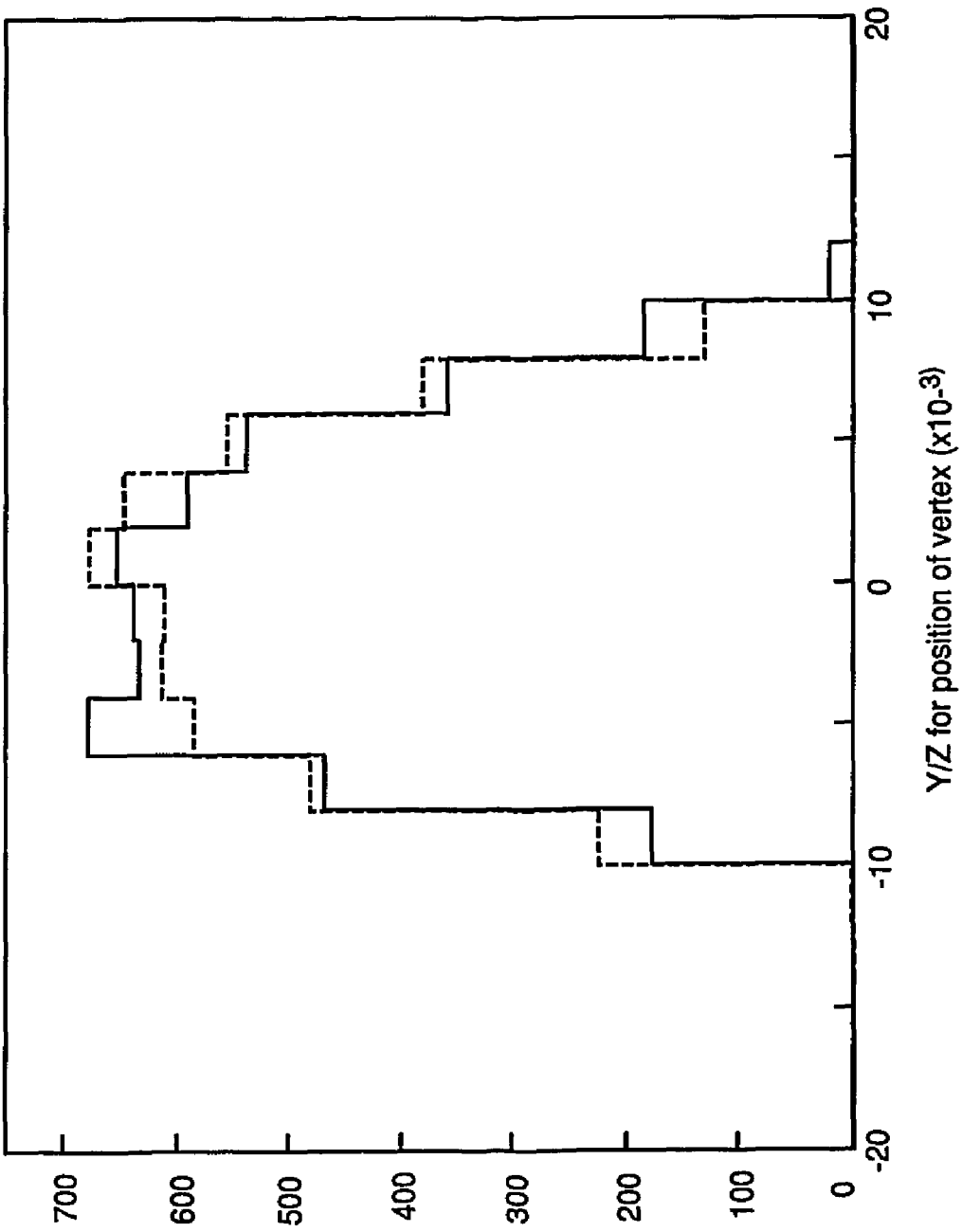


Figure 37.

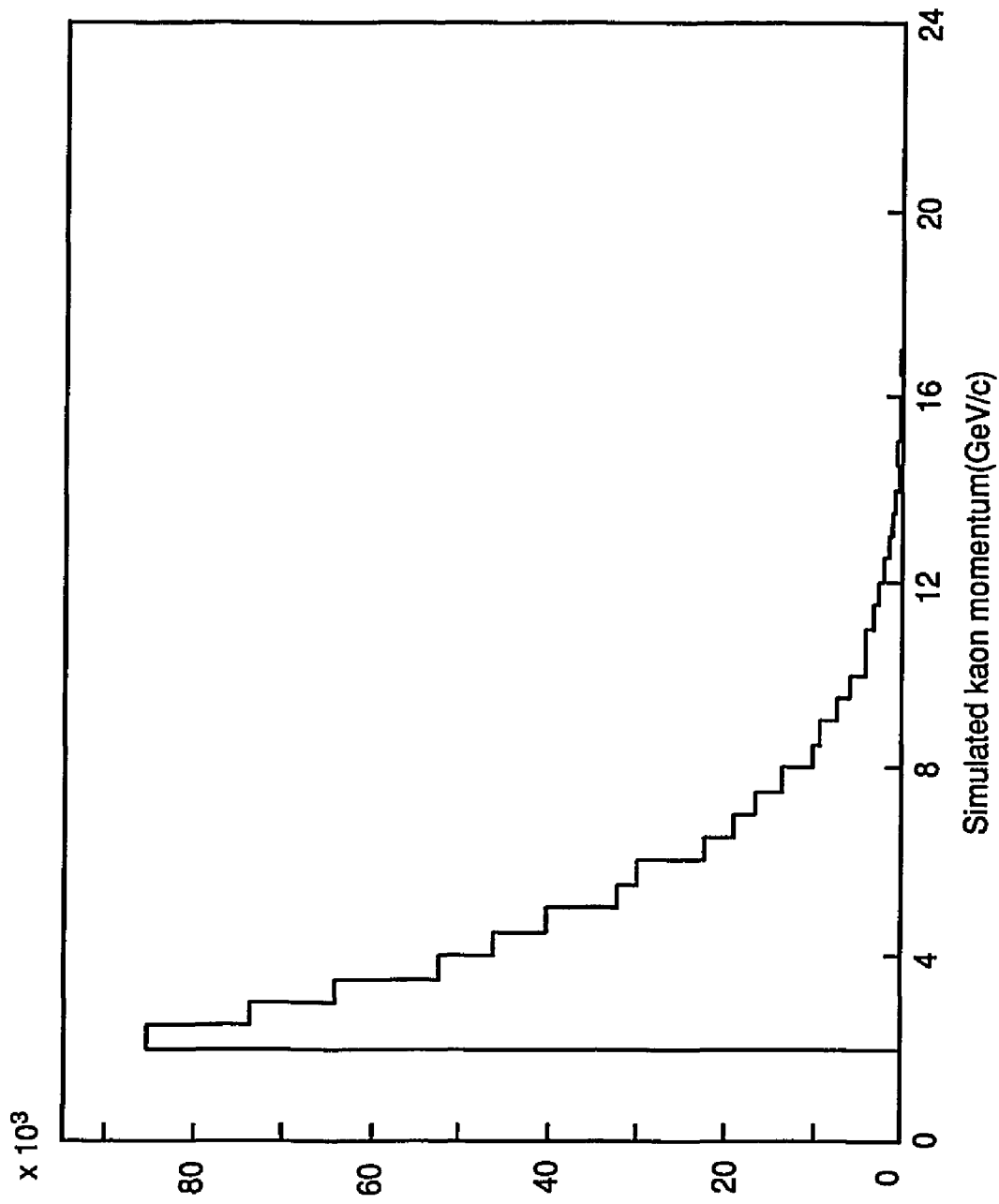


Figure 38.

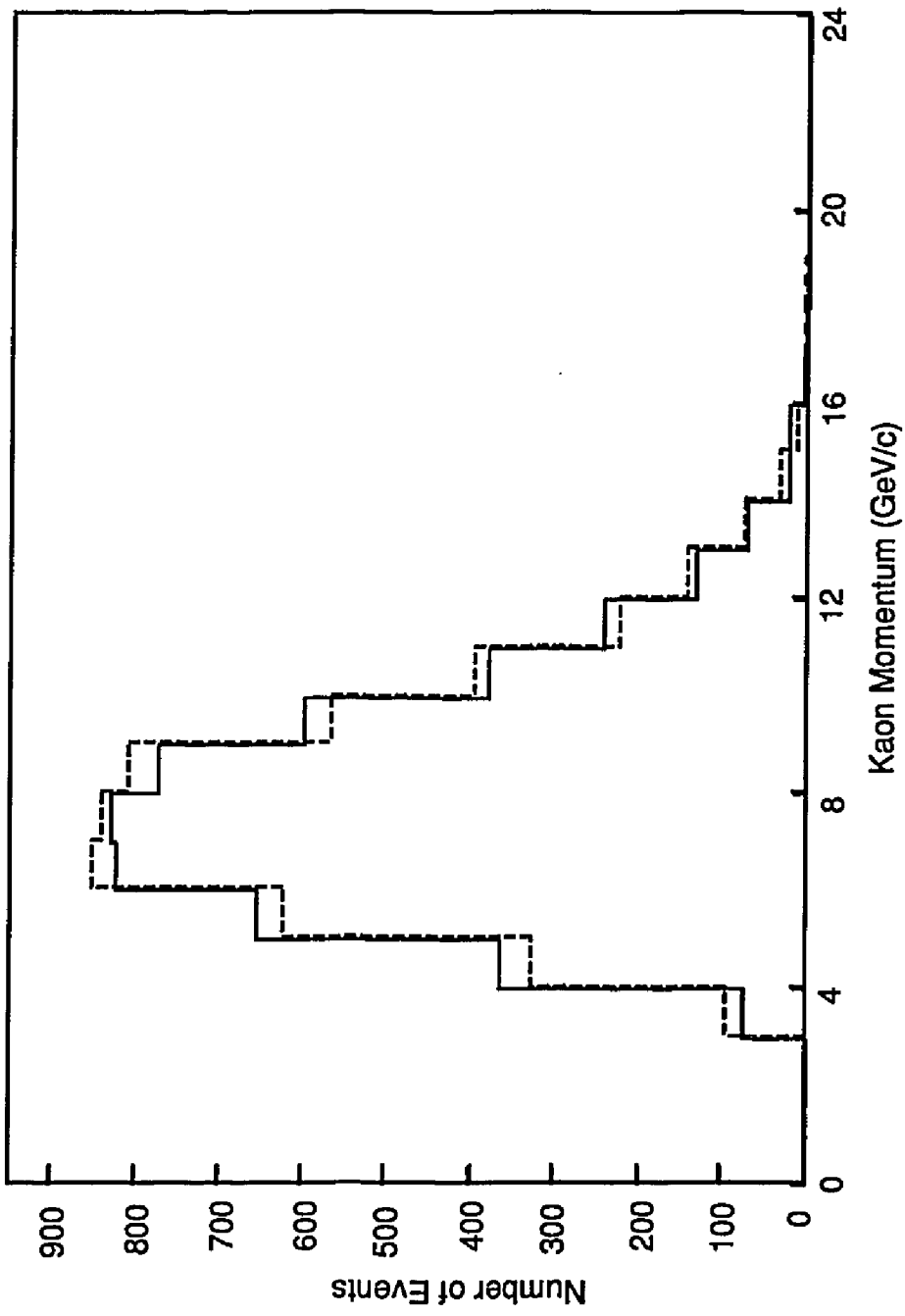


Figure 39.

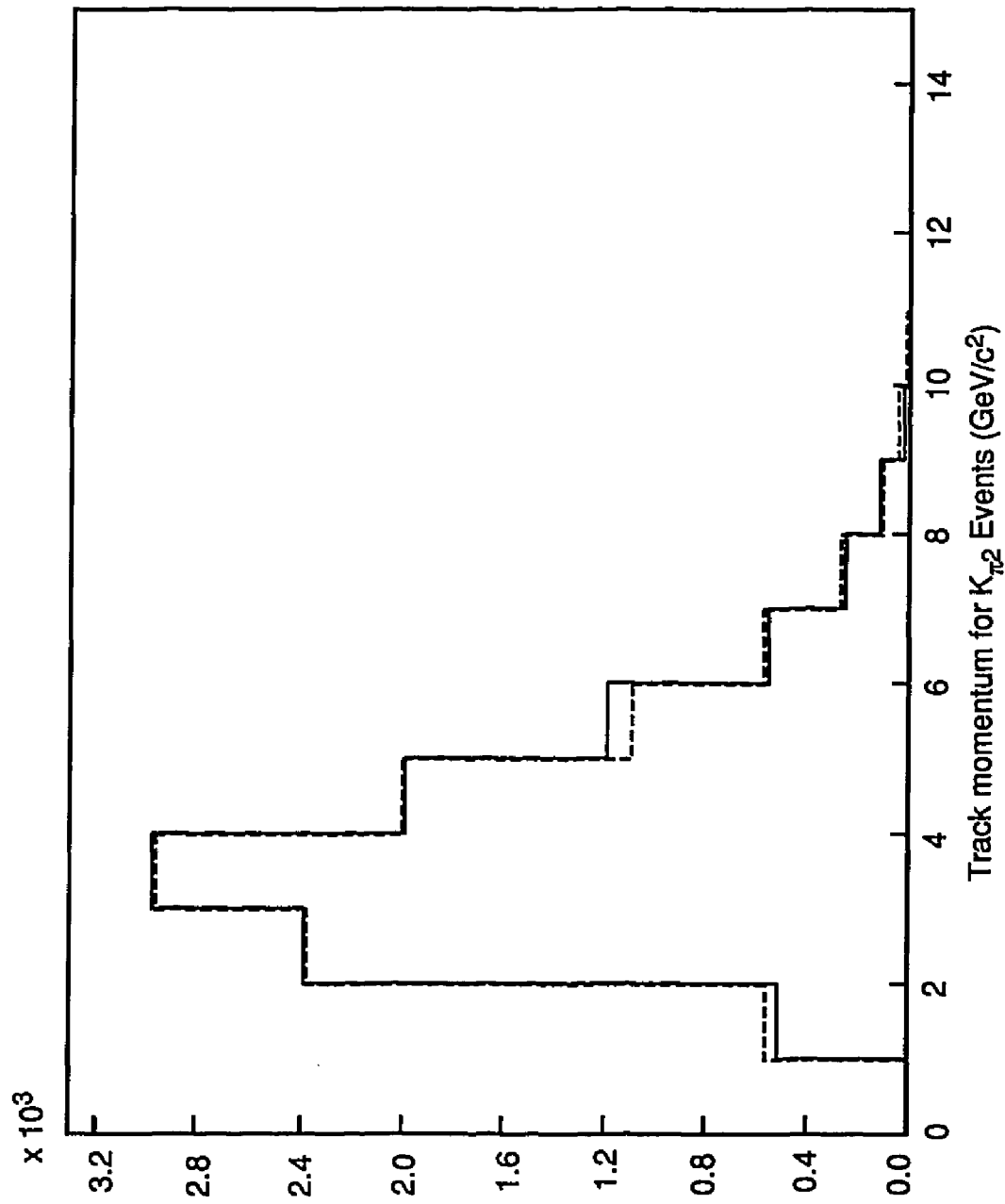


Figure 40.

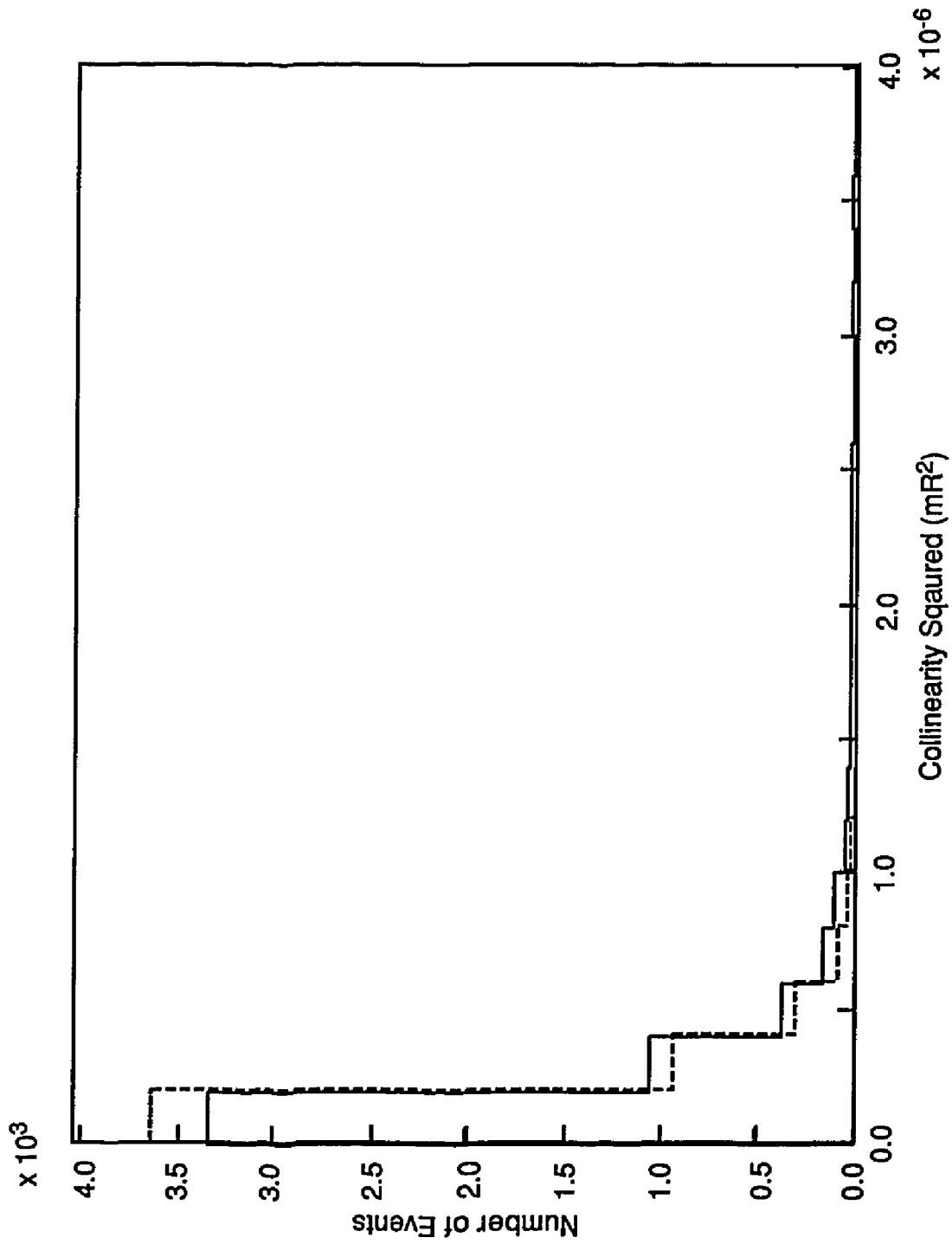


Figure 41.

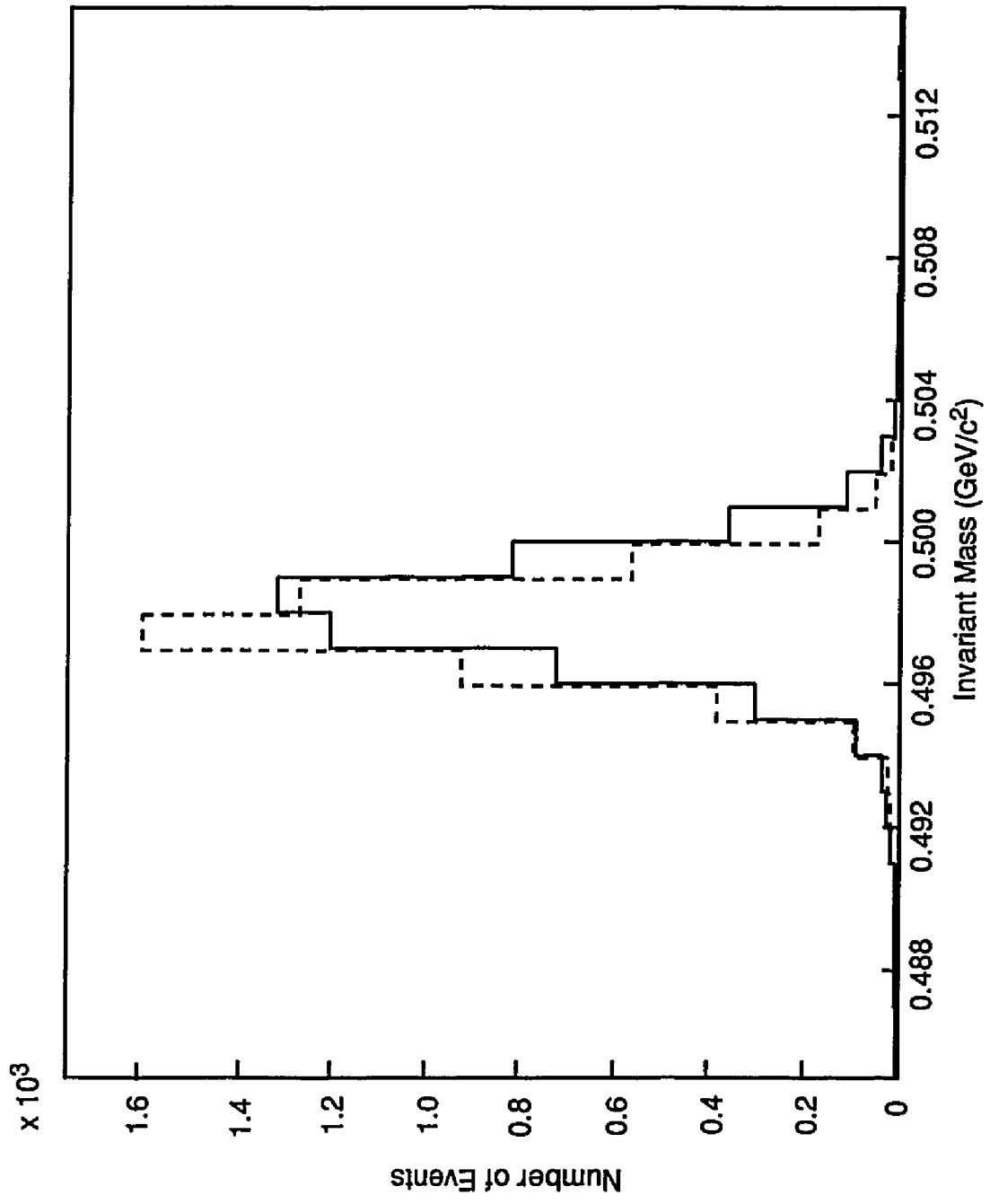


Figure 42.

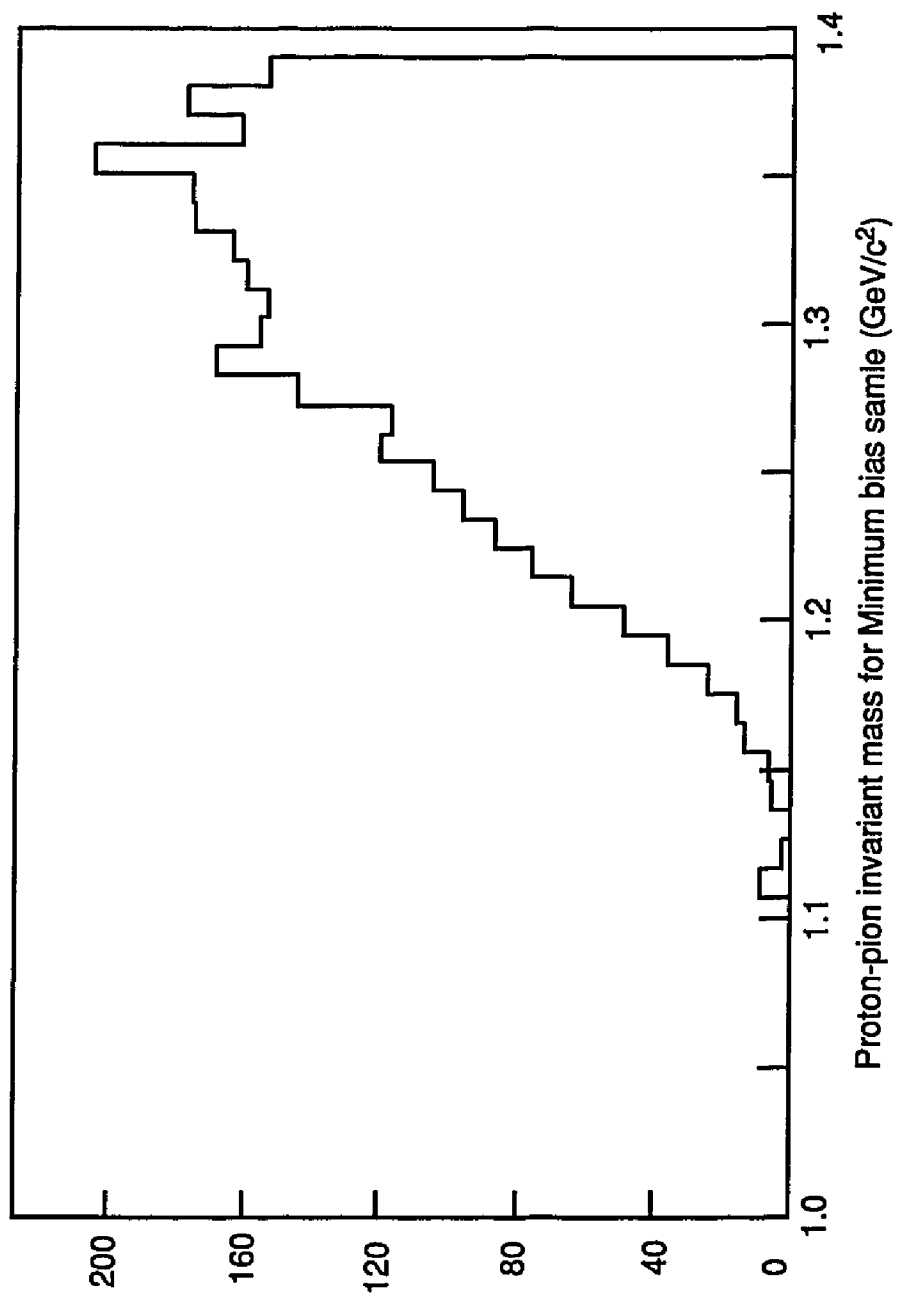
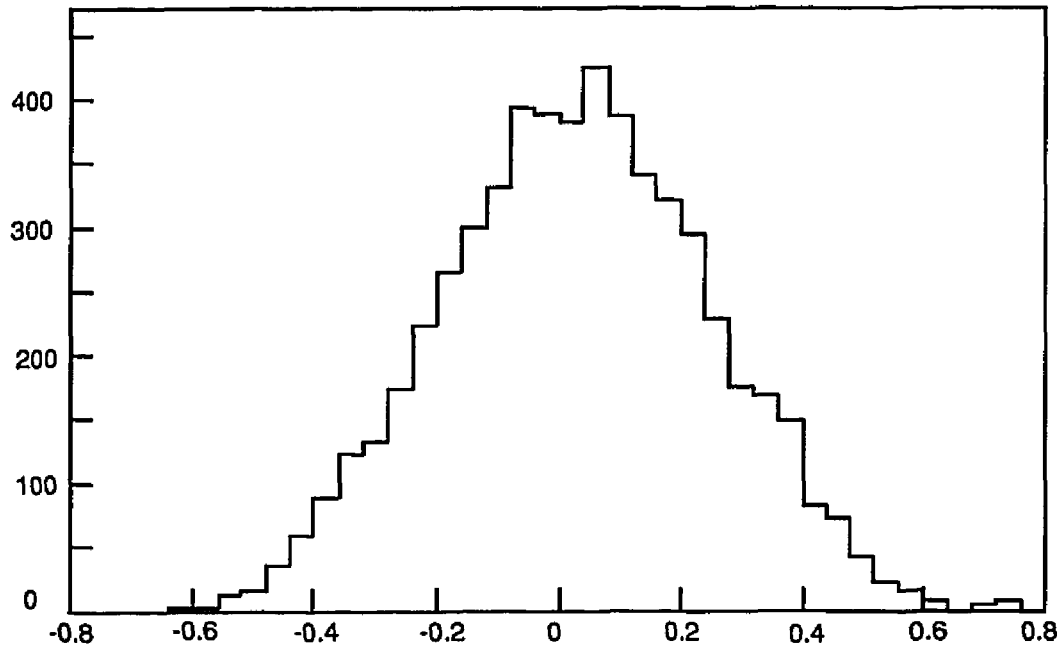


Figure 43.



Momentum asymmetry for the Minimum Bias sample.

Figure 44.

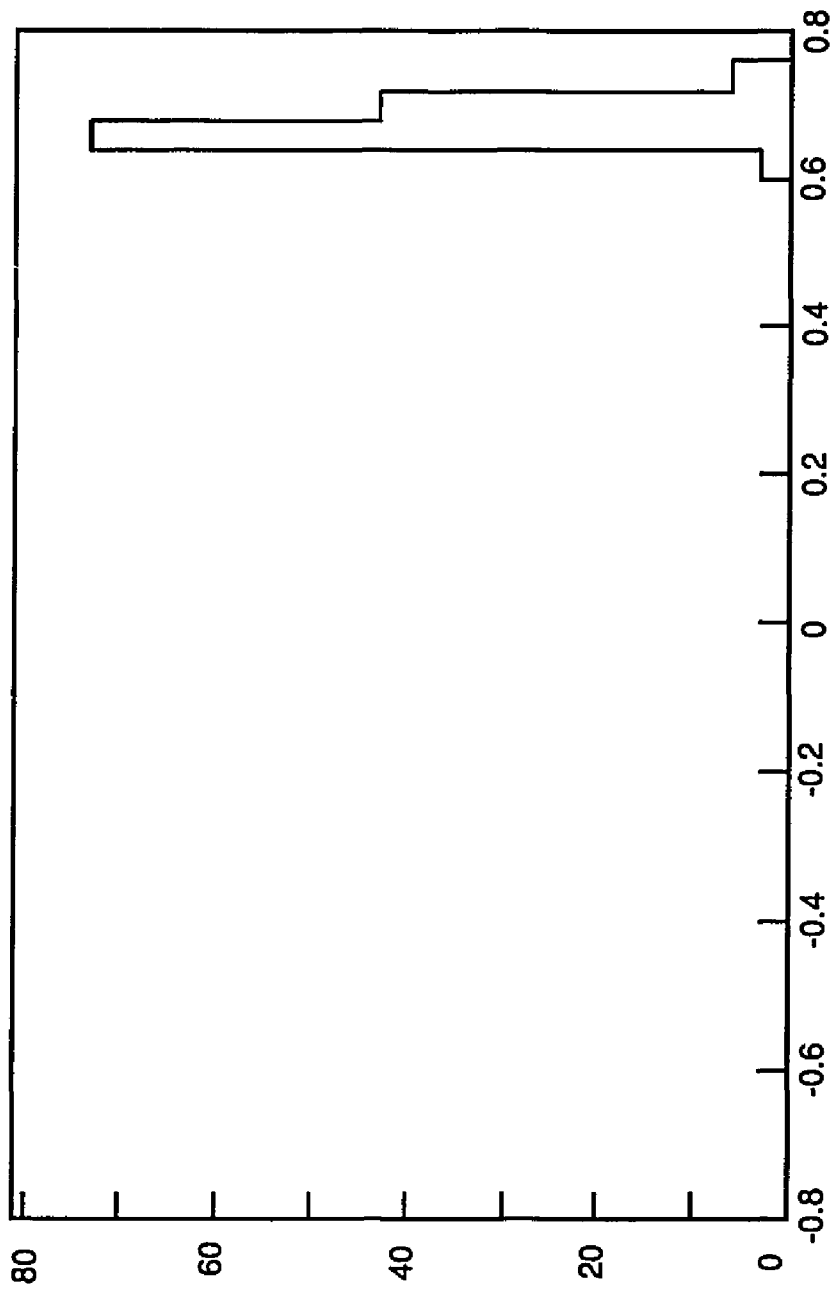
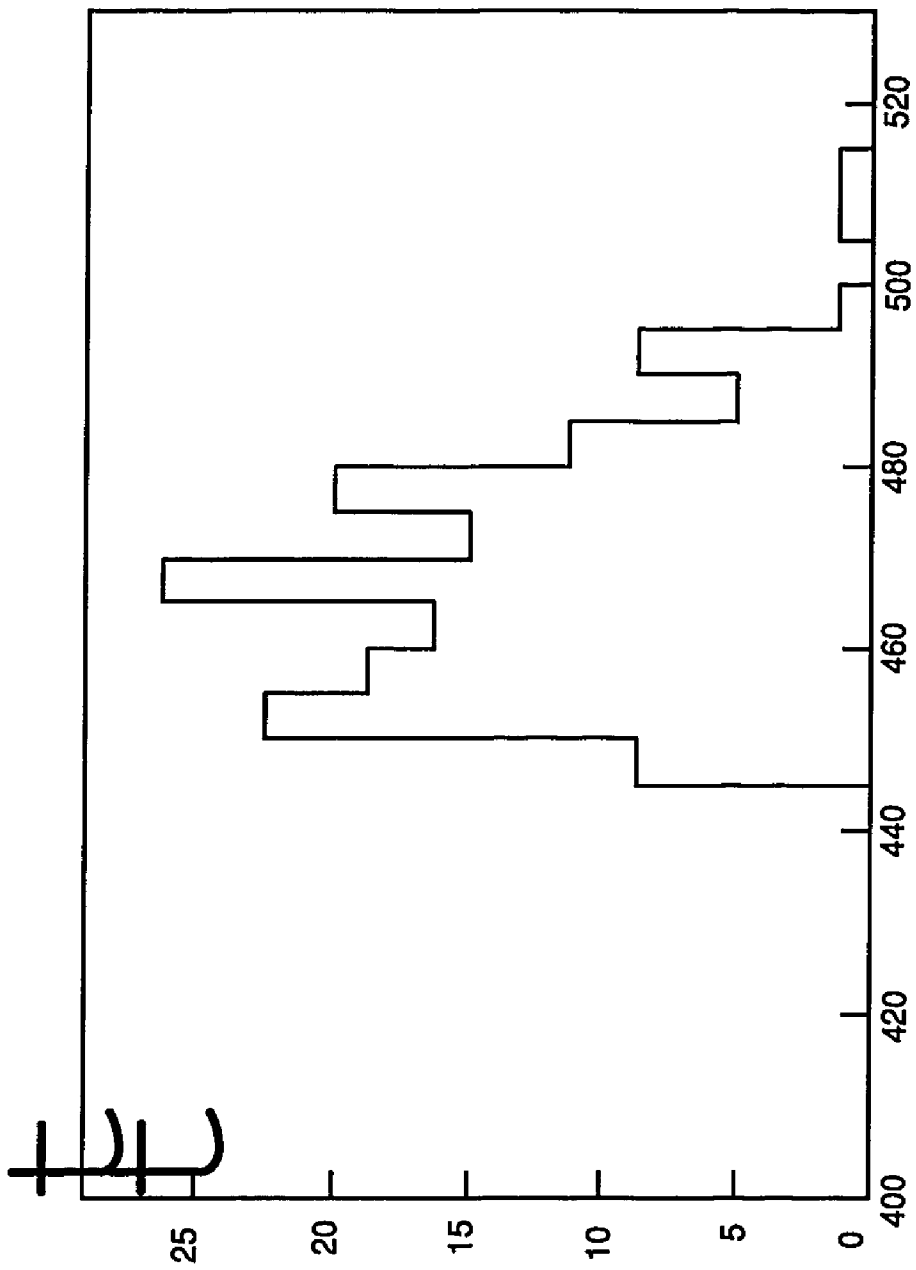


Figure 45.



Invariant mass of Λ^0 events (MeV/c^2)

Figure 46.

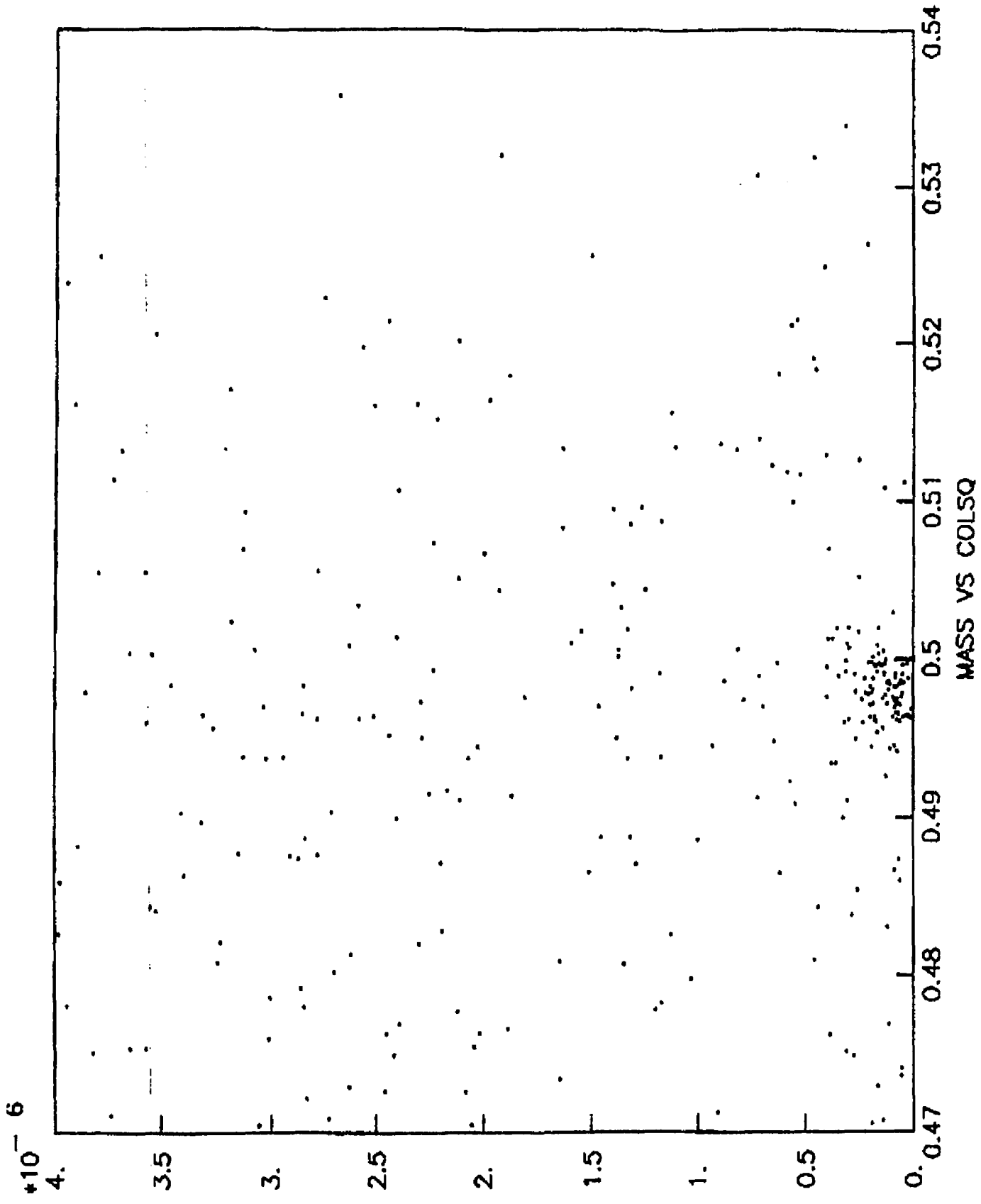


Figure 47

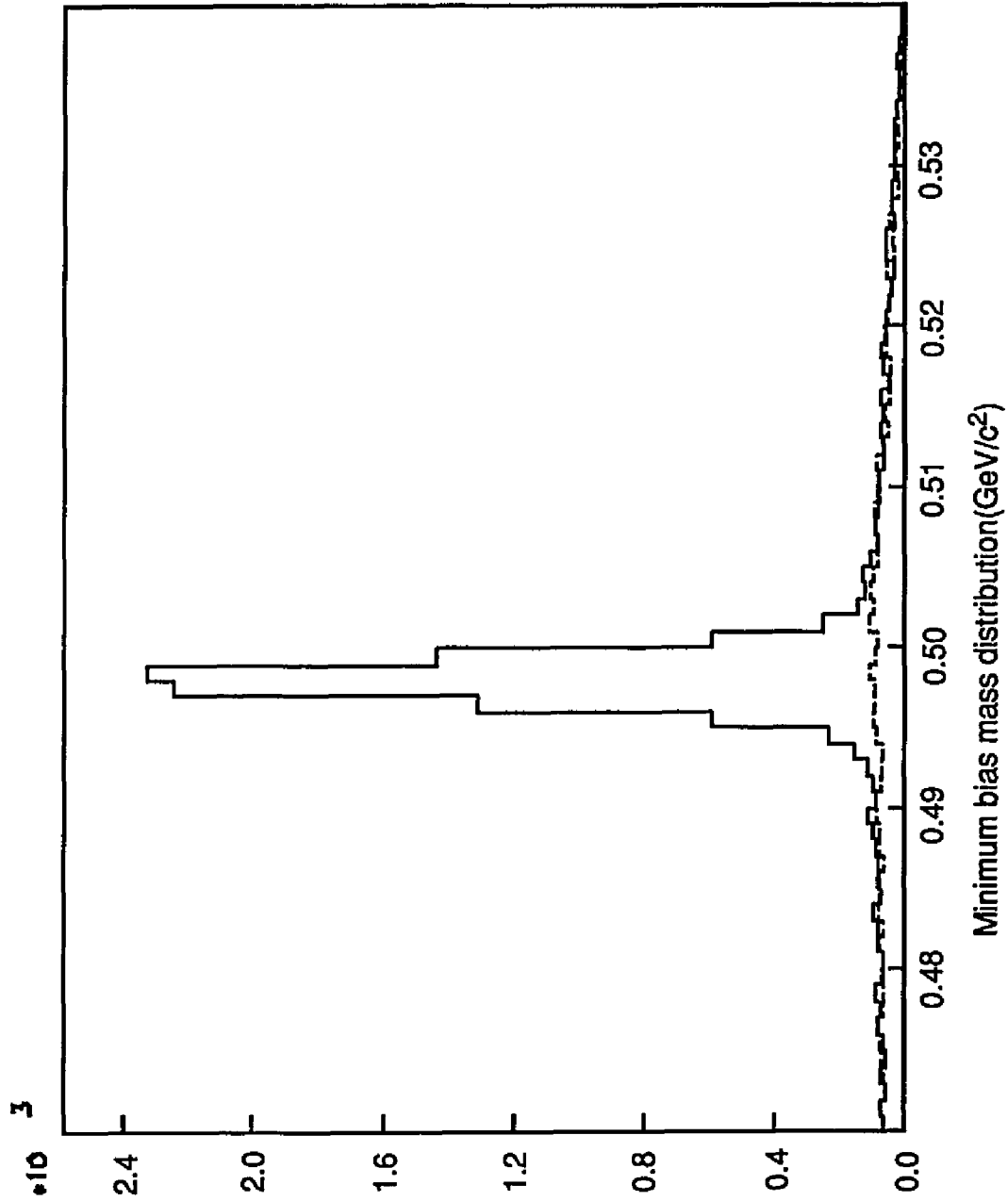
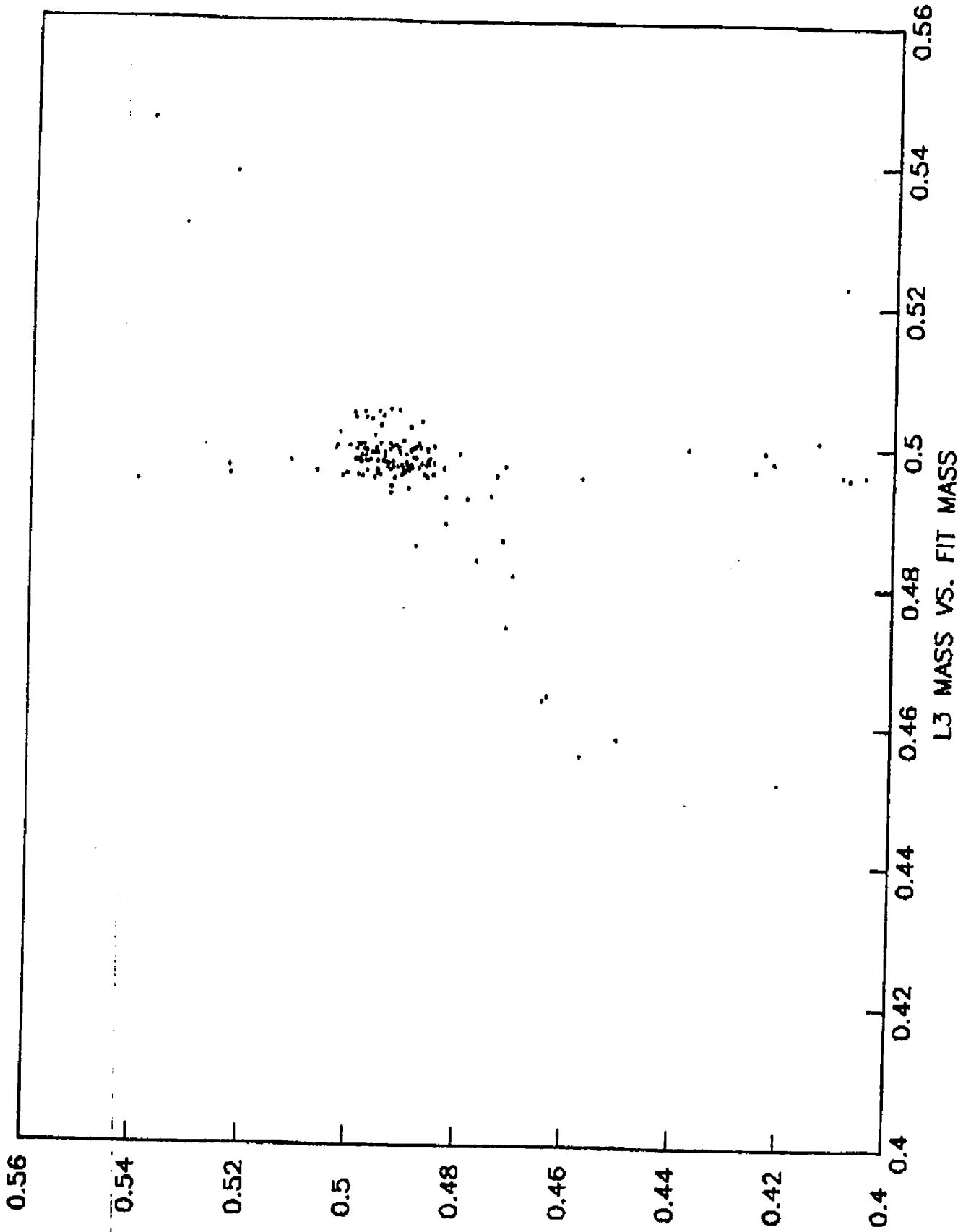


Figure 48.



L3 MASS VS. FIT MASS

Figure 49

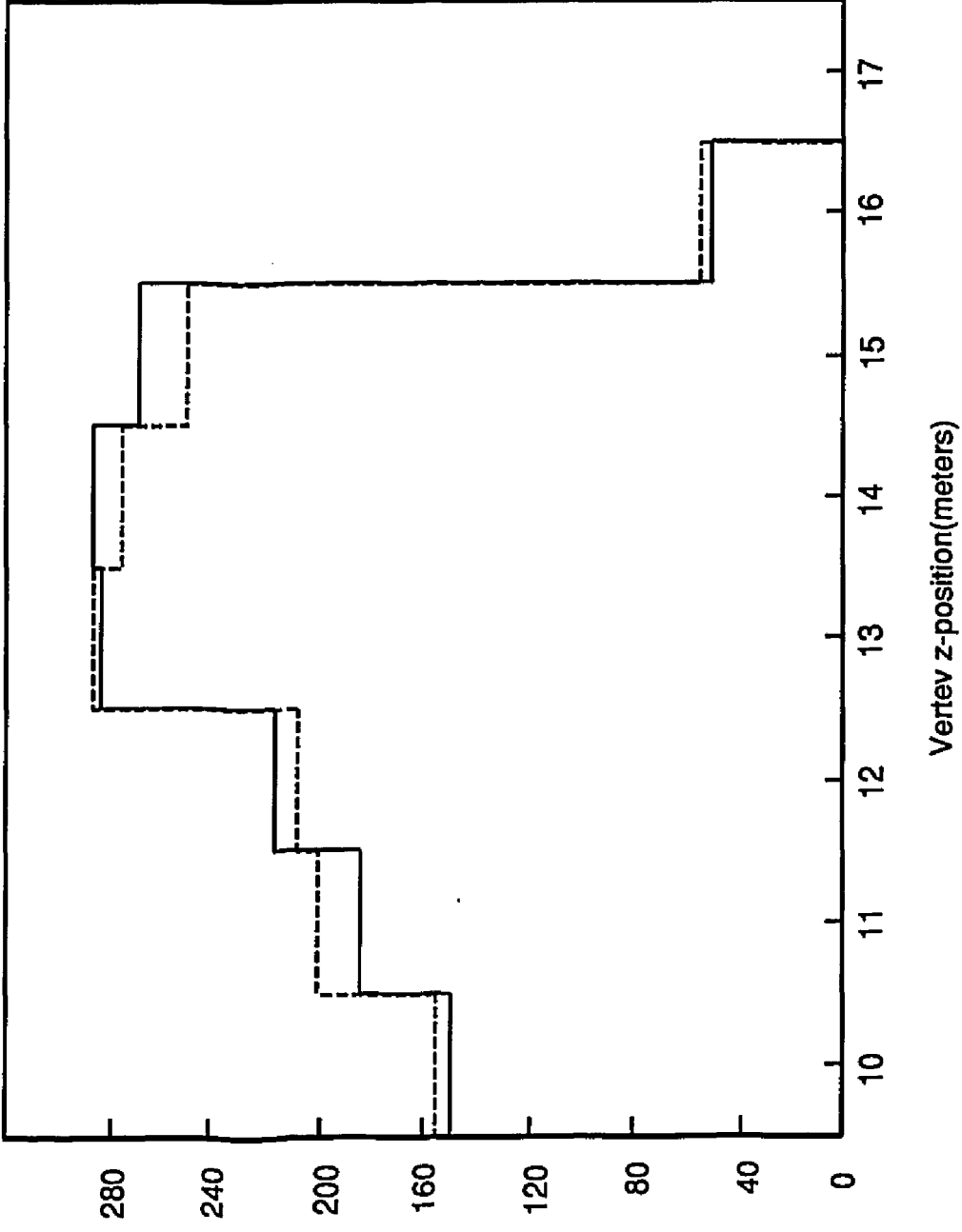


Figure 50.

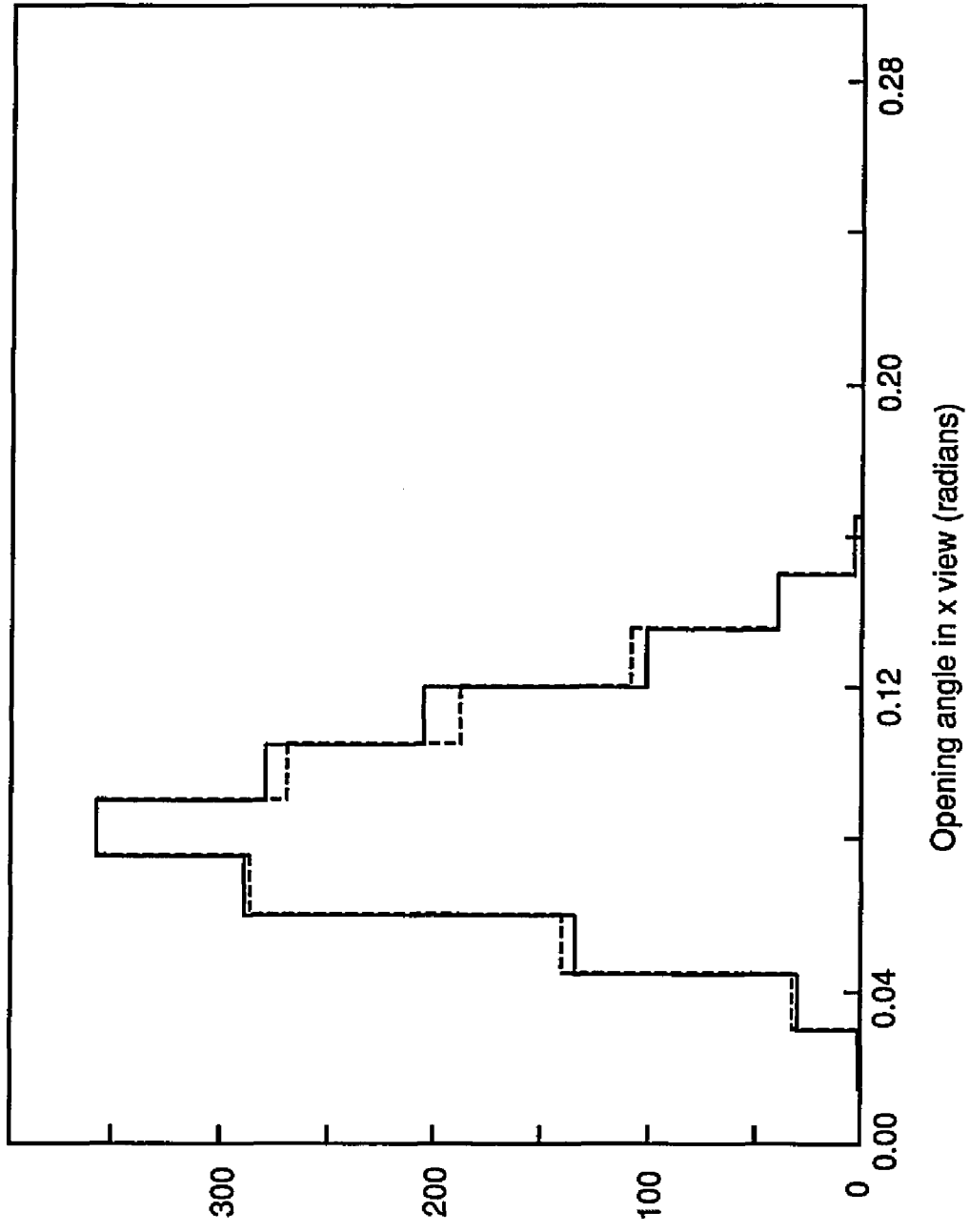


Figure 51.

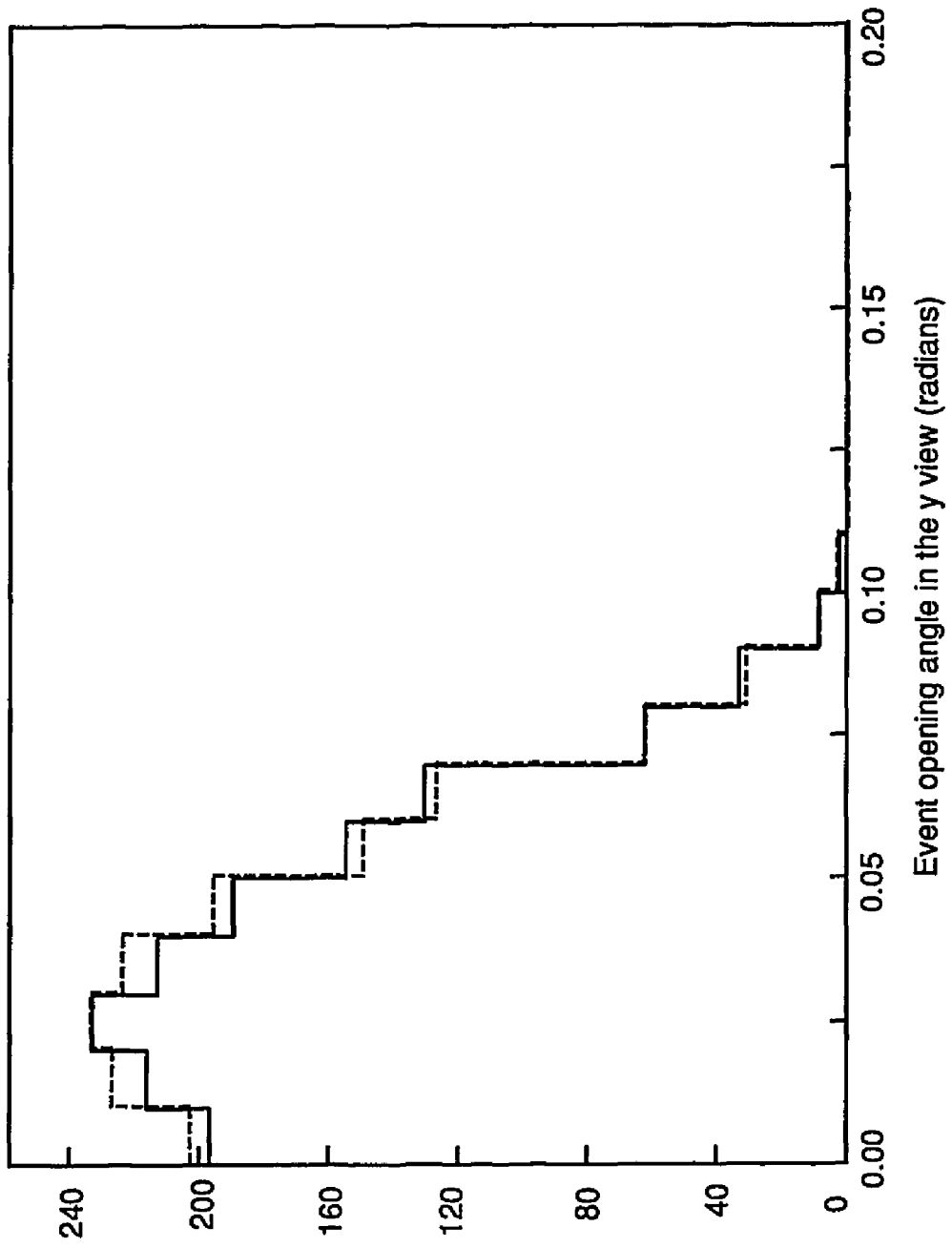
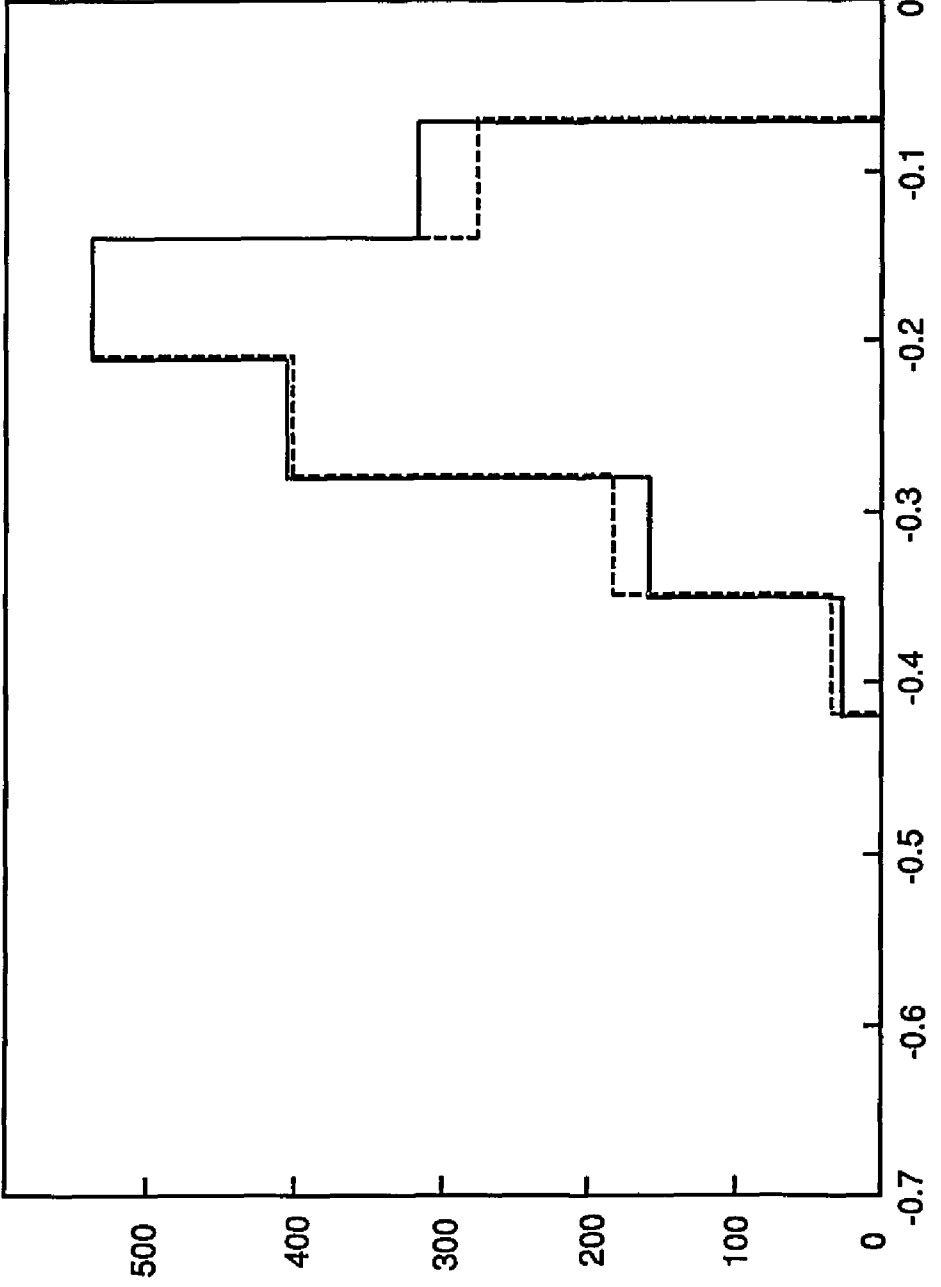
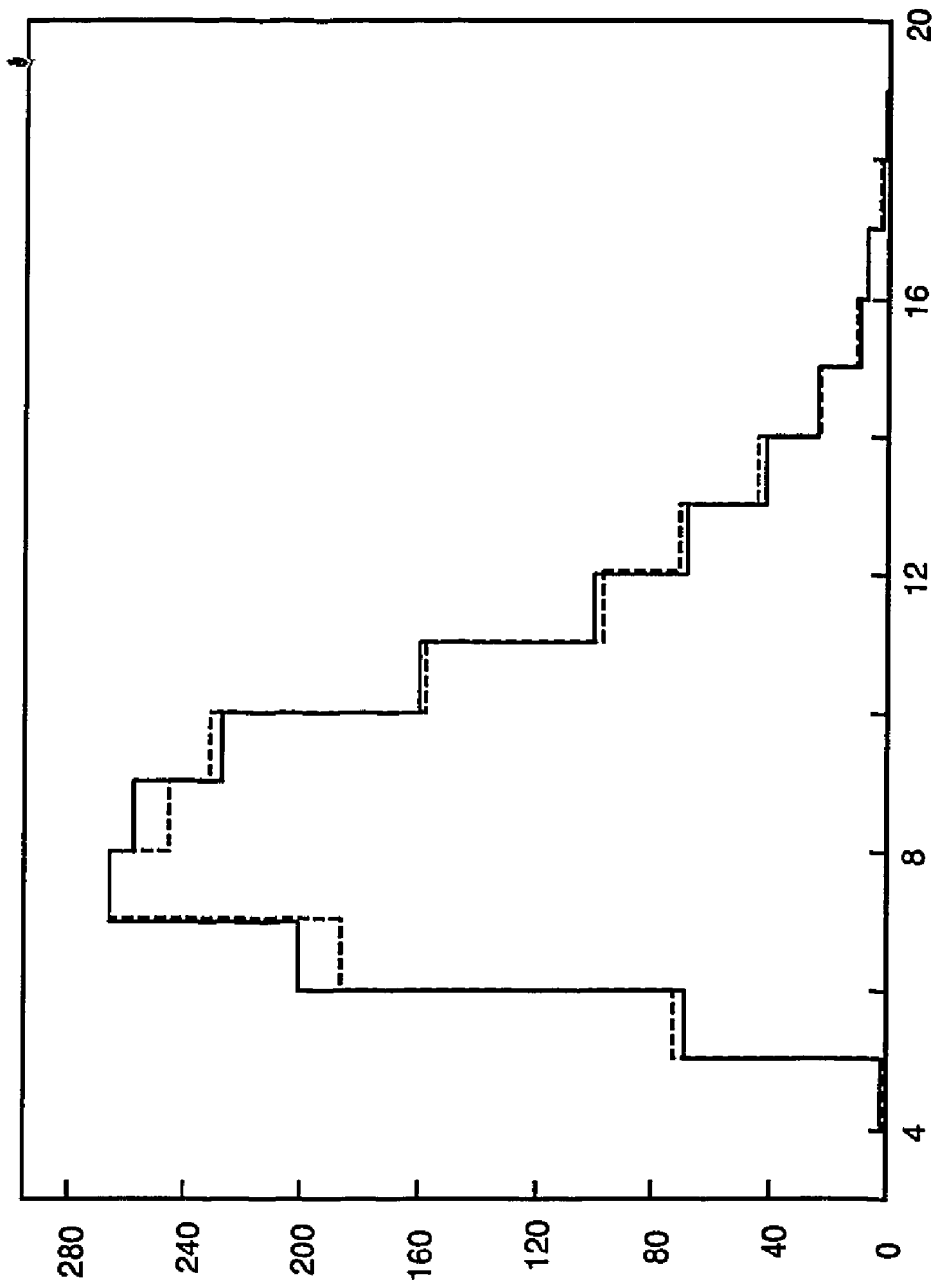


Figure 52.



X-position at 1st drift chamber(meters)

Figure 53.



Kaon momentum (GeV/c)

Figure 54.

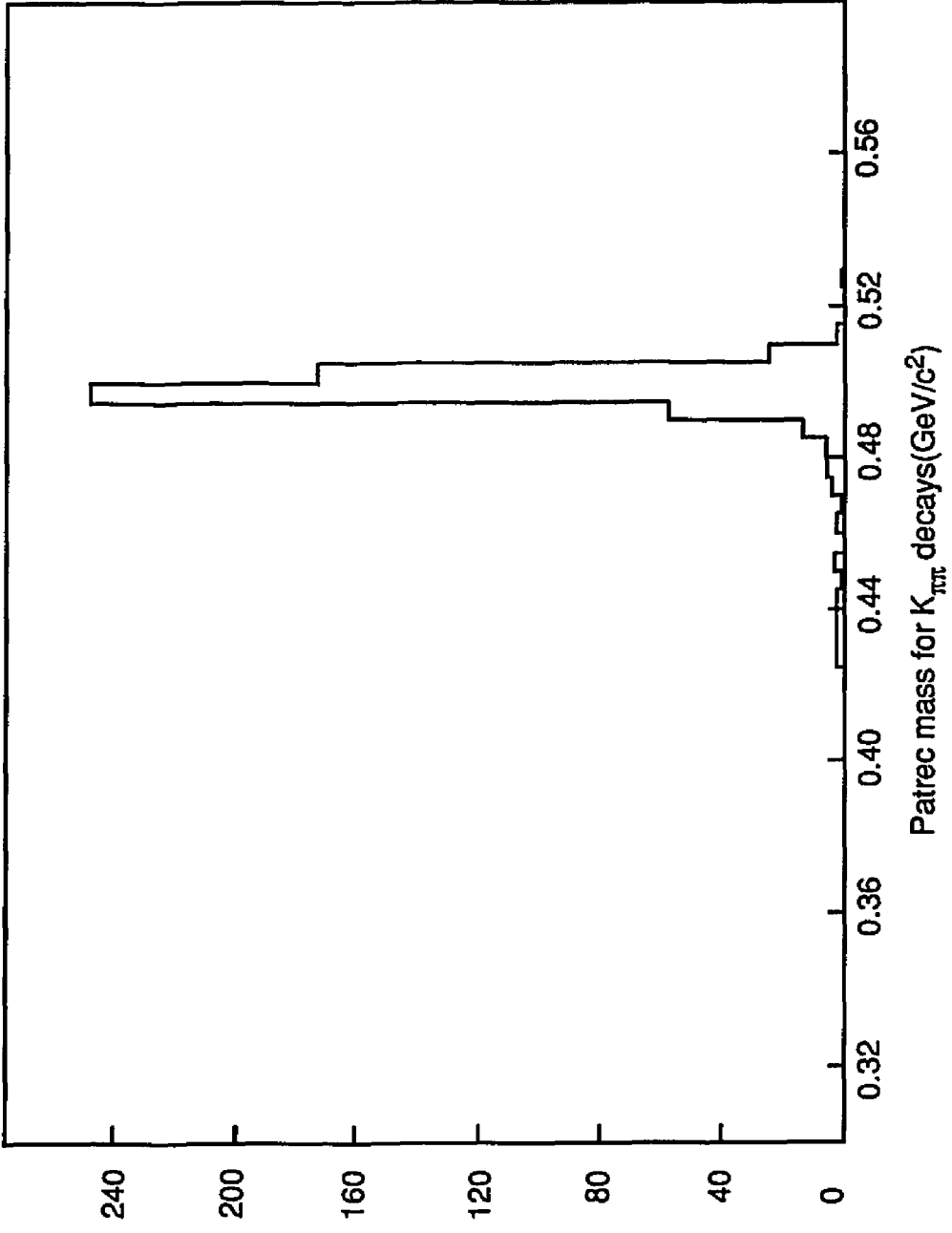


Figure 55.

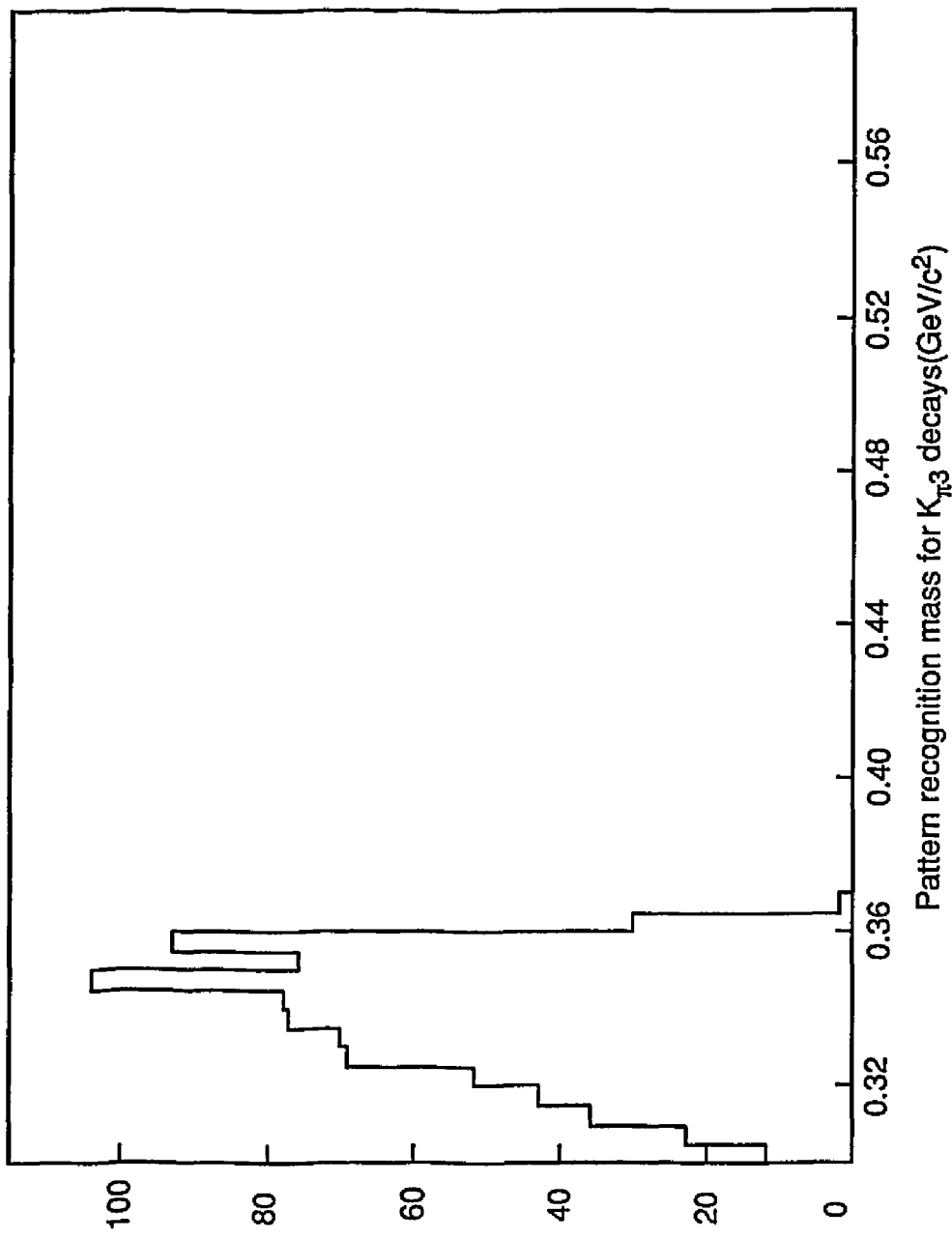


Figure 56.

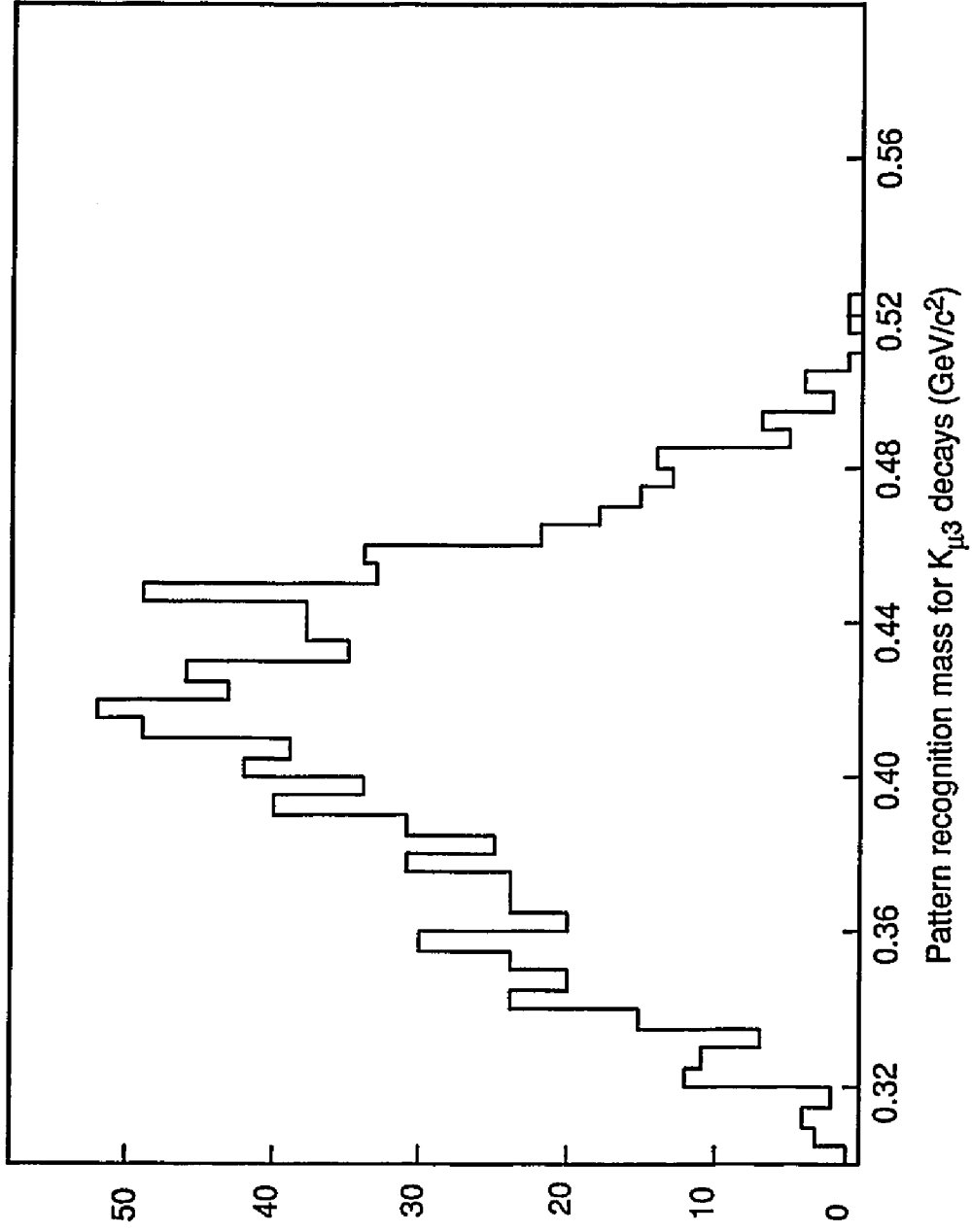


Figure 57.

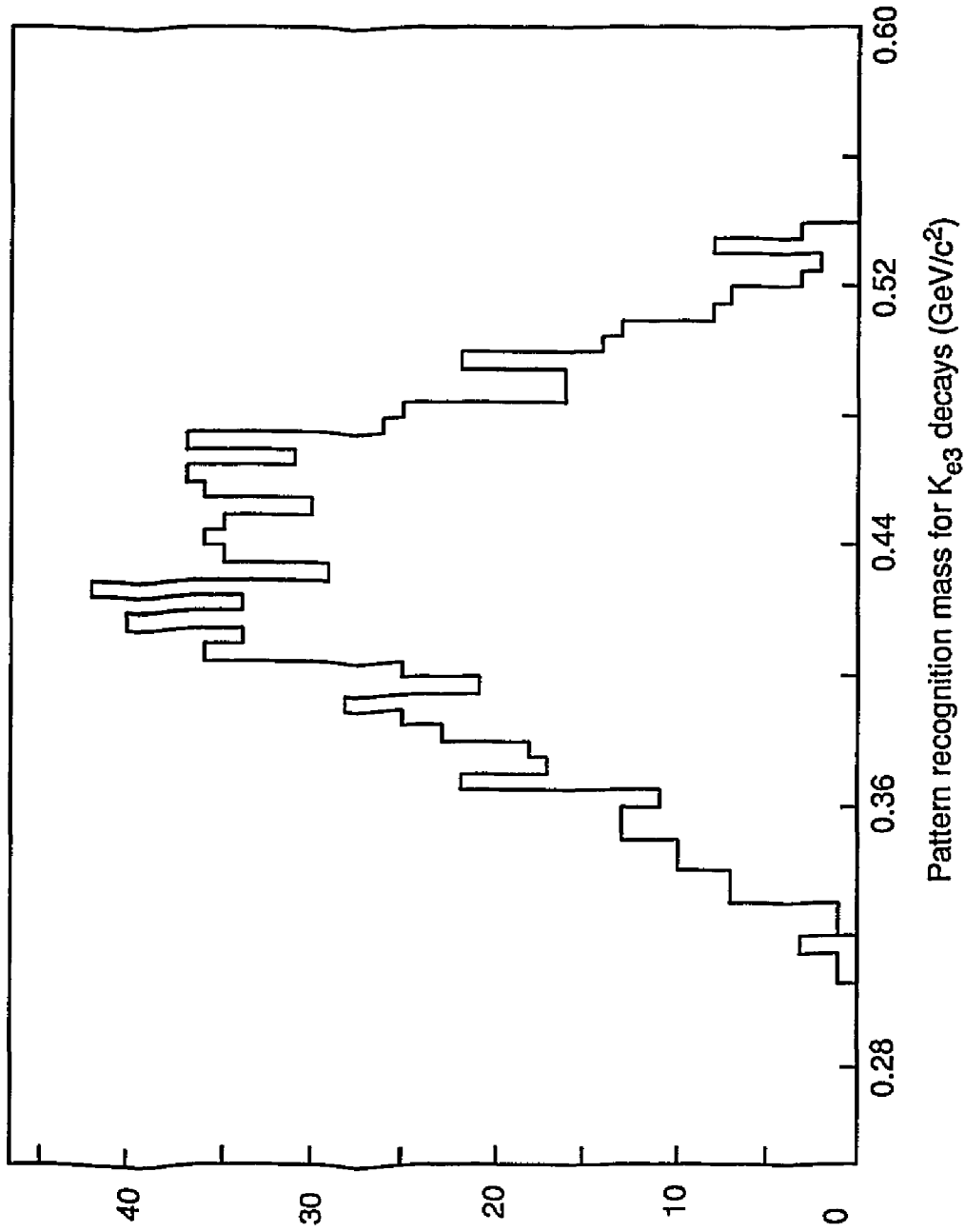


Figure 58.

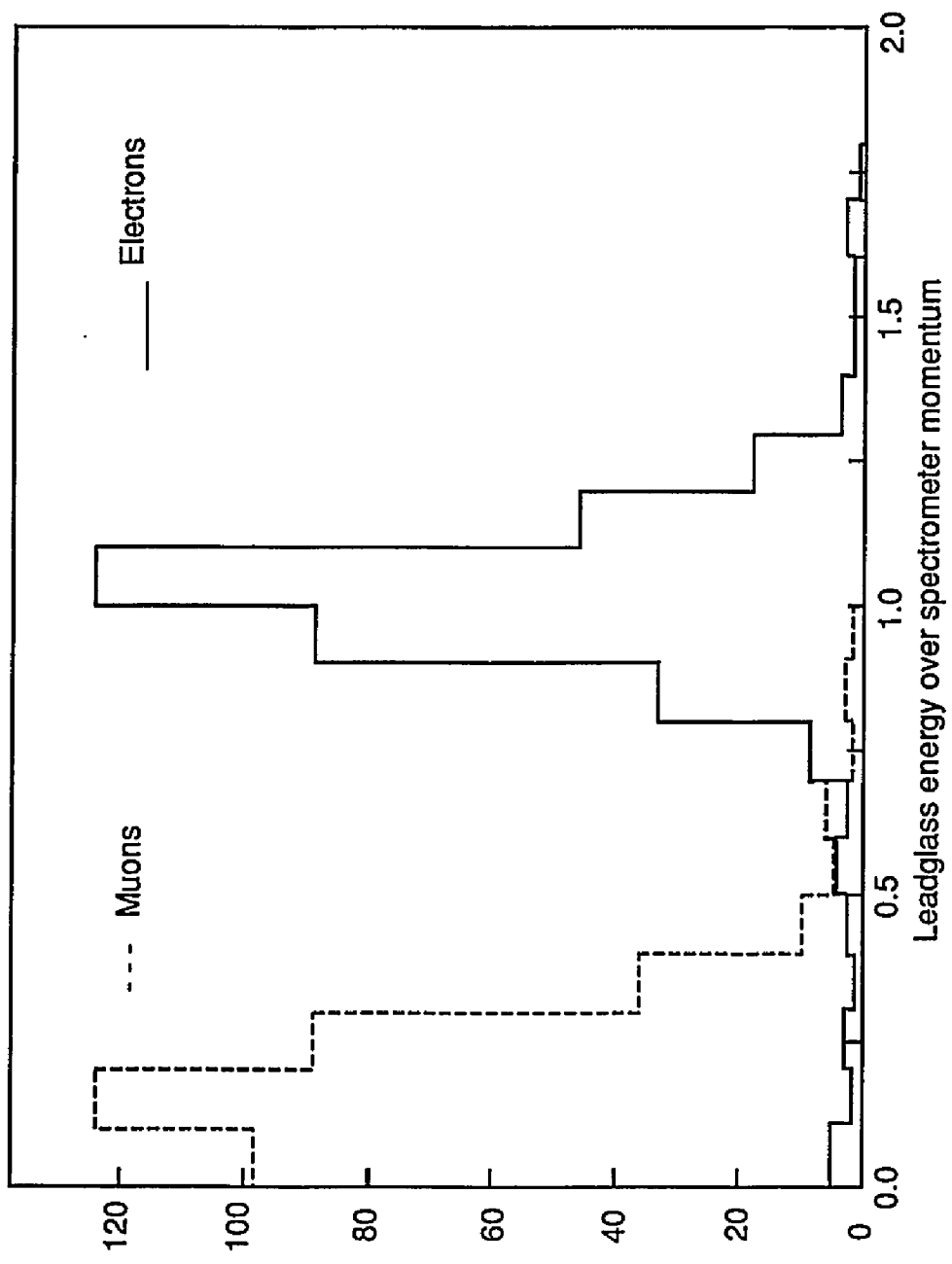
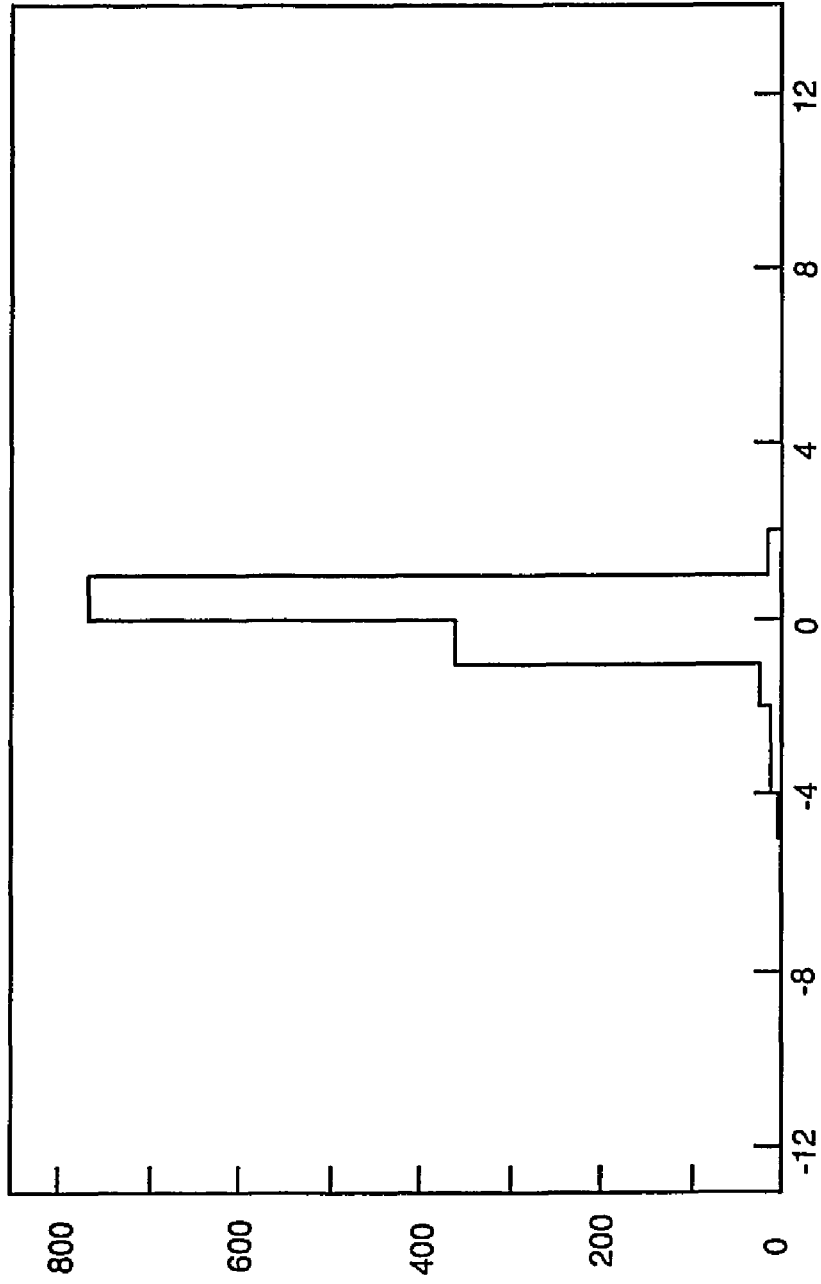
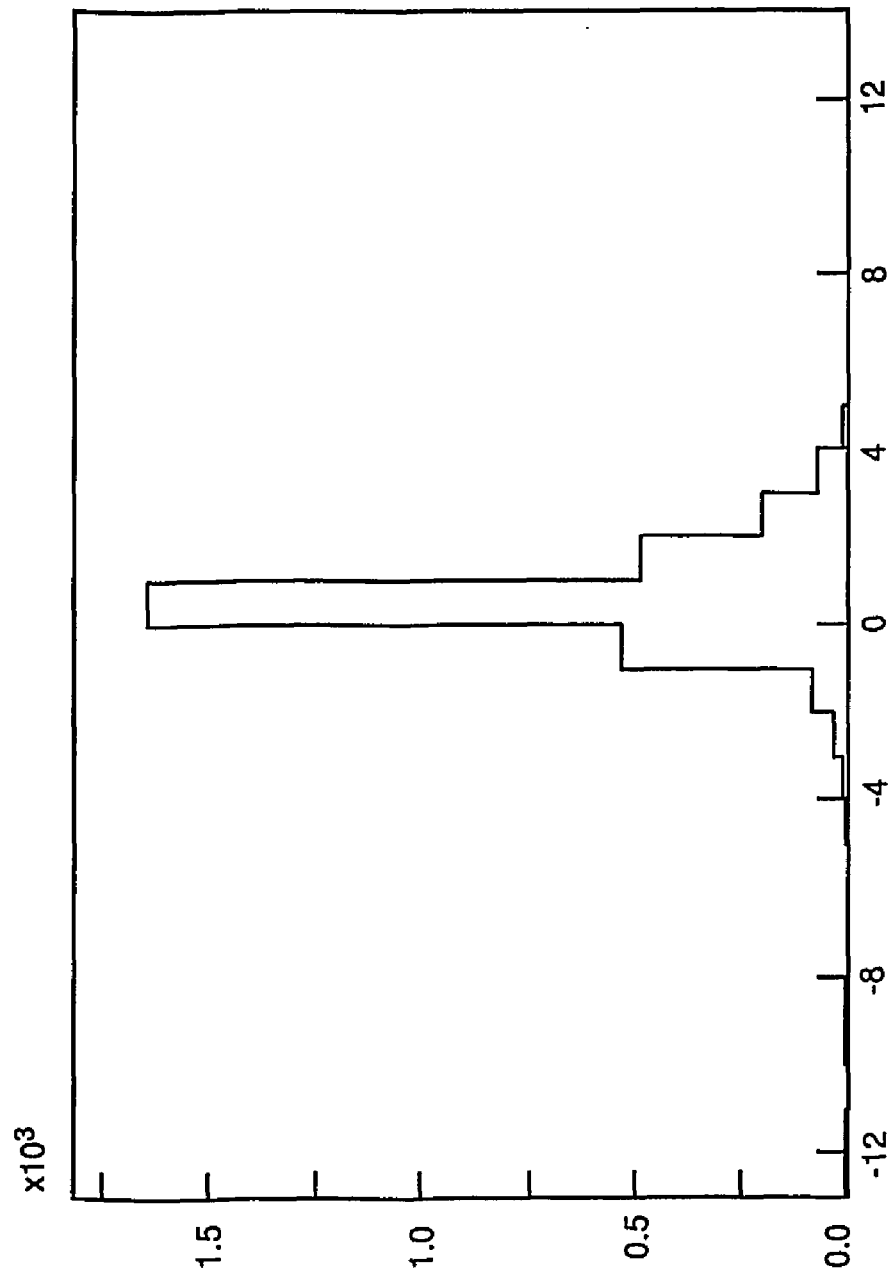


Figure 59.



GEANT simulation of differential gap distribution for K_{μ} decays

Figure 60.



Differential gap distribution for $K_{\mu 3}$ muon data sample

Figure 61.

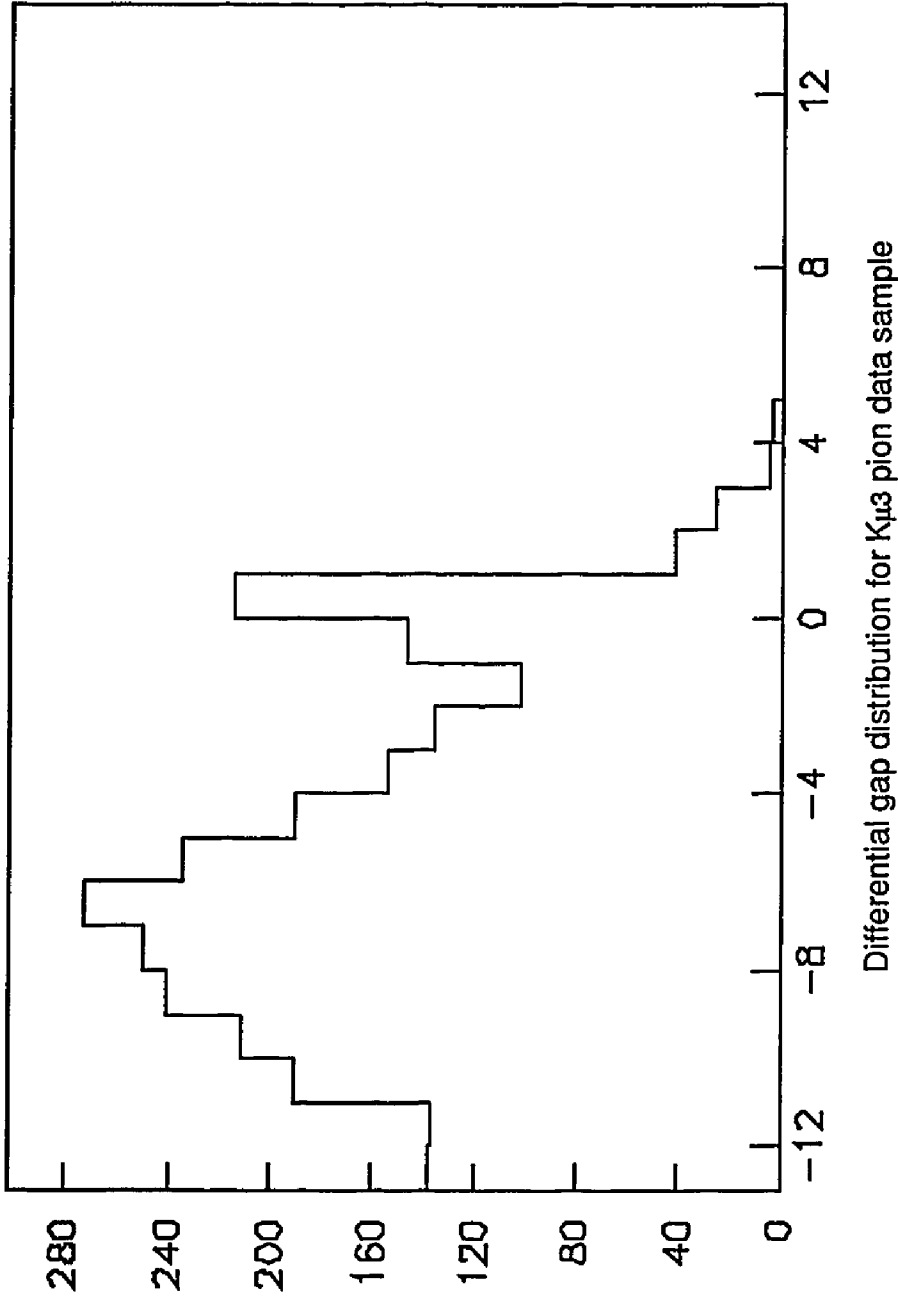
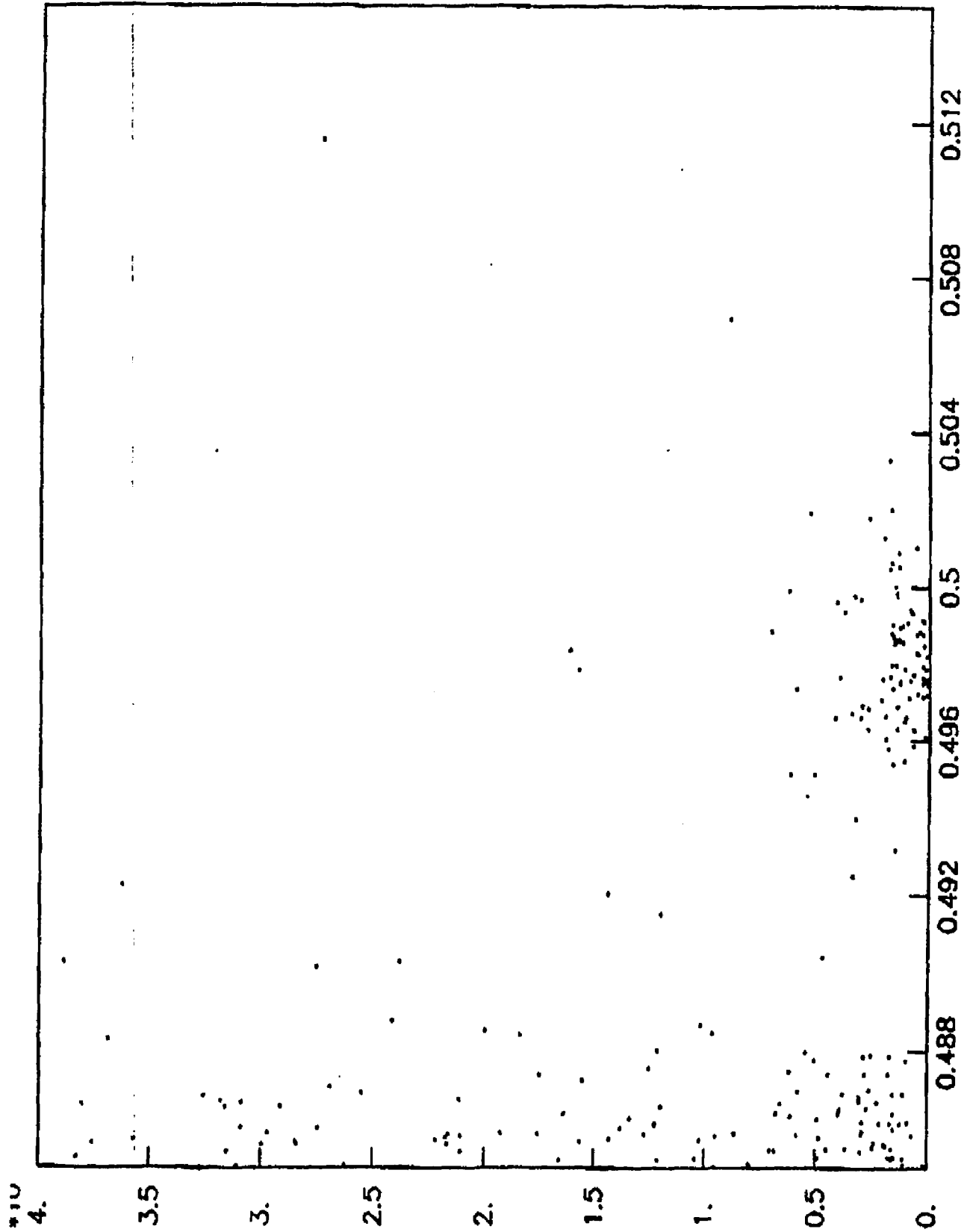


Figure 62.



MASS VS COLSQ

Figure 63

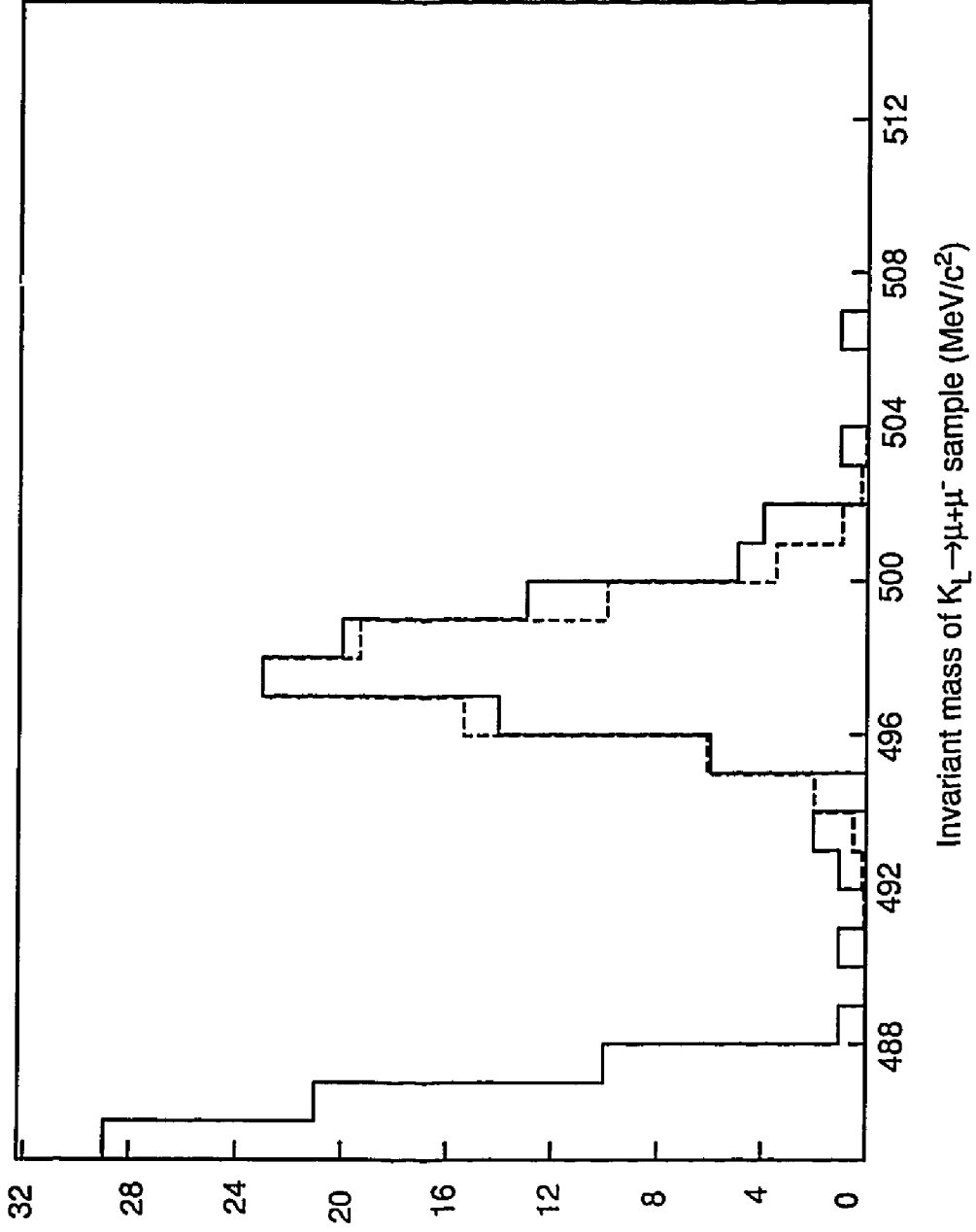


Figure 64.

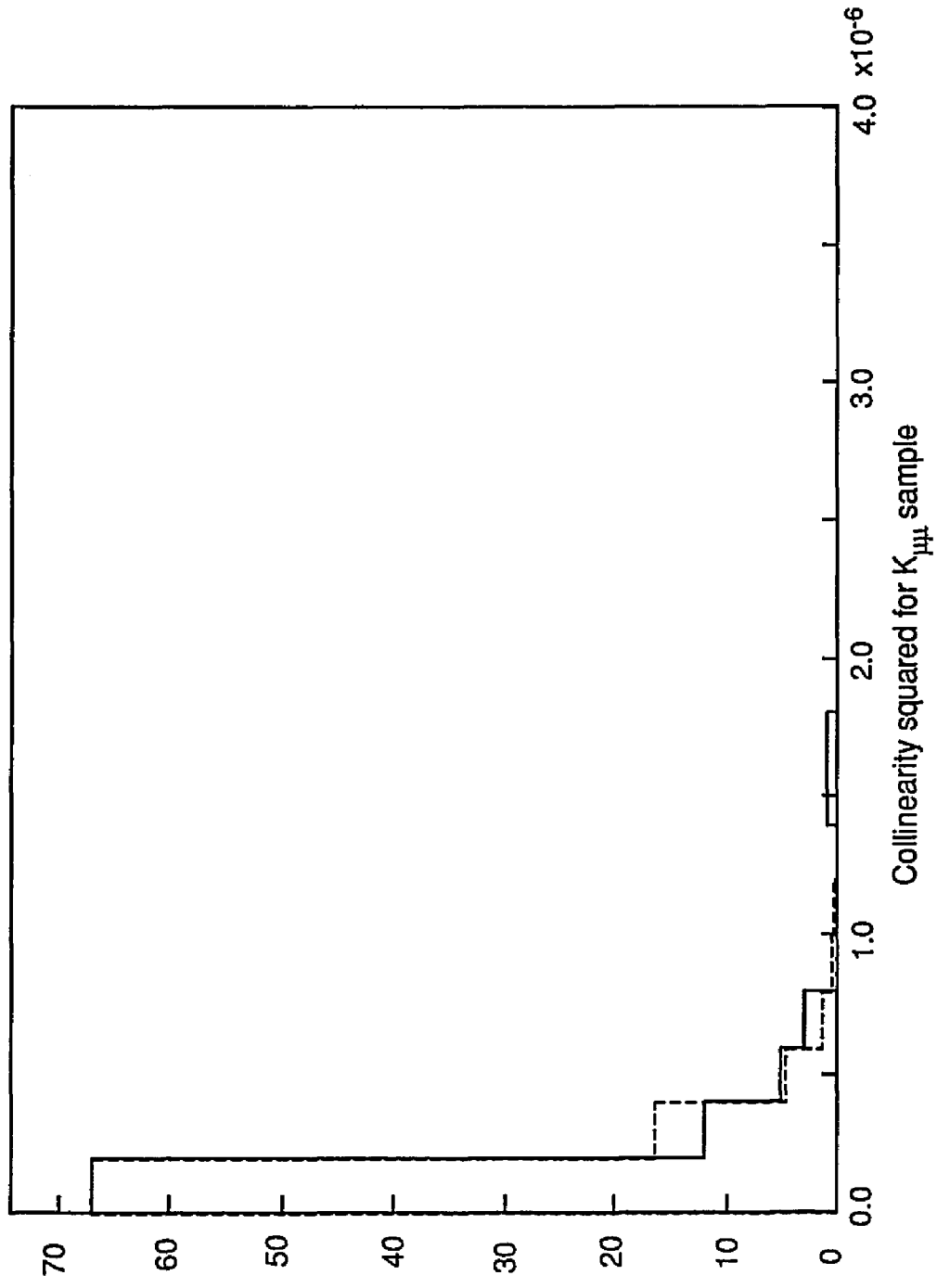


Figure 65.

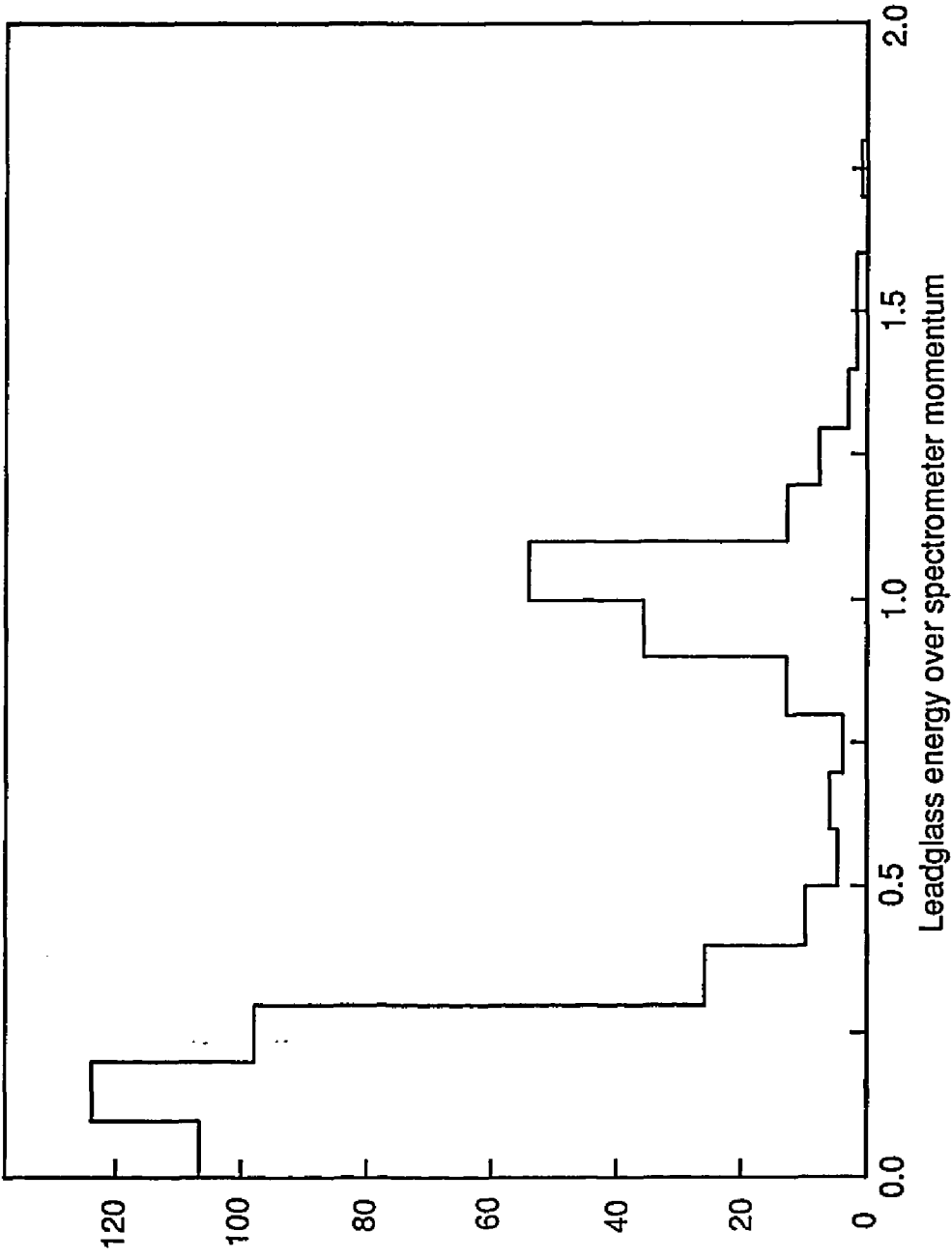


Figure 66.

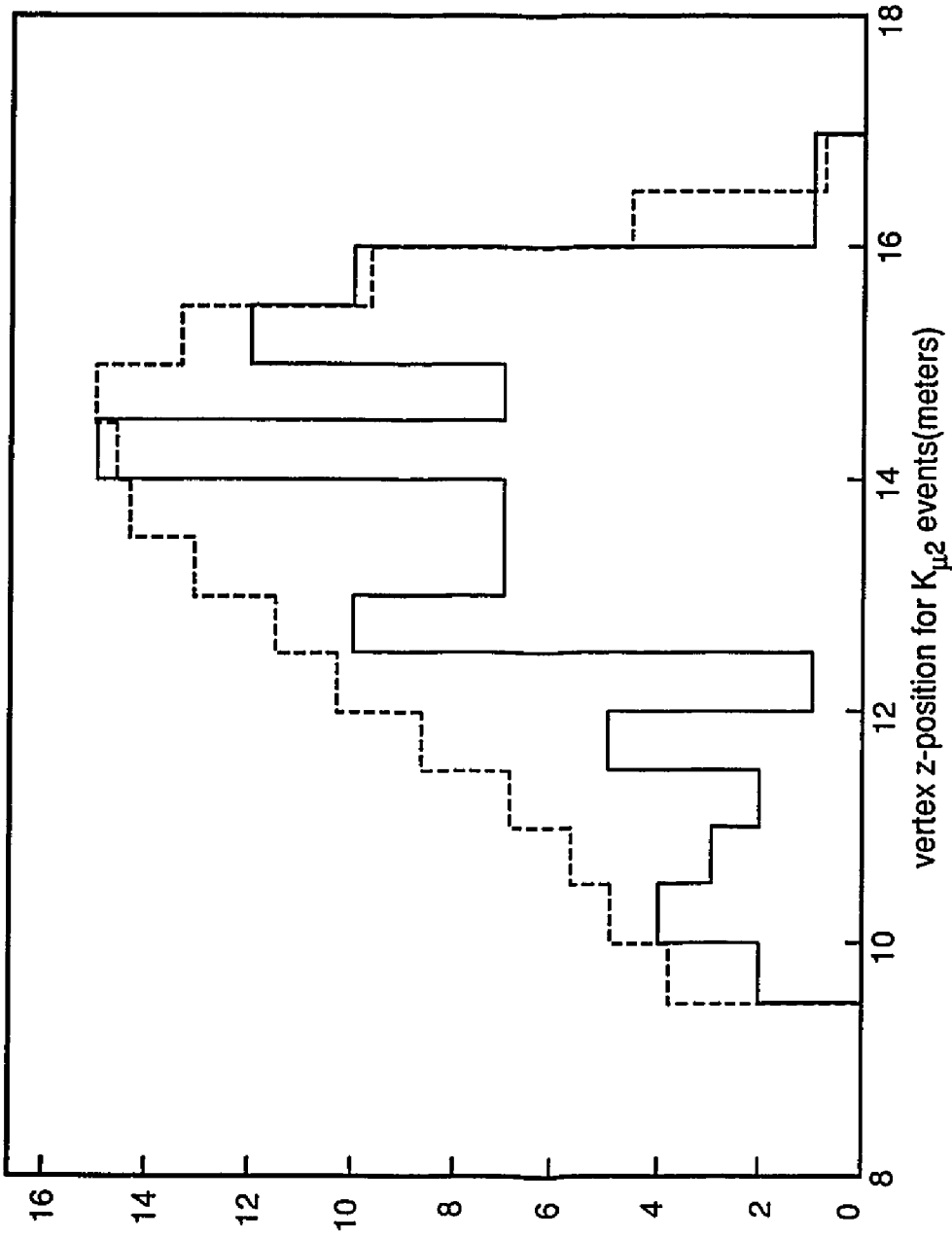


Figure 67.

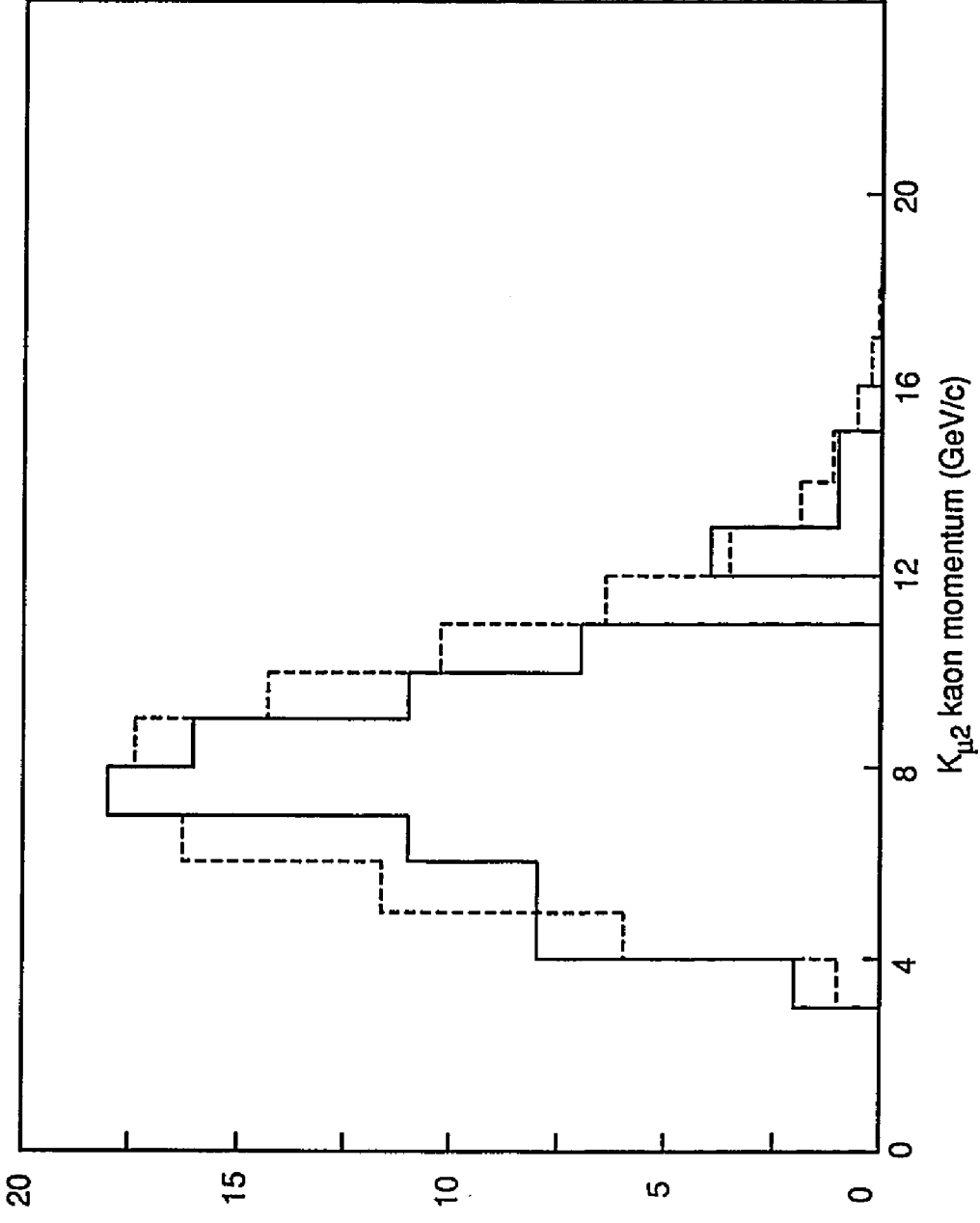


Figure 68.

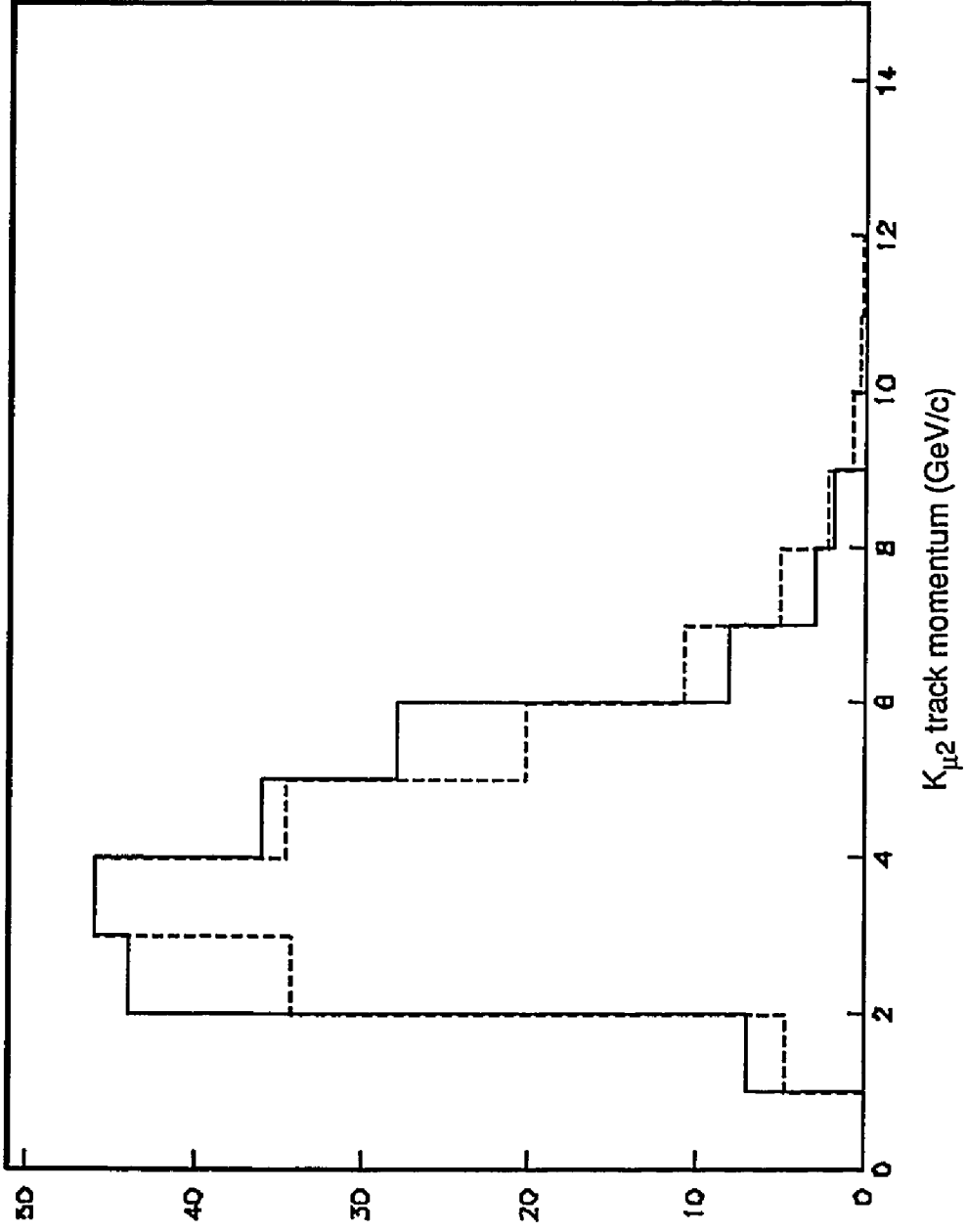


Figure 69.

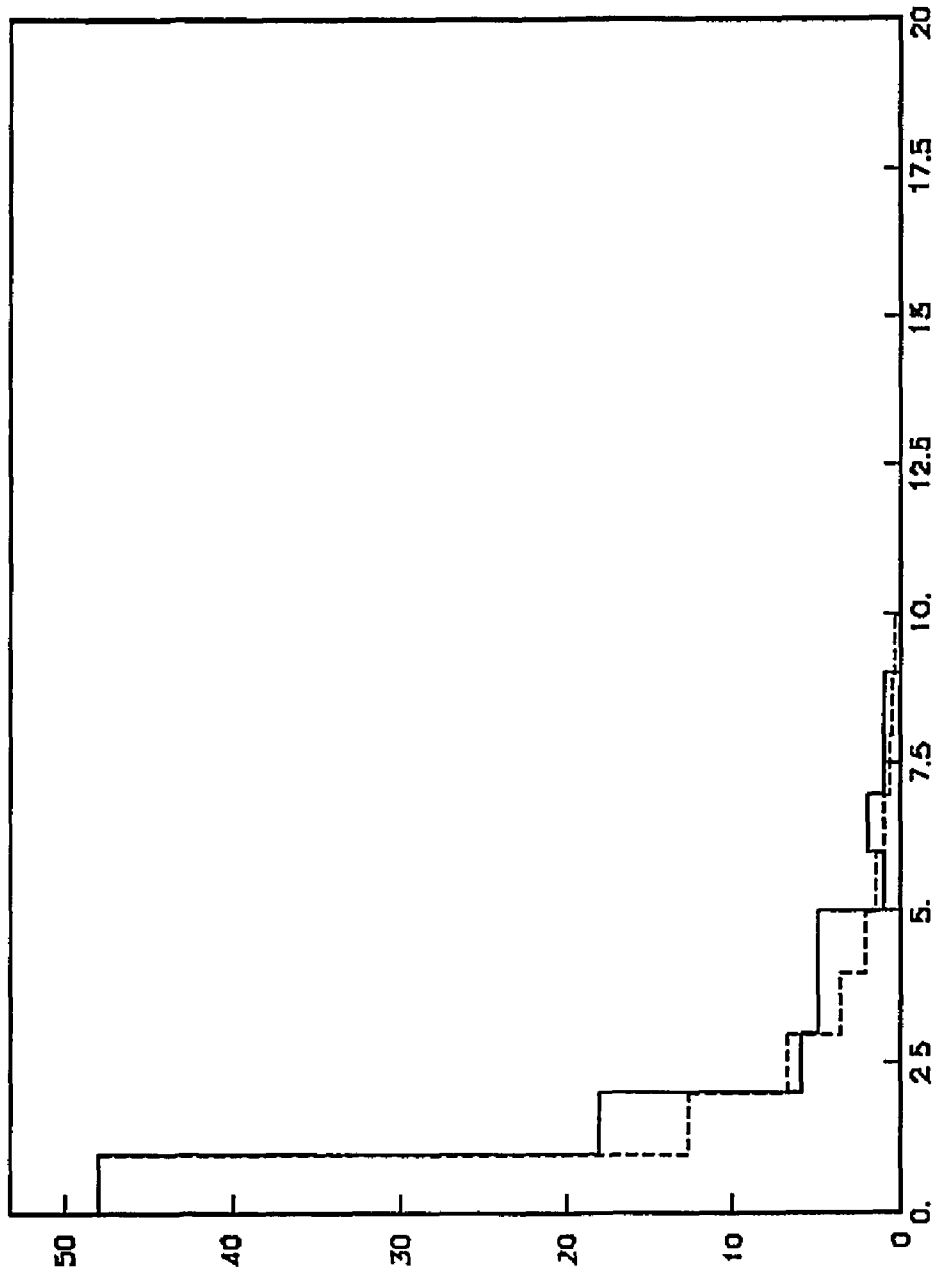
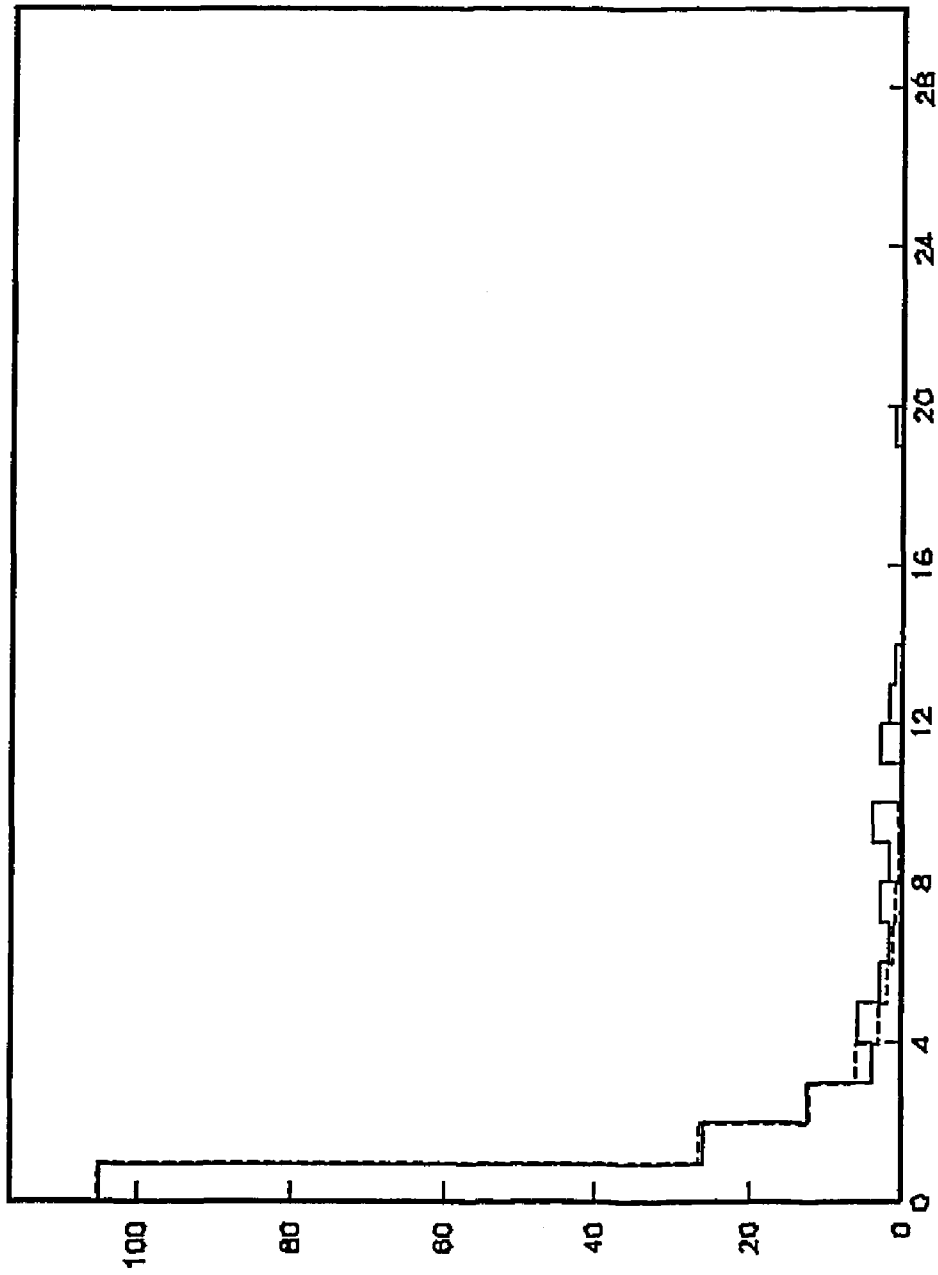


Figure 70.



X-view track χ^2 for $K_{\mu 2}$ sample

Figure 71.

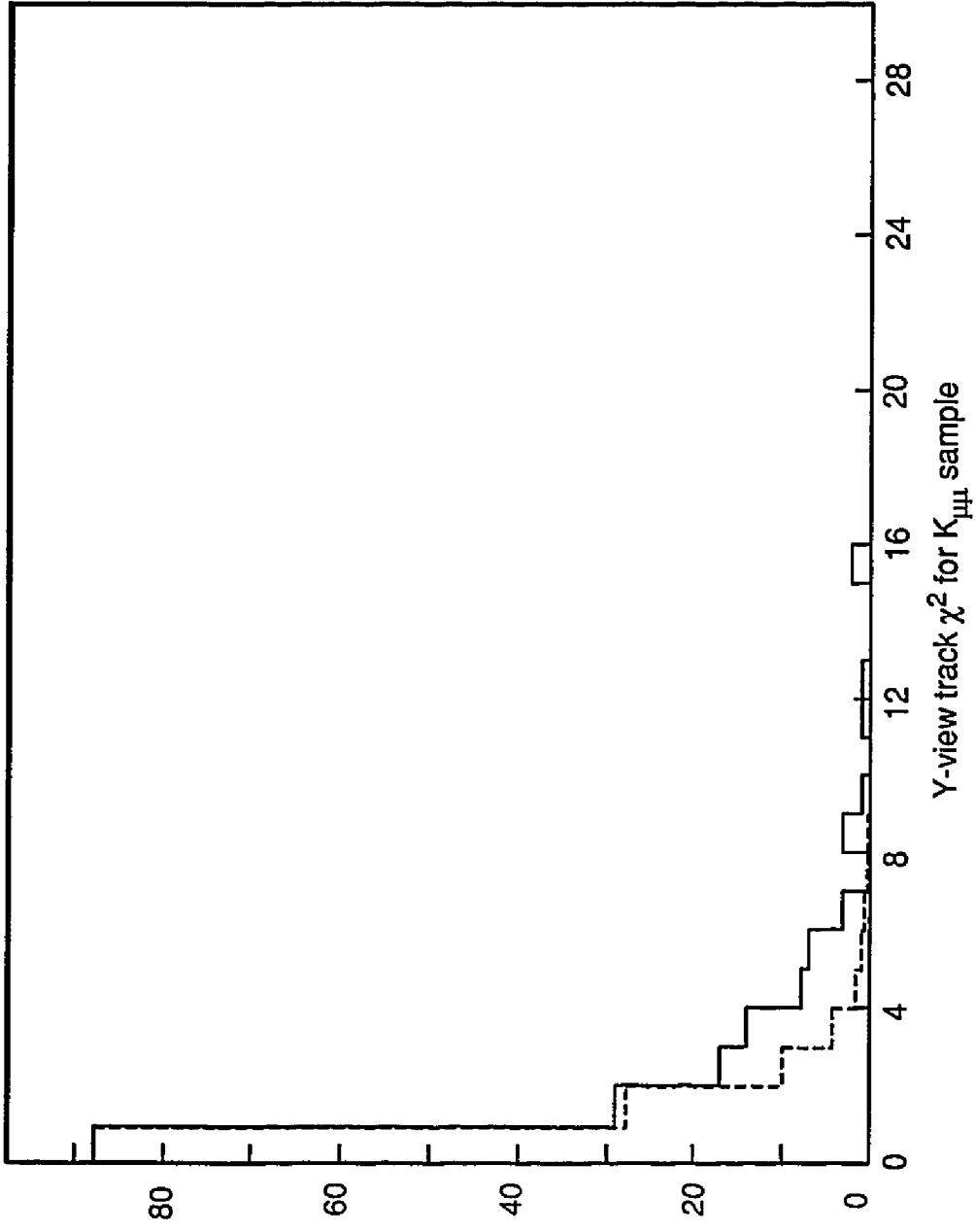


Figure 72.

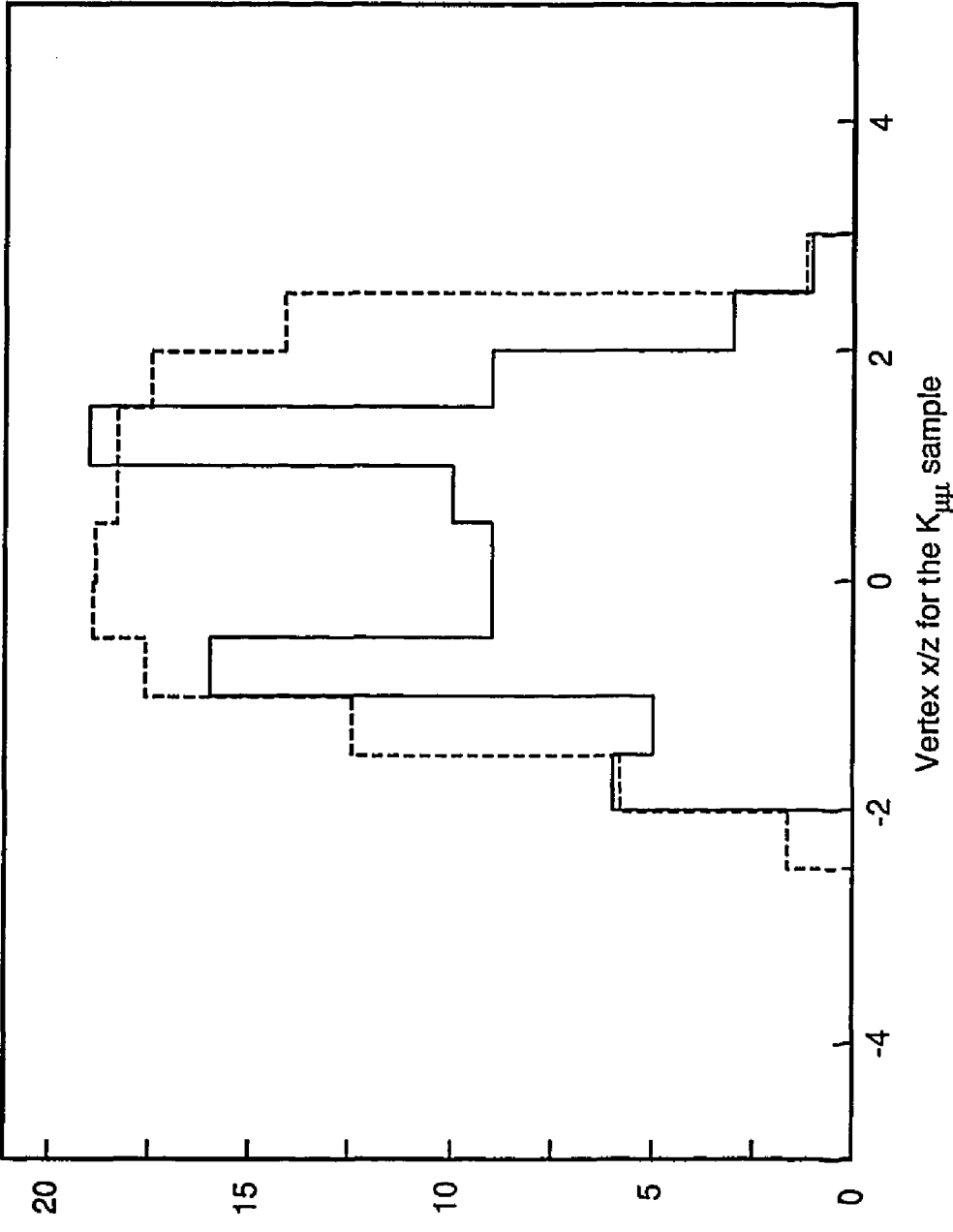


Figure 73.

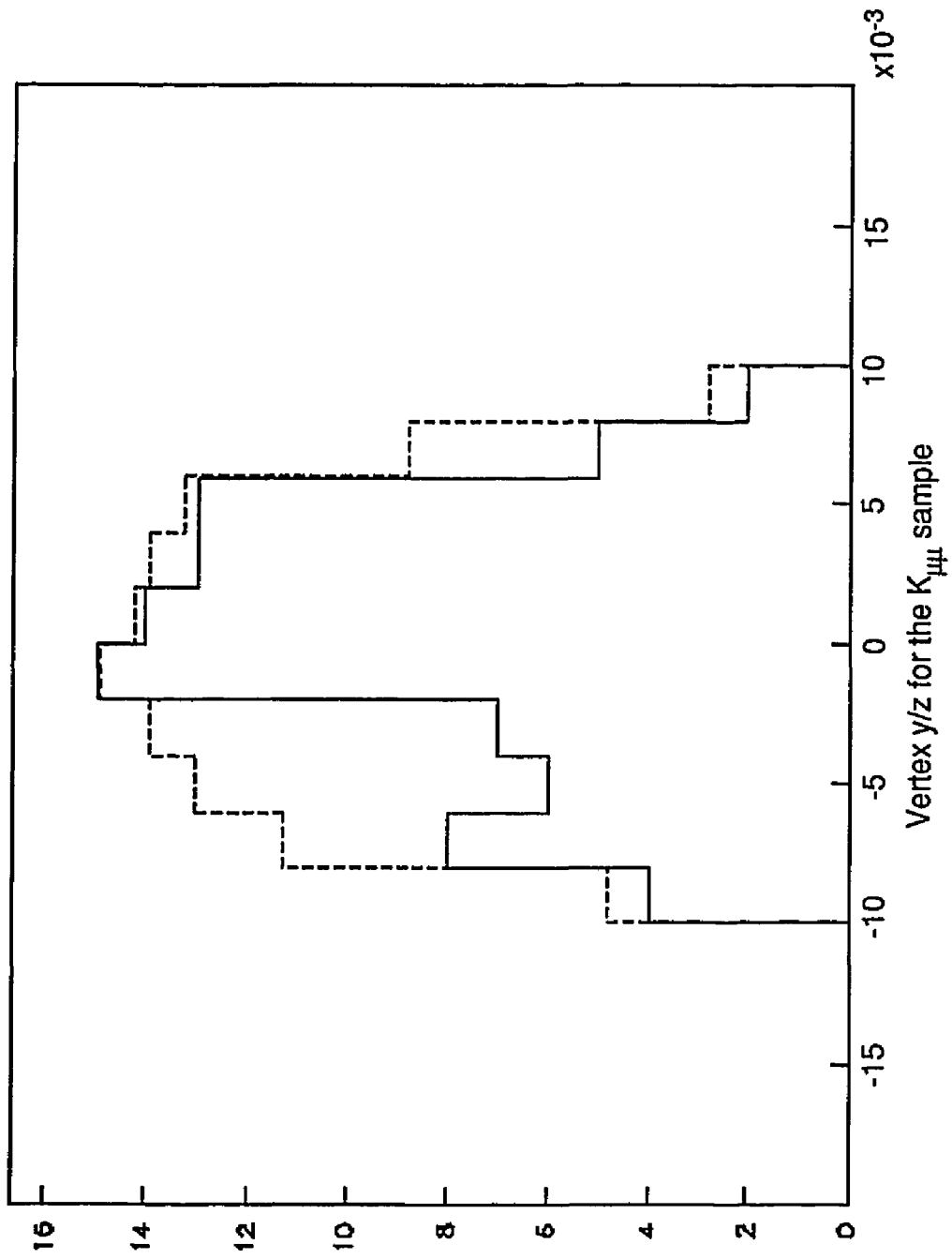


Figure 74.

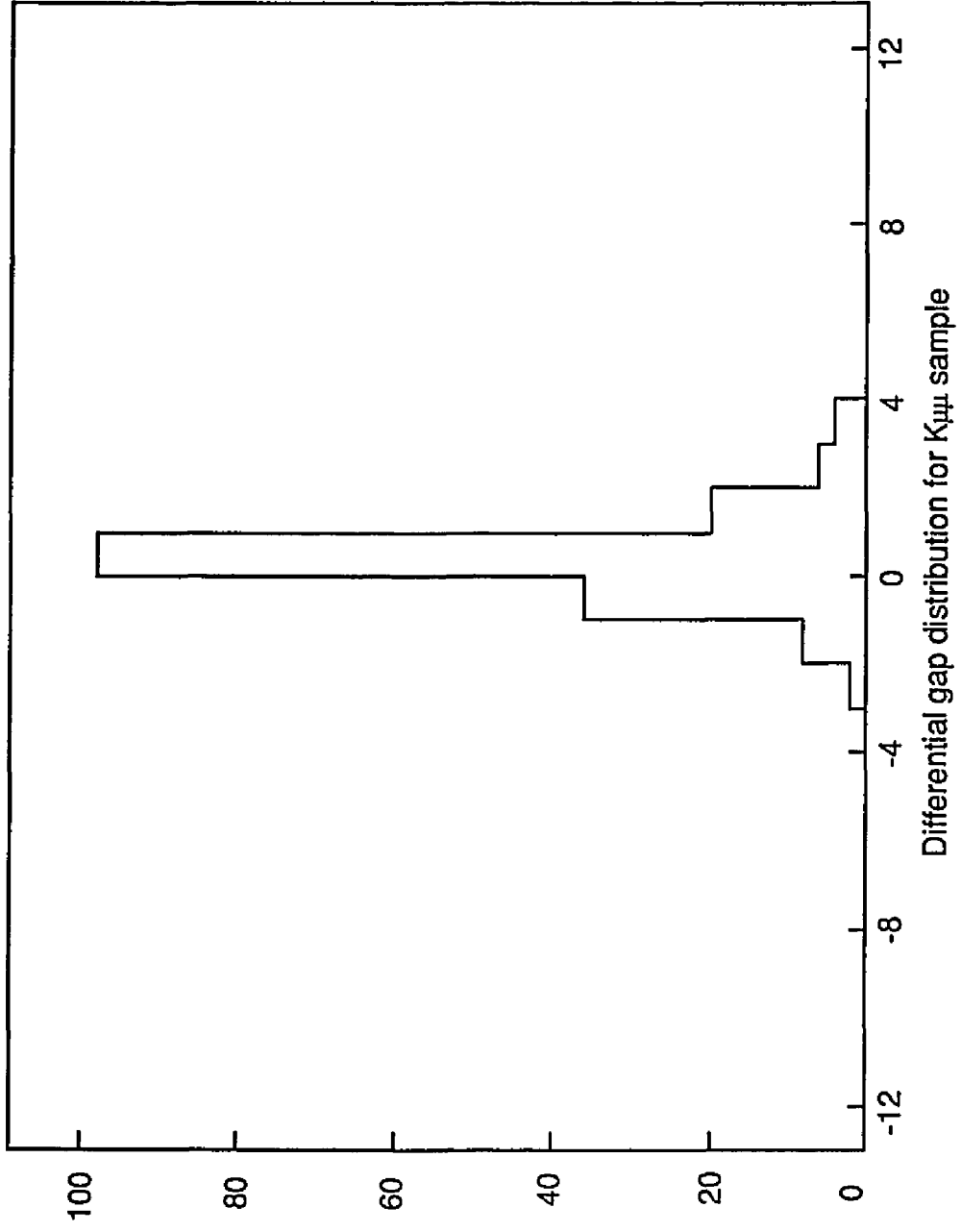


Figure 75.

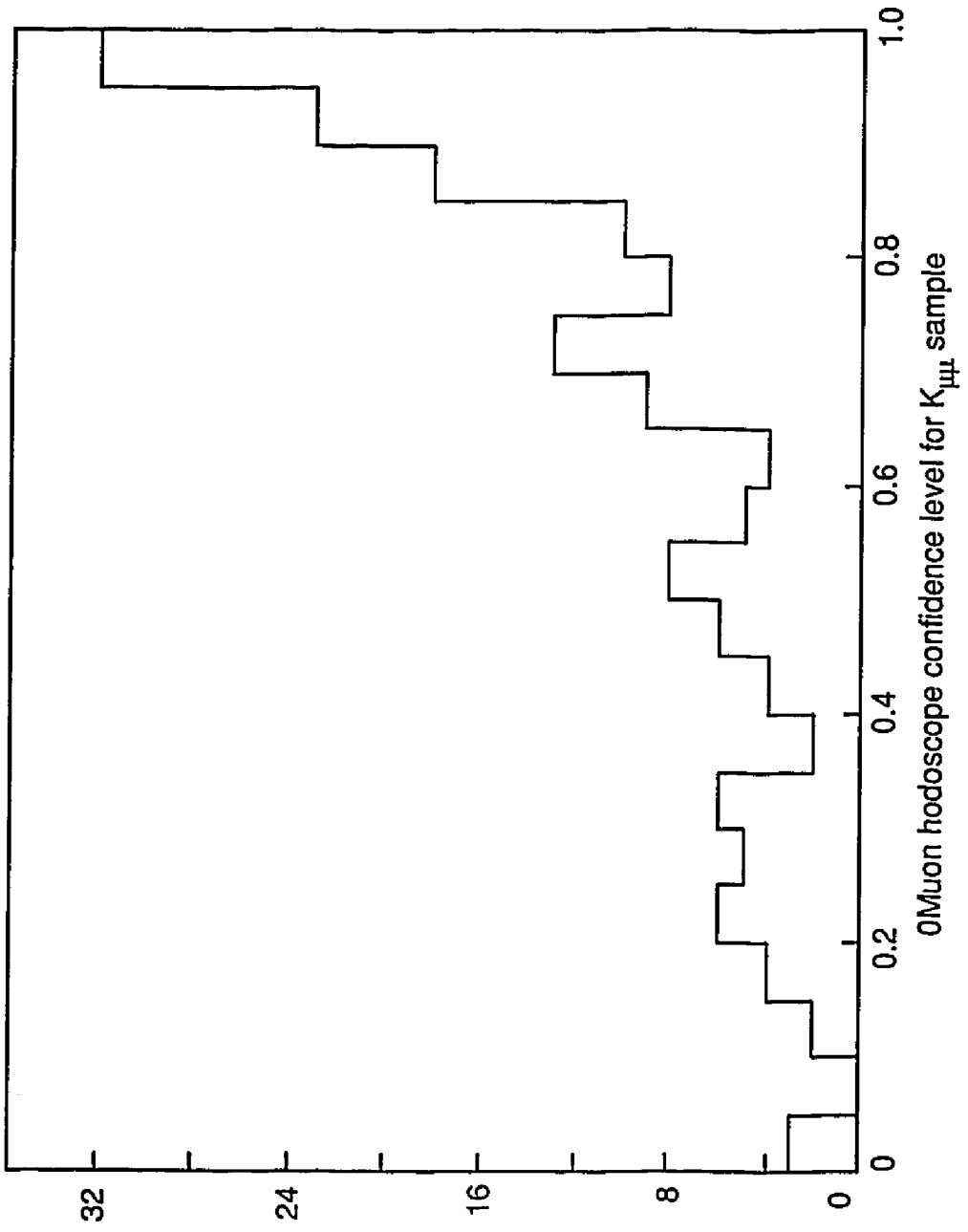


Figure 76.

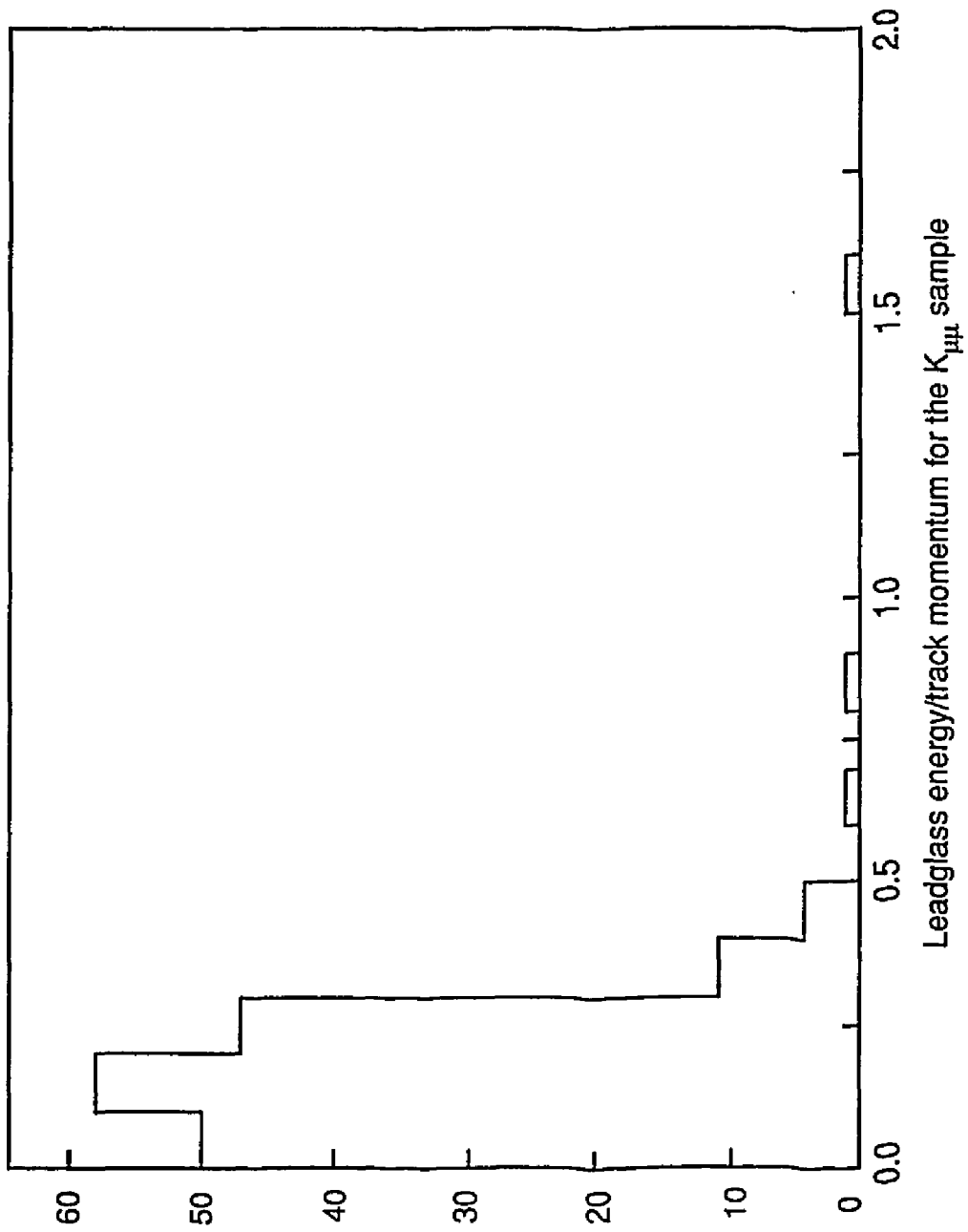
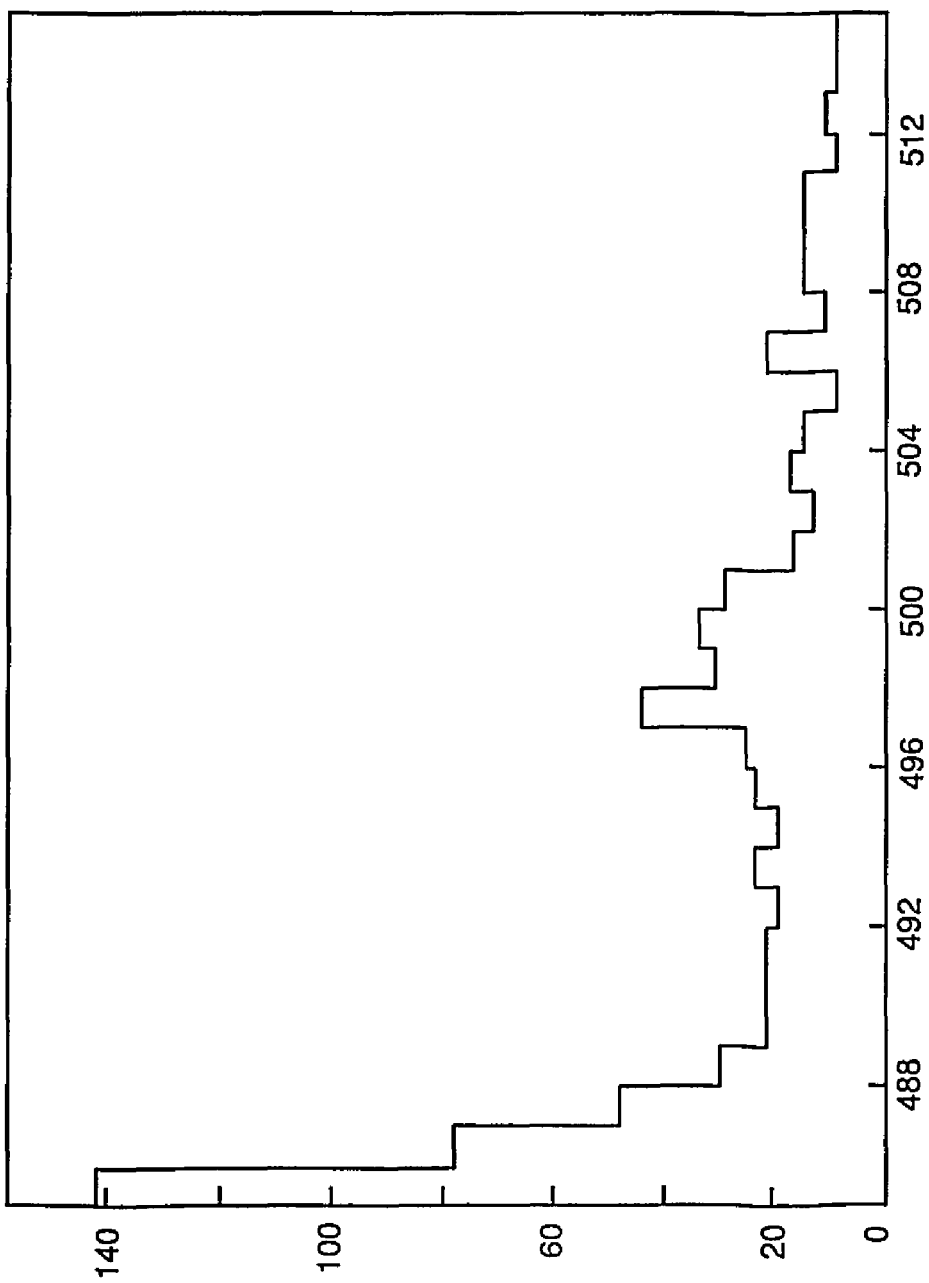


Figure 77.



Invariant mass for $K_{\mu\mu}$ sample without offline muon selection

Figure 78.

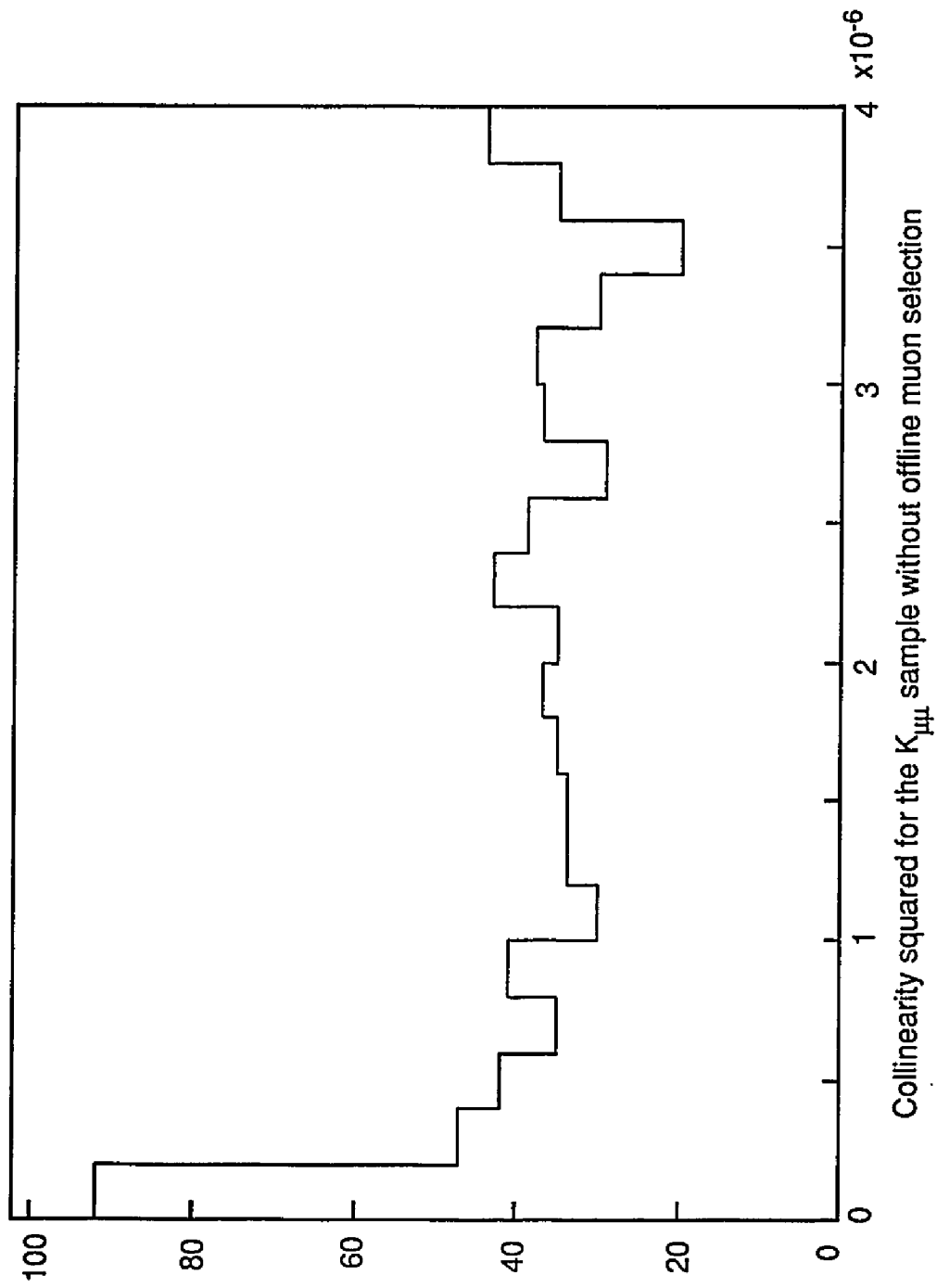


Figure 79.

<38L E-771>

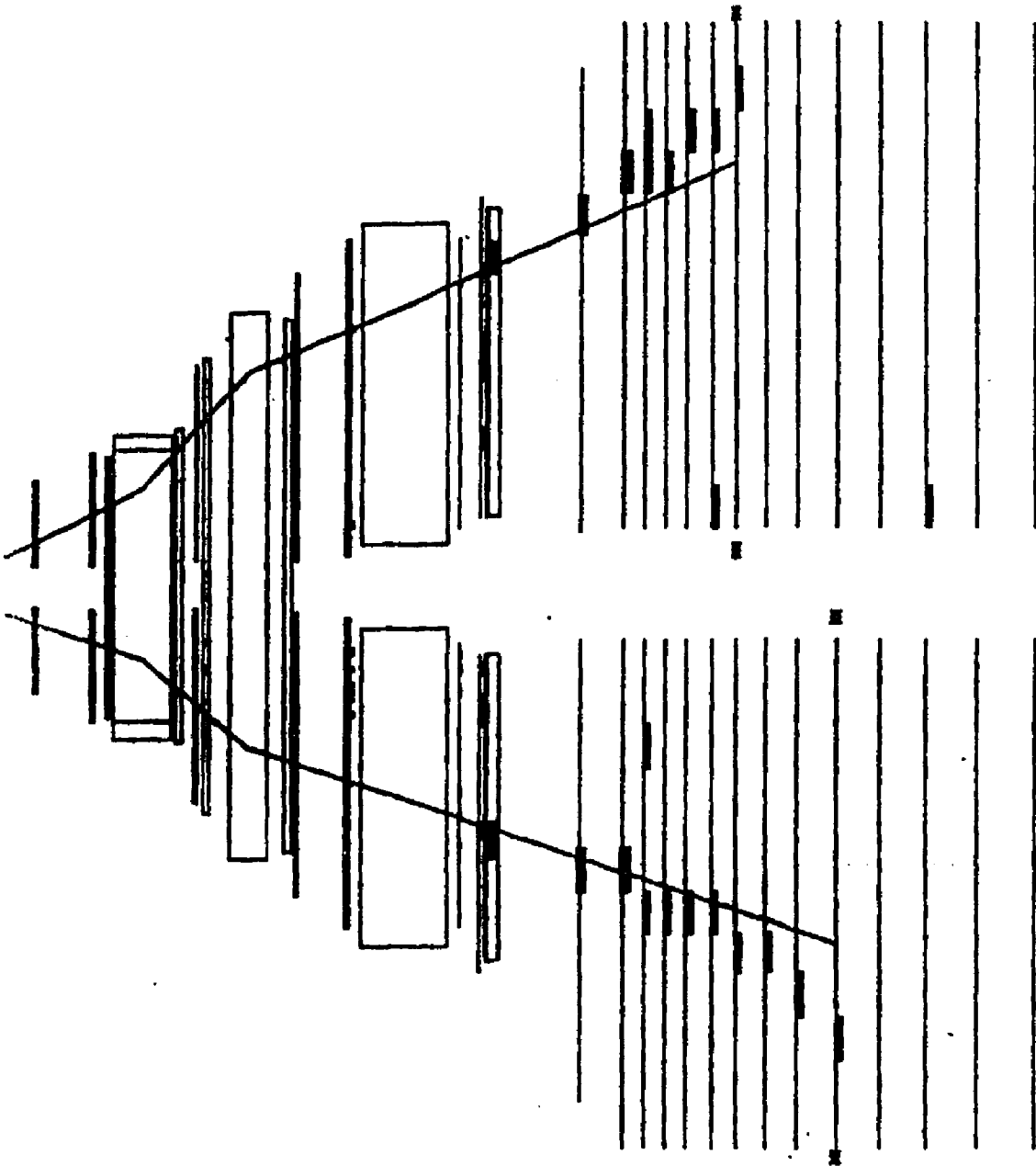


Figure 80

RUN NO. 3251, EVENT NO. 538, RECORDED 1-MAY-1988 22:151

< BM, E791 >

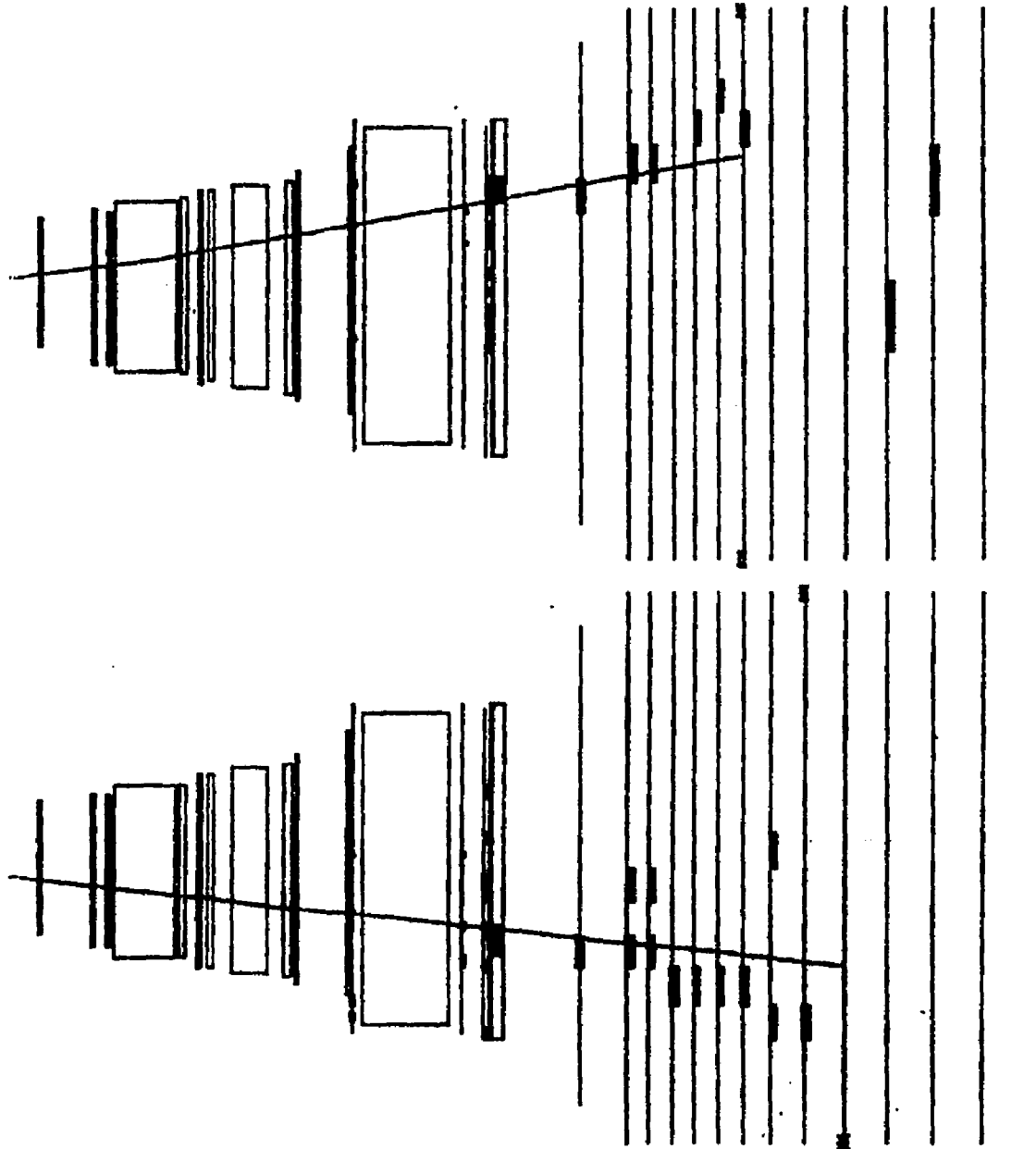


Figure 81

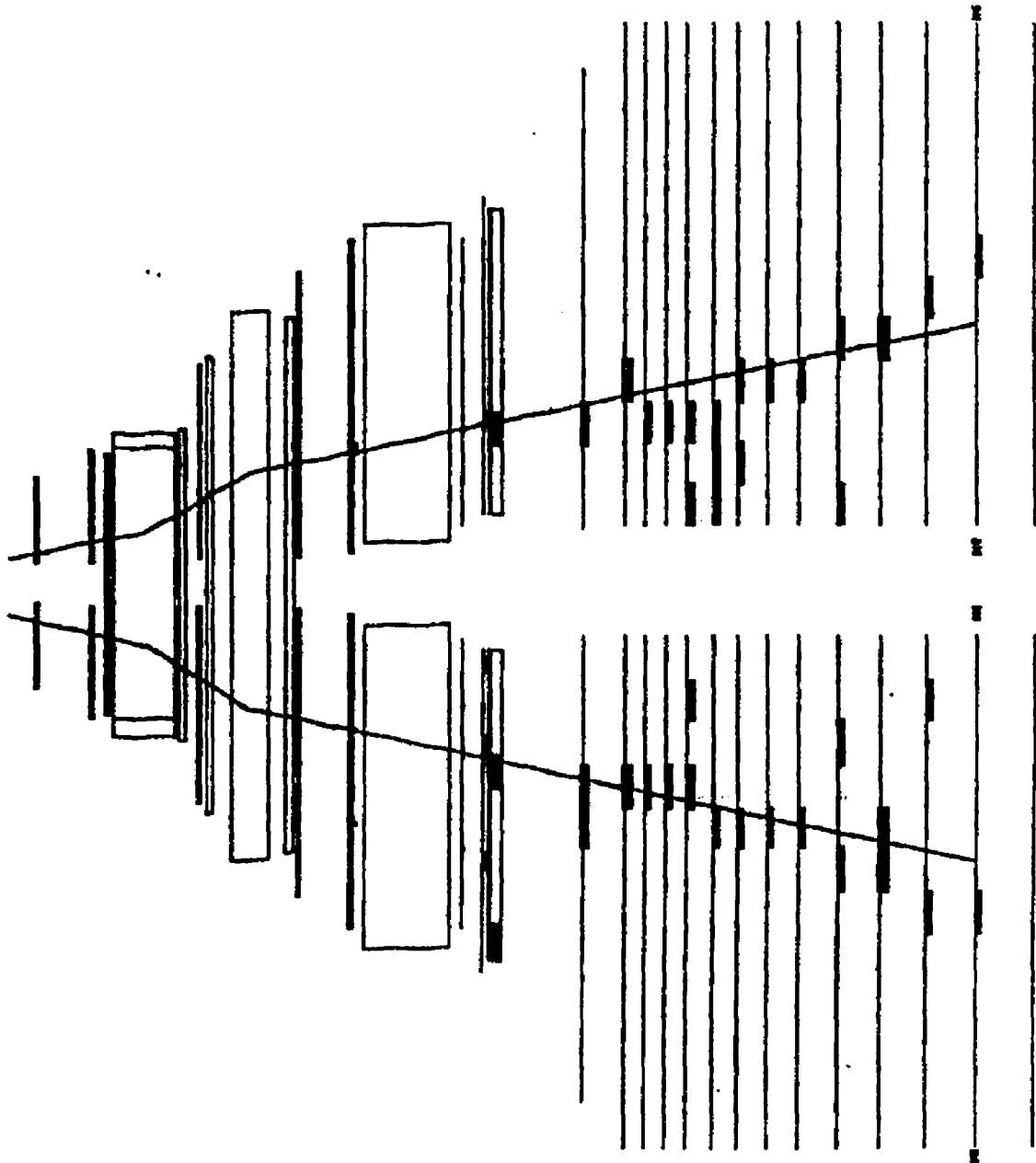


Figure 82

RUN NO. 2536, EVENT NO. 418, RECORDED 7 APR 1988 1857:10

<IML E791>

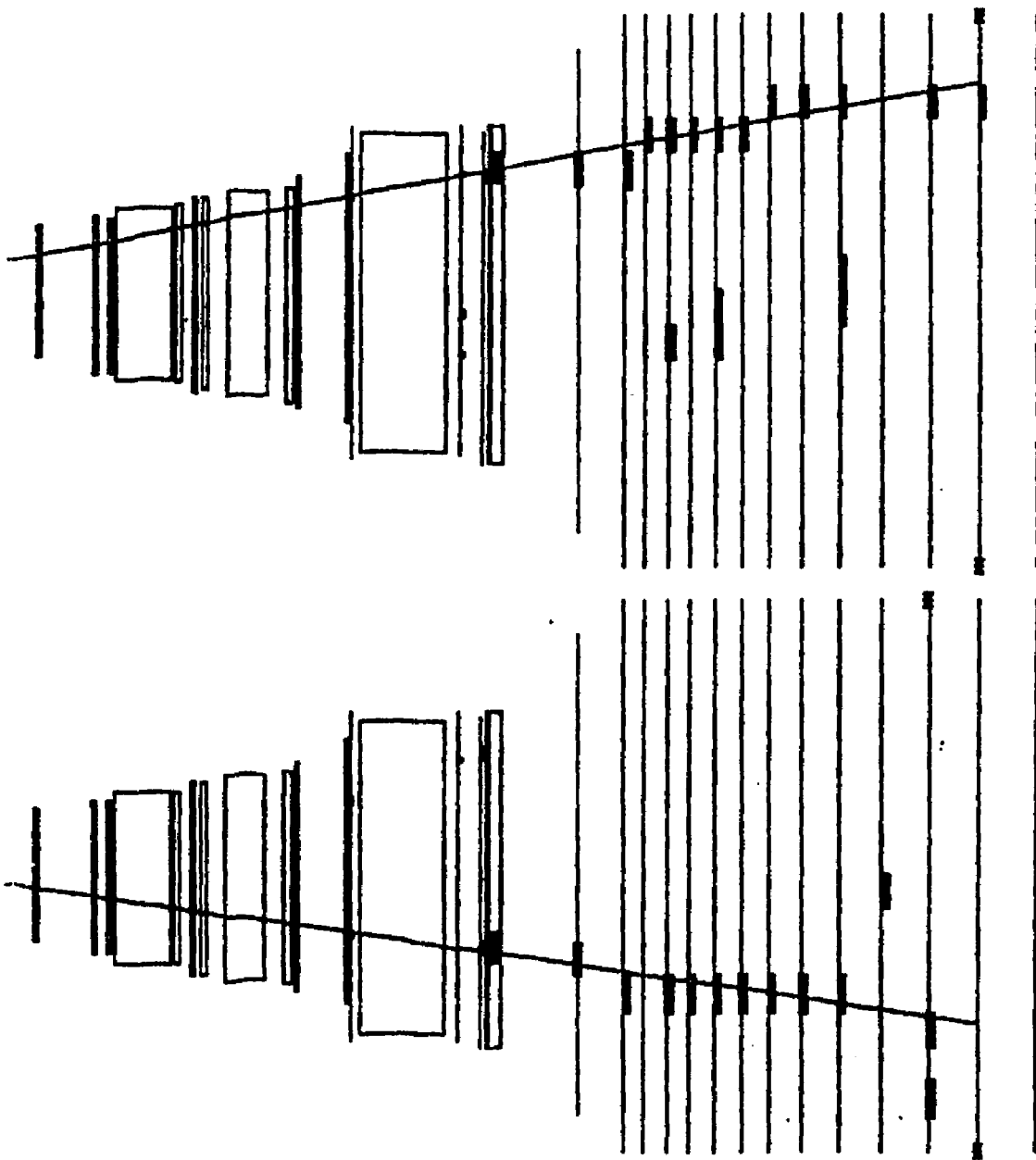


Figure 83

VITA

Christopher John Kenney

Born in Quincy, Massachusetts, September 19, 1960. Graduated from Scituate High School in Scituate, Massachusetts, June 1978, B.S., Duke University, 1982, M.S., the College of William and Mary, 1984.

In September 1984, the author became a doctoral candidate at the College of William and Mary in the Department of Physics. The author was a Virginia Commonwealth Fellow during 1987.